Application and Development of the Linear Combination of Atomic Orbitals B-spline Density Functional Theory Method for the Molecular Electronic Continuum

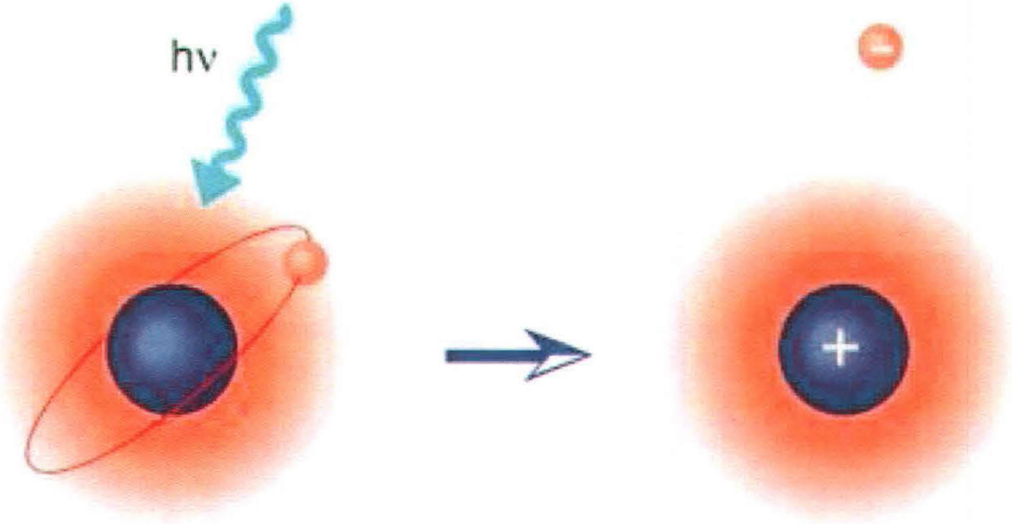

Devis DI TOMMASO

UNIVERSITÀ DEGLI STUDI DI TRIESTE

XVIII ciclo del
Dottorato di Ricerca in Scienze Chimiche

Application and Development of the Linear Combination of Atomic Orbitals B-spline Density Functional Theory Method for the Molecular Electronic Continuum

(Settore scientifico-disciplinare CHIM/02 CHIMICA FISICA)

Dottorando:
Devis DI TOMMASO 177

CS

Coordinatore del Collegio dei Docenti:
Chiar.mo Prof. Giuliana PITACCO
(Università di Trieste)
GPitacco

Relatore:
Chiar.mo Prof. Piero DECLEVA
(Università di Trieste)
Pie Dec

Contents

Overview of the Thesis

The aim of the present thesis is the application and development of the Linear Combination of Atomic Orbitals (LCAO) B-spline Density Functional Theory (DFT) method for the molecular electronic continuum.

Although in recent years promising efforts toward the accurate description of the electronic continuum have been done within both *ab initio* and DFT formalism, the formers are in general restricted to the accurate description of small systems. Despite its computational economy, the accuracy obtainable with DFT is usually comparable with the computationally more expensive *ab initio* approaches and it can be profitably applied to extended and more chemically interesting systems.

The B-spline Density Functional based methods has already proven to give accurate and realistic description of the molecular electronic continuum. Moreover, the implementation of the multicentred (LCAO) approach has allowed the treatment of rather large, low symmetric molecules, making the LCAO B-spline DFT method a competitive computational tool for the interpretation of the increasing amount of experimental data on complex molecular systems, and for carrying out in silicon experiments in order to predict connections between the physical observables of the photoionization phenomena and the electronic/structural molecular properties.

In order to make contact with the subsequent Chapters of the thesis, a brief introduction to the photoionization process and to the molecular photoionization theory are presented in Chapter 1. The computational methods actually employed throughout in the present work are illustrated in Chapter 2. The results obtained are then presented in the remaining Chapters of the thesis.

The work is conveniently subdivided in three main parts.

In the first part (Chapters 3-6) a computational study on the Circular Dichroism in the Angular Distribution (CDAD) of photoelectrons emitted from chiral molecules ionised by means of circularly polarized light of defined helicity is considered.

In Chapter 3 [J. Chem. Phys **120**, 3284(2004)] the LCAO B-spline DFT method is applied to the calculation of the CDAD effect from a series of chiral derivatives of oxirane.

In Chapter 4 [J. Chem. Phys., in press] the LCAO B-spline DFT method is applied to study the circular dichroism in core and valence photoelectron angular distribution of camphor enantiomers, and the results compared with the Continuum Multiple Scattering calculation and with the available experimental data.

In Chapter 5 [ChemPhysChem **6**, 1164-1168 (2005)] a collaborative theoretical and experimental study on the circular dichroism in the angular distribution of valence photoelectrons emitted by 3-hydroxytetrahydrofuran molecule is presented.

In Chapter 6 [ChemPhysChem, in press] the influence of conformational factors on the photoionization dynamical parameters, with special attention to the CDAD effect, is investigated by means of LCAO B-spline DFT calculations.

The second part (Chapter 7) of the thesis deals with the theoretical investigation of the correctness of the statistical ratio assumption for the Branching Ratio (BR) in core ionisation of chemically non-equivalent atomic sites of the same species.

In Chapter 7 [J. Chem. Phys. **123**, 064311 (2005)] the LCAO B-spline DFT method is employed for accurate calculations of carbon 1s photoionization cross section on selected organic molecules, in order to verify the correctness of the assumption mentioned above.

The last part of the thesis (Chapter 8) deals with the shape resonance problem.

In Chapter 8 the development of a method to localise and characterise in molecular terms the shape resonances is presented, always in the framework of the B-spline DFT approach.

1 Introduction to the Photoionization Process

The theoretical description of the molecular photoionization process is currently a field actively investigated since it provides detailed information both on the dynamics of the collision process and the intrinsic properties of the initial and final target states, and thanks to the always increasing amount of accurate experimental data on complex molecular systems, available through the use of advanced synchrotron radiation. Moreover recent measurements on a new effect connected with the ionisation of chiral systems, molecules of enormous interest both in scientific and industrial level, have started appearing in literature showing very promising potentialities. All this calls for a corresponding level of theoretical description of the photoionization process. The first purpose in photoionization properties calculation is a good representation of the final state wave function, which belongs to the continuum electronic spectrum of the target system. Despite the consistent effort in this field it is fair to say that the treatment of the continuum states is vastly more difficult than the corresponding bound state problem. Consequently the continuum state calculation is still far from being a standard approach in the area of quantum chemistry. Main difficulties are connected with the peculiar character of the unbound state of the system, which is delocalized on the whole space, i.e. not square-integrable, as a consequence of the physics that lies beyond the photoionization phenomena.

The purpose of this introductory chapter is to provide a general overview of the photoionization process with special attention to its dynamical aspects. The theory of the molecular photoionization is briefly presented, emphasizing the approximation employed in the present thesis for the description of the final state wave function. Ending the chapter, the theoretical methods currently employed for the calculation of the physical observable of the process are mentioned.

1.1 Photoemission and Photoionization. Generalities

The key process in photoelectron spectroscopy is the photoelectric effect i.e. the electron emission from atomic or molecular targets as a result of their interaction with photons of suitable energy. In this process an N-electron initial state (atom or molecule) interacts with a photon of energy $h\nu$ evolving asymptotically toward a final bound state of N-1 electrons and a free electron. The whole process can thus be sketched as in Fig. 1.1.

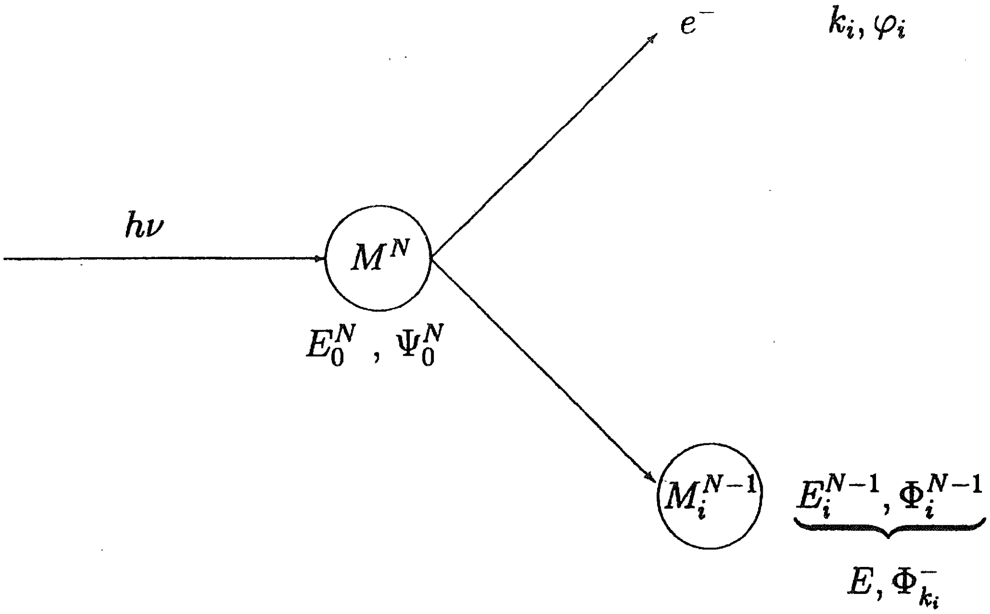

Figure 1.1: The photoionization process.

In Fig. 1.1 the various symbols have the following meanings:

Ψ_0^N	Electronic wave function of the initial state. It can be the ground state of the target system or suitable prepared excited states.
$\Phi_{k_i}^-$	Wave function of the final state (residual target *plus* photoelectron)
φ_i	Wave function of the outgoing photoelectron
k_i	Photoelectron momentum that is detected ($E = k_i^2/2m$)
Φ_i^{N-1}	Wave function of the final state of the target with N-1 electrons
$h\nu$	Photon energy

E_0^N	Energy of the initial state
E_i^{N-1}	Energy of the final state of the target

$\Phi_{k_i}^-$ represents the final state of the whole system which is asymptotically constituted by a residual target system made of N-1 electrons in a given state Φ_i^{N-1} and a free electron of momentum k_i which is detected. The experimental observable quantities are:

- The energy spectra of the photoelectrons
- The intensity and the angular distribution of the photoelectrons

From these experimental quantities the ionisation potential of the various initial states and dynamical photoionization parameters can be extracted.

1.2 Ionisation Potentials

In the photoeffect, conservation of energy and momentum requires that the kinetic energy of the excited electron, neglecting the kinetic energy of the remaining system due to recoil, is given by:

$$E_0^N + h\nu = E_i^{N-1} + \frac{k_i^2}{2m} \tag{1.1}$$

For a given photon energy, from the photoelectron spectrum the various ionisation potentials, IP_i, can be extracted:

$$IP_i = E_i^{N-1} - E_0^N \tag{1.2}$$

Within the molecular orbital framework each ionisation potential represents the ejection of an electron from a different orbital. One actually observes a band made up of vibrational and rotational levels. In photoelectron spectroscopy rotational levels are rarely observed, but vibrational structures is frequently observed and may be used for characterising the photoionization process. The observed envelope in the vibrational structure is generally the result of a Franck-Condon transition since photoionization take place in a short time compared to the time scale for nuclear motion.

1.3 The Photoionization Dynamical Parameters

In the usual experimental conditions ($h\nu < 10^3$ eV) the electric-dipole transition dominates. The photoionization process can thus be described as a dipole transition between initial and final states of the target. For atoms and unoriented (non-chiral) molecules, the dependence of the photoelectron intensity on the emission angle θ of the ejected photoelectron relative to the incident beam direction is given in terms of two parameters, σ_i, the *partial photoionization cross section*, and β_i, the *asymmetry parameter*, associated with the residual system in the i-th state. If we consider linearly polarized light, the transition rate per incident photon current density and unitary solid angle, termed *differential cross section* [1] is given by:

$$\frac{d\sigma_i}{d\Omega} = \frac{\sigma_i}{4\pi}\left[1 + \beta_i P_2(\cos\theta)\right] \qquad (1.3)$$

$$P_2(\cos\theta) = 3\cos^2(\theta) - 1$$

where P_2 is the Legendre polynomial of second degree of argument θ. The form of (1.3) follows from symmetry principles [2] The requirement that the photoelectron intensity is positive restricts β to the range $-1 \leq \beta \leq 2$. Within the independent particle model the various σ_i represent the probability that the i-th orbital is ionised. When $P_2(\cos\theta) = 0$, which happens at the so-called *magic angle*, θ_m = 54°44', the emission process is β-independent and this allows a direct comparison between ratioes of measured intensities and cross sections.

However, for the special case of the photoionization of unoriented chiral molecules with circularly polarized light, due to the reduced symmetry [3,4] the dependence of photoelectron intensity on the emission angle θ is given by a third parameter, D_i, the *dichroic parameter*. The expression for the differential cross section becomes:

$$\frac{d\sigma_i}{d\Omega} = \frac{\sigma_i}{4\pi}\left[1 + (1/2)^{|m_r|}\beta_i P_2(\cos\theta) + m_r D_i \cos\theta\right] \qquad (1.4)$$

where m_r is 0, +1 or −1 respectively for linear (and the expression (1.4) reduces to (1.3)), left circular or right circular polarization. The laboratory frame is defined by the incident photons: the polar axis corresponds to the electric vector or propagation direction respectively for linear or circular light polarization. We define left and right circularly polarized light according to the value $m_r = +1$ or $m_r = -1$ of the projection of the photon spin along its momentum. Accordingly, the electric vector describes a positive (right-handed) or negative (left-handed) screw. With circular polarized light the third term gives a contribution which changes sign according to the light helicity. The photoelectron intensity along the θ direction shows different values when, at fixed m_r, the photoelectron intensity is measured in a forward/backward geometry, showing an asymmetry in the angular distribution according to the $\cos(\theta)$ dependence of the last term in equation (1.4).

It is worth noting that the experimental observables σ, β and D can be viewed as functions of two variables, namely photon energy and ionisation energy, i.e. $\sigma(h\nu, IE)$, $\beta(h\nu, IE)$ and $D(h\nu, IE)$ which represent the dynamical aspect of the process. A complete determination of these observables leads to two-dimensional profiles which incorporate a wealth of information. Actually, sections of the $\sigma(h\nu, IE)$ profile at $h\nu =$ const. are the photoelectron spectra whereas those at IE = const. correspond to $\sigma_i(\omega)$, $\beta_i(\omega)$ and $D_i(\omega)$ and profiles related to a particular state Φ_i^{N-1} of the residual system.

1.4 Resonances

In the process of atomic and molecular photoemission different types of resonant processes can occur, which experimentally manifest as a peak or a modulation in the cross section kinetic energy profile. Resonances can give information concerning metastable negative states, electronic affinities, excited electronic states and orbital energies of unbound states. Furthermore, in scattering and photoionization processes the study of the resonance structures is one of the best techniques to validate a given quantum mechanical approach for the treatment of the phenomenon since the calculation of the resonant structures is much more sensitive to the dynamical part of the process than the cross section values of the background.

At first, resonances can be classified with the number of electrons actually involved in the process [5].

The *autoionization resonances* are a typical two-electron resonance phenomenon, commonly observed both in atoms and molecules and are a manifestation of inter-electronic correlation effects. As an example in Fig. 1.2 is schematically reported the Ar $3s^2 3p^6 \rightarrow 3s3p^6 np$ autoionization resonances. The continuum state can be reached by direct or indirect photoionization process. In the direct photoionization process the photon is absorbed and one electron is emitted directly into the continuum. In the indirect way the atom first is excited having the electron in a state which is above the first ionisation threshold. In a second step then one says that these discrete states decay by "autoionization" emitting an electron. The kinetic energy of the photoelectrons emitted in the direct process and in the indirect one is the same. The interference of both paths result in resonance profiles in the cross section as well as in the angular distribution.

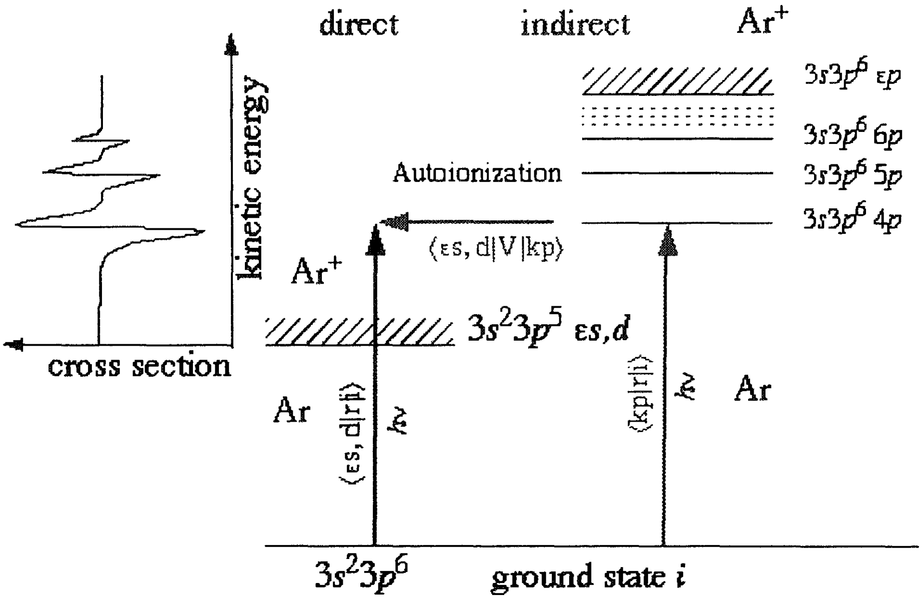

Figure 1.2: Schematic representation of the Ar $3s^2 3p^6 \rightarrow 3s3p^6 np$ autoionization resonances.

The theoretical description of the autoionization resonances should take explicitly into account the interaction between discrete and continuum states. This interaction has been treated by Fano on the basis of the configuration interaction (CI) procedure [6]. Taking aside the details of the derivation, it can be shown that the total cross section within an isolated resonance structure can be parameterized as follows:

$$\sigma(E) = \sigma_0(E)\left[\rho^2\left(\frac{(q+\varepsilon)^2}{1+\varepsilon^2} - 1\right) + 1\right] \qquad (1.5)$$

$$\varepsilon = \frac{2(E - E_{res})}{\Gamma}$$

In Eqt. (1.5) ε is the "reduced energy", E_{res} the resonance energy position and Γ the resonance width. The q parameter characterises the line profile and ρ^2, called "correlation index", represents the ratio between resonant intensity and the sum of resonant and non-resonant intensities. Resonance line profiles for selected values of the q parameter are reported in Figure 1.3. As can be seen, for $|q| > 1$ one observes a resonance peak, whereas for $|q| < 1$ the profile is a "window" resonance.

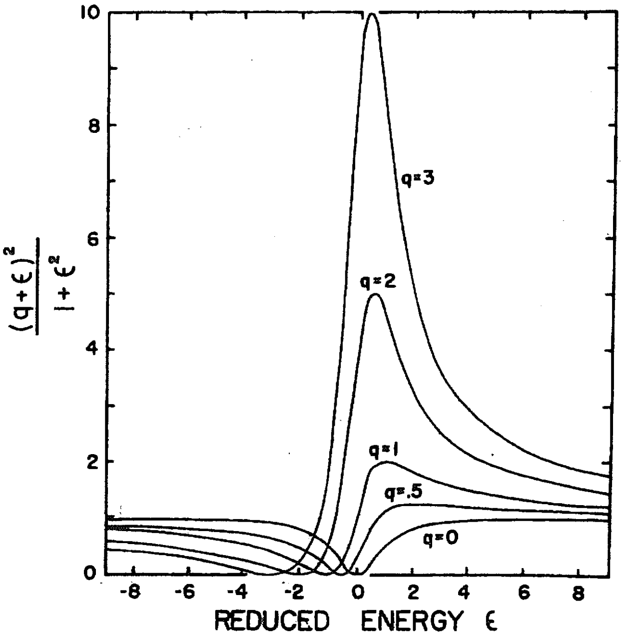

Figure 1.3: Resonance line profiles for different values of the q parameter

The computational approach employed in the present thesis for the study of the molecular photoionization process does not include explicitly the two-electron excitations, therefore the two electron resonant process will not be considered further.

Resonant structures that can be viewed as a one-electron process are classified as *giant resonances* and *shape resonances* for the atomic and molecular case, respectively. In both cases they cause large variations in the cross section profiles. In the atomic photoionization, where there is spherical symmetry, the one-electron resonances can be easily rationalised. The effective potential experienced by an electron is given by the central field potential [7] and the radial wave function is given by:

$$\left[-\frac{1}{2}\frac{d^2}{dr^2}+\frac{l(l+1)}{2r^2}+V(r)\right]\psi_{nl}(r)=E\psi_{nl}(r) \tag{1.6}$$

$V(r)$ is the Coulombic potential of the nuclei and other electrons and $(l(l+1)/2r^2)$ is the centrifugal repulsion term and results from the solution of the angular momentum part of the Schrödinger equation. For high values of l, the effect of the centrifugal term is to create a double well potential, which has an intermediate range maximum which may be positive. The presence of a double well potential for a bound electron (usually f or d) determines the appearance of a delayed maxima in their ionisation cross section profile [1]. The presence of a double well potential also for the continuum orbital gives rise to a giant resonance, due to the formation of a quasi-bound eigenstate in the inner well, with much enhanced maxima over a small energy range. Both effects give rise to a maximum in the cross section some way above threshold, but the giant resonance is characterized by a much sharper feature [8]. In molecular photoionization the one-electron resonances are the so-called shape resonances because they are critically dependent on the form of the molecular potential [9,10]. This itself is determined by the physical shape of the molecule, from which the name of the effect derives. Shape resonance manifest themselves as increases in cross section, which are frequently sharp and generally at low photoelectron kinetic energy. In analogy with the atomic case, shape resonances are generally associated with the formation of quasi-bound states in potentials well.

Since the corresponding eigenstates are well localised within the molecular region the transition moment is correspondingly high giving the observed rise in the cross section. In the molecular case, because of the three-dimensional potential, it is not always easy to predict systematically the appearance of a shape resonance. An overview of the methods currently employed for the description of the resonances in the molecular electronic continuum is given in Chapter 8. Moreover an approach developed during this thesis for the characterization of the shape resonances will be presented.

1.5 Spectroscopic Techniques

The particular requirements on a photon source for photoelectron excitation depend on the nature of application. As a general rule a source of high intensity having as small width in energy as possible is desired. Depending on the photon source which is actually used for photoelectron excitation we can fundamentally distinguish three different photoionization experiments:

1) *Ultraviolet Photoelectron Spectroscopy, UPS or PES.* Developed by Turner et Al., [12] uses the resonance radiation generated in a low pressure gas discharge. The most frequently employed line (He I at 21.22 eV) is used to excite outer valence electron spectra. In order to study the inner valence electrons the conventional way is to use the He II radiation at 40.8 eV.

2) *X-ray Photoelectron Spectroscopy, XPS or ESCA.* Developed by Siegbahn et Al. [13]. It uses mainly the Kα lines of Mg ($h\nu = 1253.6$ eV) and Al ($h\nu = 1486.6$ eV). While valence electron spectra excited by soft X-rays do not have the same resolution as UV-excited spectra, the photoelectron intensities are more readily interpreted at higher photoelectron energies (inner valence and core photoelectrons).

3) *Synchrotron Radiation, SR.* The increased availability of synchrotrons and storage rings has led to impressive development during recent years to make use of this radiation in excitation of electron spectra. The wavelength distribution of the radiation is continuous, from the infrared to the X-ray region, and it is emitted as a

well-collimated beam tangentially to the electron orbit. Furthermore, radiation emitted in the plane of the orbit is completely linearly polarised. The SR offers various advantages as compared with the use of traditional line sources. Being the wavelength distribution continuous it allows the determination of complete profiles of the dynamical observables $\sigma(\omega)$, $\beta(\omega)$ and $D(\omega)$ in a wide spectral range. The analysis of the energy dependence of these fundamental variables, which constitutes the dynamical part of the photoionization process, provides in fact valuable information concerning the initial and final states of the system under consideration.

With the ever-increasing use of high-resolution and high-flux synchrotron radiation sources a wealth of experimental data have become available in recent years. However their interpretation is usually rather difficult and theoretical approaches which treat explicitly the electronic continuum are needed for a quantitative analysis of the experimental results.

1.6 Theory of Molecular Photoionization

In this section an introduction to the molecular photoionization theory is presented. At first the approach considered in the present thesis to treat the final state wave function is given. Then the boundary conditions appropriate for ionisation processes are mentioned. The derivation of the angular distribution of electrons ejected from randomly oriented molecules is finally outlined. At the end of the section a short review of the theoretical methods currently employed for the calculation of the continuum electronic spectrum is given.

1.6.1 The Single-channel Approach

In the electric dipole approximation, the computational study of the photoionization process requires the calculation of the transition dipole moment:

$$M_{f\leftarrow 0} = \langle \Psi_f^N | \hat{P} | \Psi_0^N \rangle \tag{1.7}$$

where Ψ_0^N is the wave function of the initial state, Ψ_f^N is the wave function of the final state (residual ion *plus* photoelectron) and $\hat{P}$ is the N-electron dipole operator, $\hat{P} = \sum_{i=1}^{N} \hat{p}_i$. A specification of the initial bound-state and the final continuum-state is therefore required. Bound state calculation can be nowadays routinely performed at various levels of theory. On the other hand specification of the final state wave function is the more difficult task. In fact molecular (and atomic) photoionization is a many final state channel process and the exact expression for the stationary state wave function associated with the scattering of an electron off an ion is given by the *close coupling* expansion [14]:

$$\Psi_f^N = \sum_j \Psi_j^{N-1} \varphi_{k_j} \qquad (1.8)$$

where Ψ_j^{N-1} is a normalized N−1 electron state wave function of the j-th residual ion, φ_{k_j} is a one-electron wave function that describes the photoelectron ("channel"), and where the proper coupling and the antisymmetrization of the product has been implicitly included. At a given excitation energy *hv* a final state Ψ_j^{N-1} is accessible, and named *open* channel, if $E_j^{N-1} - E^N \geq hv$, where E^N is the total energy of the system and E_j^{N-1} is the energy of the residual ion. If $E_j^{N-1} - E^N < hv$ is negative the channel is named *closed*. The inclusion in the expression (1.8) of closed channels is necessary to treat explicitly the electron correlation, in order to describe phenomena like autoionization resonances and polarization effects. In medium-sized molecules the wave function structure for the continuum states (1.8) requires too big computational resources and therefore the full closed-coupling approach is not practicable. The theoretical method employed in the present thesis for the description of the molecular photoionization is based on the so-called *single-channel approximation*. This approach considers a single term in the expansion (1.8) and the final state wave function is approximated by:

$$\Psi_f^N \approx \Psi_{f_j}^N = \Psi_{f_j}^{N-1} \varphi_{k_j} \qquad (1.9)$$

Consider now a general full CI description of the molecule and the residual ion built over two different orthogonal molecular orbital (MO) basis sets [15]: the

MO basis $\{\varphi_q\}$ for the initial state Ψ_0^N and the MO $\{\varphi_p\}$ for the residual ion $\Psi_{f_i}^{N-1}$. It is possible to expand the final state orbitals in the initial state ones,

$$\varphi_p = \sum_q \varphi_q \langle \varphi_q | \varphi_p \rangle \qquad (1.10)$$

which for creation and annihilation operators take the form:

$$\hat{a}_p^+ = \sum_q \hat{a}_q^+ \langle \varphi_q | \varphi_p \rangle \qquad (1.11a)$$

$$\hat{a}_p = \sum_q \langle \varphi_p | \varphi_q \rangle \hat{a}_q \qquad (1.11b)$$

With respect to the MO basis $\{\varphi_q\}$ the second-quantization analogue of the dipole moment operator $\hat{P} = \sum_{i=1}^{N} \hat{p}_i$ can thus be written

$$\hat{P} = \sum_{r,q} \langle r | \hat{p} | q \rangle \hat{a}_r^+ \hat{a}_q \qquad (1.12)$$

and the transition moment (1.7)

$$M_{f_i \leftarrow 0} = \sum_{r,q} \langle r | \hat{p} | q \rangle \langle \Psi_{f_i}^N | \hat{a}_r^+ \hat{a}_q | \Psi_0^N \rangle \qquad (1.13)$$

In the single-channel approximation (see Eqt. 1.9) the final state can be written as:

$$\Psi_{f_i}^N = \hat{a}_\varepsilon^+ \Psi_{f_i}^{N-1} \qquad (1.14)$$

where $\hat{a}_\varepsilon^+$ creates an electron in the continuum orbital. The substitution of (1.14) in (1.15) and expansion of $\hat{a}_\varepsilon$ in operators for the initial state according to (1.11b) leads to the final expression for the transition dipole moment:

$$M_{f_i \leftarrow 0} = \sum_q \langle \varepsilon | \hat{p} | q \rangle \langle \Psi_{f_i}^{N-1} | \hat{a}_q \Psi_0^N \rangle + \sum_q \langle \varepsilon | q \rangle \langle \Psi_{f_i}^{N-1} | \hat{P} | \hat{a}_q \Psi_0^N \rangle \qquad (1.15)$$

where $\{\varphi_q\}$ is the MO basis set for the description of the bound state Ψ_0^N. The first term in (1.16) is named *direct transition* where the dipole operator connects to the continuum orbital, and the second sum represents *conjugate* transition where it connects to passive orbitals. Within the one channel-approximation (1.15) represents the general expression of the transition amplitude associated with the photoionization process. At this point two assumption: (a) a single-particle model (HF or DFT like approaches) is employed to describe the initial and residual ion, consequently Ψ_0^N

and $\Psi_{f_j}^{N-1}$ are represented by a single Slater determinant; (b) the MO employed to describe the initial state $\{\varphi_q\}$ are also employed to describe the residual ion (the orbitals not directly involved in the photoionising transition remain unchanged). Then:

- the summation of the first term over all MO of the molecule reduces to a single one-electron transition dipole moment $\langle\varepsilon|\hat{p}|j\rangle$, where φ_j is the ionised orbital;
- in the second term $\langle\varepsilon|p\rangle = 0$ for each MO. In fact if the same $\{\varphi_q\}$ is employed for molecule and ion, then in the single-particle picture $\{\varphi_q\}$ will be the bound states of the electrons of the ionised system, while φ_ε will represent the wave function of the electron scattered by the molecular potential of the ion. On the basis of the orthogonality theorem [16], bound eigenstates and scattering eigenstates of the same Hamiltonian are orthogonal and the conclusion $\langle\varepsilon|p\rangle = 0$ holds.

Therefore, if the final state wave function is treated in the single-channel approximation, the initial and final states are described by single determinants, and the one-electron states not involved in the process remain unchanged, then the transition amplitude for the ionisation process reduces to a dipole moment between the ionised orbital and the orbital of the photoelectron:

$$M_{f_j\leftarrow 0} = \langle\varepsilon|\hat{p}|j\rangle \tag{1.16}$$

1.6.2 Boundary Conditions for Ionisation Processes

In addition to the many-final channel character of the photoionization process further difficulties are connected with the particular boundary conditions that the final state wave function must satisfy. In ionisation processes boundary conditions are different than those applicable to collision processes because of the long-range Coulomb potential.

In what follows the boundary conditions appropriate for ionisation process in the simple case of an electron moving in a short-range spherical potential are first presented. The modifications of the single-channel one-electron wave function induced by the presence of a long-range Coulomb field are then introduced. The appropriate boundary condition for the more complicated molecular photoionization case are finally considered.

Boundary conditions for ionisation in the short range potential. Consider a system in which the photoelectron moves in a spherically symmetric, short-range potential. The single-electron Hamiltonian H_0 is given by

$$H_0 = \frac{1}{2}p^2 + V(r) \qquad (1.17)$$

where *V(r)* decreases asymptotically faster than r^{-3}. For a given energy $E = k^2/2$, the proper stationary scattering wave function of the Hamiltonian (1.18) associated to the photoionization process are the so called "out states", which have the following asymptotic form:

$$\Psi_{\vec{k}}^-(\vec{r}) \xrightarrow[r\to\infty]{} \frac{1}{(2\pi)^{3/2}}\left[\exp(i\vec{k}\cdot\vec{r}) + f^-(\vec{k}',\vec{k})\exp(-ikr)/r\right] \qquad (1.18)$$

That is, one requires that the final state wave function satisfies the so-called *incoming-wave boundary condition* [1]. Namely, at large *r* the wave function has the form of a plane wave plus *incoming* spherical waves. The function $f^-(\vec{k}',\vec{k})$ is called the scattering amplitude and represents the probability amplitude for scattering between momentum states $\vec{k}$ e $\vec{k}'$. As a consequence of the "on-shell" T matrix condition [16] $\vec{k}'$ has the same magnitude of $\vec{k}$ but is directed along $\vec{r}$.

The expansion of the stationary scattering wave function $\Psi_{\vec{k}}^-(\vec{r})$ in terms of the partial waves scattering states $\langle \mathrm{x} | E,l,m+\rangle$ can be written as [1]:

$$\Psi_{\vec{k}}^-(\vec{r}) = \frac{1}{k^{1/2}}\sum_{l=0}^{\infty}\sum_{m=-l}^{+l} i^l \exp[-i(\delta_l)]\mathrm{Y}_{lm}^*(\hat{k})R_{El}(r)\mathrm{Y}_{lm}(\hat{r}) \qquad (1.19)$$

In (1.19) the energy-normalized single electron wave function corresponding to the angular momentum state (*l,m*) is $R_{El}(r)\mathrm{Y}_{lm}(\hat{r})$. The function $R_{El}(\vec{r})$ is an eigenstate of the radial Schrödinger equations corresponding to the Hamiltonian in (1.17). The asymptotic form of the radial wave function $R_{El}(\vec{r})$ is:

$$R_{El}(r)\xrightarrow[r\to\infty]{}\left(\frac{2}{\pi k}\right)^{1/2}\frac{\sin(kr-l\pi/2+\delta_l)}{kr} \qquad (1.20)$$

which defines the l-th partial phase shift δ_l. Comparing (1.20) with the asymptotic behaviour of the free-electron radial solution, the spherical Bessel function $j_l(kr)$ [17],

$$j_l(kr)\xrightarrow[r\to\infty]{}\frac{\sin(kr-l\pi/2)}{kr} \qquad (1.21)$$

it is possible to notice that in the presence of the interaction the radial function $R_{El}(r)$ is shifted by the phase δ_l.

Boundary conditions for ionisation in a long-range Coulomb tail potential. Consider now the situation in which the potential in (1.17) has a long-range Coulomb tail

$$V(r)\xrightarrow[r\to\infty]{}-\frac{1}{r}$$

Such a potential might be appropriate for the photoelectron resulting from the photoionization of a neutral atom or molecule. The major modification is that the photoelectron always sees a Coulomb field asymptotically and the asymptotic form of the "out state" $\Psi_{\vec{k}}^{-}(\vec{r})$ is modified with respect to the short-range potential (1.18) [1]:

$$\Psi_{\vec{k}}^{-}(\vec{r})\xrightarrow[r\to\infty]{}\Psi_{\vec{k}}^{c}(\vec{r})+\frac{1}{(2\pi)^{3/2}}f^{-}(\vec{k}',\vec{k})\frac{exp[-i(kr-\gamma\, log(2kr))]}{r} \qquad (1.22)$$

Here $\Psi_{\vec{k}}^{c}(\vec{r})$ is a Coulomb wave normalized using the incoming wave boundary condition, the function $f^{-}(\vec{k}',\vec{k})$ is called *scattering amplitude*, due to the short-range part of the potential, where $\vec{k}'=k\hat{r}$ and γ is given by $\gamma=-\frac{1}{k}$.

The partial-wave expansion of the *incoming-wave normalized wave function* $\Psi_{\vec{k}}^{-}(\vec{r})$ can be written as:

$$\Psi_{\vec{k}}^{-}(\vec{r})=\frac{1}{k^{1/2}}\sum_{l=0}^{\infty}\sum_{m=-l}^{+l}i^{l}\, exp[-i(\sigma_l+\delta_l)]Y_{lm}^{*}(\hat{k})R_{El}(r)Y_{lm}(\hat{r}) \qquad (1.23)$$

In (1.23) the energy-normalized single electron wave function corresponding to the angular momentum states (l,m) is $R_{El}(r)\mathrm{Y}_{lm}(\hat{r})$. The set of eigenfunctions $\{R_{El}(r)\mathrm{Y}_{lm}(\hat{r})\}$ represent the possible states of the photoelectron scattered by the potential $V(r)$. The infinite summation over the angular momentum quantum number in (1.23) is related to the infinite degeneragy of the photoelectron wave function since, for a fixed energy $E = k^2/2$, the photoelectron angular momentum $\hat{k}$ can have infinite directions. The expression (1.23) relates $\Psi_{\vec{k}}^{-}(\vec{r})$ to the usual numerically calculated radial wave function $R_{El}(r)$, which is an eigenstate of the radial Schrödinger equation corresponding to the Hamiltonian in H_0, and that asymptotically (when $V(r)$ approaches the Coulomb tail) may be written as a linear combination of regular, $F_l(kr)$, and irregular, $G_l(kr)$, spherical Coulomb Functions [1], whose asymptotic behaviour is:

$$F_l(kr) \xrightarrow[r\to\infty]{} \sin\theta_l \qquad (1.24a)$$

$$G_l(kr) \xrightarrow[r\to\infty]{} \cos\theta_l \qquad (1.24b).$$

In Eqs. (1.24) $\theta_l = kr - l\frac{\pi}{2} - \gamma\log 2kr + \sigma_l$ is the asymptotic phase for the Coulombic long-range potential seen by the photoelectron, and σ_l is the Coulomb phase shift, defined as $\sigma_l = arg\,\Gamma(l+1+i\gamma)$.

The particular linear combination defines the l-th partial phase shift, δ_l, due to the short-range part of the potential:

$$R_{El}(r) \xrightarrow[r\to\infty]{} \frac{1}{r}\sqrt{\frac{2}{\pi k}}\sin(\theta_l + \delta_l) = \frac{1}{r}\sqrt{\frac{2}{\pi k}}(F_l\cos\delta_l + G_l\sin\delta_l) \qquad (1.25)$$

The *incoming-wave normalized state* in the presence of a long-range Coulomb potential, given by (1.23), is of the same form as the corresponding wave function in the absence of the Coulomb potential, given by (1.19). The major differences are related to the asymptotic form of the radial wave function and to the presence of the Coulomb phase shift σ_l entering in the normalization factor.

Boundary condition for molecular photoionization. For the molecular case the anisotropy of the potential introduces coupling between the different partial waves channels. In order to calculate $\Psi_{\vec{k}}^{-}(\vec{r})$, the *incoming-wave normalized wave function* of the combined system (M^{+} + e) associated to a photoelectron energy $k^{2}/2$, it is necessary to introduce a complete set of final states (channels). Consider $\Psi_{hl}^{\lambda\mu-}$, a complete set of channel functions which describe the ejected electron in the ($\lambda\mu hl$)-th channel [18]:

$$\hat{H}\Psi_{hl}^{\lambda\mu-} = \left(E_{f} + \frac{k^{2}}{2}\right)\Psi_{hl}^{\lambda\mu-} \tag{1.26}$$

where $\hat{H}$ is the Hamiltonian of the combined system (M^{+} + e), E_f is the energy of the residual ion and ε_f is the energy of the photoelectron. In the notation used an irreducible representation (IR) of the molecular point group has been denoted by λ, μ stands for a component of this representation if its dimensionality is greater than one and h distinguishes between different bases of the same IR corresponding to the same value of l. The channel functions $\Psi_{hl}^{\lambda\mu-}$ satisfy the so-called *S-matrix incoming wave boundary conditions*, which are appropriate for molecular photoionization processes [19], and for the open-channels have the following asymptotic form:

$$\Psi_{hl}^{\lambda\mu-} \xrightarrow[r\to\infty]{} i\sqrt{\frac{1}{2\pi k}}\Phi^{+}r^{-1}\sum_{h'l'}\left[e^{-i\theta_{l'}}\left(S^{\lambda}\right)^{+}_{hl,h'l'} - e^{i\theta_{l'}}\delta_{h,h'}\delta_{l,l'}\right]X_{h'l'}^{\lambda\mu}(\hat{r}) \tag{1.27}$$

Here,

- Φ^{+} is the electronic state of the residual ion.
- $\left(S^{\lambda}\right)_{hl,h'l'}$ is the scattering matrix of the collision theory. The meaning of the scattering matrix is that $\left(S^{\lambda}\right)_{hl,h'l'}$ equals the probability amplitude from the basis state $\Psi_{hl}^{\lambda\mu-}$ to the basis state $\Psi_{h'l'}^{\lambda\mu-}$ [20]. The S matrix is diagonal in p and independent of the degeneracy index μ.
- $X_{hl}^{\lambda\mu}(\hat{r})$ are the generalised harmonics defined as the symmetry-adapted linear combinations of real spherical harmonics [21]:

$$X_{hl}^{\lambda\mu}(\hat{r}) = \sum_{m} b_{mlh\lambda\mu} Y_{lm}(\hat{r}) \tag{1.28}$$

and are the bases for irreducible representation of the molecular point group under consideration.

For molecular photoionization the final state wave function $\Psi_{\vec{k}}^{-}(\vec{r})$ should represent asymptotically an *incoming-wave normalized Coulomb function* plus additional *incoming Coulomb spherical waves* generated by scattering from the non-Coulomb part of the potential [18], analogously to the simpler single-channel case (see Eqt. 1.22). The final state wave function can be expanded in terms of the *S*-matrix normalized wave functions (1.27):

$$\Psi_{\vec{k}}^{-} = \sum_{\lambda\mu h l} a_{hl}^{\lambda\mu} \Psi_{hl}^{\lambda\mu -} \tag{1.29}$$

and the expansion coefficients are to be such that $\Psi_{\vec{k}}^{-}(\vec{r})$ has the correct asymptotic form. It can be shown [22] that (1.29) reduces to:

$$\Psi_{\vec{k}}^{-} = \sum_{\lambda\mu h l} i^{l} e^{-i\sigma_{l}} X_{hl}^{\lambda\mu *}(\hat{k}) \Psi_{hl}^{\lambda\mu -} \tag{1.30}$$

The channel functions $\Psi_{hl}^{\lambda\mu -}$ satisfy *complex* asymptotic boundary condition which are computationally inconvenient. It is possible to define an equivalent set of channel functions with the '*K matrix*' normalisation whose asymptotic behaviour is in the form of real standing waves:

$$\Psi_{hl}^{\lambda\mu} \xrightarrow[r\to\infty]{} \sqrt{\frac{2}{\pi k}} \Phi^{+} r^{-1} \sum_{h'l'} \left[sin\,\theta_{l'} \delta_{h,h'} \delta_{l,l'} + cos\,\theta_{l'} K_{hl,h'l'}^{\lambda} \right] X_{h'l'}^{\lambda\mu}(\hat{r}) \tag{1.31}$$

where the real and symmetric *K* matrix is related to the *S* matrix by $S = (1 + iK)(1 - iK)^{-1}$. Then by expanding the sine and cosine factors in (1.26), in terms of exponential functions, it can be shown [23] that

$$\Psi_{hl}^{\lambda\mu -} = \sum_{h'l'} \left[\left(1 + iK^{\lambda}\right)^{-1} \right]_{hl,h'l'} \Psi_{h'l'}^{\lambda\mu} \tag{1.32}$$

1.6.3 Angular Distribution of Photoelectrons

In the present subsection the general expression, within the dipole approximation, for angular distribution of electrons ejected from randomly oriented molecules is derived [24].

Consider two coordinate systems whose origins coincide with the centre of mass of the molecule. One of the two is the photon frame of reference, which also defines a laboratory frame (LF). Its polar axis is the direction of incidence (electric vector) for non-linearly polarised (linearly polarised) light. The second coordinate system is the molecule-fixed (MF). Here the axis of the highest symmetry in a molecule is the polar axis. If β, α, γ are the Euler angles of MF in LF, then a rotation by ($-\gamma$, $-\beta$, $-\alpha$) will bring MF into coincidence with LF. Following Edmonds [25], the rotation matrices $\mathrm{D}(\omega = \alpha, \beta, \gamma)$

$$\mathrm{Y}_{lm}(\hat{r}') = \sum_{m'} \mathrm{D}^{l}_{m'm}(\omega)\mathrm{Y}_{lm'}(\hat{r}) \qquad (1.33)$$

where unprimed (primed) variables refer to the molecule (photon) frame of reference.

The angular distribution of the photoelectrons ejected into the solid angle $d\Omega$ about the direction of propagation $\hat{k}$ from a molecule with fixed orientation ω in space is given by [26]

$$\frac{d^2\sigma}{d\omega d\Omega} = 3\pi\left(\frac{e^2}{\alpha E_r}\right)^2 \left|\left(\frac{\mu}{\hbar^2}\right)^{1/2} \left\langle \Psi^-_{\vec{k}} \middle| \hat{F} \middle| \Psi_0, 1m_r \right\rangle\right|^2 \qquad (1.34)$$

Here $|\Psi_0\rangle$ and $|\Psi^-_{\vec{k}}\rangle$ are the properly normalized electronic ground state of the molecule M and the final continuum state of the (M^+ + e) system, $\hat{F}$ is the electromagnetic transition operator, E_r is the energy of the incident radiation whose state of (linear and left (right) circular) polarization is specified by m_r (= 0 and +1 (−1) respectively), α the fine-structure constant. Substitution of $|\Psi^-_{\vec{k}}\rangle$ by the expansion in terms of the *S*-matrix normalized wave functions (1.30) gives:

$$\frac{d^2\sigma}{d\omega d\Omega} = 3\pi\left(\frac{e^2}{\alpha E_r}\right)^2 \left|\sum_{\lambda\mu hl} (-i)^l e^{i\sigma_l} \left\langle \Psi^{\lambda\mu -}_{hl} \middle| \hat{F} \middle| \Psi_0, 1m_r \right\rangle X^{\lambda\mu}_{hl}\left(\hat{k}\right)\right|^2 \qquad (1.35)$$

Thus the ionisation amplitude is decomposed into a sum of transitions each involving the continuum wave function of the (M^+ + e) system belonging to a different IR of its symmetry group. Considering the dipole length approximated form for the photoemisssion operator $\hat{F}$ [18], the expansion of the photon state $|1m_r\rangle$ in the MF frame of reference using relation (1.33), and the symmetry-adapted linear combinations of real spherical harmonics (1.28). the expression (1.35) can be written as

$$\frac{d^2\sigma}{d\omega d\Omega}=4\pi^2\alpha E_r\sum_{\substack{\lambda\mu hlm\lambda_r\\ \lambda'\mu'h'l'm'\lambda'_r}}(-i)^{l-l'}e^{i(\sigma_l-\sigma_{l'})}b_{hlm}^{\lambda\mu}b_{h'l'm'}^{\lambda'\mu'*}\mathrm{D}^{l}_{\lambda_r m_r}(\omega)\mathrm{D}^{l*}_{\lambda'_r m'_r}(\omega)$$
$$\times D_{hl}^{\lambda\mu-}(\lambda_r)D_{h'l'}^{\lambda'\mu'-*}(\lambda'_r)Y_l^m(\hat{k})Y_{l'}^{m'*}(\hat{k}) \tag{1.36}$$

where

$$D_{hl}^{\lambda\mu-}(\lambda_r)\equiv\left\langle\Psi_{hl}^{\lambda\mu-}\middle|\sum_{s=1}^{N}\hat{\xi}_{\lambda_r}\cdot\vec{r}_s\middle|\Psi_0\right\rangle \tag{1.37}$$

In the last equation $\hat{\xi}_{m_r}$ is the spherical unit vector in the direction of the polarisation of the incident radiation in MF of reference.

In order to obtain a compact expression of the differential cross section for random molecular orientation, it is useful to express the dependence of the expression (1.36) on the direction of the propagation of the photoelectron from MF frame ($\hat{k}$) to the LF of reference ($\hat{k}'$) using the inverse of (1.33). It results, after averaging the resulting expression over all molecular orientations,

$$\frac{d\sigma}{d\Omega'}=4\pi^2\alpha E_r\sum_{\substack{\lambda\mu hlm\lambda_r n\\ \lambda'\mu'h'l'm'\lambda'_r n'}}(-i)^{l-l'}e^{i(\sigma_l-\sigma_{l'})}b_{hlm}^{\lambda\mu}b_{h'l'm'}^{\lambda'\mu'*}$$
$$\times b_{hlm}^{\lambda\mu}b_{h'l'm'}^{\lambda'\mu'*}D_{hl}^{\lambda\mu-}(\lambda_r)D_{h'l'}^{\lambda'\mu'-*}(\lambda'_r)\mathrm{Y}_l^n(\hat{k}')\mathrm{Y}_{l'}^{n'*}(\hat{k}') \tag{1.38}$$
$$\times\int\mathrm{D}^{1}_{\lambda_r m_r}(\omega)\mathrm{D}^{1*}_{\lambda'_r m'_r}(\omega)\mathrm{D}^{l*}_{\lambda m}(\omega)\mathrm{D}^{l'}_{\lambda' m'}(\omega)\frac{d\omega}{8\pi^2}$$

This expression can be simplified combining the first and the third D functions throughout the Clebsh-Gordan series [24], which introduce the angular momentum transfer l_t, given by coupling the angular momentum states $|lm\rangle$ and $|1m_r\rangle$. Then, using the symmetric expression for the integral over the product of the three D functions [25], the expression (1.38) reduces to

$$\frac{d\sigma}{d\Omega'}=(-1)^{m_r}\pi\alpha E_r\sum_L A_L(k)P_L(\cos\theta') \tag{1.39a}$$

where

$$\begin{aligned} A_L(k) = {} & (2L+1)\begin{pmatrix} 1 & 1 & L \\ m_r & -m_r & 0 \end{pmatrix} \sum_{ll'l_t} (-i)^{l-l'+l_t} (-1)^{1+L} e^{i(\sigma_l-\sigma_{l'})} \\ & \times \left[(2l+1)(2l'+1)\right]^{1/2} \begin{pmatrix} l & l' & L \\ 0 & 0 & 0 \end{pmatrix} \begin{Bmatrix} l & 1 & l_t \\ 1 & l' & L \end{Bmatrix} \\ & \times I(l_t, l, l') \end{aligned} \tag{1.39b}$$

and $I(l_t, l, l')$ is the product of the (l_t, m_t)-reduced transition amplitudes and represents the dynamical part of the photoionization process:

$$I(l_t, l, l') = \sum_{m\lambda_r m'\lambda_r'} D^{l_t}_{lm}(\lambda_r) D^{l_t}_{l'm'}(\lambda_r')^* \delta_{m-\lambda_r, m'-\lambda_r'} \tag{1.40a}$$

where

$$D^{l_t}_{lm}(\lambda_r) = (-1)^{l_t+m}(2l_t+1)^{1/2}\begin{pmatrix} 1 & l & l_t \\ -\lambda_r & m & \lambda_r-m \end{pmatrix} \sum_{\lambda\mu h} b_{lmh\lambda\mu} D^{\lambda\mu-}_{lh}(\lambda_r) \tag{1.40b}$$

Within the dipole approximation, the equation (1.39) is the general expression for the angular distribution of electrons ejected from randomly oriented molecules. Considering the importance of the expression (1.39) for the present thesis it merits to be commented thoroughly:

- the Wigner 3-j symbol $\begin{pmatrix} 1 & 1 & L \\ -m_r & m_r & 0 \end{pmatrix}$ in (1.39b) reduces the L-summation to three terms, namely those with $L = 0, 1, 2$;
- for linearly polarized light ($m_r = 0$) the $L = 1$ term vanishes and the Yang theorem result (1.3) is obtained whereby the lab-frame anisotropy depends only on the isotropic term (P_0) and the second Legendre polynomial term (P_2);
- for left, right circularly polarized light ($m_r = \pm 1$, respectively) the $L = 1$ term is not automatically constrained to be zero and the expression for the differential cross section reduces to (1.4). Therefore an additional term may result in the angular distribution (P_1) and it can be readily shown that $A_1^{+1} = -A_1^{-1}$, where the upper index stands for the light helicity. Furthermore, it can be shown (see Chapter 3, § 3.3) that $A_1(k)$ is not zero only when the molecule is *chiral* and $A_l^{m_r}(+) = -A_l^{m_r}(-)$, where (+), (–) stands for the dextrorotatory or levorotatory enantiomers of the optically active molecule, respectively. Therefore for

randomly oriented chiral species the photoelectron intensity along the emission angle direction shows different values when, at fixed light helicity m_r, the photoelectron intensity is measured in a forward/backward geometry, showing an asymmetry in the angular distribution, according to the cos(θ') dependence of the $L = 1$ term. This effect is referred to as **Circular Dichroism in the photoelectron Angular Distribution** (**CDAD**). Computational studies of the CDAD effect are extensively considered in the present thesis and it is referred to Chapters 3-6 for a detailed analysis on cases studied.

As it has already been mentioned in subsection 1.6.1, the method employed in the present thesis, in addition to ignoring nuclear vibrations, assumes that the initial and final states of the process, i.e. $|\Psi_0\rangle$ and $|\Psi_k^-\rangle$, are single Slater determinants and that the one-electron states not involved in the process remain unchanged. This reduces the transition amplitude (1.37) to a one-electron dipole integral.

Ending this section a short overview of various theoretical methods employed in the literature for the calculation of the molecular electronic continuum spectrum is given. The approach used in this thesis is then fully presented in Chapter 3.

- *The one-centre expansion* (OCE) was one of the first methods employed for the determination of the continuum wave functions [27]. The electronic wave function and the molecular potential are expanded in spherical harmonics centred on the CM of the molecular system. An intrinsic limit of the method is the high number of angular momenta required for the accurate description of the system, particularly in the presence of heavy atoms in off-centred positions [28].

- The *Continuum Multiple Scattering Method* (CMSM) [22,29] is a popular method capable of managing large systems with several atoms. It is based on partitioning the molecular field into closely packed spherical regions centred on each atomic site and one surrounding the molecule. The potential is spherically symmetric in each spherical region whereas the interstitial region is represented by a constant potential. The one-electron wave functions are obtained by enforcing appropriate physical boundary conditions at the nuclei and at infinity, and by requiring that the wave function and its derivative be continuous at all the spherical boundaries in the molecular field.

- The *Linear Algebraic* method developed by Schneider and Collins for electron-molecule collisions [30] reformulates the scattering problem reducing the relevant equations to a set of linear-algebraic equations.

A class of methods, which have been used recently in the literature, is based on the description of the atomic and molecular continuum by means of L^2 functions [31]. These methods offer particular advantages with respect to the traditional methods based on numerical integration because the basic algorithms are conveniently reduced to matrix operations, well suited for the modern supercomputers.

- The *Stieltjes Technique* (ST), is a completely L^2 approach and was introduced by Langhoff [32]. It is a multicentric approach and cross-section data are extracted from a pseudo-spectrum obtained after diagonalization of the Hamiltonian matrix in a conventional basis set. However the continuum wave function is not explicitly considered and angular distributions cannot be obtained from this approach.

- The *Schwinger variational method* [33] combines the use of a discrete basis set with an iterative procedure for the determination of the scattering solutions.

Finally, a mention deserves the method developed by Moccia and Spizzo [34]. In this approach, a CI procedure is realised by using a basis set which formally includes the continuum.

2 Computational Methods

This Chapter provides a description of the computational methods employed in the present thesis for the calculation of the molecular electronic continuum spectrum. In the first two sections emphasis is given to the particular basis set employed and to the algorithm adopted for the calculation of the continuum wave function. In the third section the Linear Combination of Atomic Orbitals (LCAO) B-spline Density Functional method is extensively described. The Chapter ends with a summary of the most crucial aspects that need to considered for an accurate calculation of the molecular photoionization with the LCAO B-spline DFT package.

2.1 The Basis Set

Basis set choice for the expansion of the photoelectron orbital is a crucial step towards the implementation of computational methods for the description of photoionization processes. As it has been shown in section 1.6, continuum wave functions are not L^2 in nature and the conventional nodeless basis sets employed for the bound state calculation are not suitable for a proper description of the oscillatory behaviour of the continuum states. In fact, although there are some attempts to employ Gaussian-type functions for the continuum states, the main limitation stems from the difficulty in obtaining a sufficient density of states without running into linear dependence problems.

Basis set suitable for the photoelectron orbital expansion should satisfy the following conditions:

- be able to describe the oscillating nature of the unbound state without running into linear dependencies;
- be energy-independent, in order to compute only once the Hamiltonian matrices for all considered photoelectron energy values;
- display good convergence properties with the possibility of enlargement without linear dependencies.

All these requirements can be met using the B-spline functions [1], which represent an optimum choice for an accurate representation of continuum states as well as the more slowly varying bound states [2,3].

A complete description of B-splines and their properties can be found in de Boor's book [1], while it is referred to Ref. [4] for a comprehensive review regarding to application of B-splines in atomic and molecular physics.

2.1.1 The B-spline Basis Set

In order to introduce the B-spline functions, consider an interval $I = [a, b]$ divided into l subintervals $I_j = [\xi_j \xi_{j+1}]$ by a sequence of $l+1$ points $\{\xi_j\}$ (called *breakpoints*, bp) in strict ascending order:

$$a = \xi_1 < \xi_2 < \cdots < \xi_{l+1} = b \tag{2.1}$$

Consider a second ascending sequence of points $\{t_i\}$ (called *knots*) but not necessary distinct:

$$\{t_i\}_{i=1,\ldots,m}\,, \quad t_1 \le t_2 \le \cdots \le t_m \tag{2.2}$$

which are associated with the bp's $\{\xi_j\}$ as follows:

$$\begin{aligned} &t_1 = t_2 = \ldots = t_k = \xi_1 \\ &t_{k+1} = \ldots = t_{k+\mu_2} = \xi_2 \\ &\ldots \\ &t_{n+1} = \ldots = t_{n+k} = \xi_{l+1} \end{aligned} \tag{2.3}$$

where μ_j is the multiplicity of the knots t_j at the inner bp's ξ_j. Actually only multiplicity at the inner bp's is important, and it will be always considered maximum multiplicity $\mu_1 = \mu_{l+1} = k$ at the endpoints.

As an example, it is reported in Fig. 2.1 a full set of B-spline relative to the knot sequence $\{0,0,0,1,2,3,4,5,5,5\}$. Each B-spline is a piecewise polynomial function (pp-function): a function made up of different polynomials pieces on adjacent subintervals of fixed order k ($k = 3$ in the case shown in Fig. 2.1) joined with a certain degree of freedom at the bps.

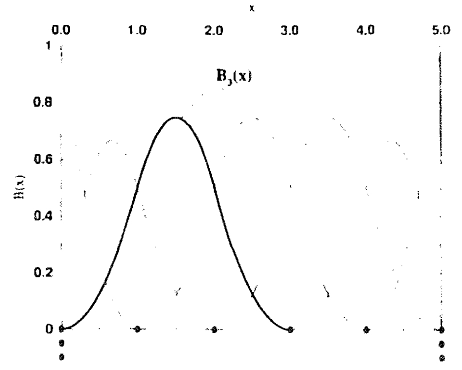

Figure 2.1: Full set of B-spline of order $k = 3$ relative to knot sequence $\{0,0,0,1,2,3,4,5,5,5\}$. Knots are represented by full circles.

A single B-spline $B(x)$ is defined by its order $k > 0$ and a set of $k+1$ knots, $\{t_i, \dots, t_{i+k}\}$ such that $t_i < t_{i+k}$. Important properties, apparent in Fig. 2.1, are the following:

1) $B_i(x)$ is a pp-function of order k over the interval $[t_i, t_{i+k}]$

2) $B_i(x) > 0$ for $x \in]t_i, t_{i+k}[$

3) $B_i(x) = 0$ for $x \notin [t_i, t_{i+k}]$

4) $B_i(x) \in C^{k-1-\mu_j}$, where μ_j is the multiplicity of the knot t_j; the maximum multiplicity is k, giving discontinuous functions, the minimum is one, giving $B_i(x) \in C^{k-2}$. The choice employed in the present thesis for the knot multiplicity is one at the inner bp's and maximum at the endpoints a, b. With this choice the number of B-spline n is given by

$$n = l + k - 1 \tag{2.4}$$

So one can vary the dimension of the basis by simply changing the order k or the knot sequence. In general, when approximating analytic functions it is best to employ high-order splines, typically in the range k = 7–10.

In general a family of B-spline functions $B_i(x), i = 1, \dots, n$ is completely defined given $k > 0$, $n > 0$ and a sequence of knots $t = \{t_i\}_{i=1,\dots n+k}$. Each $B_i(x)$ is defined over an interval $[t_i, t_{i+k}]$, which contains $k+1$ adjacent knots and is indexed by the first knot where it starts. $B_i > 0$ over the interval $]t_i, t_{i+k}[$, which is called the *support* of B_i, and $B_i = 0$ outside it. B-splines are therefore positive definite functions, which leads to matrices that are easier to diagonalize. Furthermore, B-spline are functions with compact support, i.e. they vanish identically outside at most k adjacent intervals, and this is another advantage in matrix calculation, since integrals over two B-spline of disjoint support is zero:

$$|i-j| \geq k \quad \rightarrow \quad B_i(x) B_j(x) f(x) = 0 \tag{2.5}$$

for every function $f(x)$. The resulting matrices are sparse and often, but not always, banded and a reduced number of matrix elements need to be computed and stored in memory.

In the expansion of an arbitrary function

$$f(x) = \sum_{j=1}^{n} c_j B_j(x) = \sum_{j=i-k+1}^{i} c_j B_j(x) \quad \text{for} \qquad x \in [t_i, t_{i+1}]$$

one has always only k terms contributing. Therefore, even if the B-spline basis set can be very dense, and so particularly suited for the representation of oscillatory functions like the photoelectron orbitals, the overlap is limited of at most k functions, reducing linear dependencies problems with respect to conventional basis set functions.

Imposing maximum multiplicity at the endpoints, as in (2.3), all $B_i = 0$ outside [a, b]. B-spline functions will have therefore a limited interval of definition and any arbitrary function is expanded in a limited interval. The method adopted in the present thesis to solve the Schrödinger equation for both discrete and continuum states then ideally divides radial spaces in two parts: the first, from origin a = 0 to b = R_{MAX}, dominated by the characteristic potential, large enough to contain all bound orbitals and expanded in terms of the L^2 basis set B-spline functions; the second, from R_{MAX} to infinity, where the potential can be considered essentially Coulombic, and the solution, which is known, can be fitted to the calculated one. It is worth noting that the basis set is different accordingly to the boundary conditions relative to the type of calculation. Boundary conditions are easily implemented using B-spline functions: the conditions $f(a) = 0$, $f(b) = 0$ for bound states are introduced by deleting the first and last B-spline, while for continuum states it is necessary to keep the last B-spline, which is not zero at R_{MAX} (see Fig. 2.1).

In quantum mechanical applications mostly matrix elements, i.e. definite integrals involving B-splines and their derivatives, are involved. These are best computed to machine accuracy employing Gauss-Legendre (GL) integration [5,6] of appropriate order over each subinterval I_j. Recall that a GL integration of order n (n points) is exact for a polynomial integrand of order $2n$, k GL points integrate exactly the product $B_i \cdot B_j$ and a little more is usually completely accurate even for non polynomial integrands, provided no singularity is present in the interior of I_i.

2.2 The Least-Squares Approach for the Determination of the Continuum Wave Functions

Dealing with continuum states another problem is the lack of a simple variational formulation to determine a full set of linearly independent solutions for the n_c open channels at any prefixed energy. In the bound state problem approximate solutions of the eigenvalue equation, expanded in a prefixed basis $\{\varphi_i\}_{i=1,\dots,n}$, $\Psi = \sum_i c_i \varphi_i$, can be obtained by the variational (Rayleigh-Ritz) principle, $\delta\langle H\rangle = 0$, or equivalently by the Galerkin approach, requiring orthogonality of the residual vector to all basis elements, both leading to the usual algebraic eigenvalue problem:

$$(H - ES)c = 0 \tag{2.6}$$

For the continuum state the energy is fixed, so that the equation

$$Ac = 0c, \qquad \text{where} \quad A(E) = H - ES \tag{2.7}$$

in general does not admit non-trivial solution $c \neq 0$. Let us consider the determination of the solution of $A\Psi$

$$A(E)\Psi = 0 \tag{2.8}$$

by a least-squares approach, that is requiring the minimum of $\langle A\Psi, A\Psi\rangle$, with a fixed norm $\langle\Psi,\Psi\rangle = 1$, to exclude the trivial $\Psi = 0$ solution. Then usual variation

$$\delta(\langle A\Psi, A\Psi\rangle - \lambda\langle\Psi,\Psi\rangle) = 0,$$

with the basis set expansion $\Psi = \sum_i c_i \varphi_i$ leads to the eigenvalue equation

$$Rc_k = r_k S c_k, \qquad \text{with} \qquad R_{ij} = \langle AB_i, AB_j\rangle \tag{2.9}$$

positive definite. Since the eigenvalues correspond to the square norm of the residual $A\Psi_k$, the required solution correspond to the minimum eigenvalue. Although theoretically satisfactory, implementation of the least-square approach (2.9) requires the evaluation of the matrix elements of the Hamiltonian squared, which may be computationally inconvenient. To avoid this problem it has been proposed [7] to consider only elements spanned by the basis set, approximating the residual $A\Psi$ by its projection $PA\Psi$. Then

$$\langle PA\Psi, PA\Psi\rangle = c^+ Rc, \qquad \text{with} \qquad R = A^+ S^{-1} A, \tag{2.10}$$

and the same stationary condition as before leads to the same kind of eigenvalue equation relative to the new matrix R which is still symmetric and positive definite, but requires only matrix elements of the Hamiltonian.

Starting from the projected least-square approach (2.10) different simplified eigenvalue formulations can be obtained by progressively neglecting the overlap matrix S [7]. This amounts to changing the metric on the space, but does not alter its topology, and therefore its convergence to the exact results in the limit of the basis approaching completeness. In particular the scheme

$$Rc_k = r_k c_k, \qquad \text{with} \qquad R = A^+ A \tag{2.11}$$

has been adopted in the present thesis because it is less affected by roundoff errors than the other formulated schemes and is the easiest to be implemented. For the extraction of the n_c minimum modulus eigenvectors, corresponding to the n_c open channels at each energy E in the three dimensional problems with n_c partial waves, given the generally large separation from the following eigenvalues, the lowest ones are efficiently obtained by inverse iteration applied to a subspace of dimension n_c [8,9].

Basically, one starts with n independent zero-order vectors x_i^0, at each iteration the system

$$A^+ A y_i^{k+1} = x_i^k ,$$

is solved, and the y_i^{k+1} are symmetrically orthonormalized,

$$x_i^{k+1} = S^{-1/2} y_i^{k+1}$$

The LU factorisation of $A^t A$ is employed for the solution of the linear system. The iterations are stopped when the subspace distance between two successive iterations, defined as

$$d^2 = n - \sum_{i,j} \left| \left\langle x_i^{k+1}, x_j^k \right\rangle \right|^2$$

is less than a prefixed threshold (typically, 10^{-8}-10^{-9}).

Concluding it is worthwhile mentioning that, since solutions in the continuous spectrum are required over a dense energy mesh, set up and diagonalization of the matrix $R(E)$ should be performed several times. While diagonalization is unavoidable, set up of the matrix could be drastically reduced if the basis set is energy independent, so that H and S can be computed and stored at the outset. In the context of B-spline functions this is realisable using a common set of knots, that is the step size, for the whole energy range considered. Previous tests have shown that for a prefixed accuracy the step size required is inversely proportional to the maximum energy of the photoelectron [10]:

$$h_{max} = 1 \Big/ \left(2\sqrt{2E_{max}} \right) \tag{2.12}$$

Therefore the step size that defines the B-spline basis set is chosen according to the highest photoelectron energy required and is kept fixed for all energy points. This procedure avoids recalculating the matrices H and S at every different energy with a consequential computational saving.

2.3 The Linear Combination of Atomic Orbitals B-spline Density Functional Theory Approach

In this section the method employed in the present thesis for the calculation of the molecular electronic continuum spectrum is extensively described. First the choice of the Hamiltonian is considered, and second the features of the multicentred expansion and comments relative to the implementation of Density Functional techniques in the Linear Combination of Atomic Orbitals (LCAO) B-spline basis set are presented.

2.3.1 The Hamiltonian

An approach that has become popular because of the favourable compromise between the accuracy and the computational cost, allowing the treatment of large many-electron systems is the Density Functional Theory (DFT). Since extensive presentations of DFT are available [11,12], only working equations will be presented.

Employing the usual Kohn–Sham (KS) scheme, DFT amounts to solving the coupled one-particle equations for the n electrons of the system:

$$h_{KS}\varphi_i = \varepsilon_i \varphi_i \qquad i = 1,\ldots,n \tag{2.13}$$

where

$$h_{KS} = -\frac{1}{2}\nabla^2 - \sum_p \frac{Z_p}{\left|\vec{r} - \vec{R}_p\right|} + V_C + V_{XC} \tag{2.14}$$

$$V_C = \int \frac{\rho(\vec{r}\,')d\vec{r}\,'}{\left|\vec{r} - \vec{r}\,'\right|}, \qquad V_{XC} = V_{XC}[\rho(\vec{r})]$$

is the KS Hamiltonian sum of electronic kinetic energy, electron-nuclear attraction, Coulomb interaction and the exchange-correlation potential, respectively. The ground state electron density $\rho(\vec{r})$ is given by:

$$\rho(\vec{r}) = \sum_{i=1}^{n} n_i \left|\varphi_i(\vec{r})\right|^2 \tag{2.15}$$

where n_i are the occupation numbers. The potential depends on the density $\rho(\vec{r})$ through the Hartree V_C and exchange-correlation V_{XC} terms, so the equation (2.13) are solved iteratively.

Since the calculation of the ground state density is a standard problem in quantum chemistry, in the present implementation of the LCAO B-spline DFT method the density is obtained by a conventional SCF LCAO bound state calculation and is successively decomposed in its angular components in order build the Hamiltonian in the LCAO B-spline expansion, as described in section 2.3.2.

For the complete specification of the Hamiltonian (2.14) two further points need to be considered:

1) since the density is build from the orbitals according to equation (2.15), which contains the occupation number n_i, a particular choice for the electron configuration is required;
2) a particular choice of the exchange-correlation potential V_{XC} must be done.

Concerning the electron configuration, three possibilities are equally reasonable for photoionization: the ground-state (GS) configuration, the transition-state configuration (TS), where half an electron is removed from the ionised orbital, and finally the hole configuration where one electron is completely removed from the ionised orbital. From previous analysis [13] it has been shown that the best choices are given by the GS and TS configuration. It is surprising that the completely ionised configuration, which at first sight seems the most appropriate for ionisation, has always given the worst results with respect to experiment.

The performance of a chosen configuration is actually dependent on the V_{XC}; in fact the best choices have proven to be the TS with the VWN and the GS with LB94 exchange-correlation potentials.

The VWN [14] is an exchange-correlation based on the *Local Density Approximation* (LDA) [15]. In the LDA approximation the potential V_{XC} can be separated in the exchange and correlation part. The exchange part is known exactly [16] and has the form:

$$V_X^{LDA}[\rho(\vec{r})] = -\left[\frac{3}{\pi}\rho(\vec{r})\right]^{1/3} \tag{2.16}$$

The VWN potential includes the analytic form (2.16) for the exchange part while the part of pure correlation is obtained through analytic interpolation on accurate values obtained by quantum Monte Carlo calculations [17]. The exact KS effective potential displays the asymptotic $-1/r$ decay [18,19], which is actually not displayed by the LDA potentials. In fact the VWN potential decays exponentially to zero, due to the inadequate treatment of the self-interaction term in the exchange part. For GS energies this has a little importance, but it has a larger influence for continuum state calculation, where the wave functions extends to large distances: on physical grounds the outgoing electron should experience the mean field of the ion that it leaves behind, i.e., a potential that decays Coulombically like $-1/r$.

A few potentials including the correct asymptotic Coulomb tail have been devised [20-23], among them the LB94 potential by van Leuween and Baerends [20]. The authors proposed a gradient correction to a given LDA potential in order to meet some of the requirements which have to be fullfilled by an exact V_{XC}, notably, the correct asymptotic behaviour. In the implementation of the LCAO B-spline DFT method used in the present thesis this correction has been applied to the VWN potential and the expression for the LB94 potential is the following:

$$V_{xc_\sigma}^{LB94} = V_{xc_\sigma}^{VWN} + V_{xc_\sigma}^{CORRECTION} \tag{2.17a}$$

$$V_{xc_\sigma}^{CORRECTION} = -\beta\rho_\sigma^{1/3}(\vec{r})\frac{x_\sigma^2}{1+3\beta x_\sigma \sinh^{-1}(x_\sigma)} \tag{2.17b}$$

where $x_\sigma = \dfrac{|\nabla\rho_\sigma|}{\rho_\sigma^{4/3}}$.

It is easy to show that the asymptotic behaviour of the gradient correction (2.17b) is of the form:

$$V_{xc_\sigma}^{CORRECTION} \xrightarrow[r\to\infty]{} -\frac{1}{K+r} \tag{2.18}$$

i.e. Coulombic providing $r >> K$.

Both VWN and LB94 exchange-correlation potentials have been implemented in the LCAO B-spline DFT code. Although the agreement of the VWN TS and LB94 GS results with the experiment is comparable [24], in the LB94 GS scheme the density used is independent from the ionised orbital and therefore it does not require the recalculation of the Hamiltonian for each considered ionisation. In fact the same GS potential is used and a significant saving in terms of computational time is obtained. Since in the present thesis rather large, non-symmetric molecules have been considered, the LB94 GS potential has been chosen for all calculations.

2.3.2 The LCAO Expansion

The LCAO expansion is based on a large basis set placed on a chosen origin supplemented by a limited number of off-centred functions located at the position of the nuclei. In order to give a clear description of the method, it is useful to separate the discussion in two parts: first the One Centre Expansion (OCE) is described, since it represents the core of the method, then the multicentred extension is introduced.

The Molecular One Centre Expansion (OCE) Implementation [25].

The OCE approach [26] employs an expansion of all functions of interest as products of radial functions and spherical harmonics about a common centre:

$$f(r,\vartheta,\varphi)=\sum_{lm}^{l,\max}R_l(r)Y_{lm}(\vartheta,\varphi) \tag{2.19}$$

For highly symmetric molecules a large saving can be obtained by full use of point group symmetry. If $\lambda\mu$ are the labels for the irreducible representations (IR) of the group under which the KS Hamiltonian h_{KS} is invariant, then the eigenvalue equation factorizes:

$$h_{KS}^{\lambda}\varphi_{n,\lambda\mu}=\varepsilon_{n,\lambda}\varphi_{n,\lambda\mu} \tag{2.20}$$

and the matrix elements of the Hamiltonian are diagonal in λ and independent of μ. Symmetry-adapted angular basis functions are obtained as linear combinations of spherical harmonics [27]. In order to avoid complex algebra it is computationally simpler to employ real spherical harmonics:

$$X_{lh}^{\lambda\mu}(\vartheta,\varphi)=\sum_{m}b_{lmh\lambda\mu}Y_{lm}^{R}(\vartheta,\varphi). \tag{2.21}$$

Only *Ys* with the same l are combined, and h counts the number of independent linear combinations for the same l-value. The coefficients can be obtained with standard projection operators employing rotation matrices of angular momentum theory. Since the transformation (2.21) is unitary, the X-functions are orthonormal

$$\left\langle X_{lh}^{\lambda\mu}, X_{l'h'}^{\lambda'\mu'} \right\rangle = \delta_{l,l'}\delta_{h,h'}\delta_{\lambda,\lambda'}\delta_{\mu,\mu'}. \tag{2.22}$$

Thus from a generic expansion $f(r,\vartheta,\varphi) = \sum_{lh\lambda\mu} R_{lh\lambda\mu}(r) X_{lh}^{\lambda\mu}(\vartheta,\varphi)$ one obtains the radial components of the function:

$$R_{lh\lambda\mu}(r) = \int_0^{\pi}\int_0^{2\pi} f(r,\vartheta,\varphi) X_{lh}^{\lambda\mu}(\vartheta,\varphi) \sin\vartheta d\vartheta d\varphi. \tag{2.23}$$

The OCE basis set consist therefore in

$$\chi_\mu^O \equiv \chi_{ilh,\lambda\mu}^O = \frac{1}{r} B_i(r) X_{lh}^{\lambda\mu}(\vartheta,\varphi) \tag{2.24}$$

where the B-splines are built over the interval $\left[0, R_{MAX}^O\right]$, the symmetry-adapted basis functions $X_{lh}^{\lambda\mu}$ are used up to a given maximum angular momentum L_{MAX}, that is $l \le L_{MAXO}$, and the upper index refers to the chosen origin O.

The expansion of the KS eigenvectors in terms of the basis set $\{\chi_\mu^O\}$ gives the usual Kohn-Sham $\mathbf{H_{OO}}$ and overlap $\mathbf{S_{OO}}$ matrices, where the lower index index refers to the OCE basis set. Concerning the evaluation of the matrix elements

$$h_{\mu\nu}^{OO} = \left\langle \chi_\mu^O, h_{KS} \chi_\nu^O \right\rangle, \tag{2.25a}$$

where

$$h_{KS} = -\frac{1}{2}\nabla^2 - \sum_p \frac{Z_p}{\left|\vec{r}_i - \vec{R}_p\right|} + V_C + V_{XC}, \tag{2.25b}$$

the single contributions associated with the kinetic, electron-nuclear attraction, Coulomb and exchange-correlation terms (see Eqs. 2.14) need to be determined in order to construct the Kohn-Sham matrix $\mathbf{H_{OO}}$.

Matrix elements of the kinetic energy operator and of the electron-nuclear operators are fairly easily computed employing well-tested algorithms. In particular the attractive potential due to the nuclear frame can be evaluated using the well-known formula:

$$\frac{1}{\left|\vec{r}-\vec{R}_p\right|}=\sum_{l=0}^{\infty}\sum_{m=-l}^{l}\frac{4\pi}{2l+1}\frac{r_<^l}{r_>^{l+1}}\mathrm{Y}_{lm}^{*}(\vartheta,\varphi)\mathrm{Y}_{lm}(\vartheta_p,\varphi_p) \qquad (2.26)$$

$$r_{</>}=min/max(r,R_p)$$

For the Coulomb potential it has been found more convenient to solve the Poisson equation directly

$$\Delta V_C=-4\pi\rho \qquad (2.27)$$

in the same basis set $\{\chi_\mu^\lambda\}$. Since both functions V_C and ρ are totally symmetric ($\lambda\mu=00$), introducing the index $j\equiv(lh)$, the following relations hold:

$$V_C=\sum_j V_j(r)X_j^{00}=\sum_{i,j}v_{ij}\chi_{ij00} \qquad (2.28)$$

and

$$\rho=\sum_j\rho_j(r)X_j^{00}. \qquad (2.29)$$

Multiplication on the left of each side of eqs. (2.28) and (2.29) by the bra $\langle\chi_{i'j'00}|$ then yields

$$\sum_i(\Delta)_{i'i}^l v_{ij}=-4\pi a_{i'j} \qquad (2.30)$$

with

$$a_{ij}=\langle\chi_{ij00},\rho\rangle=\int_0^\infty B_i(r)r\rho_j(r)dr \qquad (2.31)$$

$$(\Delta)_{ij}^l=\int_0^\infty B_i(r)\left\{\frac{d^2}{dr^2}-\frac{l(l+1)}{r^2}\right\}B_j(r)dr \qquad (2.32)$$

The overall scheme reduces to the solution of a linear system with the dimension of the radial basis, where the expansion coefficients of the Coulomb potential v_{ij} are the unknown quantity. Accurate solutions are obtained, provided that the correct boundary conditions on the potential are satisfied:

$$\lim_{r\to\infty}V_j(r)=\frac{A_j}{r^{l+1}}$$

$$\lim_{r\to\infty}\frac{(rV_j(r))'}{rV_j(r)}=-\frac{l}{r}$$

where A_l is the corresponding electric multipole. These boundary conditions are easily implemented by forming a linear combination of the last two splines that satisfies the boundary condition at R^O_{MAX}. As already stated in the previous section, the density is obtained by a conventional SCF LCAO type calculation for the initial state with a standard basis set. Radial components of the density $\rho(\vec{r})$ are obtained at each radial point $\vec{r}$ by numerical integration of (2.23). An angular grid is obtained as product of two standard GL sets of points and weights. For better accuracy the $[0,\pi]\times[0,2\pi]$ domain is decomposed into subdomains and GL integration separately employed in each subdomain, in order to have finer grids close to the atomic nuclei. Also only symmetry unique subdomains are considered. As a last step to obtain the coefficients a_{ij}, the projection of the radial components of the density, $\rho_l(r)$, on the B-spline basis function must be performed (see Eqt. 2.31): this is an easy task being a numerical integration between radial functions. The accuracy of the overall integration is checked verifying if the integral of the radial density is identical to the integral of the density obtained by means of a SCF LCAO calculation.

The exchange-correlation potential can be easily treated since is a function of the density and of its gradient. Therefore this function must be evaluated over the gaussian points. Then matrix elements (2.25a) are obtained by further numerical integration.

The major drawback of the OCE approach is slow convergence with L_{MAX}, due to the nuclear cusps in the OCE expansion of the potential. The cusps become sharper and sharper with increasing l and with the distance R_p of the nucleus from the origin, besides being proportional to the nuclear charge. Because of slow convergence with L_{MAX} it was believed that OCE was essentially limited to molecules with very light off-centre atoms close to the origin, in practice XH_n. Computational advances with the B-spline basis set have shown that convergent results can be obtained in much larger systems, like C_{60} and $Cr(C_6H_6)_2$, but L_{MAX} up to 40-60 is however necessary. As dimension of the matrices increases as $(l_{max}+1)^2$ the OCE approach becomes impracticable for large, non-symmetric molecules.

The Molecular Linear Combination of Atomic Orbitals (LCAO) Implementation [28].

The nuclear cusps in the wave function due to the Coulomb singularities at the nuclei are optimally described in polar coordinates around each nucleus. Unfortunately no global coordinate system is available which reduces locally to a spherical system around each nucleus.

The standard solution in quantum chemistry is the indirect introduction of a local spherical coordinate system by the use of an LCAO basis, that is a basis which is the union of separate spherical basis sets, each centred about a different nucleus. In standard quantum chemistry LCAO is implemented with global basis sets, usually Gaussian or Slater-type orbitals [29,30]. These provide fast convergence for the lowest bound states with a limited number of basis functions. However it is difficult to enlarge the basis towards completeness, because the union of separate complete sets on different centres is overcomplete, and in practice one quickly reaches numerical linear dependence in the set, because of the large overlap between functions on different centres.

The local nature of spherical B-spline functions can be used to control the overlap between functions on different centre, by retaining only a short-range expansion on each atomic centre.

An initial attempt to employ an LCAO type B-spline basis on H_2^+ and HeH^{2+} showed excellent convergence but quickly run into numerical instabilities [2,31,32]. This was due to the rather large long-range of the off-centre spherical B-spline functions employed, which overlapped considerably.

The multicentred approach employed in the present thesis is based on the observation that long-range OCE expansion with rather large L_{MAX} is needed in any case to reach the asymptotic convergence in the continuum. Therefore the off-centre functions may be limited to mutually nonoverlapping spheres, apart from the long-range OCE set.

Therefore, the LCAO basis set consists in the large OCE located on a chosen origin (2.24)

$$\chi_{\mu}^{O} \equiv \chi_{ilh,\lambda\mu}^{O} = \frac{1}{r} B_i(r_O) X_{lh}^{\lambda\mu}(\vartheta_O, \varphi_O)$$

supplemented by functions of the same type, that is symmetrized combinations of functions but centred on the off-centred nuclei p:

$$\chi_\mu^q \equiv \chi^q_{ilh,\lambda\mu} = \sum_{p\in Q_q} \frac{1}{r_p} B_i\left(r_p\right) \sum_m b_{lmh\lambda\mu p} Y^R_{lm}\left(\vartheta_p, \varphi_p\right) \tag{2.33}$$

where q is an index which runs over the non-equivalent nuclei, Q_q is the set of equivalent nuclei, p runs over the equivalent nuclei and gives the origin of the off-centred spherical coordinates, $r_p, \vartheta_p, \varphi_p$. The coefficients are determined by symmetry. Symmetry adaptation is particularly simple in abelian symmetry, since $b_{lmh\lambda\mu p}$ coefficients reduce to $\pm 1/\sqrt{2}$.

For the new basis set $\{\chi_\mu^p\}$ the B-splines are built over the intervals $\left[0, R^p_{MAX}\right]$. The off-centre B-spline are truncated: the last three functions are not included in the set in order to have the continuity of the second derivative over the surface with radius R^p_{MAX}.

In the present version of the LCAO B-spline DFT method the spheres of radius R^p_{MAX} cannot intersect each other, and therefore the matrix representation of the KS Hamiltonian in the LCAO basis set $\{\chi_\mu\} = \{\chi_\mu^{\mathrm{O}}\} \cup \{\chi_\mu^1\} \cup \{\chi_\mu^2\} \cup \cdots \cup \{\chi_\mu^{\mathrm{M}}\}$ is partitioned into submatrices, as follows:

$$\mathbf{H} = \begin{pmatrix} \mathbf{H_{OO}} & \mathbf{H_{O1}} & \cdots & \mathbf{H_{Op}} & \cdots & \mathbf{H_{On}} \\ \mathbf{H_{1O}} & \mathbf{H_{11}} & \cdots & 0 & \cdots & 0 \\ \vdots & \vdots & \vdots & \vdots & \vdots & \vdots \\ \mathbf{H_{pO}} & 0 & \cdots & \mathbf{H_{pp}} & \cdots & 0 \\ \vdots & \vdots & \vdots & \vdots & \vdots & \vdots \\ \mathbf{H_{nO}} & 0 & \cdots & 0 & \cdots & \mathbf{H_{nn}} \end{pmatrix} \tag{2.34}$$

A block $\mathbf{H_{OO}}$ between elements of the set $\{\chi_\mu^O\}$, which is actually equal to the previous OCE Hamiltonian (2.25), other blocks $\mathbf{H_{pp}}$ between elements of the set $\{\chi_\mu^p\}$ belonging to the same p-th centre are easily obtained since locally can be recast to a shifted OCE expansion, and finally blocks $\mathbf{H_{Op}}$ between the sets $\{\chi_\mu^O\}$ and $\{\chi_\mu^p\}$:

$$h_{\mu\nu}^{Op} = \left\langle \chi_{\mu}^{O}, h_{KS}\, \chi_{\nu}^{p} \right\rangle \tag{2.35}$$

The construction of these latter Hamiltonian elements represents most of the effort of the LCAO implementation, since there is no standard technique available. To perform this task a product of GL grids in r, ϑ, φ is employed: the weights and points are distributed in spherical coordinates around the p-th off-centre nucleus, with polar axis rotated and passing through the origin O of the large OCE. This change of coordinate framework improves dramatically the performance of the numerical integration: the axial symmetry of the two-centre system O plus p-th make the integration over three variables (r, ϑ, φ) to an integration over two variables (r, ϑ). Within the rotated framework only the molecular potential V must be numerically integrated over the azimutal φ angle with fixed r and ϑ, with respect to the angular factor $\Phi_m(\varphi)$ of the real spherical harmonics dependent on the φ variable:

$$\int_0^{2\pi} \Phi_{m'}(\varphi) V(r, \vartheta, \varphi) \Phi_m \, d\varphi = V_{m'm}(r, \vartheta) \tag{2.36}$$

The completeness of the basis allows an accurate solution of the Poisson equation along similar lines as in the OCE case. Matrix elements of the Laplacian operator in the full LCAO basis are already available, and scalar products of the density with respect to the basis $\left\langle \chi_{\mu}^{p}, \rho \right\rangle$ are evaluated employing the product grid already defined inside each atomic sphere. The Coulomb potential is then obtained as an expansion in the basis and can be quickly evaluated at the grid points, together with the local exchange-correlation potential to obtain the matrix elements of the Hamiltonian. The density is obtained by a conventional SCF LCAO type calculation for the initial state with a standard basis set.

Once the Hamiltonian elements have been computed bound-state solutions in the same basis are obtained by conventional diagonalization of the Hamiltonian matrix, with bound-state boundary conditions, which are then employed for the calculation of the dipole matrix elements. Continuum states are extracted by means of the the least-squares algorithm in the formulation $\mathbf{A}^{+}\mathbf{A}$ (see section 2.2). The number of open channels corresponds to the number of angular momentum functions for which a complete radial basis set, including the last spline, is kept. A corresponding number of eigenvectors $\varphi_n^{\lambda\mu}(\vec{r})$ are extracted at each selected energy and are fitted to a linear combination of regular and irregular Coulomb wave functions at the boundary [33]:

$$\varphi_n^{\lambda\mu}(\vec{r}) \xrightarrow[r \to \infty]{} \sqrt{\frac{2}{\pi k}} r^{-1} \sum_{h'l'} \left[\mathrm{A}_{h'l',n} sin\,\theta_{l'} + \mathrm{B}_{h'l',n} cos\,\theta_{l'} \right] X_{h'l'}^{\lambda\mu}(\hat{r}) \qquad (2.37)$$

obtaining therefore the two matrices A and B. The K matrix is defined as K = BA^{-1} and the continuum is then normalised to the K-matrix boundary conditions according to equation (1.31). The K-normalized continuum orbitals are further transformed to incoming waves S-matrix boundary conditions (1.27), and from such states the dipole matrix elements are finally obtained (see Eqt. 1.37)

$$D_{hl}^{\lambda\mu-}(\lambda_r) \equiv \left\langle \Psi_{hl}^{\lambda\mu-} \middle| \sum_{s=1}^{N} \hat{\xi}_{\lambda_r} \cdot \vec{r}_s \middle| \Psi_0 \right\rangle$$

Cross sections, asymmetry and dichroism parameters for randomly oriented molecules are then computed according to the angular momentum formalism as outlined in section 1.6.3.

2.4 Set Up a LCAO B-spline DFT Calculation

Most important aspects to be considered for an accurate calculation of the molecular electronic continuum spectrum by means of the LCAO B-spline DFT package are here outlined.

A. Calculation of the density for the initial state. Electron density $\rho(\vec{r})$ is obtained by means of the ADF program [34,35] on the GS of the molecule under study employing the LB94 exchange-correlation potential. Basis set usually employed is an all-electron double zeta plus polarization (DZP) basis set of Slater-type orbitals taken from the ADF database, since instabilities in the long range behaviour of the density are occasionally met with larger basis.

B. Specification of the LCAO basis set. The LCAO basis set $\{\chi_\mu\} = \{\chi_\mu^{\mathrm{O}}\} \cup \{\chi_\mu^1\} \cup \{\chi_\mu^2\} \cup \cdots \cup \{\chi_\mu^{\mathrm{M}}\}$ is completely defined by:

B.1. The maximum value for the angular expansion L_{MAXO} and L_{MAXi} for each set of equivalent centres. The choice of the maximum angular momentum is probably the most important for the convergence in the continuum, and it will be considered in detail in the following subsection. Concerning the maximum angular momentum employed in the off-centre expansion $L_{MAXi} = 1$ for hydrogen and $L_{MAXi} = 2$ for the heaviest atoms has been usually found satisfactory. Higher values bring marginal improvement [28].

B.2. The order of the B-splines, k, which is common to all splines. As stated in section 2.1.1, when approximating analytic functions it is best to employ high-order splines, typically in the range k = 7–10. In all calculations performed in the present thesis $k = 10$ has been considered.

B.3. The set of knots, or equivalently the radial grids, one for the OCE and one for each set of equivalent centres. The grids usually employed are linear, and therefore are defined by the radius R^{i}_{MAX} and the step size h. For the OCE R^{O}_{MAX} is placed at a distance where the potential can be considered essentially Coulombic and the solution, which is known, can be fitted to the calculated one. The step size h is chosen according to the expression $h_{max} = 1/\left(2\sqrt{2E_{max}}\right)$ (see section 2.2) but the intervals are usually supplemented with additional knots near the position of the nuclei in order to make the OCE basis more flexible in the region of core orbitals. To take maximum advantage of the off-centre expansion, the radial intervals $\left[0, R^{i}_{MAX}\right]$ should have different extension depending on the atomic weight of the nuclei and the distance of the atom from the one-centre expansion, under the constraint that in the present implementation of the LCAO B-spline DFT method the spheres of radius R^{i}_{MAX} cannot intersect each other.

It must be finally observed that numerical stability is always an issue in large LCAO expansions. This is especially true for atomic spheres close to the OCE origin, and it disappears for atomic spheres located far from the expansion centre, precisely those for which the addition of LCAO functions is more important.

C. Choice for the OCE origin. First calculations considered the centre of mass of the molecule as the origin of the one centre expansion. Experience has shown instead that in order to improve convergence it is more convenient to fix the OCE on the point with minimal distance from all heavy atoms of the molecule under study. A simple algorithm has been implemented for the determination of this point for every polyatomic system. Anyway, if the point mentioned above is close to a heavy atom it is convenient to set the origin on this nucleus.

2.4.1 The Asymptotic Angular Momentum Requirement

The maximum angular momentum (L_{MAXO}) employed in the expansion over the origin is a critical choice to have convergence in the continuum, since dramatic deterioration of the photoionization dynamical parameter profiles is observed if L_{MAXO} is inadequate. In order to avoid convergence analysis for each new calculation, a simple model has been proposed for a rough estimate of the required asymptotic angular momentum [28]. Consider first a definition of the asymptotic angular momentum. At a given photoelectron energy *E*, the ionisation cross section relative to each of the occupied orbitals may be split into partial final contributions of given angular momentum *L*, associated with the *L* of the continuum partial waves. This distribution, in general, increases from low *L* up to a maximum, and then decays rapidly so that high *L* values give negligible contribution. These relative contributions $\sigma_L^{rel}(E)$ can be cumulated to $\sigma_L^{cum}(E)=\sum_{L,1=0}^{L}\sigma_L^{rel}(E)$. The asymptotic angular momentum (L_{asy}) is defined as the *L* for which the cumulated relative contribution to the cross section exceed a given threshold *T* in percentage of the total cross section: $L_{asy}(E)=\min(L),\{L:\sigma_L^{cum}(E)\geq T\cdot\sigma\}$. This definition depends slightly on the chosen initial state, therefore in order to have a definition of the asymptotic moment independent by the initial orbital, the maximum L_{asy} has been chosen with respect to the set of values given by each initial state.

Evaluation of L_{asy} at various E for a series of benchmark molecules has shown L_{asy} is essentially proportional to the photoelectron momentum $k = \sqrt{2E}$ and to the target size. The following model equation has been therefore proposed:

$$E = \frac{L_{asy}\left(L_{asy}+1\right)}{2r_{eff}^{2}} - \Delta \qquad (2.38)$$

where r_{eff}, the effective molecular size, and the offset, Δ, are two adjustable parameters, which can be obtained by least-square fitting of the calculated asymptotic L_{asy} associated with a given accuracy T. The effective molecular size r_{eff} increases with the spatial expansion of the system but also with the distance of the heavy atoms from the origin of the OCE, revealing the importance of the point chosen as the origin of the one centre expansion. The offset Δ decreases as the size of the system increases. Employing the equation (2.38) it is possible to estimate, for a certain photoelectron kinetic energy E, the asymptotic angular momentum required to have convergence of the continuum up to a certain value of the photoelectron kinetic energy

2.5 This Thesis

In the present thesis the LCAO B-spline DFT method is applied to the computational study of the molecular photoionization process. Special attention is given to the Circular Dichroism in the Angular Distribution (CDAD) of photoelectrons emitted from chiral molecules ionised by means of circularly polarized light of defined helicity. Dichroism in photoemission has been theoretically discovered at the seventies, but just in the last few years first experimental studies have started appearing in literature thanks to the easier availability of tunable circularly polarized light from synchrotrons of third generation. Theoretical origin of the CDAD effect is well understood, but there is a lack of information concerning, for example, the relation between the dichroism and the electronic/geometrical structure of the chiral molecule, or how important are the dichroic effects in terms of relative intensities.

In Chapter 3 the LCAO B-spline DFT is applied to a series of chiral derivatives of oxirane, with the aim to calculate the CDAD effect and to identify trends along the series. The analysis of the dichroism from core states and valence states retaining their nature along the series shows a rather unexpected sensitivity of the dichroic parameter to changes in the electronic structure. The comparison with the cross section and asymmetry parameter points how the dichroic parameter could be the most suitable photoionization property for the investigation of the electronic structure of chiral molecules. Furthermore, the calculated values show that the magnitude of the CDAD effect does not seem to be associated with the initial state chirality, but it should mainly be attributed to the ability of the delocalized final continuum state to probe the asymmetry of the molecular effective potential.

The computational study of the CDAD effect continues in Chapter 4, where the LCAO B-spline DFT method is applied to the enantiomers of camphor molecule. The calculated values are compared with the results obtained by means of the Continuum Moltiple Scattering approach and with the available experimental data. Generally good agreement is found between the two theoretical methods, suggesting that the underlying physical model, entailing interference effects in the pure electric dipole approximation, is well implemented in either formalisms. The comparison with the experimental measurements for the carbonyl carbon 1s data is excellent across the full range of electron energies studied. In valence dichroism the agreement is less quantitive but still substantial accordance is found. These results show therefore that the LCAO B-spline DFT method could be an important tool for the interpretation of the CDAD measurements.

In Chapter 5 a collaborative theoretical and experimental study on the circular dichroism in the angular distribution of valence photoelectrons emitted by 3-hydroxytetrahydrofuran molecule is presented. This molecule is a rather floppy system and this work sheds light on new features of the dichroism in photoemission, which appear to be highly sensitive to conformational factors.

A detailed investigation on the influence of conformational factors on the photoionization dynamical parameters, with special attention to the CDAD effect, is considered in Chapter 6. The B-spline DFT method is applied to the conformers of (1R,2R)-1,2-dibromo-1,2-dichloro-1,2-difluoroethane molecule. The cross section, asymmetry, and dichroic parameters relative to core and to valence orbitals retaining their nature along the conformational curve are systematically studied. While the cross section and the asymmetry parameter are weakly affected, the dichroic parameter shows to be rather sensitive to the particular conformer of the molecule, suggesting that the energetic profile of this dynamical property could be used as a *fingerprint* of the conformers of a chiral molecule. The computational method is also applied to the methyl rotation in (S)-methyloxirane in order to verify the assumption that methyl rotation does not significantly affect the calculated values of the CDAD effect. Unexpected and dramatic variations of the dichroic parameter profile with the methyl rotation, both in core and valence states, are found instead. The magnitude of the CDAD variations is rationalised in terms of anysotropic variation of the final-state wave function with respect to the whole molecular structure, and therefore to transition dipole moment effects.

Part of the research activity considered in the present thesis concerns also the theoretical investigation on the correctness of the statistical ratio assumption for the Branching Ratio (BR) in core ionisation of chemically non-equivalent atomic sites of the same species. When two peaks are superimposed in the experimental photoelectron spectra often a single, broad and featureless peak is apparent. To resolve the peaks the statistical ratio is generally assumed. In Chapter 7 the LCAO B-spline DFT is employed for accurate calculations of carbon 1s photoionization cross section on selected organic molecules. It is shown that cross section variations induce strong non-statistical behaviour of the BRs relative to core ionisation up to several tens of eV above threshold.

A further research topic is the shape resonance problem, which is considered in Chapter 8. Rationalisation of the resonant structures that appear in the continuum molecular spectra is still a controversial argument in photoionization and scattering literature. In Chapter 8 an attempt to design a new method to localise and characterise in molecular terms the shape resonance phenomena is presented, always in the framework of the B-spline DFT approach.

3 Density Functional Study on the Circular Dichroism of Photoelectron Angular Distribution from Chiral Derivatives of Oxirane

The Linear Combination of Atomic Orbitals B-spline Density Functional method has been successfully applied to a series of four chiral derivatives of oxirane, to calculate the photoionization dynamical parameters, the Circular Dichroism in the Angular Distribution effect and to identify trends along the series. The computational algorithm has proven numerically stable and computationally competitive. The photoionization cross section, asymmetry and dichroic parameter profiles relative to valence orbitals have been systematically studied for the states which retain their nature along the series: the identified trends have been ascribed to the different electronic properties of the substituents. A rather unexpected sensitivity of the dichroic parameter to changes in the electronic structure has been found in many instances, making this dynamical property suitable to investigate the electronic structure of chiral compounds. The magnitude of the Circular Dichroism in the Angular Distribution effect does not seem to be associated to the initial state chirality, but rather to be governed by the ability of the delocalized photoelectron wave function to probe the asymmetry of the molecular effective potential.

3.1 Introduction

Circular dichroism, i.e. the difference in the absorption intensity between right and left components of circularly polarized light, is a well established technique, nowadays routinely employed to investigate structural and optical properties of chiral molecules. Apart conventional experiments in the UV/vis. range, this spectroscopic technique has been recently developed to higher energies (up to X-ray) [1] and to more elaborate experiments, for example in presence of an external magnetic field (Magnetic Circular Dichroism, MCD [2]), due to the easier availability of tunable circularly polarized light from synchrotrons of third generation. Apart the evolution of the experimental design and of the technical devices, in these experiments the intensity considered refers to the total absorption, whose dependence with respect to the sign of circular light polarization is governed by the second order electric dipole-electric quadrupole E1-E2 and electric dipole-magnetic dipole E1-M1 operators, therefore a rather weak effect, of the order of 10^{-5}, is actually measured. On the other hand, as originally pointed out by Ritchie [3] and successively by Cherepkov [4], in photoemission the dichroic effect shows up already at the electric dipole level (E1), if the experiment is performed with angular resolution. More precisely, as it will be discussed in detail in the next Section, a dichroic term appears in the differential cross section expression, which is non zero only for chiral molecules and circularly polarized light. In this case the dichroism arises only from the electric dipole operator, and therefore its relative magnitude is expected to be around 10^{-2}, much higher than that of conventional experiments in absorption regime. These experiments are referred as Circular Dichroism in the photoelectron Angular Distribution (CDAD) and only recently the first data have been collected on bromocamphor [5], camphor [6] and methyloxirane [7].

Despite the experimental emerging activity, also theoretical calculations of CDAD spectra have recently appeared [8,9], directing attention to more complex biomolecules (glyceraldehyde, lactic acid and L-Alanine). From the computational point of view, the calculation of CDAD needs the transition dipole moments between the ionized orbital and the photoelectron continuum state, as well as the continuum phase shifts, so in practice the unbound photoelectron wave-function must be calculated previously. This task is still challenging in quantum chemistry, in fact, at variance from standard bound state calculations, for the continuum spectrum there are not yet standard method available, due to the difficult implementation of the oscillatory boundary conditions of the continuum states with standard basis sets. For this reason, the most popular computational approach for the continuum is still the Multiple Scattering (MS)-Xα, which employs the very crude muffin-tin approximation of the potential, an approximation which introduces severe uncertainties in the quality of the numerical results and therefore has a poor predictive potentiality. In this work we have employed the LCAO B-spline DFT method, which does not introduce any approximation on the potential, treats properly the continuum boundary conditions with B-spline basis functions, and employs a Kohn-Sham hamiltonian. It is important to underline that such CDAD calculations are computationally very demanding, because usual chiral molecules are rather large and non symmetric, therefore such calculations are stringent tests to demonstrate the actual potentialities in terms of efficiency of the present computational method. For this reason, it has been mandatory to employ a parallel version of the computer code, in order to take maximum advantages of the architecture of modern supercomputers.

The principal aim of this work is to calculate the CDAD as well as the usual photoionization parameters, namely the cross section and the asymmetry parameter, in a series of analogue compounds, in order to identify specific trends which may be employed to highlight those molecular and chemical characteristics which may have an important effect on the assessment of CDAD and therefore may be employed in future studies to control the effects and to suggest new experiments. We have decided to focus our attention on four derivatives of the oxirane, which are shown in Scheme 3.1 and are: **(I)** (S)-methyloxirane; **(II)** *trans*-(2S,3S)-dimethyloxirane; **(III)** (S)-fluoroxirane; **(IV)** *trans*-(2S,3S)-difluoroxirane. **(I)** and **(III)** have no symmetry elements, while in **(II)** and **(IV)** a binary C_2 axis is present. We have chosen these chiral molecules because they have the important characteristic to be in a rigid conformation, if we exclude the free rotation of the methyl group. This quality is hard to be found in usual chiral molecules, but simplifies considerably the study since multiple calculations at different conformations are avoided. Of course, the assumption that the free rotation of the methyl group does not affect heavily the results should be checked, so we will reserve more attention to this point in a future work.

From the experimental point of view, **(I)** and **(II)** are well known and stable molecules, in particular Photo Electron Spectra (PES) [10] and experimental

CDAD [7] have been measured for **(I)**. For **(II)** only PES data are available [11], but its CDAD could be obtained in a future experiment, so present results may be a useful reference. The fluorinated compounds are difficult to be obtained, only for **(III)** a synthesis is reported [12], but no PES data are available. Despite the lack of experimental data, we have considered also these molecules because the F atom is the simplest electronegative electron-acceptor substituent, which may represent a useful model to mimic real but more complex chiral molecules, since we are more interested to identify relations between the CDAD and the molecular electronic structure, than a direct comparison between theory and experiment.

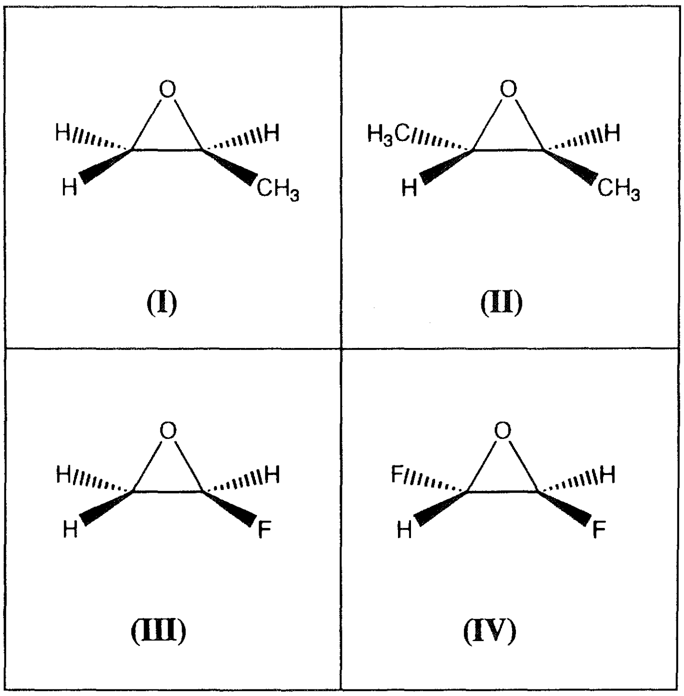

Scheme 3.1: Structures of the chiral molecules considered in this study: **(I)** (S)-methyloxirane; **(II)** *trans*-(2S,3S)-dimethyloxirane; **(III)** (S)-fluoroxirane; **(IV)** *trans*-(2S,3S)-difluoroxirane.

3.2 Theoretical Method

The LCAO B-spline DFT method has been employed in this work to calculate the photoionization properties of the series of chiral derivatives of oxirane reported in Scheme 3.1, in the gas phase with random molecular orientation. Such process is described by the differential cross section $\frac{d\sigma}{d\hat{k}}$ [13], that is the angular distribution of the photoelectrons in the solid angle $d\hat{k}$ along their direction of propagation $\hat{k}$, which can be completely defined by three quantities, namely the cross section σ, the asymmetry parameter β and the dichroism parameter D:

$$\frac{d\sigma}{d\hat{k}} = \frac{\sigma}{4\pi}\left[1+\left(-\tfrac{1}{2}\right)^{|m_r|}\beta P_2(\cos\theta)+m_r D P_1(\cos\theta)\right] \qquad (3.1)$$

where P_i is the Legendre polynomial of i-th order, θ is the scattering angle between $\hat{k}$ and the laboratory frame, m_r is 0, +1 or −1 respectively for linear, left circular or right circular polarization. The laboratory frame is defined by the incident photons: the polar axis corresponds to the electric vector or propagation direction respectively for linear or circular light polarization. We define left and right circularly polarized light according to the value $m_r = +1$ or $m_r = -1$ of the projection of the photon spin along its momentum. Accordingly, the electric vector describes a positive (right-handed) or negative (left-handed) screw.

From the computational point of view the photoionization process is completely described, at the one-electron level, by the dipole transition moment between the ionised orbital and the photoelectron continuum orbital. Therefore the problem is recast to have efficient and accurate algorithms for the molecular continuum. The LCAO B-spline DFT method has been recently developed [14], and has proven to be accurate, computationally economic and numerically stable to be routinely employed to study the photoionization of medium sized molecules with explicit treatment of the continuum photoelectron wave-function. In the following we review the essential parts which constitute the LCAO B-spline DFT method, but we refer the reader to Ref. [14] for more technical details on the computational implementation.

The present LCAO B-spline DFT method may be profitably considered as an extension of the previous One Center Expansion (OCE) B-spline DFT version [15], by supplementing the OCE basis set with a small number of proper off-center functions, which improve dramatically the convergence properties and reduce the dimension of the matrices. In order to give a short but still self-contained description of the method, it is useful to proceed in four steps: first the new basis set is described, second the Hamiltonian is defined, third the extraction process of the continuum orbitals recalled, fourth the randomly oriented molecule properties are given.

3.2.1 The LCAO B-spline DFT Method

The LCAO basis set consists in a large OCE of functions, all centered on the same origin *O*:

$$\chi^{O}_{nlh\lambda\mu} = \frac{1}{r_O} B_n(r_O) X_{lh\lambda\mu}(\vartheta_O, \varphi_O) \tag{3.2}$$

where

$$X_{lh\lambda\mu}(\vartheta,\varphi) = \sum_{m} Y^{R}_{lm}(\vartheta,\varphi) b_{lmh\lambda\mu} \tag{3.3}$$

are symmetry adapted linear combinations of real spherical harmonics $Y^{R}_{l,m}(\vartheta,\varphi)$ [16], and B_n is the n-th spline monodimensional function [17]. These OCE functions are supplemented by functions of the same type, which instead are symmetrized combinations of functions centred on the off-centre arbitrary positions *j*:

$$\chi^{i}_{nlh\lambda\mu} = \sum_{j\in Q_i} \frac{1}{r_j} B_n(r_j) \sum_{m} b_{lmh\lambda\mu j} Y^{R}_{lm}(\vartheta_j, \varphi_j) \tag{3.4}$$

where i is an index which runs over the non-equivalent nuclei, Q_i is the set of the equivalent nuclei, j runs over the equivalent nuclei and gives the origin of the off-center spherical coordinates, r_j,θ_j,φ_j. The coefficients $b_{lmh\lambda\mu}$ and $b_{lmh\lambda\mu j}$ are determined by symmetry. The indexes have the following meaning: l and m are the usual angular momentum quantum numbers, λ indicates the Irreducible Representation (IR), μ the subspecies in case of degenerate IR and h is used to identify different elements with the same $\{l,\lambda,\mu\}$ set.

The B-splines are built over the radial interval $[0, R^{O}_{MAX}]$ for the set $\{\chi^{O}{}_{nlh\lambda\mu}\}$ and over the intervals $[0, R^{i}_{MAX}]$ for the sets $\{\chi^{i}{}_{nlh\lambda\mu}\}$. The B-splines are completely defined by their order and by the grids of knots for all the radial intervals $[0, R^{O}_{MAX}]$ and $[0, R^{i}_{MAX}]$.

In particular, the most important computational choice regarding the basis set which has a fundamental impact on the accuracy and the computational economy is the maximum value of the angular expansion L_{MAXO} for the OCE and L_{MAXi} for each set of equivalent centers.

The system is described at the DFT Kohn-Sham level [18], the ground state density is taken from a conventional bound state LCAO-DFT calculation, performed with the program ADF [19,20]. Such density is then employed to build the hamiltonian represented in the LCAO B-spline basis.

The LB94 [21] exchange-correlation potential has been employed, since it supports the asymptotically correct Coulomb tail, which is very important for the accurate description of the continuum properties [22]. The bound states of the system are obtained by means of a generalized diagonalization of the KS Hamiltonian matrix. The continuum states are extracted for each photoelectron energy E, as the eigenvectors of the energy dependent matrix $\mathbf{A}^{+}\mathbf{A}$:

$$\mathbf{A}^{+}\mathbf{A}(\mathrm{E})\boldsymbol{c}=\boldsymbol{ac}, \qquad \mathbf{A}(\mathrm{E})=\mathbf{H}\text{-}\mathbf{ES} \tag{3.5}$$

corresponding to minimum modulus eigenvalues, employing a very efficient inverse iteration procedure [23], where in equation (3.5) **H** and **S** correspond to the Hamiltonian and overlap matrix respectively, *a* and *c* refer to minimum modulus eigenvalues and continuum eigenvectors respectively

The continuum states are then normalized to the **K** matrix conditions, matching the asymptotic part of the continuum eigenvectors with respect to the regular and irregular Coulomb wave-functions [24]. The Coulomb wave-functions employed are of charge +1, due to the correct asymptotic behaviour of the LB94 potential. The **K** normalized continuum orbitals are further transformed to incoming waves **S**-matrix boundary conditions, and from such states the dipole matrix elements are finally obtained:

$$D_{lh}^{\lambda\mu-}(\lambda_r)=\sqrt{\frac{4\pi}{3}}\left\langle\varphi_{lh}^{\lambda\mu-}\middle|rY_{1\lambda_r}\middle|\varphi_i\right\rangle \tag{3.6}$$

where in expression (6) λ_r indicates the three projection of the l = 1 dipole vector operator.

3.2.2. Randomly Oriented Molecules Properties

The cross section, the asymmetry and dichroism parameters profiles for randomly oriented molecules are then computed according to the angular momentum transfer formalism [13] as follows. Dipoles (3.6) are transformed, using the Wigner 3j symbols [25], introducing a further angular momentum transfer l_t:

$$D_{lm}^{l_t}(\lambda_r) = (-1)^{l_t+m}(2l_t+1)^{1/2}\begin{pmatrix} 1 & l & l_t \\ -\lambda_r & m & \lambda_r - m \end{pmatrix}\sum_{\lambda\mu h} b_{lmh\lambda\mu} D_{lh}^{\lambda\mu-}(\lambda_r) \quad (3.7)$$

which are employed to build the following product:

$$I(l_t, l, l') = \sum_{m\lambda_r m'\lambda_r'} D_{lm}^{l_t}(\lambda_r) D_{l'm'}^{l_t}(\lambda_r')^* \delta_{m-\lambda_r, m'-\lambda_r'} \quad (3.8)$$

From the quantities defined in expression (3.8) all the dynamical quantities split by angular momentum transfer contributions are obtained:

$$\sigma(l_t) = I(l_t, l_t+1, l_t+1) + I(l_t, l_t, l_t) + I(l_t, l_t-1, l_t-1) \quad (3.9)$$

$$\beta(l_t) = \begin{bmatrix} (l_t+2)I(l_t, l_t+1, l_t+1) + (l_t-1)I(l_t, l_t-1, l_t-1) \\ +3\sqrt{l_t(l_t+1)}\left(e^{i(\sigma_{l_t+1}-\sigma_{l_t-1})} I(l_t, l_t+1, l_t-1) + c.c.\right) - (2l_t+1)I(l_t, l_t, l_t) \end{bmatrix} / (2l_t+1)$$

(3.10)

$$\begin{aligned} D(l_t) = &\left[\left((-i)e^{i(\sigma_{l_t}-\sigma_{l_t-1})} I(l_t, l_t, l_t-1) + c.c.\right)\sqrt{\frac{l_t+1}{2l_t+1}}\right] \\ &+\left[\left((i)e^{i(\sigma_{l_t}-\sigma_{l_t+1})} I(l_t, l_t, l_t+1) + c.c.\right)\sqrt{\frac{l_t}{2l_t+1}}\right] \end{aligned} \quad (3.11)$$

where in (3.10) and (3.11) σ_l are the Coulomb phase shifts. From partial contributions (3.9), (3.10) and (3.11) the cross section σ, the asymmetry parameter β and the dichroism parameter D, which appear in equation (3.1) are finally obtained as sums of partial contributions:

$$\sigma = \frac{4\pi^2\omega}{3c}\sum_{l_t}\sigma(l_t) \quad (3.12)$$

$$\beta = \sum_{l_t}\beta(l_t) \Big/ \sum_{l_t}\sigma(l_t) \quad (3.13)$$

$$D = \frac{3}{2}\left(\sum_{l_t} D(l_t) \Big/ \sum_{l_t} \sigma(l_t)\right) \tag{3.14}$$

3.3 Computational Details

For all the systems considered in the present work, the calculations have been executed as follows. First the Ground State (GS) electron density is calculated by means of the ADF program [19,20], employing an all-electron Double Zeta plus Polarization (DZP) basis set of Slater Type Orbitals (STO), taken from the ADF database. Such density is then used to build the KS hamiltonian with the B-spline LCAO program, from which the bound and continuum states are extracted and used to calculate the cross section, the asymmetry and dichroism parameter. B-spline functions of order 10 are employed in all the calculations performed with the B-spline LCAO program. Since the experimental geometry is not available for all the molecules under study, and to be internally consistent, we have employed the optimized molecular geometries, obtained with the ADF program with the same DZP basis set, but with the VWN [26] exchange correlation functional, which is well known to furnish accurate molecular structures [27]. Notice that the VWN potential has been employed only for the geometry optimizations, in all the other instances the LB94 potential has been employed, as stated in the previous section.

The origin of the expansion has been set on the substituted C atom for **(I)** and **(III)**, while for **(II)** and **(IV)** the origin is set on the O atom, in this way it is possible to exploit the C_2 point group symmetry for **(II)** and **(IV)**.

The most important choice for the calculations (which will be considered in detail in the discussion of the results) is the maximum angular momentum (L_{MAXO}) employed in the expansion on the origin, which has been changed in preliminary tests from L_{MAXO} = 10 up to L_{MAXO} = 20. The choice L_{MAXO} = 15, as it will be justified in the next section, has proven to furnish convergent results with respect to the basis set size for all the molecules considered in this work. The maximum angular momentum (L_{MAXi}) employed in the off-center expansions has been kept fixed to $L_{MAXi} = 2$ for C and O and to $L_{MAXi} = 1$ for H. The expansion on the origin is divided with a radial linear grid with step size of 0.2 au up to $R^O_{MAX} = 20\,\mathrm{au}$, the intervals so obtained are supplemented with additional knots near the positions of the nuclei in order to make the basis more flexible in the region of core orbitals. The expansion on the off-center nuclei is divided with a radial linear grid with step size of 0.2 au up to values of $R^i_{MAX} = 1\,\mathrm{au}$.

3.4 Results and Discussion

The photoionization process of a sample of randomly oriented molecules in the gas phase is completely described, at one-particle level and for each orbital corresponding to a main line in the photoelectron spectrum, by the differential cross section of Eq. (3.1), which can be expressed in terms of three energy dependent parameters (σ, β and D) which are molecular properties independent from the nature of light polarization, which is defined by the projection m_r. Therefore, when the light is linearly polarized the third right hand side does not contribute ($m_r = 0$) and the coefficient of the second order Legendre polynomial is β. On the other hand, in presence of circularly polarized light, the coefficient of the second order Legendre polynomial is opposite and reduced by a factor of ½ with respect to linear polarization, and, more interesting, the third term gives a contribution which changes sign according to the sign of circular polarization and a dichroism effect arises. Moreover, it can be shown that $D \neq 0$ only when the molecule is chiral: from expression (3.11) it is evident that the D parameter will get non-zero contributions only when the quantities $I(l_t, l, l')$ from expression (3.8) will carry contributions of different parity, since $l = l' \pm 1$. In presence of inversion symmetry, states are classified accordingly to their parity (even or odd). Since the electric dipole operator is of odd parity, the continuum wavefunction will be of opposite parity with respect to the initial state, therefore only even or only odd l will contribute to the continuum and D will therefore be zero. With similar arguments, also in presence of a symmetry plane D must be zero: in fact consider the contributions to the sum (3.8), they are selected by the Kronecker symbol when $m-\lambda_r = m'-\lambda_r'$, each term has the counterpart $-m+\lambda_r = -m'+\lambda_r'$ which contributes to the sum and can be shown to be opposite in presence of a reflection plane, therefore in the sum there are only pairs of opposite sign which eliminate each other giving zero total contribution. To show that the contributions are opposite consider expression (3.7): when the sign of m and λ_r are changed the Wigner 3j symbol changes sign according to the parity of $1+l+l_t$, and since in expression (3.8) $l=l_t$ and $l'=l_t+1$ there is always a difference of 1 between the parity of the dipoles and therefore their product will change sign. Of course the integral (3.6) is invariant by symmetry reflection and therefore the only sign change is due to the Wigner 3j symbol in (3.7). These considerations complete the formal theoretical treatment, but other specific questions arise:

- how important are, in practice, the dichroic effects in terms of relative intensity?
- Is there a simple relation between the *D* parameter and the electronic or geometrical structure of the molecule?
- How a difference in the chemical bond along a series of molecules is reflected on the *D* parameter?

To give a reliable answer to these and other important related questions, a large set of experimental measures would be necessary, which at the moment are not available. Therefore the theory and its computational implementation in the present algorithm offers an important help, since allows to collect a large set of calculated *D* parameter profiles to be analysed and rationalized.

In this work four chiral derivatives of oxirane reported in Scheme 1 have been considered, for each molecule the photoionization parameters have been calculated for all the one-electron orbitals, from the outer valence to the core states. The discussion of the results will be structured, for sake of clarity, in four sections: first the discussion of the photoelectron spectrum in terms of the Ionisation Potentials, second the convergence properties of the present method for the description of the photoionization dynamical parameters, third the results of outer valence relevant orbitals, fourth the results regarding core states.

3.4.1 The Ionisation Potentials

It is well established that in Density Functional Theory the exact Kohn-Sham eigenvalue of the Highest Occupied Molecular Orbital (HOMO) corresponds, with the sign changed, to the Ionisation Potential (IP) [28]. However, it has been pointed out that also the Kohn-Sham eigenvalues of inner orbitals are actually approximations to the IP's [29], therefore we have collected in Tables 3.1-3.4 the Kohn-Sham eigenvalues of the four systems of Scheme 3.1, together with the experimental IP's where available.

In general we have considered the ADF results as well as the B-spline LCAO results, the latter obtained with different values of maximum angular momentum expansions on the origin (L_{MAXO}) in order to check the convergence of the B-spline basis set and therefore to judge the quality of the calculation.

In Table 3.1 the results relative to (S)-methyloxirane (**I**) are considered: for the comparison with the experiment [10] it is more convenient to take the ADF results: apart from the differences between the absolute values, the internal shifts (i.e. the level spacing) are very well reproduced by the calculation, the deviations being in general well below 0.2 eV, apart for the largest gaps 15a – 14a and 9a – 8a which are 1.72 and 2.43 eV in the experiment and 1.39 and 1.95 eV in the calculation respectively. This finding indicates that the LB94 KS eigenvalues spectrum gives a realistic description of the ionisation potentials. The molecular orbitals are in general rather delocalized on the whole molecule, however some of them have a peculiar character which is worth describing here since it will be employed in the further discussion. From simple analysis of the ADF KS eigenfunction, it is possible to identify the 16a orbital (HOMO) with the oxygen lone pair, the 15a (HOMO-1) with the σ(C-C) and σ(C-O) bonds which constitute the oxiranic ring and the 9a with an orbital which involves C 2p atomic contributions orthogonal to the ring, which can be addressed as a π(C-C) interaction. The other orbitals have a less clear-cut nature and therefore it is less easy to describe them in simple terms.

The next step consists to compare the eigenvalues of the LCAO B-spline method obtained with basis set of increasing size by rising the L_{MAXO} value with those from the ADF program, in order to check the quality of the B-spline basis set which will be employed to calculate the continuum properties. In Table 3.1 the results for $L_{MAXO} = 10$ and 15 are reported, together with the difference between the $L_{MAXO} = 15$ and the ADF eigenvalues (Δ). It is worth noting that the LCAO $L_{MAXO} = 15$ eigenvalues are always lower than the corresponding ADF ones, for the HOMO even by 0.27 eV, and this indicates that the LCAO B-spline basis set is better than that employed by ADF. As far as inner orbitals are considered, lower differences are found with respect to ADF, and only for two orbitals (2a and 6a) a slightly higher value than in ADF is found. It is important to underline the excellent LCAO results for the core states (1a – 4a), which would not have been practicable at all with the previous OCE implementation [15] for such large and non symmetric molecule. So from this eigenvalue analysis we can conclude that for **(I)** the LCAO B-spline basis set with $L_{MAXO} = 15$ gives an adequate description of the eigenvalues of the bound states. For comparison, the $L_{MAXO} = 10$ results show some differences, at most 0.63 eV for 16a, so we are led to choose $L_{MAXO} = 15$ as a reasonable choice also for the continuum calculations. In Table 3.2 the eigenvalue analysis is performed on *trans*-(2S,3S)-dimethyloxirane **(II)**, for whom only few experimental IP's are available [11]. The calculations have been performed employing the C_2 point group symmetry so its MO's are classified accordingly and the computational economy derived by the symmetry allowed to rise L_{MAXO} up to 20 in the convergence tests. Also in this case the energy shifts between the IP's are properly reproduced by the theory in the ADF results, with the HOMO (9b) well separated by 0.67 eV (0.75 eV in the experiment) from the following orbital (11a), while the next one (8b) is 1.61 eV deeper (1.69 eV in the experiment). Preliminary LCAO test calculations have shown a rather fast convergence from $L_{MAXO} = 10$ up to 15, a further rising of L_{MAXO} up to 20 gives only a small effect: a lowering of 0.29 eV on 7b orbital but much smaller for the other ones. So it seems that also for **(II)** the choice $L_{MAXO} = 15$ is adequate, as it will be confirmed by an analysis on the photoionization properties in the next section, therefore only $L_{MAXO} = 15$ eigenvalues have been reported in Table 3.2.

Table 3.1: The KS-LB94 eigenvalues (ε) of (S)-methyloxirane (**I**) obtained with the B-spline LCAO approach and with the ADF program. Also reported are the differences $\Delta = \varepsilon_{LCAO} - \varepsilon_{ADF}$ for $L_{MAXO} = 15$ and the available experimental ionisation potentials (IP) (Ref. [10]). Values in eV.

MO	ε				
	L_{MAXO} LCAO				
	10	15	ADF	Δ	IP
1a	-537.52	-537.28	-537.23	-0.05	
2°	-292.04	-292.04	-292.08	+0.04	
3°	-291.99	-291.89	-291.85	-0.04	
4a	-290.61	-290.53	-290.50	-0.03	
5a	-31.92	-31.95	-31.92	-0.03	
6a	-23.34	-23.37	-23.38	+0.01	
7a	-21.18	-21.24	-21.21	-0.03	
8a	-19.56	-19.63	-19.58	-0.05	19.65
9a	-17.61	-17.76	-17.63	-0.13	17.22
10a	-16.57	-16.76	-16.60	-0.16	16.18
11a	-15.51	-15.75	-15.61	-0.14	15.12
12a	-14.70	-15.05	-14.93	-0.12	14.46
13a	-14.16	-14.40	-14.27	-0.13	13.57
14a	-13.85	-14.00	-13.91	-0.09	13.04
15a	-12.52	-12.70	-12.52	-0.18	11.32
16a	-11.21	-11.84	-11.57	-0.27	10.44

Table 3.2: The KS-LB94 eigenvalues of trans-(2S,3S)-dimethyloxirane (**II**) obtained with the B-spline LCAO approach and with the ADF program. Also reported are the differences $\Delta = \varepsilon_{LCAO} - \varepsilon_{ADF}$ and the available ionisation potential (IP) (Ref. [11]). Values in eV.

MO	ε		IP
	L_{MAXO} LCAO= 15	ADF	
1a	-537.06	-537.02	
2a	-291.88	-291.91	
3a	-290.66	-290.43	
4a	-31.79	-31.77	
5a	-23.25	-23.31	
6a	-20.07	-20.07	
7a	-16.75	-16.70	
8a	-15.11	-15.27	
9a	-14.56	-14.68	
10a	-13.66	-13.79	12.87
11a	-12.14	-12.11	10.73
1b	-291.88	-291.91	
2b	-290.66	-290.43	
3b	-23.21	-23.27	
4b	-19.42	-19.40	
5b	-17.15	-17.07	
6b	-15.38	-15.49	
7b	-14.23	-14.49	
8b	-13.63	-13.72	12.42
9b	-11.72	-11.44	9.98

Finally Table 3.3 and Table 3.4 report the results concerning (S)-fluorooxirane **(III)** and *trans*-(2S,3S)-difluorooxirane **(IV)** respectively, in this case to our knowledge there are no experimental data for comparison. The substitution of the methyl moiety with fluorine is expected to worsen the LCAO convergence, due to the less diffuse fluorine atomic orbitals: this effect is actually negligible for **(III)**, where similar convergence properties to **(I)** are actually found, while a more pronounced deterioration is found for **(IV)**, ascribed to the larger distance from the origin of F atoms in **(IV)** with respect to **(III)**.

Table 3.3: The KS-LB94 eigenvalues of (S)-fluoroxirane **(III)** obtained with the B-spline LCAO approach and with the ADF program. Also reported are the differences $\Delta = \varepsilon_{LCAO} - \varepsilon_{ADF}$. Values in eV.

	ε	
MO	L_{MAXO} LCAO= 15	ADF
1a	-689.92	-689.90
2a	-538.33	-538.28
3a	-294.44	-294.48
4a	-292.66	-292.63
5a	-36.71	-36.71
6a	-33.05	-33.01
7a	-22.52	-22.47
8a	-21.69	-21.58
9a	-19.61	-19.42
10a	-18.83	-18.60
11a	-17.61	-17.37
12a	-16.59	-16.34
13a	-16.45	-16.25
14a	-15.19	-14.94
15a	-13.64	-13.39
16a	-13.06	-12.78

3.4.2 Convergence of the Photoionization Properties

In the previous section a preliminary convergence analysis has been reported, based on the KS eigenvalues, however it has been found in many instances that σ and β convergence behaviour may be different with respect to that of the eigenvalues [14,30], so in this section we check the convergence for σ, β

and, more important, for *D*, whose convergence property has not been yet addressed.

Table 3.4: The KS-LB94 eigenvalues of trans-(2S,3S)-difluoroxirane **(IV)** obtained with the B-spline LCAO approach and with the ADF program. Also reported are the difference $\Delta = \varepsilon_{LCAO} - \varepsilon_{ADF}$ for $L_{MAXO} = 20$ eV.Values in eV.

	ε				
	L_{MAXO} LCAO				
MO	10	15	20	ADF	Δ
1a	-695.92	-691.24	-690.70	-690.58	-0.12
2a	-539.09	-539.09	-539.09	-539.04	-0.05
3a	-295.15	-295.06	-295.06	-295.09	0.03
4a	-37.84	-37.58	-37.58	-37.56	-0.02
5a	-33.86	-33.84	-33.84	-33.81	-0.03
6a	-22.90	-23.08	-23.20	-23.14	-0.06
7a	-19.38	-19.92	-20.25	-20.08	-0.17
8a	-18.15	-18.46	-18.64	-18.46	-0.18
9a	-15.82	-17.07	-17.92	-17.81	-0.11
10a	-11.69	-15.19	-16.23	-16.14	-0.09
11a	-9.50	-13.07	-13.83	-13.65	-0.18
1b	-695.92	-691.24	-690.70	-690.57	-0.13
2b	-295.16	-295.05	-295.06	-295.08	0.02
3b	-37.72	-37.30	-37.32	-37.29	-0.03
4b	-22.11	-22.35	-22.52	-22.42	-0.1
5b	-20.25	-20.52	-20.66	-20.48	-0.18
6b	-17.48	-18.32	-18.84	-18.70	-0.14
7b	-14.43	-15.73	-16.95	-16.91	-0.04
8b	-12.05	-14.95	-15.69	-15.48	-0.21
9b	-10.65	-14.17	-14.34	-14.03	-0.31

In Fig. 3.1 the photoionization dynamical parameter profiles of the HOMO (orbital 9b) of **(II)** are reported, calculated with L_{MAXO} = 10, 15 and 20. It is well apparent that convergence is already gained for L_{MAXO} = 15, since the raising of angular momentum gives only a very marginal improvement, whose effect is reflected only in the near threshold region of the cross section, while β and *D* parameters seem to be no more sensitive to the basis set enlargement. This finding is very promising since indicates that the *D* parameter is not very demanding in terms of basis set requirements. The same convergence analysis has been done for **(I)** as well, and for this system an even faster convergence with respect to L_{MAXO} has been found, confirming that L_{MAXO} = 15 is an appropriate choice.

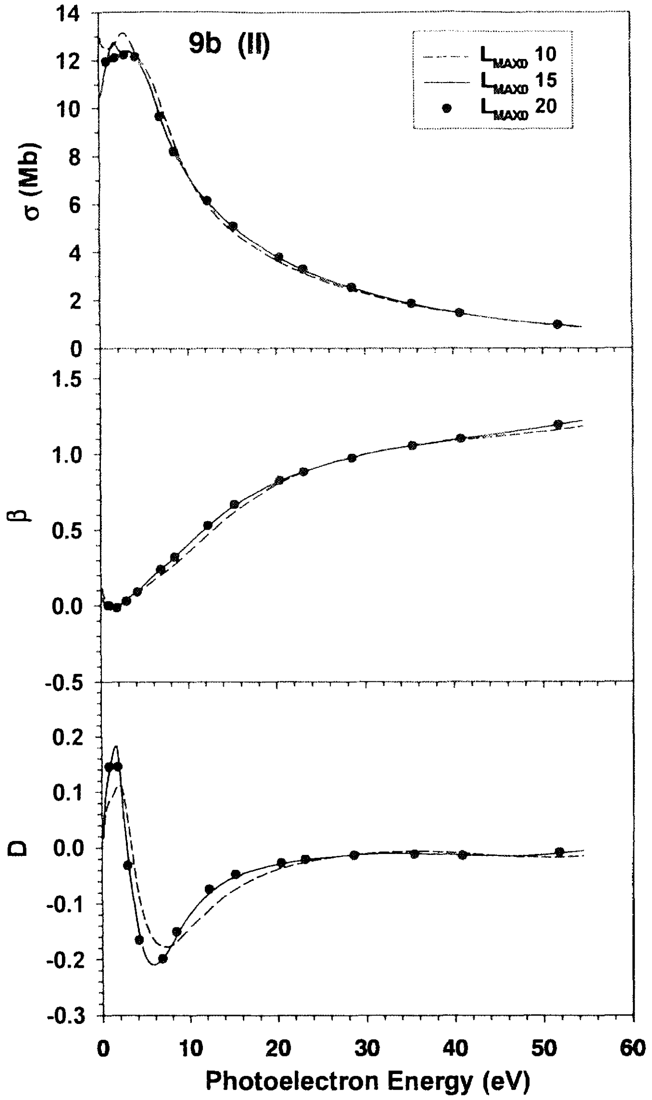

Figure 3.1: Cross section (σ), asymmetry parameter (β) and dichroic parameter (*D*) relative to the 9b orbital (HOMO) of *trans*-(2S,3S)-dimethyloxirane (**II**) calculated with L_{MAXO} = 10, 15 and 20.

From the results of such analysis we have chosen L_{MAXO} = 15 for all the successive calculations, a choice which guarantees practically convergent results for both system with still practicable numerical effort. Moreover, L_{MAXO} = 15 is employed as well in the calculations of (**III**) and (**IV**), whose requirements are expected to be comparable to those of (**I**) and (**II**) respectively. We have performed additional convergence test calculations for (**IV**) which confirmed the choice L_{MAXO} = 15 also for this system.

3.4.3 Valence Dichroism

In Fig. 3.2 the σ, β and *D* parameter profiles of the molecular orbitals corresponding to the oxygen lone pair of all four systems studied in the present work are considered. Such comparison among different molecules is meaningful, because we have checked that in all cases the oxygen lone pair keeps its nature along the series. The first observation concerns the different sensitivity of the parameters to the oxiran substitution: σ and β do not show important differences, the latter is even almost identical for all the molecules considered, while in the cross section only the curve of **(IV)** is shifted towards the threshold with respect to the other ones. On the other hand the *D* parameter shows two interesting qualities: first its values oscillate in a rather wide range (from −0.2 up to +0.2 roughly) and this means that the CDAD effect is of the order of 20% in terms of relative intensity, a rather large effect which should be easily experimentally detectable. Second, the *D* parameter proves to be very selective with respect to the chemical substitution of the oxirane ring: the profiles are quite different for the various molecules and this is a quite unexpected and a very promising spectroscopic characteristic: *D* seems to be much more sensitive than σ and β to changes in the electronic structure of the system under study.

In particular, the *D* profile in **(I)** decreases very rapidly at threshold, followed by a broad minimum and a very slow rise to high energy. In **(II)** the following differences are observed: the profile is shifted to higher energy by a couple of eV's and the amplitude of the oscillation is enhanced by about 25%. These differences are quite large and it would be very desirable to have an experimental confirmation in further measurements. In any case the energy shift to higher energy is ascribed to the electronic effect of the increasing number of methyl groups, which act as electron donors and therefore will increase the electron density on the O atom [31]. The *D* profile in **(III)** is much less structured, while in **(IV)** rather large negative values are calculated near the threshold, this suggests that the electronegative effect of F substitution competes gradually with that of the O atom, so in **(III)** the effects are mutually comparable but in **(IV)** the presence of two F atoms changes the behaviour of the *D* parameter. Moreover, the *D* parameter tends asymptotically to zero at high energy for all the systems, as already observed in previous works [8,9], suggesting that CDAD effect should be in general investigated within 20 – 30 eV above the threshold. Finally it is worth noting that despite the large predicted CDAD effect, the lone pair ionized orbital is not 'chiral' by itself, since it is essentially constituted by O 2p atomic functions orthogonal to the oxiranic ring, and therefore it has, with good approximation, a local symmetry reflection plane. This means that the observed dichroism cannot be ascribed to the initial state, but rather should be attributed to the molecular effective potential which acts on the photoelectron wave-function, which is completely delocalized and therefore feels the global asymmetry of the molecule.

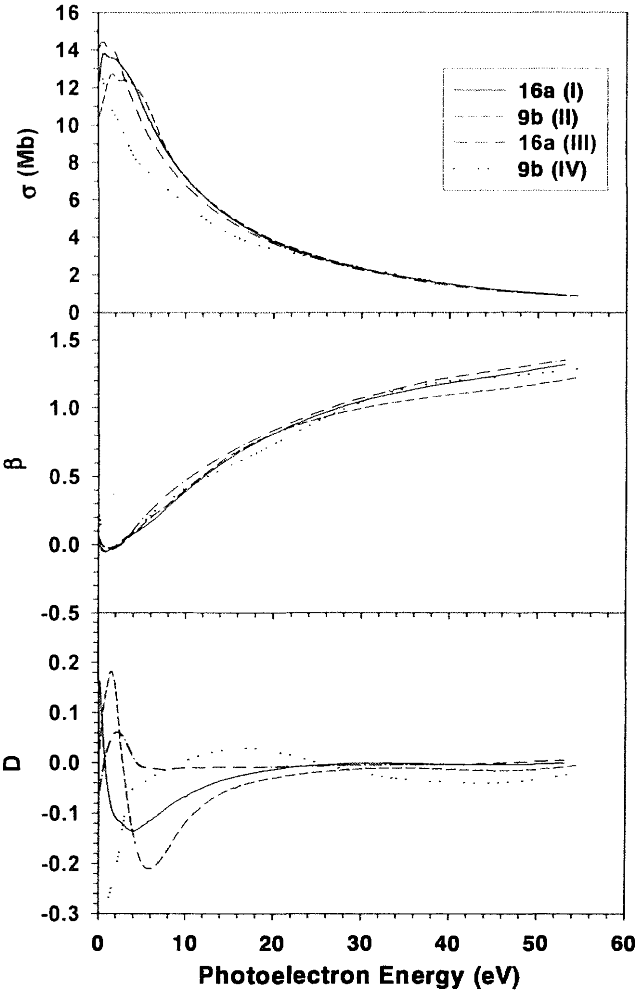

Figure 3.2: Cross section (σ), asymmetry parameter (β) and dichroic parameter (D) relative to the 16a (**I**), 9b (**II**), 16a (**III**) and 9b (**IV**) orbitals and molecules respectively, calculated with L_{MAXO} = 15.

It would be interesting also to identify a possible correlation between the D parameter and the geometrical structure of the systems under study. To this end we have reported in Table 3.5 the most relevant bond lengths and bond angles of the four molecules obtained from the geometry optimization performed with the VWN exchange correlation functional. However, it is well apparent from the reported data that only very tiny variations of structural properties are present along the series, the most relevant one being a shortening of the O-C(2) bond length in the fluorinated oxiranes by about 7% with respect to the methyl-substituted ones. Therefore in the present series we may expect that the observed trend are caused mainly by electronic rather than geometric effects. On the other hand, it would be interesting to consider, as a possible future work, a similar analysis in a series with pronounced geometrical variations but without strong differences in the electronic structure, to verify the importance of purely geometrical effects on the CDAD.

Table 3.5: Optimized bond lengths (Å) and bond angles (°) of the chiral molecules considered in this study: **(I)** (S)-methyloxirane; **(II)** *trans*-(2S,3S)-dimethyloxirane; **(III)** (S)-fluoroxirane; **(IV)** *trans*-(2S,3S)-difluoroxirane.

	(I)	(II)	(III)	(IV)
$O–C^a$	1.423		1.443	
$O–C^b$	1.423	1.426	1.371	1.397
$C^a–C^b$	1.456	1.458	1.446	1.443
$C^b–CH_3$	1.480	1.480		
$C^b–F$			1.358	1.348
$O–C^b–C$	59.2	59.3	61.6	58.9
C–O–C	61.5	61.5	61.8	62.2
$X–C^b–O$	115.9	115.8	115.4	115.1
$X–C^b–C$	121.4	122.2	118.3	120.1

[a] C not substituted
[b] C substituted
[c] X indicates the substituent (CH_3 or F) of the oxirane ring.

In Fig. 3.3 the photoionization parameters relative to the orbital just below the oxygen lone pair are considered, which means 15a for **(I)** and **(III)** and 11a for **(II)** and **(IV)**. These orbitals have a very similar nature along the series, as already found for the oxygen lone pair previously considered: their KS wavefunctions have been plotted over the ring plane in Fig. 3.4. As can be seen from the four plots, in all cases these orbitals belong to the σ(C-C) and σ(C-O) chemical bonds of the oxiran ring, and minor differences can be observed along the series: only a slight asymmetry in the C-O interaction is found in **(I)** and **(III)** and indicates a stronger interaction between O and the substituted C atoms. We can start the discussion with the cross section profiles (Fig. 3.3, upper panel), which for these orbitals show more pronounced variations along the series than in the previous Fig. 3.2: **(I)** displays a maximum in the cross section just above the threshold, which is slightly shifted at higher energy in **(II)**. On the other hand the fluorinated derivatives **(III)** and **(IV)** display a maximum reduced in intensity by almost a factor of two with respect to the former ones. However, the asymmetry parameter (Fig. 3.3, central panel), remains insensitive to the chemical substitution, only a very minor effect is found for **(IV)**. Finally we consider the dichroic parameter D in the lower panel: also in this case a very large effect is found both in terms of relative intensity (range from -0.3 up to $+0.25$) and sensitivity to the chemical substitution. If we compare the shape of the curves, the following behaviours emerge: going from **(I)** to **(II)** a shift to higher energy and an amplitude enhancement is evident, as already observed and discussed previously in terms of methyl electronic effect. An interesting similarity is found if we compare internally the curves of mono-substituted **(I)** and **(III)**: they show significant resemblance apart the shift on the energy scale, and the same behaviour holds for the di-substituted **(II)** and **(IV)**. This finding suggests that also structural characteristics are somehow mapped in the D parameter, although this was not evident for the orbitals previously considered in Fig. 3.2. A possible reason which may rationalize the different behaviour found is the more delocalized nature of the ring σ(C-C) and σ(C-O) bonds (orbitals), which can feel the structural changes more effectively than the very localized oxygen lone pair, rather far from the region where the chemical substitution happens.

The orbitals from 10a to 14a of **(I)** are rather specific of this system, so it is difficult to find a clear correspondence with those of the other molecules, and since we are more interested in the trends along the series we do not consider them now.

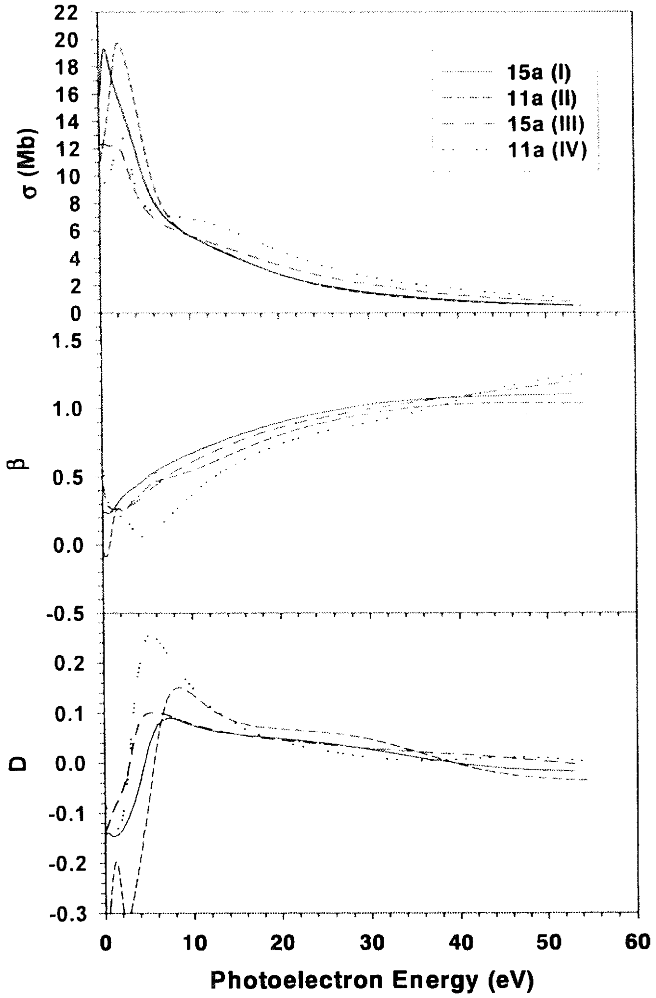

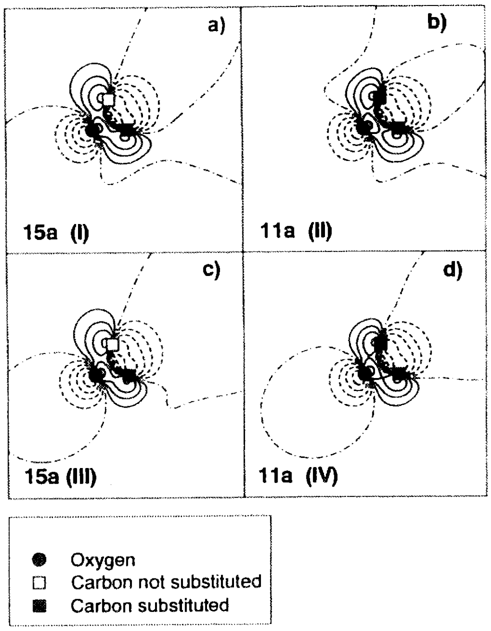

Figure 3.4: Contour plots relative to the 15a (I), 11a (II), 15a (III) and 11a (IV) orbitals and molecules respectively, taken over the oxirane ring plane. Solid, dashed and dot-dashed isolines indicate positive, negative and zero (nodal) contributions respectively.

Figure 3.3: Cross section (σ), asymmetry parameter (β) and dichroic parameter (*D*) relative to the 15a **(I)**, 11a **(II)**, 15a **(III)** and 11a **(IV)** orbitals and molecules respectively, calculated with $L_{MAXO} = 15$.

However, the orbital 9a in **(I)** is found to correspond nicely with the orbitals 5b, 9a and 5b of **(II)**, **(III)** and **(IV)** respectively, their σ, β and *D* parameter profiles are reported in Fig. 3.5 and the orbital plots are displayed in Fig. 3.6. The orbitals have been plotted in a plane perpendicular to the oxirane and passing through the two carbon atoms of the ring, and it is evident from Fig. 3.6 that their nature is conserved along the series. In particular these orbitals have large contributions from C 2p functions orthogonal to the ring, which have bonding π(C-

C) character, but also an important interaction with substituent (F 2p and methyl C 2p) of σ character is present.

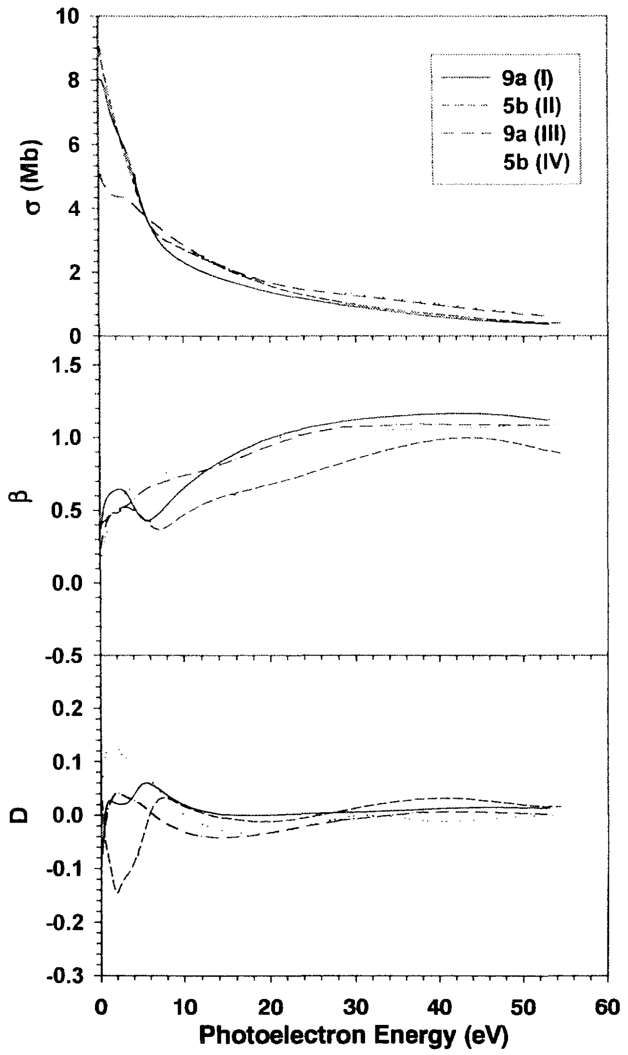

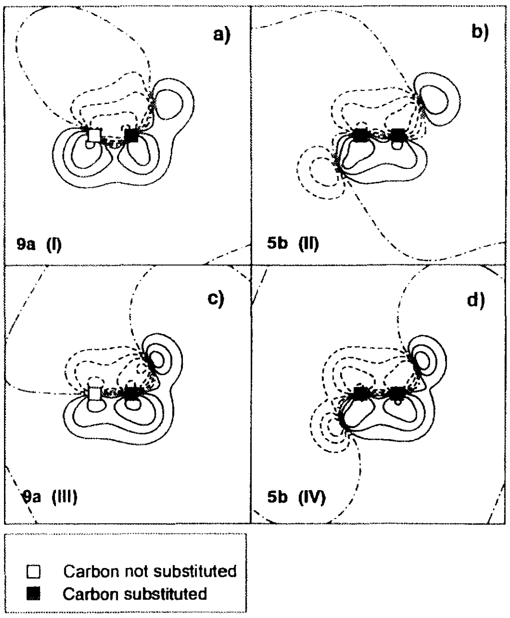

Figure 3.6: Contour plots relative to the 9a (**I**), 5b (**II**), 9a (**III**) and 5b (**IV**) orbitals and molecules respectively, taken over the plane orthogonal to the oxirane ring and passing through C(2) and C(3). Solid, dashed and dot-dashed isolines indicate positive, negative and zero (nodal) contributions respectively.

Figure 3.5: Cross section (σ), asymmetry parameter (β) and dichroic parameter (*D*) relative to the 9a (**I**), 5b (**II**), 9a (**III**) and 5b (**IV**) orbitals and molecules respectively, calculated with $L_{MAXO} = 15$.

In this case the cross section profiles (upper panel in Fig. 3.5) are very similar if the same substituent is present, and remains roughly independent to the substitution degree, a very similar situation of what has been already found for the orbitals considered in Fig. 3.3. The asymmetry parameter β shows, at least just above the threshold, some variations along the series: while the fluorinated compounds give a monotonic increase with energy, in **(I)** and **(II)** a weak oscillation is present. The dichroism *D* now decays very quickly, after 10 eV above the threshold only a very smooth and weak wave survives. At threshold the behaviours are very well separated, if we take **(I)** as reference, **(II)** is shifted at higher energy while **(III)** and **(IV)** are pulled to threshold, in line with electron donor/acceptor arguments already considered. In any case, also for this π(C-C) orbital, the dichroism *D* parameter has proven to be the most informative in terms of sensitivity to electronic structure changes along the series.

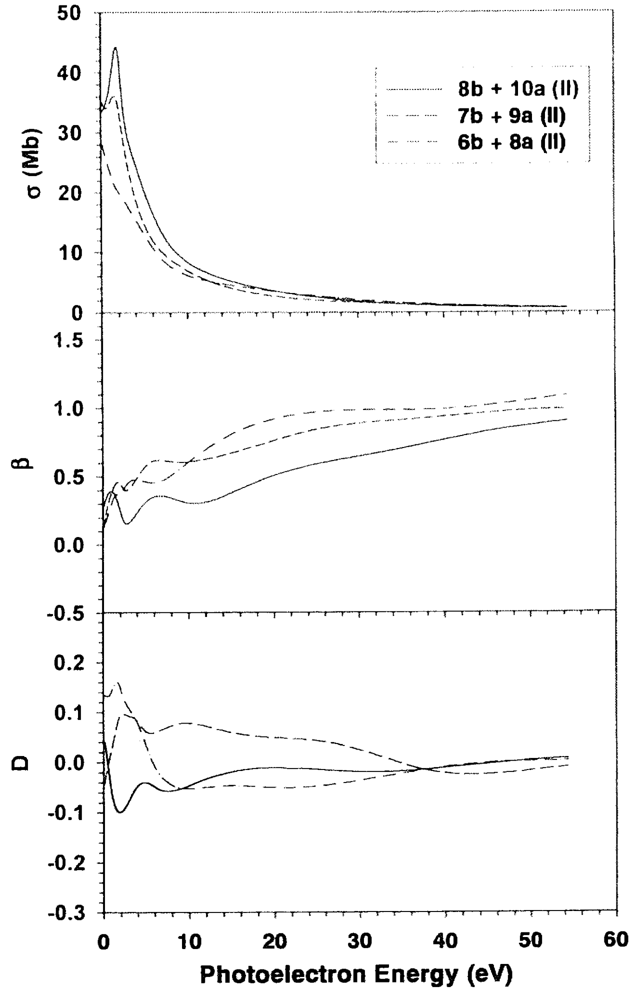

Figure 3.7: Cross section (σ), asymmetry parameter (β) and dichroic parameter (*D*) relative to the 8b + 10a, 7b + 9a and 6b + 8a bands in **(II)**, calculated with $L_{MAXO} = 15$.

Before concluding the valence photoionization section, we considered important to report some results which might be relevant for comparison with future possible experimental measurements. Since this aspect has been already addressed in [7] for **(I)**, and **(III)**–**(IV)** are less suitable for experimental measurements, we have focussed our attention on **(II)**. Recalling the calculated PES of **(II)** reported in Tab. 3.2, it can be noticed that eigenvalues are grouped in almost degenerate pairs for the orbitals in the range 8a – 10a and 6b – 8b, this means that it is very likely that in the experimental PES only unresolved bands including each two separate ionisations could be actually detected. For this reason we have considered in Fig. 3.7 the photoionization parameters calculated for three bands, each corresponding to the following summed contribuition: 8b+10a, 7b+9a and 6b+8a respectively. The predicted cross section displays a narrow maximum for the two outer bands, while the inner one decreases rapidly at threshold. The asymmetry parameter becomes less structured going from the outer to the inner band: the waving behaviour is more and more weakened and smoothed. The dichroism parameter gives its usual good sensitivity: 8b+10a and 6b+8a profiles are pronounced only just within roughly 10 eV above the threshold, where they give a dichroism of different sign, while 7b+9a keeps a much higher dichroism value up to about 30 eV.

3.4.4 Core Dichroism

The profiles relative to the O 1s orbital of the systems under study are considered in Fig. 3.8. All the cross section curves display a maximum just above the threshold followed, a couple of eV's at higher energy, by a second minor structure which appears as a shoulder, these features are ascribed to shape resonances associated with low-lying valence virtual states or, possibly, to trapping effects caused by the cyclic molecular structure. Interestingly at high photoelectron energy (50 eV) a very smooth maximum is clearly visible, and it is ascribed to the first EXAFS oscillation. It is interesting to compare these results with that of the O 1s cross section of H_2O and CO. The former is completely structureless [32] and its threshold value is around 0.8-0.9 Mb, in the latter a shape resonance [22] is well known to be present and the cross section starts at threshold with a value of 0.5 Mb and grows up to 0.9 Mb at the shape resonance. The behaviour of the systems of the present work lies somehow in between: it seems that the shape resonances are actually present but they are less pronounced than in CO. Another hint which suggests the presence of shape resonances comes from the asymmetry parameter profiles: in **(I)** and **(II)** there is a narrow structure near to the ionisation limit constituted by a maximum and a minimum very close each other, as it has been theoretically [22] and experimentally [33] found for the O 1s orbital shape resonance counterpart in CO, while in H_2O the β profile is quite straight [32] due to the absence of resonances. The *D* parameter assumes relevant values only within 14 eV above the threshold, however its range remains less wide than what has been previously found in the outer valence orbitals: in all cases it does not go beyond 0.08 in absolute value, although for **(I)** it remains below 0.02. For the dichroism the presence of a shape resonance does not seem to have an enhancing or reshaping effect, and this suggests that the *D* parameter is more sensitive to tiny asymmetries of the molecular effective potential than to continuum collapse effects. It is worth noting that for core states the dicroism must be definitely a final state effect, in fact initial state 1s orbitals retain their atomic nature and their spherical symmetry: therefore the dicroism is ascribed to the photoelectron wavefunction which is delocalized and can probe the whole effective molecular potential extracting information on its dissimmetry.

In Fig. 3.9 the C 1s core ionisations of the C(2) atom are considered, which corresponds to the substituted ring carbon: in order to be consistent in the cross section absolute scale, we have normalized for one C 1s orbital the results of **(II)** and **(IV)**, which have two substituted C atoms, dividing by two the sum of the contributions of the two core states. The cross section profiles display rather similar shapes, this time two distinct maxima are present, the second one at higher energy being more intense and broader, moreover the methyl-derivatives **(I)** and **(II)** give profiles shifted to higher energy by about 2 eV. The asymmetry parameter also this time does not perform well in terms of changes along the series, which remain rather modest. On the other hand, the *D* parameter carries interesting structures, which however decay rapidly within 10 eV, beyond that limit only very weak and smooth oscillations are predicted. In this case **(I)** and **(II)** do not resemble each other, only **(II)** and **(IV)** have very similar shapes, enhanced in the latter.

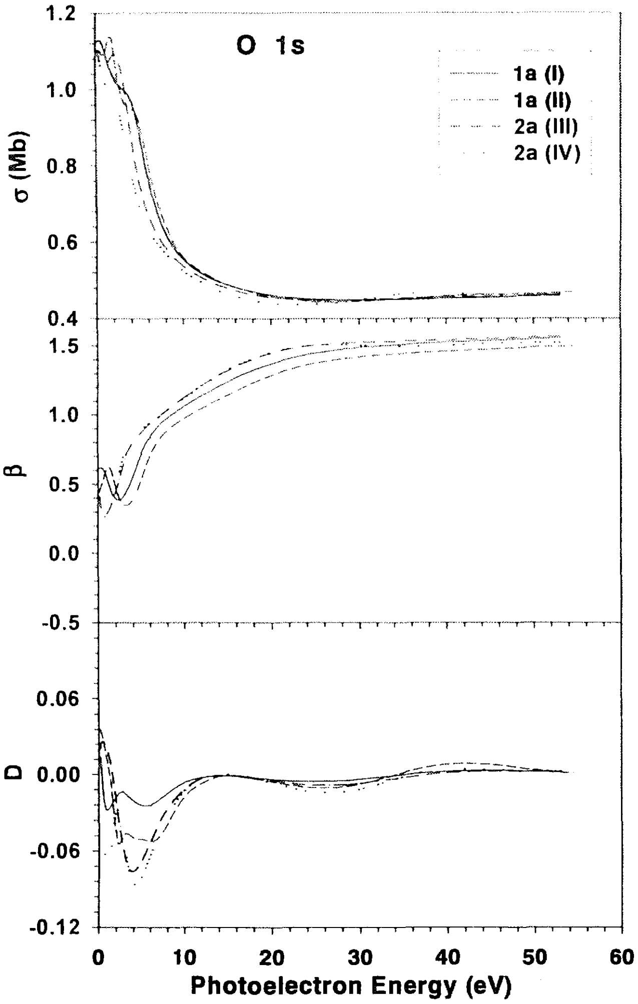

Figure 3.8: Cross section (σ), asymmetry parameter (β) and dichroic parameter (*D*) relative to the core O 1s orbitals, calculated with $L_{MAXO} = 15$.

In **(I)** and **(III)** the C(3) atoms do not carry any substituent, and their C 1s dynamical parameters are collected in Fig. 3.10. In the cross section a clear cut shape resonance is found, about 4 and 3 eV above the threshold for **(I)** and **(III)** respectively, while a just sketched maximum is also found for **(I)** and the usual energy shift is present. The β profile shows a rather different behaviour with respect that of C(2): for C(3) the minimum is followed by a sudden rise and successively by a flat tail while for C(2) the rise was more uniform over the whole energy range. This finding suggests that the asymmetry parameter, which up to now did not show interesting behaviours along the series, may be more useful to probe profitably different core states within the same system than the same core ionisation along a series. The dichroism parameter *D* is calculated to be rather weak even near the threshold, this may be a consequence of the absence of chirality on this center, but this should be excluded because for the achiral O atomic site a more pronounced dichroism was actually predicted (Fig. 3.8).

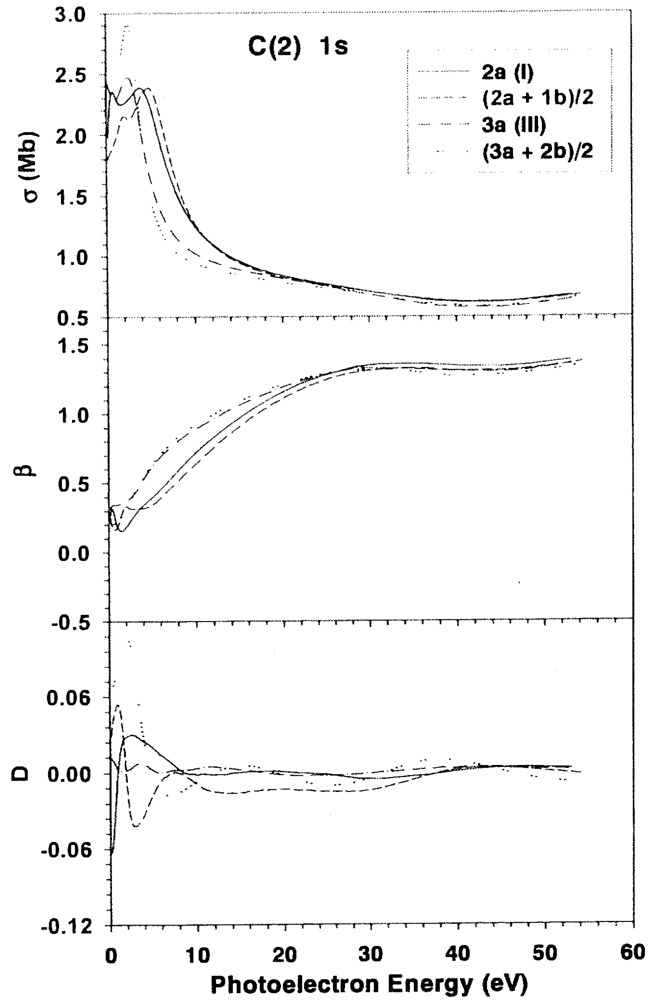

Figure 3.9: Cross section (σ), asymmetry parameter (β) and dichroic parameter (*D*) relative to the core C(2) 1s orbitals, calculated with $L_{MAXO} = 15$.

Finally the methyl group C(4) 1s ionisation is considered in Fig. 3.11, normalized as before for one C atom for sake of comparison. In the cross section the double structure is present again, now the first peak is narrow and intense while the second is broader and less intense. The asymmetry parameter displays a shape which lies in between that of C(2) and C(3), and is not sensitive along the series. The dichroism remains rather weak for **(I)**, while in **(II)** it assumes appreciable values which make it suitable for an experimental detection.

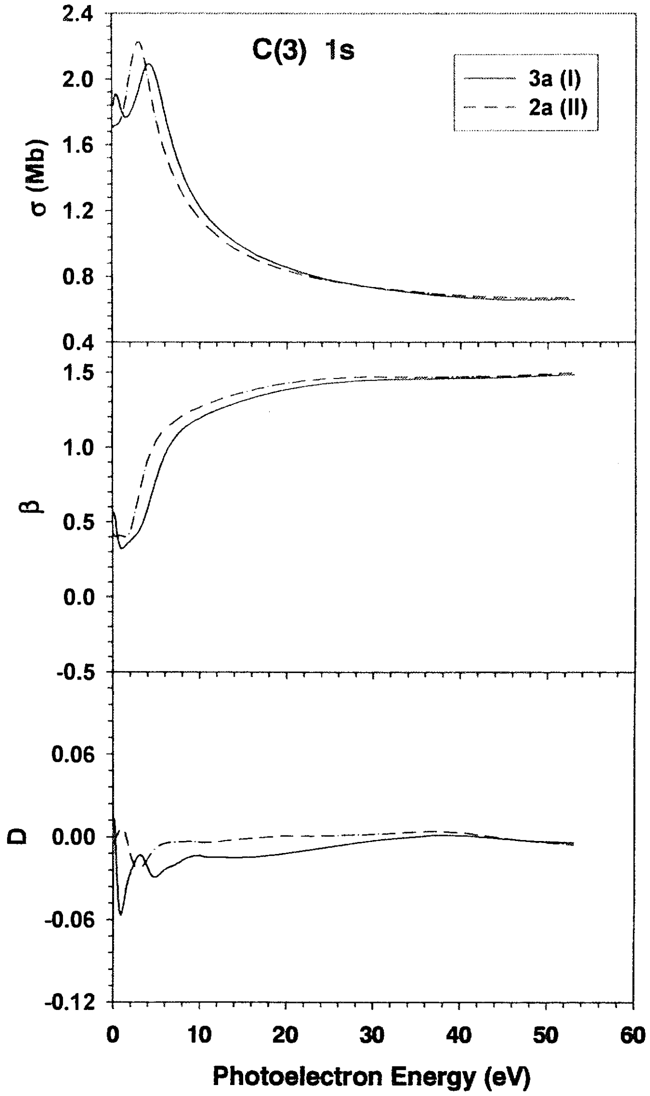

Figure 3.10: Cross section (σ), asymmetry parameter (β) and dichroic parameter (*D*) relative to the core C(3) 1s orbitals, calculated with $L_{MAXO} = 15$.

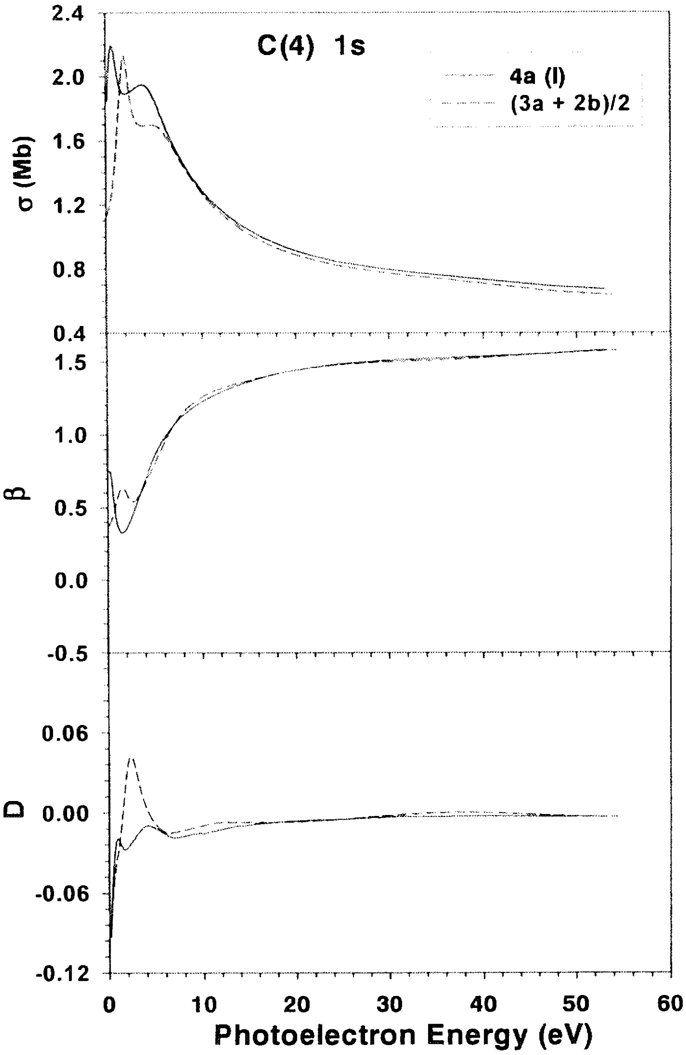

Figure 3.11: Cross section (σ), asymmetry parameter (β) and dichroic parameter (*D*) relative to the core C(4) 1s orbitals, calculated with $L_{MAXO} = 15$.

3.5 Conclusions

The LCAO B-spline DFT method has been successfully applied to a series of four chiral derivatives of oxirane, with the aim to calculate the photoionization dynamical parameters, with special attention to the CDAD effect and to identify possible trends along the series.

The computational algorithm, based on multicentric basis set with proper continuum boundary conditions, has proven numerically stable and computationally competitive, since it has allowed to obtain convergent results (with respect to basis set enlargement) on the molecules under study, which for their low symmetry and moderately large size represent stringent tests for the method efficiency.

The photoionization cross section, asymmetry and dichroic parameter profiles relative to valence orbitals have been systematically studied for the states which retain their nature along the series: the identified trends have been ascribed to the different electronic properties of the substituents. A rather unexpected sensitivity of the *D* parameter to changes in the electronic structure has been found in many instances, making this dynamical property suitable to investigate the electronic structure of chiral compounds. The magnitude of the CDAD effect does not seem to be associated to the initial state chirality, but rather to be caused by the ability of the delocalized photoelectron wave function to probe the asymmetry of the molecular effective potential.

For core ionisations (O 1s and C 1s) a CDAD effect less intense than in the valence shell is found and the chiral center is not necessarily connected with the most pronounced dichroism, this finding corroborates the attribution to the final continuum as the main origin of the observed behaviours and less importance to the characteristics of the initial state. Two distinct shape resonances have been identified in the core C 1s cross section, however we did not find any dichroism enhancement in correspondence of such resonances.

The study of the CDAD effects of chiral molecules is a promising tool to investigate the electronic structure of such systems. In general the CDAD effect is calculated to decay rapidly with the photoelectron energy, usually within 20 eV above the threshold and it has been found for core ionisation as well, although less intense than in the valence.

Further studies to enlarge the set of the investigated systems would be desirable, in particular to identify more precisely the physical causes of the observed patterns in the *D* profiles and to address more specific topics, like for example the importance of conformational effects for more complex molecules.

4 Theoretical Study on the Circular Dichroism in Core and Valence Photoelectron Angular Distributions of Camphor Enantiomers

In the present work the photoelectron circular dichroism of camphor has been theoretically studied using B-spline and CMS-Xα methods, and comparisons made with available experimental data. In general, rather large dichroism effects have been found both for valence and for core (O 1s, C 1s) photoionization. The agreement between the two calculations reported here and previous experimental measurements for core C 1s data is essentially quantitative. For valence ionisation satisfactory agreement between theory and experiment has been obtained and the discrepancies have been attributed to both exchange-correlation potential limitations and the absence of response effects in the adopted formalism. The calculations predict, moreover, important features in the cross section profiles, which have been discussed in terms of dipole-prepared continuum orbitals.

4.1 Introduction

Chirality plays a fundamental role in nature especially in biological systems. In fact, it is well known that naturally occurring organic molecules such as amino acids exist in only one enantiomeric form. The spectroscopic study of chiral systems can be profitably done by employing the dichroism effect that arises as a consequence of the interaction with circularly polarized light. Conventional experiments employ differential light absorption between left and right circularly polarized light, but the magnitude of such dichroism depends upon electric quadrupole or magnetic dipole operator contributions making the total effects rather weak, of the relative order of about 10^{-5}. On the other hand it was proposed some considerable time ago [1] that angle resolved photoionization experiments may give dichroism effects which are governed purely by the electric dipole operator, so with an intensity which may be anticipated to be orders of magnitude stronger than in conventional absorption experiments. Of course, practical realization of angle resolved photoionization experiments with circularly polarized light is not a straightforward issue, but recently synchrotron radiation technology evolution has allowed such measures, which have started to appear in the literature [2-6]. Moreover, efforts to perform theoretical calculations of dichroism effects based on CMS-Xα [7,8] and B-spline [6,9] methods on large organic chiral molecules have recently started. It is worth noting that the calculation of the dichroism needs a knowledge of the continuum photoelectron wavefunction, a task which is not yet standard in quantum chemistry due to the difficulty of implementing the continuum boundary conditions with a conventional basis set. So at present two methods are available for this task; the CMS-Xα which simplifies the problem by introducing a rather crude approximation on the potential (muffin-tin), and the B-spline method which treats the potential according to the Density Functional Theory (DFT) method employing the correct boundary conditions with a finite set of basis functions.

Camphor is an excellent candidate to be studied both experimentally and theoretically, because it is a rigid molecule (conformational freedom is limited to the rotation of methyl moieties), is commercially available in pure enantiomeric form, and has been already studied in conventional photoelectron spectroscopy [10].

Measurements of the camphor photoelectron circular dichroism have recently been reported as a function of photon energy for both the core electron region [4] around 300 eV and for the outer valence region using VUV synchrotron radiation [3,5,11]. In the core region attention was focussed on the well resolved carbonyl C 1*s* photoemission and measurements were made from near threshold to some 70 eV above edge. Perhaps surprisingly in view of the highly localised, spherically symmetric nature of this initial orbital, a strong asymmetry of up to 12% was inferred in the forward-backward electron scattering (referred to the propagation direction of the photon beam). However, comparison with a preliminary theoretical estimate shows that this is fully expected from the final state scattering of the photoelectron off the chiral molecular core [4].

In the valence region, ionisation of the outermost orbital, which can be characterised as the carbonyl oxygen lone pair, has been examined over a photon energy range extending from near threshold [3,11] to some 15 eV above [5,11]. Again, this orbital is reasonably strongly localised at a site other than a chiral stereogenic centre, but the observed asymmetries in the angular distribution are of similar magnitude to the C 1s data.

4.2 Theoretical Methods

In this work both the B-spline LCAO DFT and the CMS-Xα methods have been employed to calculate the photoionization properties of the R-(+) enantiomer of camphor (Scheme 4.1), in the gas phase with random molecular orientation. Such a process is described, for each different orbital, by the differential cross section [12] $d\sigma/d\hat{k}$, that is the angular distribution of the photoelectrons in the solid angle $d\hat{k}$ along their direction of propagation $\hat{k}$, which, in the electric dipole approximation, is completely defined by the partial cross section σ, the asymmetry parameter β and the dichroism parameter D:

$$\frac{d\sigma}{d\hat{k}} = \frac{\sigma}{4\pi}\left[1 + \left(-\tfrac{1}{2}\right)^{|m_r|} \beta P_2(\cos\theta) + m_r D P_1(\cos\theta)\right], \qquad (4.1)$$

where P_i is the Legendre polynomial of i-th order and θ is the scattering angle between $\hat{k}$ and the laboratory frame. The polarization index, m_r, is 0, +1, –1, respectively, for linear, left circular, or right circular light polarization. The laboratory frame is defined by the incident photons: the polar axis corresponds to the electric vector or propagation direction respectively for linear or circular light polarization. We define left or right circularly polarized light according to the value $m_r = +1$ or $m_r = -1$ of the projection of the photon spin along its momentum. Accordingly, the electric vector describes a positive (right-handed) or negative (left-handed) screw.

From the computational point of view the photoionization process is completely described, at the one-electron level, by the dipole transition moment between the ionized orbital and the photoelectron continuum orbital. Therefore the problem is recast to have efficient and accurate algorithms for the molecular continuum.

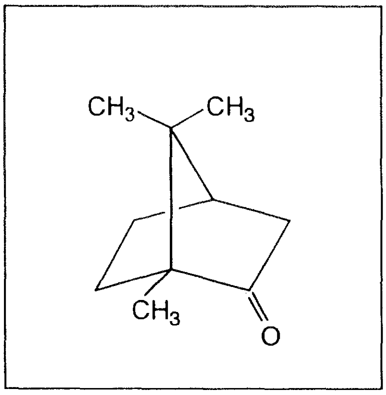

Scheme 4.1: Structure of the (1R)-(+) enantiomer of camphor.

4.2.1 The B-spline LCAO DFT Method

The B-spline LCAO DFT method [13] has proven to be accurate, computationally economic and numerically stable and it has already been employed to study the photoionization of medium-sized molecules with explicit treatment of the continuum photoelectron wave function [6,9,14]. A short review of the B-spline LCAO DFT method is given in the following referring to Ref. [13] for a detailed description of the method.

Continuum calculations are performed at the DFT Kohn-Sham level. The initial ground state density, which fixes the potential, is obtained by a conventional LCAO calculation employing the ADF program [15,16]. The LB94 exchange correlation potential [17] has been employed, because of the correct Coulomb tail, which is important for the accurate description of the continuum properties [18]. It is worth noting that in the present scheme the potential felt by the photoelectron is identical for all the ionic states considered. Therefore the scattering wave-function is the same for all the different ionic states and the cross section, but the asymmetry and the dichroic parameters will be different because the dipole matrix elements will depend also on the initial ionised state. The shape resonances, which appear in the cross section profiles, are ascribed to quasi bound states in the continuum, and therefore appear at energy independent by the initial states. Both bound and continuum orbitals are expanded in a very accurate basis, built from B-spline radial basis functions, which can describe both decaying and oscillatory behaviour. This avoids any approximation to the molecular potential, as in the CMS-Xα approach, but is still able to treat rather large, non symmetric molecules, which are not manageable with pure one center expansions.

The LCAO basis set consists in a large one center expansion (OCE) located on a chosen origin O:

$$\chi^{O}_{nlh\lambda\mu} = \frac{1}{r_O} B_n(r_O) X_{lh\lambda\mu}(\vartheta_O, \varphi_O), \tag{4.2}$$

where

$$X_{lh\lambda\mu}(\vartheta, \varphi) = \sum_{m} Y^{R}_{lm}(\vartheta, \varphi) b_{lmh\lambda\mu} \tag{4.3}$$

are symmetry adapted linear combinations of real spherical harmonics [19] and B_n is the n-th spline monodimensional function [20]. These are supplemented by functions of the same type, which are symmetrized combinations of functions centered at the off-center positions j:

$$\chi^{i}_{nlh\lambda\mu} = \sum_{j \in Q_i} \frac{1}{r_j} B_n(r_j) \sum_{m} b_{lmh\lambda\mu j} Y^{R}_{lm}(\vartheta_j, \varphi_j), \tag{4.4}$$

where i is an index which runs over the non-equivalent nuclei, Q_i is the set of equivalent nuclei, j runs over the equivalent nuclei and gives the origin of the off-center spherical coordinates $r_j, \vartheta_j, \varphi_j$. The coefficients $b_{lmh\lambda\mu}$ and $b_{lmh\lambda\mu j}$ are determined by symmetry: λ is the irreducible representation (IR) label and μ identifies the subspecies in case of degeneracy. The B-splines are built over the radial intervals $[0, R^{O}_{MAX}]$ for the set $\{\chi^{O}_{nlh\lambda\mu}\}$ and $[0, R^{i}_{MAX}]$ for the set $\{\chi^{i}_{nlh\lambda\mu}\}$.

The B-splines are completely defined by their order and by the grids of knots for all the radial intervals $[0, R^{O}_{MAX}]$ and $[0, R^{i}_{MAX}]$. In practice the most important computational choice regarding the basis set, which has a fundamental impact on the accuracy and the computational economy, is the maximum value of the angular expansion L_{MAXO} for the OCE and L_{MAXi} for each set of non equivalent centers.

The bound states of the system are obtained by means of a generalized diagonalization of the KS Hamiltonian matrix in the B-spline LCAO basis set. The continuum states are calculated employing a very efficient inverse iteration procedure [21] and normalized according to the K matrix condition. The K-normalized continuum orbitals are further transformed to incoming wave S-matrix boundary conditions and from such states the dipole matrix elements are finally obtained. The cross section, the asymmetry and dichroism parameters profiles for randomly oriented molecules are then computed according to the angular momentum transfer formalism [22,9].

Since the LB94 exchange correlation potential employed in the present B-spline LCAO calculations is slightly too attractive, the resulting cross section, asymmetry and dichroic parameters profiles are shifted towards lower energy by fews eV's. In order to correct this error for a more effective comparison with the experiment, all valence and core B-spline LCAO profiles reported in all the figures of the present work have been shifted by 3 eV, which have been added to the photoelectron kinetic energy.

4.2.2 The CMS-Xα Method

The CMS-Xα method [23] for calculating the continuum functions is well established and its application here follows previously described procedures [24,7]. In brief, this continuum multiple scattering approach requires the construction of a self-consistent ground state potential in which the exchange contribution to an effective one-electron potential is represented using the Xα local density approximation [25]. This entails partitioning the molecule into overlapping spherical regions about each atomic center, enclosed within an outer, spherically symmetric region. Electron wavefunctions can then be expressed in a symmetry-adapted basis of spherical harmonic functions with radial terms obtained by direct numerical integration within the spherical zones of the potential. An initial trial potential for the neutral molecule is iteratively converged to self-consistency. Continuum electron wavefunctions are subsequently calculated using a potential derived directly from the fully converged ground state potential, but adapted to the correct asymptotic Coulombic form for ion plus electron. This modification only applies in the outer sphere region, and so has a minimal perturbing effect on the bound, initial wavefunctions, which are nevertheless re-calculated after the potential modification and before calculation of the photoionization matrix elements. These matrix elements are then calculated in a frozen core approximation, in the same potential for initial and final (ionised) states, ensuring orthogonality of the orbital functions. The calculation of photoionization cross-sections, and particularly of the angular distribution parameters from these matrix elements has been described elsewhere [7].

4.3 Computational Details

An optimized B3LYP/6-311G(d) molecular geometry for R-(+) camphor was obtained using the Q-Chem program [26] and has been used for both the CMS–Xα and B-spline LCAO calculations.

The calculation with the B-spline LCAO approach has been executed as follows. First the ground-state (GS) electron density is calculated by means of the ADF program [15,16] employing an all-electron double zeta plus polarization (DZP) basis set of Slater type orbitals (STO), taken from the ADF database. Such density is then used to build the KS hamiltonian with the B-spline LCAO program, from which the bound and the continuum states are extracted and used to calculate the cross section, the asymmetry and dichroic parameters. B-splines functions of order 10 are employed in all calculations performed with the B-spline LCAO program. In order to improve convergence the origin of the one centre expansion has been fixed on the point that minimize the distance from all heavy atoms of camphor. The most important choice for the calculation is the maximum angular momentum (L_{MAXO}) employed in the expansion on the origin. Following the analysis in Ref. [13], $L_{\mathrm{MAXO}} = 15$ seems to be an optimum choice for convergent results with respect to the basis set size for the molecule considered in this work. The maximum angular momentum (L_{MAXi}) employed in the off-center expansions has been fixed to $L_{\mathrm{MAXi}} = 2$ for C, O and $L_{\mathrm{MAXi}} = 1$ for H. The expansion on the origin is divided with a radial grid with step size of 0.2 a.u. up to $R^{O}_{MAX} = 20$ a.u.; the intervals so obtained are supplemented with additional knots at the nuclei positions in order to make the basis more flexible in the region of core orbitals. To take maximum advantage of the off-center expansion, for the radial intervals $[0, R^{i}_{MAX}]$ have taken different extensions depending on the atomic number of the nuclei and on the distance of the atom from the origin, under the constraint that in the present implementation of the method the spheres of radius R^{i}_{MAX} cannot intersect each other [13]. The expansion on the off-center nuclei is divided with a five-steps radial linear grid up to: $R^{i}_{MAX} = 1.33$ a.u. for oxygen, $R^{i}_{MAX} = 0.85$ a.u. for hydrogen, while for the carbon R^{i}_{MAX} has values from 0.8 a.u. to 1.2 a.u. depending on the distance of the atom from the one centre expansion.

A starting point for the CMS-Xα calculations involves selection of an appropriate set of radii for the atomic spheres into which the potential is partitioned. Two alternative parameterisation schemes have been evaluated in this work: the use of fixed, optimised radii for C, H, and O atoms proposed by Takai and Johnson [27], or the Norman procedure for individually determined radii with a default 0.88 scaling factor [28]. In practice the final results for the cross section and the angular distribution parameters do not vary significantly between these two alternatives, but the latter appears somewhat more stable with respect to basis set size variations, and so is used in the final results presented here. The spherical harmonic basis expansions in each spherical region are truncated at some value, $l_{\max}$. For the neutral ground state an angular basis with $l_{\max}=7$ for the outer sphere, $l_{\max}=2$ for the C and O atomic spheres and $l_{\max}=1$ for the H atomic spheres was found to be sufficient for convergence. However, these limits are expected to require an increase to higher l for the continuum calculation, reflecting the anticipated scattering into higher l-waves caused by the anisotropic ion potential. The convergence properties have been checked independently of the B-spline calculations by a series of calculations and for the final state $l_{\max}$ values of 15, 6, 3 for (respectively) the outer sphere, the C and O atoms, and H atoms were found to be required.

In both B-spline LCAO and CMS-Xα calculations it proved necessary to include partial waves up to $l=15$, considerably higher, by perhaps a factor of two, than normally deemed necessary for adequate convergence in theoretical treatments of photoionization dynamics. This seems to be a feature of the low molecular symmetry in such chiral molecules, and similarly large basis set expansions have been identified to be necessary in other chiral molecule calculations [**9**,**29**]. Truncation errors stemming from a smaller basis are most acute at higher electron kinetic energies, as may be seen by comparing preliminary CMS-Xα calculations [**4**] for the carbonyl C 1*s* dichroism, where the partial wave expansion only extended to l_{max}=7 with the present, fully converged results.

4.4 Results and Discussion

Before discussing the results in terms of the photoionization dynamics, it is useful to comment on the electronic structure of camphor, calculated with both ADF program and with the B-spline LCAO method. The core and outermost valence Kohn-Sham eigenvalues are reported in Table 1, together with the available experimental ionisation potentials. It is convenient to start with the ADF eigenvalues and to split the analysis between core and valence orbitals. The 1a orbital is obviously ascribed to the unique O 1s core state, while the following ten 2a – 11a orbitals are associated with the ten C 1s core states. Unfortunately, experimental data relating to the O 1s ionisation are not available, although this core state would be a very suitable candidate for studies of the photoemission dichroism due to its unambiguous character. Considering next the C 1s core states, it is interesting to observe that the 2a C 1s orbital is very well separated by about 1.15 eV from the following ones, which instead have very small energy gaps between each other, of the order of few tenth of eV, in line with the experimental core photoelectron spectrum [10]. The well separated 2a orbital is easily assigned to the carbonyl moiety, which displays higher binding energy due to the vicinity of the highly electronegative oxygen atom. Only 2a orbital is considered for further analysis of dynamical parameters, since it would be very difficult to extract the dynamical parameters for the remaining C 1s orbitals from an experiment due to their very close binding energy and consequent spectral overlap.

The valence orbitals are also rather close to each other in energy, with the exception of the innermost ones and the HOMO. Inner valence orbitals, however, are not suitable for a study such as here, due to the occurrence of shake-up processes which generate satellite structure with intensity redistribution and which cannot be accounted for by the present level of theory. On the other hand the HOMO orbital is very well separated in energy with respect to the following terms, with a calculated gap of 1.54 eV. This observation is in line with the experimental valence photoelectron spectrum of camphor [10], which is characterised by a very well resolved peak with binding energy at 8.70 eV ascribed to the HOMO main line, followed by a rather congested structure which envelopes the main lines of inner ionisations, whose binding energies are rather close to each other. Therefore only HOMO orbital photoionization is suitable for a detailed investigation of the dichroism in photoemission, since it would be very difficult, if not impossible, to discriminate the separate contribution of the inner, almost degenerate, orbitals.

For the reasons just outlined, in this work we will limit our attention only to the HOMO orbital of the valence spectrum and to the carbonyl C 1s and O 1s core states.

Table 4.1: The core and outermost valence KS-LB94 eigenvalues of R-(+)-camphor obtained with the ADF and with the B-spline LCAO approach. Also reported are the differences $\Delta = \varepsilon_{LCAO} - \varepsilon_{ADF}$ and the available experimental ionisation potentials (IP) [10]. Values in eV.

	ε			
MO	ADF	LCAO	Δ	IP
1a	− 536.48	− 536.69	− 0.21	
2a	− 292.57	− 292.50	+ 0.07	293.0
3a	− 291.42	− 291.12	− 0.30	
4a	− 291.26	− 291.00	+ 0.26	
5a	− 291.04	− 290.82	− 0.22	
6a	− 290.82	− 290.77	+ 0.05	
7a	− 290.73	− 290.68	− 0.05	
8a	− 290.68	− 290.66	+ 0.02	
9a	− 290.37	− 290.47	− 0.10	
10a	− 290.32	− 290.40	− 0.08	
11a	− 290.19	− 290.22	− 0.03	
39a	− 12.80	− 12.75	+ 0.05	
40a	− 12.58	− 12.50	+ 0.08	
41a	− 12.20	− 12.14	+ 0.06	10.25
42a	− 10.66	− 10.67	− 0.01	8.70

In Table 4.1 also the B-spline LCAO eigenvalues and their differences with respect to the ADF results are also shown: such differences are always rather small, at most 0.3 eV for some core states but in general even smaller than 0.1 eV, and this indicates that the B-spline LCAO method is able to accurately describe the electronic structure of camphor. The comparison between the calculated (ADF) results with the reported experimental IP indicates that although the absolute values are overestimated by the theory, the calculated gap between HOMO and HOMO-1 orbitals of 1.47 eV is in excellent agreement with the measured value of 1.55 eV. The absolute values overestimate of the method is ascribed to the too attractive character of the LB94 potential and has been already observed in previous works on large molecules like, for example, C_{60} [30]. For the core C 1s 2a orbital, however, the deviation with respect to the experiment is below 0.5 eV, and it is interesting to observe that in the core photoelectron spectrum [10] the experimental gap between the carbonyl C 1s line and the maximum of the feature ascribed to the all other orbitals is of 2.5 eV, which is in very good accordance with the 2a–11a calculated gap of 2.38 eV. In Table 4.1 only experimental IPs for orbitals 2a, 41a and 42a have been reported, although the PES analysis of Ref. [10] furnishes an almost complete set of experimental IP values. We do not here report the other experimental IPs because we are not very confident with an assignment made with respect to the present calculated IP; the near-degeneracy observed in many instances makes the camphor PES assignment a tricky problem, beyond the scope of the present work which is devoted primarily to consideration of the dichroism in photoemission.

4.4.1 Carbonyl Core C 1s and O 1s Ionisations

The results for the carbonyl C 1s ionisation (2a molecular orbital) are reported in Figure 4.1. Starting with the cross section, both the B-spline LCAO and the CMS-Xα methods predict a profile with many corresponding structures, which can be ascribed to shape resonances. In particular four features can be identified: a maximum at 4.4 eV followed by a shoulder at 5.7 eV and two well separated maxima at 10.6 (indicated by label A in Figure 4.1) and at 21.5 eV (label B). We will consider features A and B in more detail later, while we will not analyse further the two features at lower energy (4.4 and 5.7 eV). This is because we may expect that the present theoretical methods could be less accurate at very low photoelectron energy and also because features A and B are much more resolved and therefore more favourable candidates for experimental detection. The asymmetry profile (middle panel, Fig. 4.1) also displays interesting features ascribed as counterparts of those found in the cross section, especially the deep absolute minimum.

A general analysis of shape resonance features in this molecule follows in section 4.4.3. However, we may here remark that their prominent occurrence in camphor is not surprising since there are many valence virtual orbitals lying above the threshold. In fact a minimum basis calculation has furnished 28 such unbound valence states, in the energy range between 1 and 11 eV above the ionisation threshold. Another mechanism which may enhance the formation of shape resonances could be the trapping of photoelectron waves due to the cage effect ('giant resonances') connected with the bicyclic geometry of camphor, which has been observed experimentally in cyclopropane [31] and theoretically in cubane [32].

A generic difficulty for such calculations is the selection of potential parameters which reproduce quantitatively the overall attractiveness of the molecular potential. In the present B-spline LCAO method our choice is that of the LB94 exchange-correlation (XC) potential. This potential performs very well on photoionization calculations on small molecules, because it has the correct asymptotic behaviour which is not supported by most of the other available XC potentials. However it has been noted in several instances that the performances of the LB94 XC potential worsen when the size of the molecule increases, like for example in C_{60} [30], since it becomes too attractive. The consequences of this excessively attractive characteristic of the potential on the photoionization parameters is a general shift of the profiles towards lower energy. A pragmatic way to correct this problem is to shift the profile to higher energy when comparing with the other data and this has been introduced in the plotting of the data in Fig. 4.1 with the B-spline results being offset by +3 eV relative to the CMS-Xα. Although in this instance the comparison with experiment does not require any shift of the CMS-Xα energy scale, this is not universally the case, and the Xα potential generally will also have such problems in fixing precisely the energy scale. Most likely in this instance there is a fortuitous cancellation of errors.

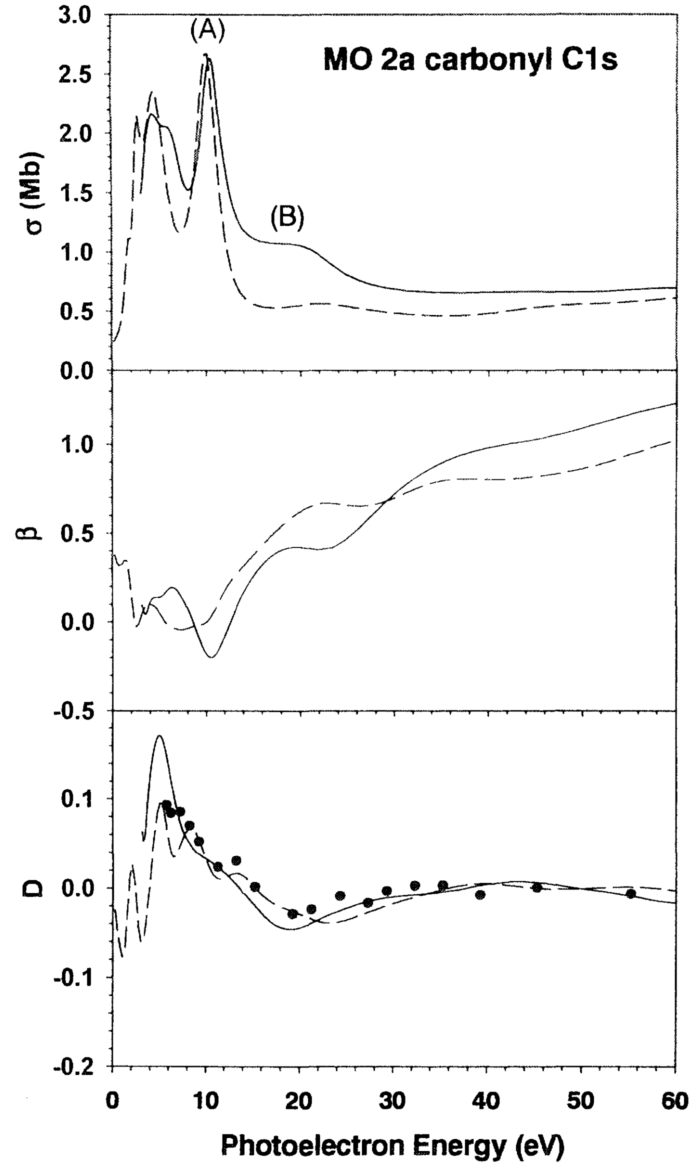

Figure 4.1: Cross section (σ), asymmetry parameter (β) and dichroic parameter (*D*) relative to the camphor 2a (carbonyl C 1s) orbital. Solid line: B-spline LCAO DFT calculation, dashed line: CMS-Xα calculation, symbols are experimental data, Ref. [4].

One other consequence of this relative shift of the B-spline results is that the calculation provides no data for the region up to 3 eV above threshold, and in either case this region might be expected to pose the greatest difficulty for calculation due to the enhanced sensitivity at low energy to the precise molecular potential and to electron correlation effects.

The calculated R-(+) camphor dichroic parameters, *D*, have maxima just above the threshold, followed by a minimum and then by a very smooth behaviour at high energy. In this case the set of experimental data [4] is very wide and complete and it is well apparent that the comparison between theory and experiment is excellent, essentially with quantitative agreement. It is worth noting that also for the core orbital the dichroic parameter is rather high at low kinetic energies, and then decreases to very low values within 30 eV. This finding is significant, because it must be considered that the initial C 1s core orbital is highly localised and retains its atomic spherical character, so it is not asymmetric. Therefore the dichroism cannot be attributed simply to the chirality of the initial state but rather must be associated purely with the continuum final state, which is completely delocalized over the molecule and therefore feels the asymmetry of the effective potential. This somehow surprising finding had been already found in a theoretical study on chiral oxirane derivatives [9], but now is confirmed by both present theory and previous experiment [4].

In Figure 4.2 the calculations for the core O 1s orbital are reported. Unfortunately in this case there are currently no experimental data for comparison, but since this is the only O 1s orbital present in camphor it is a good candidate for future experiments. Again a relative shift of 3 eV is applied in plotting the results after which there is excellent agreement between the calculations.

It is interesting to discuss the profiles in comparison with the core C 1s 2a orbital: the cross section and the asymmetry parameters are qualitatively similar for both ionisations, the main features (A) and (B) display a large resemblance in each case and the most relevant differences consist in the two unresolved peaks just above the threshold in C 1s cross section which coalesce to only one in O 1s, and in the asymmetry parameter profile where the minimum around 8 eV is narrower in O 1s than in C 1s. The surprising contrast comes when comparing the dichroic parameters which change dramatically between the two core orbitals: in fact in O 1s a few eV above threshold it has opposite sign than in C 1s and the shape at higher energy is also qualitatively different between them. This indicates and confirms the very high sensitivity of the photoemission dichroism to the chemical environment of the atom, already found along a series of analogue compounds [9] as well as in present core analysis.

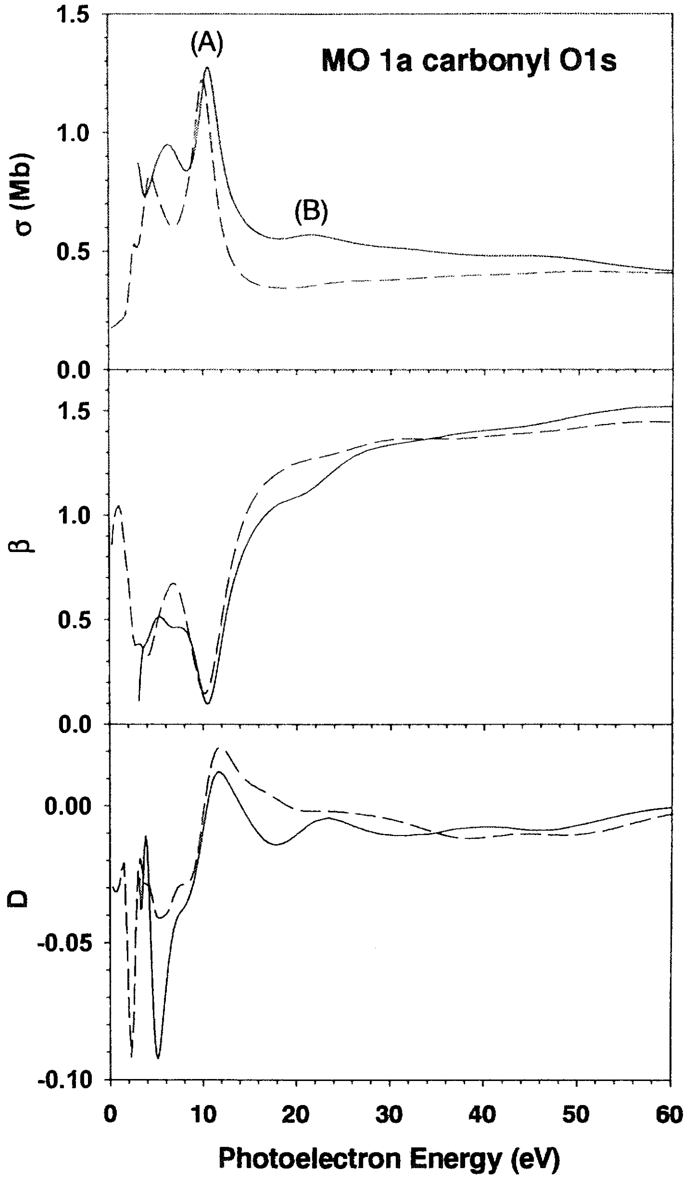

Figure 4.2: Cross section (σ), asymmetry parameter (β) and dichroic parameter (*D*) relative to the camphor 1a (carbonyl O 1s) orbital. Solid line: B-spline LCAO DFT calculation, dashed line: CMS-Xα calculation.

4.4.2 HOMO Ionisation

In Figure 4.3 the cross section, the asymmetry parameter and the dichroic parameter profiles relating to the HOMO orbital of camphor are reported. From an inspection of the molecular orbital coefficients, and as well as those already found in previous work [10], this orbital is ascribed to the oxygen lone pair with considerable mixing with adjacent C-C σ bonds. Again the two sets of theoretical results are plotted with a relative offset of 3 eV applied to the B-spline results.

The B-spline LCAO cross section profile (top panel Fig. 4.3) displays two important features: a narrow maximum just above the threshold and a clear shape resonance, the latter is labelled as feature (A) in the figure. The CMS-Xα profile resembles closely the B-spline LCAO one, with the exception of the threshold region where the former displays rather intense and sharp structures which do not appear in the latter, probably because the too attractive LB94 potential pushes them below the ionisation limit.

The B-spline LCAO calculated asymmetry parameter profile (β, central panel in Figure 4.3) displays also some features below 15 eV as well as a smooth modulation at high energies. The structures a few eV above the threshold are the counterparts of those already discussed in the cross section. The agreement between the B-spline LCAO and CMS-Xα methods is good, with the exception of the low energy region, for reasons noted above in connection with the cross-section. In this case experimental data are available which have been recorded during the dichroism experiments and these are reported in the figure. The agreement between theory and experiment is not quantitative, however there is a clear indication of the presence of a maximum around 10 eV, and the initial rise from zero immediately above threshold is captured in the CMS-Xα calculation.

In the lower panel of Figure 4.3 the R-(+) dichroic parameter, *D*, is considered: the B-spline LCAO predicts a very strong negative value (about –0.2) just above the threshold, which decays rapidly changing sign and reaching a maximum of +0.057, followed by a series of oscillations of decreasing amplitude with the energy. In contrast, the CMS-Xα dichroism parameter is less negative at threshold (-0.09), while experimentally smaller negative values are found in the near threshold region. The CMS-Xα data then pass through an auxiliary positive peak at ~3 eV above threshold, though this cannot be corroborated from the present experimental data and contrasts with the corresponding B-spline value. However, above ~5 eV the calculations are in reasonably good agreement with each other. Their common behaviour, namely the rapidly decaying of the D parameter to low values within few tens of eV of kinetic energy, has been already found in previous calculations [7,8,9].

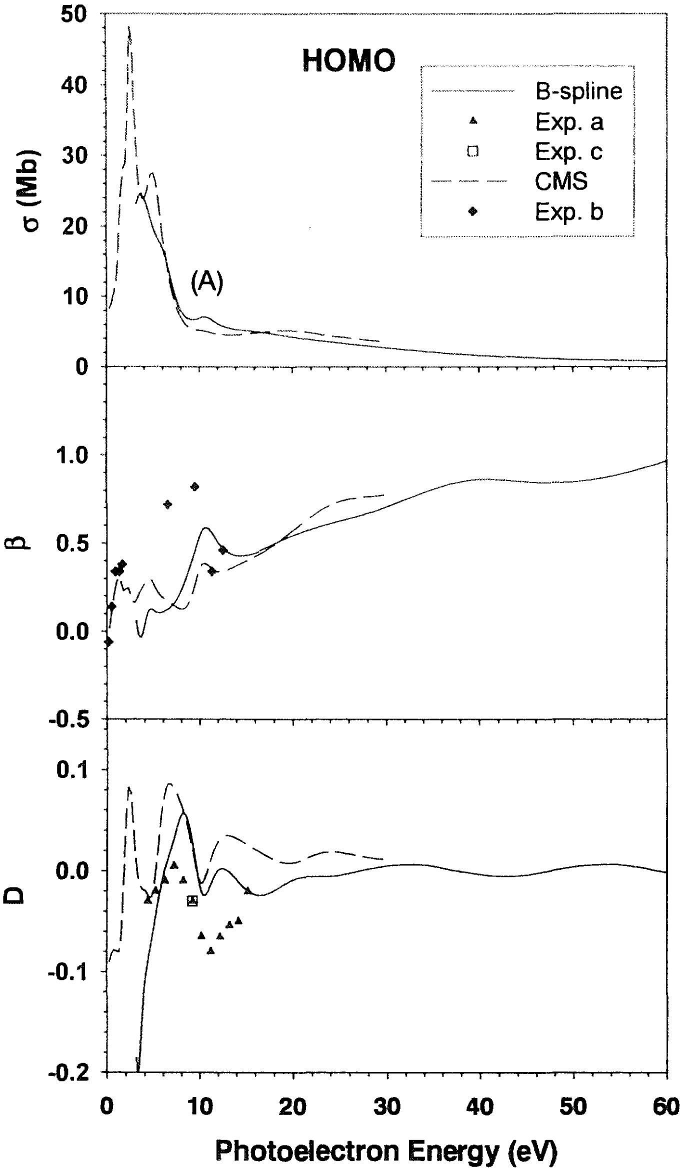

Figure 4.3: Cross section (σ), asymmetry parameter (β) and dichroic parameter (D) relative to the camphor HOMO orbital. Solid line: B-spline LCAO DFT calculation, dashed line: CMS-Xα calculation, symbols are experimental data, a: Ref. [5], b: Ref. [11], c: Ref. [3].

In Figure 4.4 the energy range is reduced in order to analyse in detail only the region containing the experimental dichroism data. Now the comparison between theory and experiment is easier, in fact the shape of the experimental profile between 4 and 16 eV is satisfactorily reproduced by the theory. Some discrepancies still remain, for example both the calculated profiles are too positive and also the energy gap between the maximum and the minimum is calculated to be too narrow. The agreement between the B-spline LCAO and CMS-Xα calculations for the dichroism is not quantitative, although the global shapes above 5 eV are in quite good agreement with each other. The available experimental dichroism data reported in the figure [3,5] are in only qualitative agreement with the calculations, so it is necessary to identify critically the possible origins of the observed deterioration. The experimental data have been shown to be consistent when re-evaluated using different experimental techniques [3,5,11] and so should be reliable, so it is reasonable to ascribe discrepancies to common difficulties of the theoretical methods. The present B-spline LCAO formalism is numerically very accurate, since the convergence of the results have been checked with respect to basis set enlargement, therefore problems are more likely to be associated with a limitation of the DFT KS hamiltonian employed.

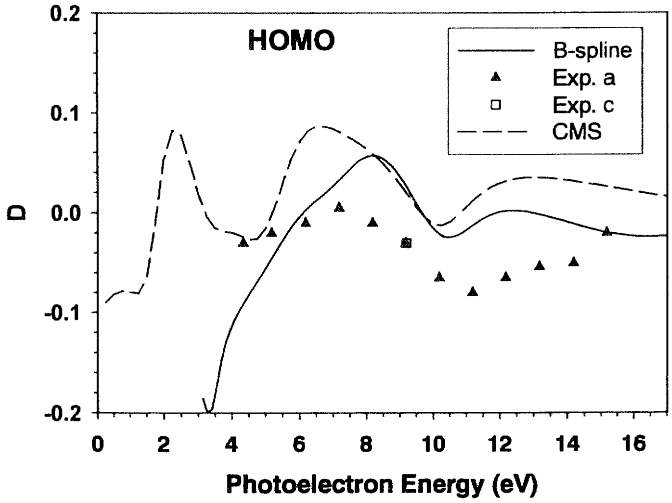

Figure 4.4: Dichroic parameter (*D*) relative to the camphor HOMO orbital. Solid line: B-spline LCAO DFT calculation, dashed line: CMS-Xα calculation, symbols are experimental data, a: Ref. [5], c: Ref [3].

It is important to recall that apart from requiring a proper XC potential choice, the B-spline LCAO DFT KS approach (and also the CMS-Xα approach) is a static formalism, so the response of the electron density to the external electromagnetic field is completely neglected. These response effects can be included in the calculations employing the Time Dependent (TD) DFT method, and calculations on small molecules [33-35] have shown that they have important consequences on the photoionization parameters. In fact in the TDDFT formalism the density induced by the time dependent perturbation generates an induced potential, as a result of Coulomb and exchange-correlation responses. This induced potential is contributed by all the channels and therefore interchannel coupling naturally arises in TDDFT. This effect can generate continuum-continuum coupling with intensity transfer between different photoionization channel, or discrete-continuum coupling, which may give rise to autoionization Feschbach resonances.

It is significant that for the core ionisation an excellent matching between B-spline calculations and experiment is obtained, much better than that found in the HOMO orbital. This suggests rather clearly that such response effects, not included in either the CMS-Xα or the B-spline LCAO KS formalism, should play a much more important role in valence ionisation than in the core, as already found with TDDFT calculations on smaller systems [34,35].

In fact it is well known that response effects become very large in presence of highly polarizable valence electrons, typically when *3p* shells are filled like in Ar [36] or second row hydrides [35]. At high photon energies necessary to ionise core orbitals, valence shell cross-sections are quite small and therefore valence response effects are strongly reduced. It is also worth noting that for core ionisation the agreement between the B-spline LCAO and CMS-Xα methods is very good, and better than that achieved in the valence calculations. This is probably due to the much better description of core states in the CMS-Xα approach, which due to their atomic nature do not suffer so much from the crude 'muffin-tin' approximation of the potential. In summary we are led to attribute the observed discrepancies to both XC potential and a neglect of response. TDDFT continuum calculations for camphor, however, are still impracticable due to their very demanding computational efforts required. At the moment a serial version of the B-spline LCAO TDDFT continuum code [37] is already available, so further efforts to parallelize the code are justified in order to envisage its application to a very large and asymmetric system like camphor or other chiral molecules.

4.4.3 Shape Resonances Analysis

In order to analyse the shape resonances identified in both valence and core cross section profiles, namely the features labelled (A) and (B) in the Figures 4.1-4.3, we have inspected the continuum wavefunction at photoelectron energies corresponding to the cross section maxima, namely at 10.6 eV and 21.3 eV in the shifted energy scale employed in Figures 4.1-4.3. It is worth noting that, in principle, the continuum has an infinite degeneracy due to all the possible directions of the momentum *k* of the photoelectron. Working with a finite basis set the degeneracy is no longer infinite but remains high since it is equal to the number of the open channels which obey the asymptotic continuum boundary conditions. However, it is still possible to remove the degeneracy employing the so-called dipole-prepared continuum orbitals which are obtained by performing a unitary transformation on the degenerate set in order to extract only one orbital which will carry all the cross section. All the details of such procedure have been already described elsewhere [38], and in this section we will discuss the photoelectron wavefunction in terms of dipole-prepared continuum orbitals obtained with the B-spline LCAO method.

In Figure 4.5 the dipole-prepared continuum orbitals corresponding to the features (A) and (B) for the states 1a (core O 1s), 2a (carbonyl core C 1s) and 42a (HOMO oxygen lone pair) have been reported as contour plots over the plane identified by the following three atoms: carbonyl O, carbonyl C, and the C belonging to the CH_2 moiety adjacent to the CO group. We have selected this plane as a result of a preliminary analysis of the dipole prepared continuum orbitals over various different molecular regions, which showed that the continuum orbitals corresponding to the shape resonances are localized near the carbonyl moiety.

Let's start with feature (A) in the 1a (core O 1s orbital) considered in the left upper panel: it is readily apparent that the shape of the continuum orbital in the region between the C and O atoms of the carbonyl group is qualitatively compatible with a σ^* C–O virtual valence orbital, in fact it displays a change of sign going along the C–O bond direction and its shape is, to a good approximation, of cylindrical symmetry. Moreover, there is a rather complicated pattern which connects the continuum orbital from the region of the C–O fragment with the other atoms, and this consists in various bonding and antibonding interactions around the other C atoms. It is worth noting that this component of the dipole-prepared orbital has been obtained with respect to the dipole component parallel to the C–O chemical bond, since the perpendicular components give much weaker contributions (not shown in the figure). This is consistent with the local symmetry of the process: the initial O 1s orbital retains its atomic spherical shape, the final continuum has high σ^* C-O virtual valence character with O 2p component along the chemical bond, therefore the dipole component which gives non-zero transition moment must be along the bond.

Passing to the next feature (B) in the same 1a (core O 1s orbital) considered in the right upper panel, and obtained with the same parallel dipole component, we observe that in the vicinity of the C-O fragment, the same σ^* C-O virtual valence behaviour is observed. However in this case the interaction with the rest of the molecule is completely different than in previous feature (A): now the interaction with the other C atoms is very weak but a new feature emerges that is a localization of the continuum in the center of the cage, as can be seen by the accumulation of negative (dashed) isolines around one point located ~3 au on the X axis and ~6 au on the Y axis of the panel. So in this case we observe a cage effect which interacts with the σ^* C-O virtual valence orbital and generates another resonance. In summary we can say that features (A) and (B) are both associated with a σ^* C-O virtual valence orbital shape resonance, but while in (A) it is mixed with other virtual valence components, in (B) it is mixed with a state which derives from cage effects which trap the photoelectron inside the molecular cavity.

The features (A) and (B) in the C 1s core ionisation (2a orbital) considered in the central panels of Figure 4.5, show very minor differences with respect to the O 1s ones, therefore the discussion and their assignment remains the same.

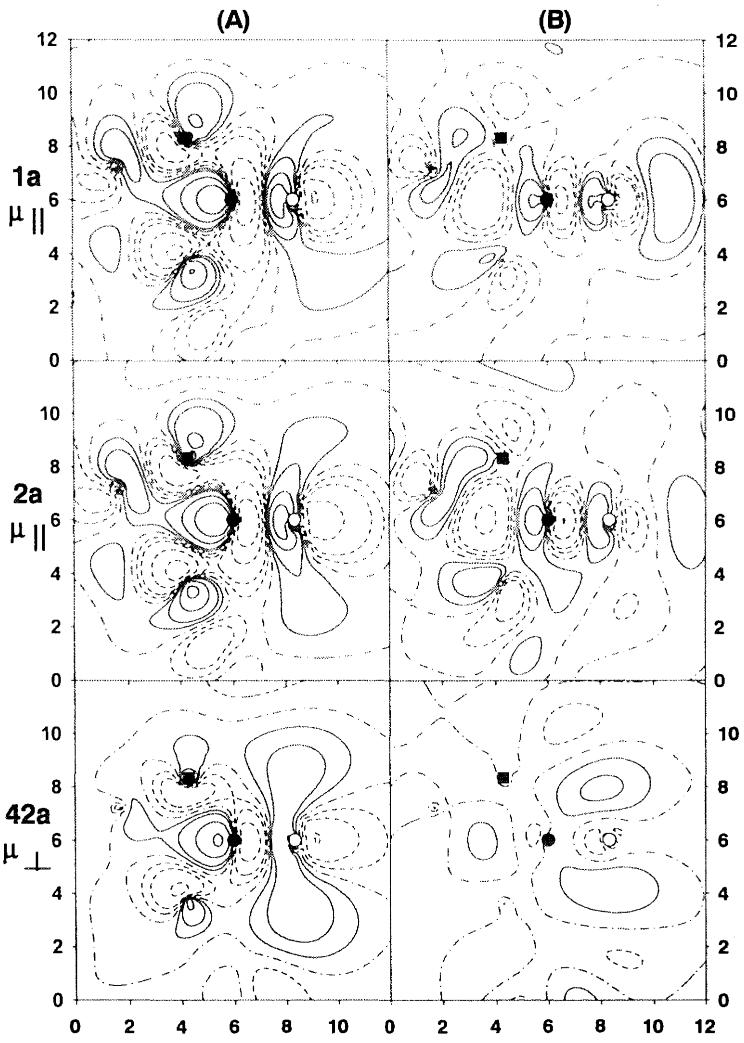

Figure 4.5: Contour plots of the dipole prepared continuum orbitals for the 1a, 2a and 42a ionisations corresponding to the features (A) and (B) identified in the cross section profiles. Side in atomic units, solid line positive contribution, dashed line negative contribution, dash-dotted line zero contribution (nodal line). The plots are in the plane defined by the positions of the following three atoms indicated in the figure: hollow circle carbonyl O, filled circle carbonyl C, filled square adjacent C belonging to the CH_2 moiety.

In the left lower panel of Figure 4.5 the HOMO feature (A) is considered, in this case the dipole component which carries most of the contribution is perpendicular to the bond direction. This is not surprising since now the initial state (HOMO) is the oxygen lone pair and therefore the dipole component which gives non-zero contribution with a final virtual valence σ^* C-O in the continuum must be orthogonal to the chemical bond. So also in this case the nature of the shape resonance is the same as in the core. In the HOMO cross section profile (Figure 4.3) there is no evidence of any structure at the photoelectron energy value corresponding to the feature (B) found in O 1s and C 1s core ionisation. Actually, we have considered the dipole-prepared continuum orbital corresponding to HOMO initial state and at a photoelectron energy corresponding to feature (B) in the right lower panel of Figure 4.5. As expected, the wavefunction is relatively weak if compared with the previous situations where a shape resonance was present (the isolines have the same values for all the plots so relative comparison is consistent), there is no evidence of virtual valence σ* C-O contribution and also the confinement inside the cage is just sketched. This pronounced difference with respect to the core states is not so easily rationalised, but a possible explanation may be that the cross section of core orbitals decays much more slowly than in the valence, and this allows to high energy features to survive. Supporting this we note that also feature (A) is much more evident in core than in valence ionisations.

4.5 Conclusions

In the present work camphor photoionization has been studied by two different theoretical models, with particular emphasis on the circular dichroism in the photoelectron angular distributions. Generally good agreement is displayed between the B-spline and CMS-Xα approaches, suggesting that the underlying common physical model for the dichroism, entailing interference effects in the pure electric dipole approximation, is well implemented in either formalism.. These theoretical calculations are compared with available experimental results. For the carbonyl C 1s ionisation theory and experiment are found to be in excellent accord across the full range of electron energies studied. In the valence shell ionisation of the HOMO carbonyl lone pair electron rather more modest agreement is achieved between theory and experiment and the discrepancies have been attributed to both XC potential limitations and the absence of response effects in the adopted formalism. Conversely, the better agreement between calculations and measurements for the core C 1s data is in keeping with the reduced response expected for core ionisation. These findings justify future efforts to consider more elaborate XC potential as well as the extension of the B-spline LCAO TDDFT code to a parallel implementation to manage large asymmetric chiral systems.

An analysis of the shape resonant structures noted in this work, in terms of dipole-prepared continuum orbitals, has furnished interesting insight into the mechanism responsible for their appearance in the cross section profiles and, in particular, has identified possible cage effects which can trap the photoelectron inside the molecular cavity.

Future perspectives concern both the improvement of the theoretical method in order to gain quantitative agreement with the experiment, as well as gaining a deeper rationalization of the dichroism behaviour. Our experiences indicate that this is somehow surprisingly sensitive to small changes assumed for the calculations which, at the same time, have almost no appreciable effect on the calculated cross section or asymmetry parameter. Such a rationalization needs both an improvement of the theoretical analysis as well as more studies on many different chiral molecules, in order to identify similarities and trends along series of analogues compounds.

5 Angle-Resolved Photoelectron Spectroscopy of Randomly Oriented 3-Hydroxytetrahydrofuran Enantiomers

Circular dichroism in the angular distribution of valence photoelectrons emitted from randomly oriented 3-hydroxytetrahydrofuran enantiomers (**Th**^{S} and **Th**^{R}) has been observed in gas-phase experiments using circulary polarized vacuum ultraviolet (VUV) light. The measured dichroism for both **Th**^{S} and **Th**^{R}, acquired at the single magic angle $\theta = 234.73^\circ$ and at photon energies of 22, 19, 16, and 14 eV, points to an asymetric forward-backward scattering of the photoelectrons from their highest occupied molecular orbitals (HOMO), HOMO-1 and HOMO-2, of up to 5%, depending on the photon energy. The asymmetry reverses on exchange of either the helicity of the radiation or the configuration of **Th**. The photonization dichroic *D* parameters of **Th**^{S} and **Th**^{R} have been measured and their values discussed in the light of LCAO B-spline density functional theory (DFT) predictions. While an acceptable agreement is found between the dicroic parameter measured and calculated at the highest photon energy for the HOMO-1 and HOMO-2 orbitals of **Th**, a significant discrepancy is observed for the HOMO-1 state which is attributed to the floppiness of **Th**, in particular to the comperatively large sensitivity of the size and shape of its HOMO-1 on nuclear vibrational motion.

5.1 Introduction

The discovery of abiogenic sources of homochirality and the understanding of the underlying principles are important steps towards the explanation of the origin of life. Chirogenesis usually leads to racemates, but spontaneous symmetry breaking has been achieved through only a handful of methods. One of them is acknowledged as the “chiral enrichment mechanism” and is based on the preferential destruction of one enantiomer of a racemate by interaction with a chiral agent, whether a massive species or a circularly polarized photon.

Asymmetry in the interaction of circularly polarized light with chiral molecules has been studied since Pasteur's pioneering experiments on optical activity [1]. While optical techniques with UV/visible and IR light are routinely used in this context, only a few studies have been performed on the interaction of chiral molecules with ionising (VUV and X-ray) radiations that pervade interstellar clouds and outer planetary atmospheres. In these experiments, the total light absorption is governed by the second-order electric dipole-electric quadrupole and electric dipole-magnetic dipole operations and, thus, a relatively weak affect can be measured (of the order of 10^{-3}–10^{-5}). However, as originally pointed out by Ritchie [2] and later discussed in detail by Cherepkov [3,4,5], helicity-dependent effects should be observed in photoelectron emission from chiral molecules even if randomly oriented. In this case, the dicroism arises only from the electric dipole operator and, therefore, its magnitude is expected to be of the order of 10^{-2}, significantly larger than the conventional absorption effects [6,7,8]. These phenomena are referred to as circular dichroism in the photoelectron angular distribution (CDAD) and only recently have its effects been experimentally investigated on rigid chiral molecules, such as bromocamphor [9], camphor [10,11] and methyloxirane [12].

The aim of this work is to measure the dichroic effects on the photoelectron angular distribution on floppy cyclic molecules, such as the (R)-(–)-3-hydroxytetrahydrofuran (**Th**$^{\mathbf{R}}$) and (S)-(+)-3-hydroxytetrahydrofuran (**Th**$^{\mathbf{S}}$) enantiomers that, because of the similarity to the nucleotide systems, can be considered as prototypical building blocks of living matters. The experimental results will be discussed in the light of computational predictions.

5.2 Background

For randomly oriented chiral species, the dependence of thephotoelectron intensity $I(\theta,\omega)$ on the emission angle θ is expressed by equation (5.1):

$$I(\theta,\omega) = \sigma(\omega)[1 - 0.5\beta(\omega)P_2(\cos\theta) + mD(\omega)\cos(\theta)]/4\pi \qquad (5.1)$$

where $\sigma(\omega)$ is the energy-dependent cross-section, $\beta(\omega)$ is the asymmetry parameter, $D(\omega)$ is the dichroism parameter, and $m = \pm 1$ is the light helicity [2-5]. The P_2 term in Equation (5.1) refers to the second-order Legendre polynomial and θ is the scattering angle between the photoelectron momentum and light propagation. The helicity of the circularly polarized light is defined according to the value $m = +1$ (left circular polarization) or $m = -1$ (right circular polarization) of the projection of the photon spin along its momentum. Accordingly, the electric vector describes a positive (right-handed) or negative (left-handed) screw. The photoelectron intensity along the θ direction shows different values not only in case of a change of the light helicity ($m = \pm 1$) but also when, for fixed value of m, the photoelectron intensity is measured in a forward/backward geometry, showing an asymmetry also in angular distribution [the $\cos(\theta)$ dependence of the last term of Eq. 5.1].

5.3 Experimental Section

The experiments were performed at the circular polarization beam line at Elettra, Trieste (Italy), which is downstream of an electromagnetic winggler/undulator [13], equipped with grazing and normal incidence angle monochromators sharing the same entrance and exit slits [14].

The angle-resolved photoemission experiments were carried out randomly oriented **Th**$^{\mathbf{S}}$ or **Th**$^{\mathbf{R}}$ molecules using a differentially pumped vacuum chamber [15], equipped with two hemispherical electron analysers set at the collecting magic angle θ_{m} = 54.73° with respect to the light propagation axis in the forward (θ_{m}) and backward (θ_{m} + 180°) direction. This particular value of the collecting angle was chosen to set zero the second Legendre polynomial, P_2, which therefore does not contribute to $I(\theta,\omega)$. The effusive gas source was mounted perpendicular to the plane defined by the photoelectron detector and the light propagation axes. Pure **Th**$^{\mathbf{S}}$ and **Th**$^{\mathbf{R}}$ enatiometers (Aldrich Co., 99% ee) were admitted to the ionisation region via a gas pipe through a 1-mm in diameter needle heated to 60 °C. The background pressure in the experimental chamber was kept at $\approx 10^{-6}$ mbar. Magnetic fields were controlled to a few microTesla. The total bandwidth and energy resolution were about 200 meV. We operated at a degree of circular polarization of 82%, as determined by a prodedure previously described [16]. The analyser acceptance angle was ±3° with 25 eV pass energy. The trasmission functions and kinetic energy calibrations of the two analysers were determined measuring the $3p$ photoemission of argon. The validity of the experimental procedure, involving circular polarization switching to measure the dichroism parameter, D, was checked by using the **Th** racemate. The D parameter was determined from Equation (5.2):

$$D(\omega)=\left[I^{+}(\theta_{m},\omega)-I^{-}(\theta_{m},\omega)\right]/\cos\theta_{m}\left[I^{+}(\theta_{m},\omega)+I^{-}(\theta_{m},\omega)\right] \qquad (5.2)$$

where the $I^{+}(\theta_{m},\omega)$ and $I^{-}(\theta_{m},\omega)$ are the photoelectron intensities measured at the magic angle (θ_m) with left-handed circularly polarized light, respectively. The simultaneous acquisition by a second hemispherical electron energy analyser placed at 180° from the first one significantly improves the experimental precision by providing an additional measurement of the same D value, though with opposite sign, under the same conditions. The comparison between the dichroism D parameters of the two **Th**$^{\mathbf{S}}$ and **Th**$^{\mathbf{R}}$ enatiometers will further corroborate the reability of the experimental methodology adopted.

5.4 Theoretical Method

The photoionization process is described, at the one-electron level, by the dipole transition moment between the ionised orbital and the photoelectron continuum orbital. The LCAO B-spline density functional theory (DFT) method, recently developed by some of us [8], has proven to be suitable and convenient for these purposes. A one-particle description based on a DFT Hamiltonian shown in Equation (5.3)

$$h_{KS}\varphi_{E} = E\varphi_{E} \tag{5.3}$$

is employed and both bound and continuum states are obtained, without further approximations to the potential, by expansion on a large multicenter (LCAO) basis of B-spline functions [17]. S-matrix normalized continuum orbitals $\varphi_{Elm}{}^{(-)}$ give the corresponding dipole matrix elements of Equation (5.4)

$$D^{(-)}{}_{lm}(\lambda_r) = \left\langle \varphi_{Elm}{}^{(-)} \middle| rY_{1\lambda_r} \middle| \varphi_i \right\rangle \tag{5.4}$$

relative to the initial orbital φ_i. From these cross-sections, σ, the asymmetry parameter, β, and dichroic parameter, *D*, are obtained by standard angular momentum analysis [8,18]. In the present case, the initial ground state density ρ has been obtained for the two most astable conformations employing the ADF program [19] and the DZP basis from the ADF library. In the B-spline LCAO calculations, a one-center expansion up to L_{MAXO} = 15 has been employed with a radial grid with step size of 0.2 a.u. centred so as to minimize the heavy atom distance from the origin. L_{MAXi} values of 2 have been employed for the heavy atoms (C and O) and of 1 for the hydrogen atoms. Excellent agreement of bound state eigenvalues as well as comparable distances from the expansion center as in previous calculations [8] makes one confident of the convergence of the calculated parameters with respect to the chosen basis.

The energetic and the structural parameters of the transition state connecting the two more stable fully geometrically optimized configurations of the **Th$^{\mathbf{R}}$** have been calculated by using the transit-guided quasi-Newton (STQN) methodology [20] at the MP2/6-31G* level theory using Gaussian 03 [21].

5.5 Results and Discussion

According to previous theoretical studies [22], 3-hydroxytetrahydrofuran is a relatevily floppy molecule which may exist in several conformations differing in energy by as much as 3.3 Kcal/mol. Among these, stuctures A and B are the most stable, with the later 1.34 Kcal/mol less stable than the first as calculated with an

MP2 Hamiltonian using a modified 6-31G* basis set. This stability difference is a stubstantial agreement with that calculated by us at the QST2-MP2-6-31G* level of theory (ΔE = 1.28 Kcal/mol; Figure 5.1) which points to an A→B conformational transition involving an activation barrier as large as 3.37 Kcal/mol. This means that, at the inlet temperature (60°C), both conformations are populted in an [A]/[B] ratio ranging from 3 to 4.

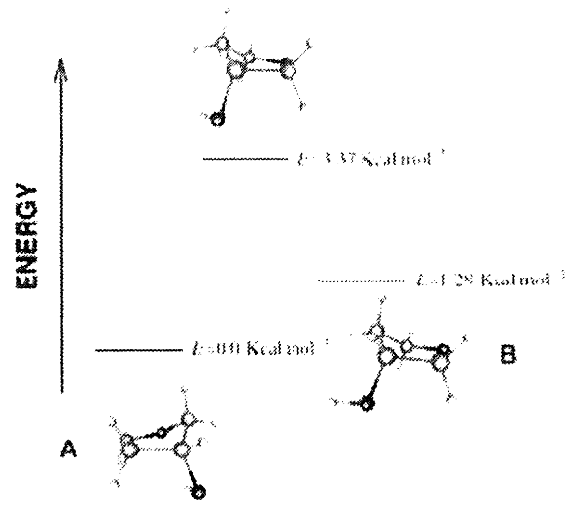

Figure 5.1: Energetics and structures of the most stables conformers of 3-hydroxytetrahydrofuran and their connecting transition state. Full geometrical optimization has been carried out at the MP2/6-31G* level; the properties of the transition state have been calculated using the STQN algorithm.

Figure 5.2 illustrates the valence spectrum of the **Th**^{R} enatiometer acquired using the 22 eV photon energy. The spectrum is characterized by two well-resolved bands at 9.75 and 10.7 eV binding energies followed by an unresolved manifold at higher energies. The IE values of the corresponding orbitals, computed with the Koopmans theorem, exceed the experimental values by about 1.8 eV. The calculated IE of the 16-th up to 24-th molecular orbitals, shiffted by 1.8 eV, are marked in Figure 5.2. Representations (isosurfaces) of the 24-th (HOMO), 23-th (HOMO-1), and 22-th (HOMO-2) orbitals of the most stable conformers A and B are given in the figure insets. Mulliken population analysis indicates that the electron in the HOMO, HOMO-1, HOMO-2 of A is shared beteen the O(2) and O(6) centers (see the inset in Figure 5.2). Instead, the electron is essentially located at the ring O(2) oxygen in the

HOMO and HOMO-2 orbitals of B and at the O(6) hydroxyl oxygen in its HOMO-1 orbital (see the inset in Figure 5.2).

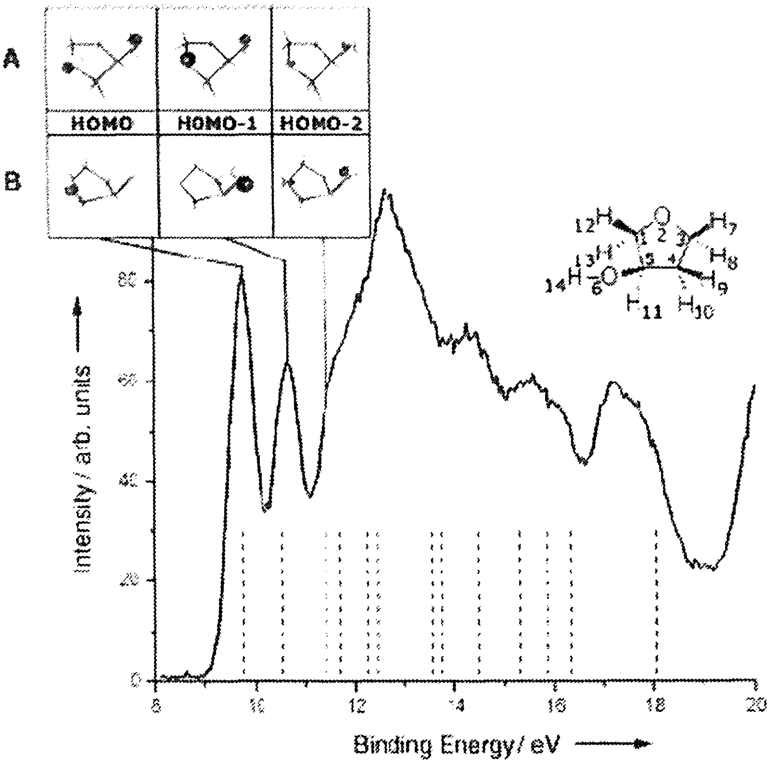

Figure 5.2: Valence spectrum of 3-hydroxytetrahydrofuran acquired at a photon energy of 22 eV. The shapes of the three highest occupied molecular orbitals of the two most stable conformers of $\mathrm{Th^R}$ are shown in the inset.

A portion of the spectrum of Figure 5.3a relative to the 8–12 eV binding energy range is illustrated in Figure 5.3a and Figure 5.4a. Figures 5.3b and 5.3c report the measured dichroism for $\mathbf{Th^S}$, taken respectively at the photon energies of 22 and 19 eV at the magic angles of $\theta = 54.73°$ and 243.73°, using the two analyzers placed in the backward and forward directions. Instead, Figures 5.4b, 5.4c, and 5.4e give the measured dicroism for both $\mathbf{Th^S}$ and $\mathbf{Th^R}$, acquired at the single magic angle of of $\theta = 243.73°$ and at photon energies of 22, 19, 16, and 14 eV.

According to Equation (5.1), opposite dichroic spectra are observed at the magic angle for the $\mathbf{Th^S}$ and $\mathbf{Th^R}$ enatiometers and for the same enatiometers with the two analysers. The experimental D values, calculated according to Equation

(5.2), appear to be strongly dependent on both the specific molecular orbital considered and the photon energy.

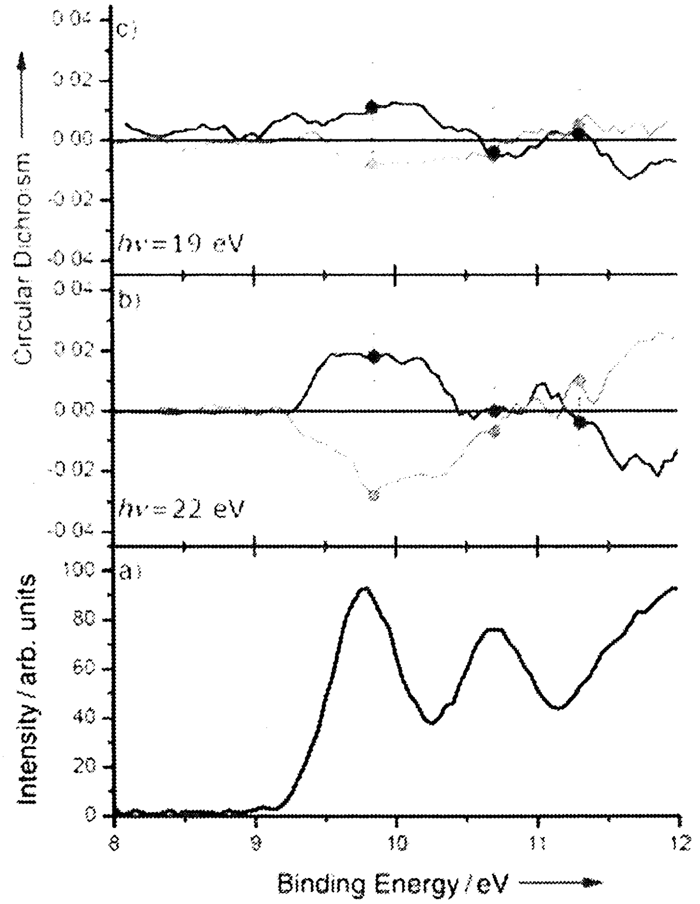

Figure 5.3: Dichroism of 3-hydroxytetrahydrofuran. Valence spectrum of **Th** obtained at 22 eV photon energy in the binding energy range 8–12 eV (a). Dichroism of $\mathbf{Th}^{S}$ at the magic angle θ_m = 54.73° (black curves) and θ_m + 180° = 234.73° (grey curves) at 22 eV (b) and 19 eV (c). The error bars include the experimental dispersion of each data set at different photon energies

For instance, at the 22 eV photon energy (Figure 5.4b), the HOMO exhibits pronounced dichroic effects while no significant effect is observed with HOMO-1 and HOMO-2. Besides, comparison figures 5.4b, 5.4c, 5.4d, and 5.4e reveals that the dichroic effects of HOMO-1 and HOMO-2 increase when decreasing the photon energy to a much larger extent than the observed for HOMO. At the photon energy of 16 eV (Figure 5.4d), the magnitude of the dichroic effects is large enough is large enough to allow discrimination between the HOMO-1 and HOMO-2 contributions and to single out the presence of the HOMO-2 orbital at 11.3 eV, which is hardly discernible from the large state envelope of Figure 5.2.

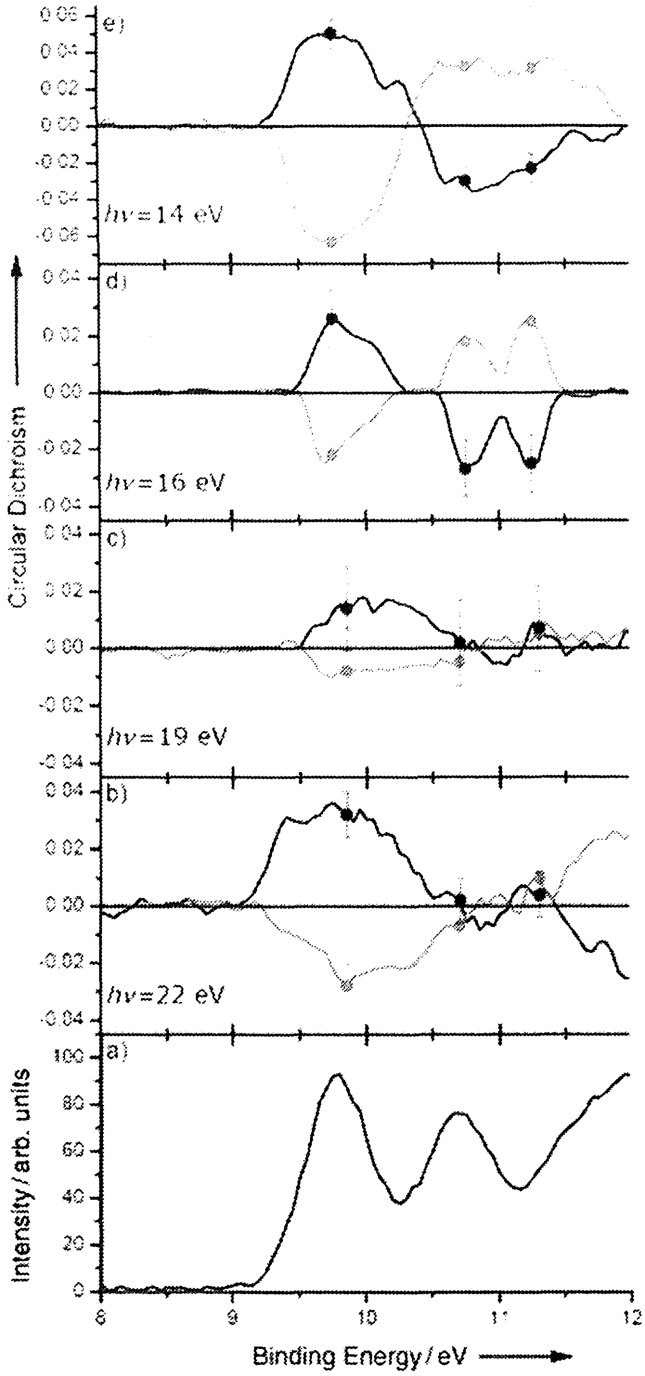

Figure 5.4: Dichroism of 3-hydroxytetrahydrofuran. Valence spectrum of **Th** obtained at 22 eV photon energy in the binding energy range 8–12 eV (a). Dichroism of **Th**^{S} at the magic angle θ_m = 54.73° (black curves) and θ_m + 180° = 234.73° (grey curves) at 22 (b), 19 (c), 16 (d), and 14 eV (eV). The error bars include the experimental dispersion of each data set at different photon energies

As expected [8] the σ and β parameters of Equation (5.1) exhibit relatively weak dependence upon the conformation of $\mathbf{Th}^S$ and $\mathbf{Th}^R$ enantiometers (not shown herein) whereas the dichroic *D* parameter is found to be most sensitive to conformational effects. Figure 5.5 reports the dependence of the *D* factor on the kinetic energy of the electron photoemitted from the HOMO (Figure 5.5a), HOMO-1 (Figure 5.5b), and HOMO-2 (Figure 5.5c). In this figures the solid lines refer to the computed profile for the most stable conformer, A, while the broken lines refer to the second more stable conformer B (see Figure 5.1). The experimental *D* values are symbolized by the dots and the bars correspond to the estimated experimental uncertainty. It is observed that, at the highest photon energies (19 and 22 eV), the experimental *D* values fit the theoretical curves for all the high- energy orbitals of the most abundant conformer, A. A satisfactory agreement is also found for its HOMO and HOMO-2 orbitals at lower photon energies, whereas large deviations are observed for HOMO-1. This discrepancy is probably due to the neglect of the electronic-vibrational coupling in the LCAO B-spline DFT computational procedure, which assumes a fixed molecular geometry, while the $\mathbf{Th}^S$ and $\mathbf{Th}^R$ enatiometers cannot be taken to be rigid at 60°C [7]. Indeed, as pointed out before, MP2/6-31G* [22] and QST2- MP2/6-31G calculations identified two low-lying conformations A and B for **Th** which may be present, though in unbalanced proportions, in the analysed sample at 60 °C (Figure 1). Furthermore, at this temperature, several low frequency torsional modes of A and B may be populated. Indeed preliminary calculations reveal that the size and the shape of the highest occupied molecular orbitals of A and B adapt themselves adiabatically to the zero-point vibrational motion of the nuclei in a largely different way. In particular, for both conformers A and B, the shape of the relevant HOMO-1 orbitals change to a much greater extent relative to that of the corresponding HOMO and HOMO-2 orbitals in the low-frequency modes of **Th** (eg. ring puckering at 110 cm^{-1}) and OH···H intramolecular hydrogen-bond streching at 188 cm^{-1}. Furthermore, at 60°C, these two modes are characterized by partially excited vibrational functions that may contribute to the different shape dependence of the HOMOs of A and B with the nuclei vibrational motion. In this sence, the pronounced discrepancy between the experimental and the theoretical photon-energy-depended *D* values of Figure 5.5b can be reasonably accounted for the ensemble of largely different sizes and shapes of the HOMO-1 orbitals experienced by the photoemitted electron owing to the low-frequency modes active in **Th** at 60°C.

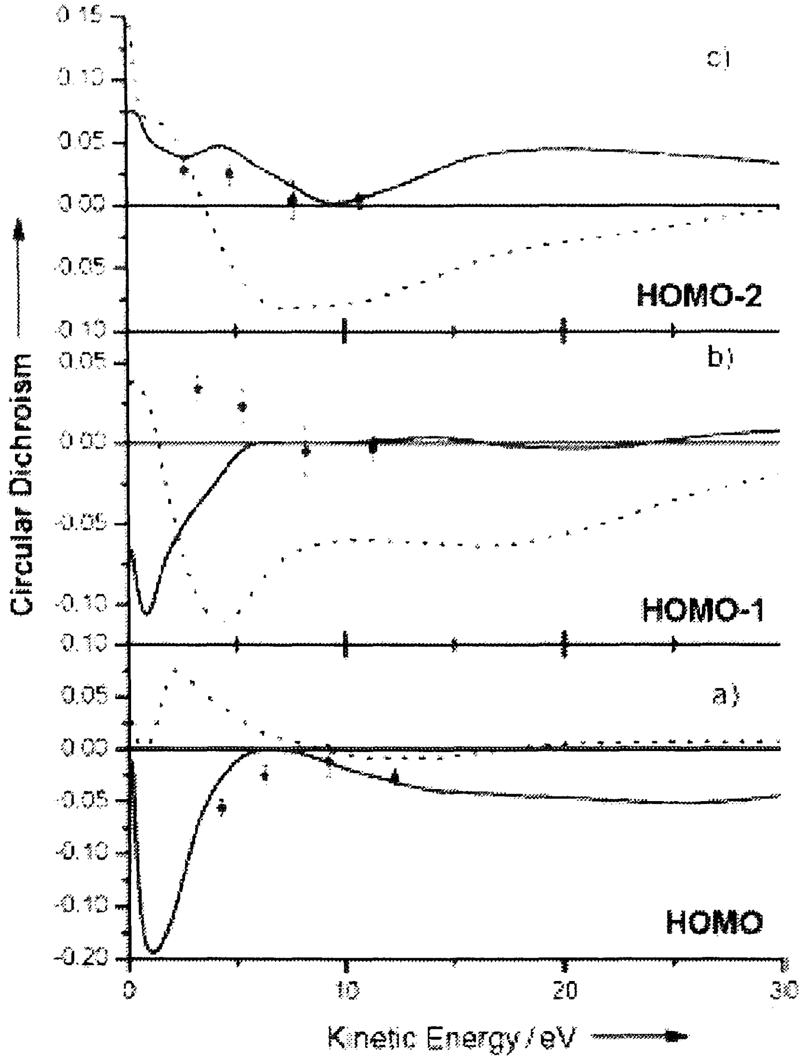

Figure 5.5: Dependence of the experimental *D* factor (dots) on the kinetic energy of the photoelectrons of the HOMO (a), HOMO-1 (b) and HOMO-2 (c). The error bars include the experimental dispersion of each data set at different photon energies. The solid curves refer to the computed *D* factor for conformer A, the broken curves refer to the computed *D* factor for conformer B.

5.6 Conclusions

The photoionization dichroic *D* parameter of the pure enantiometer of 3-hydroxytetrahydrofuran has been measured and its value discussed in the light of the LCAO B-spline DFT predictions. Substantial agreement is observed for the valence HOMO and HOMO-2 orbitals, thus providing further experimental support for the performance of the theoretical approach used [8]. The significant discrepancies observed for the HOMO-1 state are attributed to the floppiness of **Th**, in particular to the comparatively large sensitivity of the size and shape of its HOMO-1 to nuclei vibrational motion. The present study sheds light on a new feature of photoemissiom decroism, which appears to be sensitive not only to electronic factors [8], but also to structural, conformational, and vibrational factors. It is concluded that helicity depended effects in photoelectron emission from chiral molecules may be a potential abiogenic source of homochirality provided that favourable condition are met. Furthermore, the same factors may be conveniently employed to investigate the isomeric and conformational distribution of the chiral molecules themselves.

6 Conformational Effects on the Circular Dichroism in the Photoelectron Angular Distribution

A theoretical study of the influence of conformational factors on photoionization dynamical parameters, with special attention to the circular dichroism in the photoelectron angular distribution from chiral molecules, has been performed. The B-spline density functional method has been applied to the conformers of (1R,2R)-1,2-dibromo-1,2-dichloro-1,2-difluoroethane molecule. The cross section, asymmetry, and dichroic parameters relative to core and to valence orbitals retaining their nature along the conformational curve have been systematically studied. While the cross section and the asymmetry parameter are weakly affected, the dichroic parameter shows to be rather sensitive to the particular conformer of the molecule, suggesting that this dynamical property could be a useful tool for conformational analysis. The computational method has also been applied to methyl rotation in methyloxirane. Unexpected and dramatic sensitivity of the dichroic parameter profile with the methyl rotation, both in core and valence states, has been found. Boltzmann averaging over the conformers reproduces however quite closely the profiles previously obtained for the minimum energy conformation, in good agreement with the experimental results.

6.1 Introduction

The spectroscopic study of chiral systems can be profitably achieved by employing the dichroic effect that arises as a consequence of the interaction with circularly polarized light (CPL). Conventional experiments employ differential light absorption between left and right circularly polarized light, but the magnitude of such dichroism depends upon electric quadrupole or magnetic dipole operator contributions making the total effects rather weak, of the relative order of 10^{-3}-10^{-5}.

On the other hand it has been demonstrated theoretically [1,2] that the lack of inversion symmetry or a plane of symmetry in free molecules – optically active chiral molecules – produces asymmetry with respect to the propagation direction of the incident light in the photoelectrons emitted by CPL of defined helicity. This effect, referred to as Circular Dichroism in the photoelectron Angular Distribution (CDAD), occurs within a pure dipole approximation mechanism and its magnitude is expected to be of the order of 10^{-2}, significantly stronger than in conventional absorption experiments.

Practical realization of angle resolved photoionization experiments with circularly polarized light is not a straightforward issue, but recently synchrotron radiation technology development has allowed such measurements [3-8]. Moreover, efforts to perform theoretical calculations of the CDAD effect based on CMS-Xα calculations and B-spline methods on large molecules have recently started [7-12]. The calculation of the CDAD needs a knowledge of the continuum photoelectron wave function, a task still challenging in quantum chemistry due to the difficulty of implementing the continuum boundary conditions with a conventional basis set. The method employed in the present work is the LCAO B-spline DFT approach, which does not introduce any approximation on the potential, treats properly the continuum boundary conditions with B-spline basis funtions, and employs a Kohn–Sham Hamiltonian. The comparison of the LCAO B-spline DFT calculation of the dichroism effects with the available experimental data [7,8,12] has shown a substantial or quantitative agreement, showing that the present theoretical approach could be an important tool for the interpretation of the CDAD measurements. In particular, a recent computational and experimental study on the circular dichroism in valence photoelectron angular distribution of the 3-hydroxytetrahydrofuran enantiomers [8] has shed light on the sensitivity of dichroic parameter to the conformational factors. A previous theoretical work on the L-alanine employing the CMS-Xα method [10] has also shown different CDAD responses depending on the conformation of the molecule.

It is well known that conventional circular dichroism in differential absorption is widely used to reveal the conformation of molecules, especially biochemical systems. It is a question therefore if circular dichroism in photoemission can also be used as a pratical tool in conformational analysis, for example for the determination of the most stable molecular conformation or in the evaluation of the fractional population of the conformers.

The principal aim of the present work is to establish the sensitivity of the photoionization parameters to the conformations of a molecule, and to examine the possibility of employing the dichroic parameter profiles as *fingerprints* of the conformers. For this purpose we decided to calculate the CDAD effect as well as the usual photoionization parameters, namely the cross section and the asymmetry parameter, in a chiral system that could exist in several conformations. Since the determination of the conformers of a molecule can be a non-trivial task, in order to reduce the complexity of the problem we have considered a system with a single conformational degree of freedom. We have focused our attention on the molecule (1R,2R)-1,2-dibromo-1,2-dichloro-1,2-difluoroethane, labeled **(I)** in Fig. 6.1, whose possible conformations derive from the C–C bond rotation. The synthesis of the molecule (1R,2R)-1,2-dibromo-1,2-dichloro-1,2-difluoroethane **(I)** with a positive (+) enantiomeric excess is reported in literature [13], but the assignment of the absolute configuration of the chiral centers is missing.

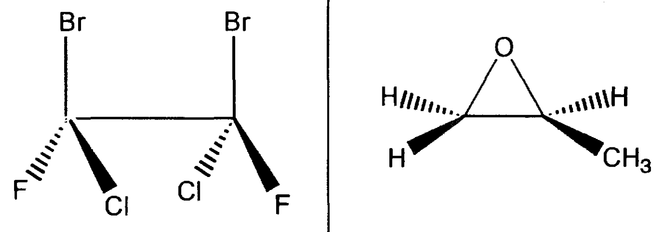

(I) **(II)**

Figure 6.1: Configurational structure of the molecules considered in the present study: (1R,2R)-1,2-dibromo-1,2-dichloro-1,2-difluoroethane **(I)**; (S)-methyloxirane **(II)**.

Another aim of the present work is to verify the assumption, made in previous theoretical studies on methyloxirane and camphor molecules [11,12], that in the calculation of the CDAD effect the rotation of the methyl group does not affect the results. We have therefore performed calculations on a set of conformations of methyloxirane, labeled **(II)** in Fig. 6.1, obtained from internal rotation about the C–CH_3 bond.

6.2 Theoretical Method

In this work the LCAO B-spline DFT method has been employed to calculate the photoionization properties of the enantiomers of the molecules considered in the gas phase with random molecular orientation. Such process is described, for each different final state, by the differential cross section $d\sigma/d\hat{k}$ [15], that is the angular distribution of the photoelectrons in the solid angle $d\hat{k}$ along their direction of propagation $\hat{k}$, which, in the electric dipole approximation, is completely defined by the partial cross section σ, the asymmetry parameter β and the dichroic parameter D

$$\frac{d\sigma}{d\hat{k}} = \frac{\sigma}{4\pi}\left[1 + (-1/2)^{|m_r|}\beta P_2(\cos\theta) + m_r D P_1(\cos\theta)\right], \qquad (6.1)$$

where P_i is the Legendre polynomial of i-th order and θ is the scattering angle between $\hat{k}$ and the laboratory frame, m_r is 0, +1, −1 for linear, left circular, or right circular light polarization, respectively. The laboratory frame is defined by the incident photons: the polar axis corresponds to the electric vector or propagation direction for linear or circular light polarization respectively. We define left or right circularly polarized light according to the value $m_r = +1$ or $m_r = -1$ of the projection of the photon spin along its momentum. Accordingly, the electric vector describes a positive (right-handed) or negative (left-handed) screw.

From the computational point of view the photoionization process is completely described, at the one-electron level, by the dipole transition moment between the ionized orbital and the photoelectron continuum orbital. Therefore the problem is recast to have efficient and accurate algorithms for the molecular continuum. The LCAO B-spline DFT method [16] has proven to be accurate, computationally economic and numerically stable and it has already been employed to study the photoionization of medium-sized molecules with explicit treatment of the continuum photoelectron wave function [7,8,11,12,14]. A short review of the

LCAO B-spline DFT method is given in the following referring to Ref. [16] for a detailed description of the method.

Continuum calculations are performed at the DFT Kohn-Sham level. The initial ground state density, which fixes the potential, is obtained by a conventional LCAO calculation employing the ADF program [17,18]. The LB94 exchange correlation potential [19] has been employed, because of the correct Coulomb tail. Moreover, good results are obtained with the same ground-state potential for all ionic final states, allowing to obtain all cross sections with a single calculation. Both bound and continuum orbitals are expanded in a very accurate basis, built from multicentric B-spline radial basis functions, which can describe both decaying and oscillatory behavior. This avoids any approximation to the molecular potential but still allows to treat rather large, non-symmetric molecules, difficult to treat with pure one center expansions.

The LCAO basis set consists of a large one center expansion (OCE) located on a chosen origin O:

$$\chi^{O}_{nlh\lambda\mu} = \frac{1}{r_O} B_n(r_O) X_{lh\lambda\mu}(\vartheta_O, \varphi_O), \tag{6.2}$$

where

$$X_{lh\lambda\mu}(\vartheta, \varphi) = \sum_{m} Y^{R}_{lm}(\vartheta, \varphi) b_{lmh\lambda\mu} \tag{6.3}$$

are symmetry adapted linear combinations of real spherical harmonics [21] and B_n is the *n*th spline monodimensional function [22]. These are supplemented by functions of the same type, which are symmetrized combinations of functions centered on the off-center positions j

$$\chi^{i}_{nlh\lambda\mu} = \sum_{j \in Q_i} \frac{1}{r_j} B_n(r_j) \sum_{m} b_{lmh\lambda\mu j} Y^{R}_{lm}(\vartheta_j, \varphi_j), \tag{6.4}$$

where i is an index which runs over the nonequivalent nuclei, Q_i is the set of equivalent nuclei, j runs over the equivalent nuclei and gives the origin of the off-center spherical coordinates $r_j, \vartheta_j, \varphi_j$. The coefficients $b_{lmh\lambda\mu}$ and $b_{lmh\lambda\mu j}$ are determined by symmetry, $\lambda\mu$ are the irreducible representation (IR) labels. The B-splines are built over the radial intervals $[0,R^{O}_{MAX}]$ for the set $\{\chi^{O}_{nlh\lambda\mu}\}$ and $[0,R^{i}_{MAX}]$ for the set $\{\chi^{i}_{nlh\lambda\mu}\}$.

The B-splines are completely defined by their order and by the grids of knots for all the radial intervals $[0,R^{O}_{MAX}]$ and $[0,R^{i}_{MAX}]$. In practice the most important computational choice regarding the basis set, which has a fundamental impact on the accuracy and the computational economy, is the maximum value of the angular expansion L_{MAXO} for the OCE.

The bound states of the system are obtained by means of a generalized diagonalization of the KS Hamiltonian matrix in the LCAO B-spline basis set. The continuum states are calculated employing a very efficient inverse iteration procedure [23] and normalized according to the **K** matrix condition. The **K**-normalized continuum orbitals are further transformed to incoming wave **S**-matrix boundary conditions and from such states the dipole matrix elements are finally obtained. The cross section, the asymmetry and dichroism parameters profiles for randomly oriented molecules are then computed according to the angular momentum transfer formalism [24].

6.3 Computational Details

For all the systems considered in the present work the calculations have been executed as follows. First the ground-state (GS) electron density is calculated by means of the ADF program [17,18] employing an all-electron double zeta plus polarization (DZP) basis set of Slater type orbitals (STO), taken from the ADF database. Such density is then used to build the KS hamiltonian with the LCAO B-spline program, from which the bound and the continuum states are extracted and used to calculate the cross section, asymmetry parameter and dichroism parameter. B-splines of order 10 are employed.

For both molecules a starting geometry was obtained by geometry optimization employing a DZP basis and the VWN potential [25], which furnishes accurate molecular structures. Conformational energies where then obtained by rigid rotation around the C–C bond, with the Becke-Perdew potential [26,27]. In cross section calculations the LB94 potential was instead employed.

To improve convergence the origin of the expansion should minimize the distance from all heavy atoms. If such a point is close to a heavy atom it is convenient to set the origin on this nucleus. The OCE has been set on the middle point of the C–C bond for **(I)** and on the substituted C atom for **(II)**. Point-group symmetry has been exploited in molecule **(I)** imposing the C_2 point-group symmetry for its conformers.

For both molecules $L_{MAXO} = 15$ has been employed. In fact previous analysis on the convergence of the photoionization parameters of methyloxirane **(II)** have been performed [11], showing that $L_{MAXO} = 15$ is certainly adequate for this molecule. For (1R,2R)-1,2-dibromo-1,2-dichloro-1,2 difluoroethane **(I)**, the model proposed in Ref. [16], the analysis of the LCAO B-spline eigenvalues and the experience based on previous calculation [8,11,12,14] on others medium-sized molecules suggested that $L_{MAXO} = 15$ should give convergent results with respect to the basis set size.

The expansion on the origin is divided with a radial grid with step size of 0.2 a.u. up to $R^{O}_{MAX} = 20$ a.u.; the intervals so obtained are supplemented with additional knots near the position of the nuclei in order to make the basis more flexible in the region of core orbitals.

The maximum angular momentum in the off-center expansion has been chosen as $L_{MAXi} = 1$ for H and $L_{MAXi} = 2$ for all heavy atoms. Radial expansion is defined by R_{MAXi}, which in the present implementation cannot intersect each other. The values chosen are for **(I)**: 0.8 au for C, 1.5 au for F and Cl, 1.8 for Br. For **(II)** a common value of 1.0 au was employed. A linear grid was adopted, dividing the radial interval in five steps.

6.4 Results and Discussion

6.4.1 (1R,2R)-1,2-dibromo-1,2-dichloro-1,2-difluoroethane (I)

Potential Barrier

Potential barrier analysis for internal rotation about the C–C bond has been performed by scanning the torsion angle from 0° to 360° at 15° intervals. The calculated potential energy curve in the upper panel of Fig. 6.2 shows a three-fold barrier. The arrows indicate the three staggered conformations considered in the cross section calculation: **(Ia)** and **(Ic)** are conformations with bromine atoms in gauche position, while in **(Ib)** the bromine atoms are in the anti position. Actually, **(Ib)** is not at the exact minimum, which is at 172.5°, but it is very close. This conformational structure is slightly more stable than **(Ia)**, 0.10 Kcal/mol, and 0.81 Kcal/mol lower in energy than **(Ic)**. The maxima of the potential energy correspond to eclipsed structures with barrier heights having values of 9.44, 8.38 and 10.78 Kcal/mol for the first, second and third barrier respectively.

This conformational analysis shows that the rotational barriers are high enough that at room temperature the molecule (1R,2R)-1,2-dibromo-1,2-dichloro-1,2-difluoroethane can be considered frozen in the three conformational isomers **(Ia)**, **(Ib)** and **(Ic)**. The fractional population of these conformers given by the Boltzmann distribution law is **(Ia)**/**(Ib)**/**(Ic)** = 0.40/0.48/0.12 at room temperature.

Ionisation Potentials

In the following the electronic structure of **(I)** in the conformations **(Ia)**, **(Ib)** and **(Ic)** will be briefly discussed on the basis of the KS-LB94 eigenvalues, obtained with both the ADF and the LCAO B-spline method. Experimental values are actually not available for this molecule. Nevertheless, previous calculations using the same computational scheme applied to medium-sized organic molecules have shown that the comparison between the LB94 eigenvalues and experimental IPs presents reasonably good agreement apart from a rigid shift [11,14]. We will split the analysis between core and valence states. The calculations have been performed imposing the C_2 point-group symmetry for the conformers, therefore the MOs are classified accordingly.

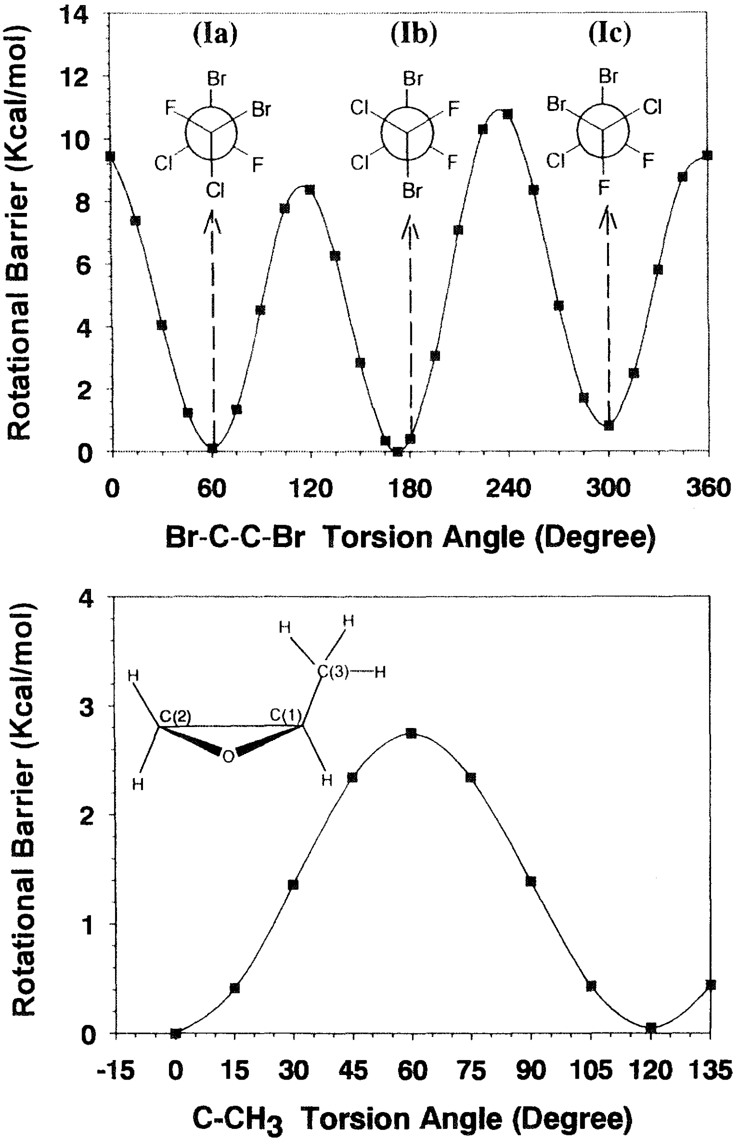

Figure 6.2: Upper panel: potential energy curve for internal rotation about the C–C bond of (1R,2R)-1,2-dibromo-1,2-dichloro-1,2-difluoroethane (**I**); the arrows indicate the conformational structures of the molecule considered in the present study. Lower panel: potential energy curve for internal rotation about the C–CH_3 bond of (S)-methyloxirane (**II**). The filled squares indicate the conformational structures considered in the present study, obtained by rigid rotation around the C–CH_3 bond with respect to the VWN/DZP optimized geometry.

The core KS-LB94 eigenvalues of the conformer (**Ia**) are reported in Table 6.1. The results for the other conformers are within 0.1 eV. It is worth noting that the LCAO B-spline calculation performs very well on describing the core states of heavy off-center atoms like Br and Cl, for which extreme localization of 1s functions represents a stringent test for the multicenter approach. The core states worst described by the LCAO B-spline are the C1s functions 8a 8b, since for all conformers **(Ia)**, **(Ib)** and **(Ic)** the eigenvalues are approximately 0.2 eV higher than the ADF results. This result is quite surprising because the large one center expansion is placed between the carbon atoms. Also incompleteness of DZP basis may affect the result up to a few tenths of eV. It is interesting to note that the same trend has already been observed in the molecule $CF_3COCH_2CH_3$, previously considered [14], where the C 1s state of $-CF_3$ showed the same deviation between B-spline LCAO and DZP LCAO calculation.

Table 6.1: The core KS-LB94 eigenvalues of (1R,2R)-1,2-dibromo-1,2-dichloro-1,2-difluoroethane **(I)** in the conformation **(Ia)** obtained with the ADF and with the LCAO B-spline DFT approach. Values in eV. The underlined MOs are those considered in the analysis of the conformational effect on the photoionization parameters.

	ε **(Ia)**	
MO	ADF	LCAO
1a - Br 1s	−13184.54	−13184.45
2a - Cl 1s	−2790.24	−2790.25
3a - Br 2s	−1711.52	−1711.89
4a - Br 2p	−1548.06	−1548.12
5a - Br 2p	−1547.89	−1547.95
6a - 2p Br	−1547.88	−1547.95
7a - F 1s	−691.25	−691.21
8a - C 1s	−296.85	−296.62

The KS-LB94 eigenvalues of the outermost valence orbitals, which are essentially associated with the outer p functions of the halogen atoms, are reported in Table 6.2. It is possible to notice that passing from **(Ia)** to **(Ib)** and then to **(Ic)** there is inversion of the MOs order. We have reported the LCAO eigenvalues and the difference Δ just for the conformer **(Ic)** as the same holds for the other conformers. For valence orbitals LCAO B-spline and ADF results are in substantial agreement, with differences being at most 0.22 eV for 28b orbital, confirming the quality of the expansion employed. The valence orbitals are very close to each other, except of 28b orbital, which is very well separated from the following ones by about 1–1.5 eV, depending on the conformer; furthermore its energy position is very similar for the three conformers, being approximately −17.3 eV. This makes the 28b state a very suitable candidate to measure the photoemission dichroism from molecule **(I)**. From simple analysis of the ADF-KS eigenvectors it is possible to identify the 28b orbital as the fluorine lone pair and it is evident from the F 2p atomic contribution that the nature of 28b orbital is distinctly maintained along the conformers **(Ia)**, **(Ib)** and **(Ic)**. This orbital has been therefore considered for a further analysis of the photoionization parameters, in order to investigate the influence of the conformational structure on the photoemission dichroism.

Table 6.2: The outermost valence KS-LB94 eigenvalues of (1R,2R)-1,2-dibromo-1,2-dichloro-1,2 difluoroethane (I) in the conformations (Ia), (Ib) and (Ic) obtained with the ADF and with the LCAO B-spline DFT approach. Also reported are the differences $\Delta = \varepsilon_{LCAO} - \varepsilon_{ADF}$ for the conformer (Ic). Values in eV. The underlined MOs are those considered in the analysis of the conformational effect on the photoionization parameters.

ε **(Ia)**		ε **(Ib)**		ε **(Ic)**			
MO	ADF	MO	ADF	MO	ADF	LCAO	Δ
27b	−18.77	27b	−18.60	28a	−18.68	−18.87	−0.19
28a	−18.56	28a	−18.56	27b	−18.37	−18.56	−0.19
28b	−17.31	28b	−17.27	28b	−17.34	−17.56	−0.22
29a	−16.04	29b	−15.94	29a	−15.79	−15.94	−0.15
30a	−15.90	29a	−15.87	29b	−15.69	−15.85	−0.15
29b	−15.25	30a	−15.34	30a	−15.48	−15.64	−0.16
30b	−14.07	31a	−14.26	30b	−14.07	−14.12	−0.05
31a	−13.89	30b	−13.98	31b	−13.82	−13.83	−0.01
32a	−13.57	31b	−13.56	31a	−13.81	−13.85	−0.04
31b	−13.49	32a	−13.54	32a	−13.47	−13.48	−0.01
33a	−12.96	32b	−12.89	33a	−13.11	−13.15	−0.04
32b	−12.82	33a	−12.68	32b	−12.56	−12.59	−0.03
34a	−12.61	33b	−12.39	34a	−12.47	−12.50	−0.03
33b	−12.10	34a	−12.34	33b	−12.43	−12.48	−0.05

Concerning the outermost orbitals (HOMO and HOMO-1) it is worth noticing that passing from **(Ia)** to **(Ib)** and then to **(Ic)**, there is inversion in the order of the orbitals corresponding to HOMO and HOMO-1 states. Furthermore for all conformers HOMO and HOMO-1 states are almost superimposed, except of 34a orbital in **(Ia)** which is quite well separated by 0.51 eV from 33b. The ADF-KS eigenvector analysis of the AO contribution shows a clear correspondence between HOMO-1 states of the three conformers. It is in fact possible to identify both 34a in

(Ia), **(Ic)** and 33b in **(Ib)** as an orbital having contribution from the Br 4p function orthogonal to the C–C bond ($4p_y$ for **(Ia)** and **(Ic)**, $4p_z$ for **(Ib)** with C–C placed along the x axes). For the HOMO states, 33b orbitals of **(Ia)** and **(Ic)** are very similar in terms of AO composition, since they are constituted by a comparable contribution of the Br 4p functions. The 33b orbital of **(Ib)** can also be ascribed to 4p Br functions, but for this state the contribution of the component parallel to the C–C bond is predominant. Despite this difference, the HOMO state can be undoubtedly identified as the lone pair of Br atoms for all the conformers, justifying therefore the comparison of the photoionization parameters relative to the three HOMO states.

Core Dichroism

In Fig. 6.3 the total core F 1s (7a + 7b) and C 1s (8a + 8b) cross section, asymmetry parameter and dichroic parameter of the conformers **(Ia)**, **(Ib)** and **(Ic)** are considered. We evaluate that the fractional population of these conformers is **(Ia)**/**(Ib)**/**(Ic)** = 0.40/0.48/0.12 at room temperature.

We start the analysis of the F 1s orbital [see Fig. 6.3(a)]. The different sensitivity of the photoionization parameters is striking: σ and β do not show important differences; the latter is almost identical for all conformers, while the cross section profile of **(Ia)** is shifted by about 1 eV towards the threshold with respect to the **(Ib)** and **(Ic)**. On the other hand the *D* parameter proves to be rather selective with respect to the conformational structure of the molecule. In particular, the *D* profile of conformer **(Ia)** shows a sharp peak near the threshold up to +0.05 followed by an oscillating behavior from –0.015 up to +0.02 within 40 eV above the threshold. The following main differences are observed for conformer **(Ib)**: very near the threshold the *D* profile displays a pronounced minimum up to –0.06 while in the 14–30 eV higher energy range the *D* values are similar in magnitude but opposite in sign with respect to **(Ia)**. The *D* parameter relative to **(Ic)** shows larger oscillations than **(Ia)** and **(Ib)** in the range 10–26 eV, with values up to +0.05 at 16 eV. At this energy, for example, absolute differences of the order of 0.06 between **(Ic)** and **(Ib)**, and of the order of 0.04 between **(Ic)** and **(Ia)** are predicted in the CDAD effect. Non-trivial correlation between *D* profiles and structure of the conformers seem to be present. In Fig. 6.3 the solid thick line is the averaged values of the *D* parameters relative to conformers **(Ia)**, **(Ib)** and **(Ic)** obtained by the Boltzmann's statistics. For a gaseous sample of molecule **(I)**, the CDAD effect associated with F 1s state is predicted to be rather weak at room temperature, with *D* values oscillating from –0.02 near the threshold up to +0.01 at 16 eV, suggesting that the CDAD effect from the F 1s state of molecule **(I)** should be investigated within 30 eV above the threshold. In fact, despite the structures in the profiles, the rather different shapes and opposite *D* values displayed by the three conformers tend to reduce the averaged *D* values. For example at energies very near the threshold, **(Ia)** and **(Ib)** have *D* values up to 0.05 in magnitude, but due to their different sign and the fraction population **(Ia)/(Ib)** = 0.40/0.48, the averaged *D* values are drastically lowered. Furthermore, even if the conformer **(Ic)** displays rather high values around 16 eV, it is weakly populated at room temperature

Similarly to the F 1s state, the cross section and asymmetry parameters relative to C 1s state display very similar behavior along the conformers [see Fig. 6.3(b)]. Concerning the cross section parameter, all conformers show three maxima structures: the first just above the threshold and the second centered at 12 eV could be ascribed to shape resonance processes, while the third structure, which appears as a smooth maximum centered at 54 eV, could be ascribed to the first EXAFS oscillation. The appearance of analogous maximum structures has been observed in the cross section profile of the C 1s state of $–CF_3$ atom in the molecule $CF_3–CO–CH_2CH_3$ [14], which suggests that these structures in the σ profile should carry some information about the ligands and the configuration of the C atom. For the asymmetry parameter, small differences are observed between the conformers **(Ia)**, **(Ib)** and **(Ic)** within 6 eV above the threshold while at high energies the three profiles are superimposed. Finally, we consider the dichroic parameter in the lower panel: the C 1s orbital shows high sensitivity to the conformational changes as well. Rather large differences between the *D* profiles are especially found near the threshold: **(Ia)** oscillates from –0.04 up to +0.04 while **(Ib)** and **(Ic)** display large oscillations up to 0.1 in magnitude but opposite in sign. Within 30 eV above the threshold all conformers display a smoother out-of-phase oscillating behavior. It is interesting to note that up to this energy, the conformer **(Ib)** has exclusively negative *D* values. The averaged *D* values obtained on the basis of the Boltzmann's statistics (solid thick line) stay in between the profiles of the most populated conformers **(Ia)** and **(Ib)**. Like the F 1s, the averaged CDAD effect from core C 1s state is predicted to be rather weak, due to the different core 1s shapes of the dichroic parameter profiles, which tend to cancel in the Boltzmann's statistics.

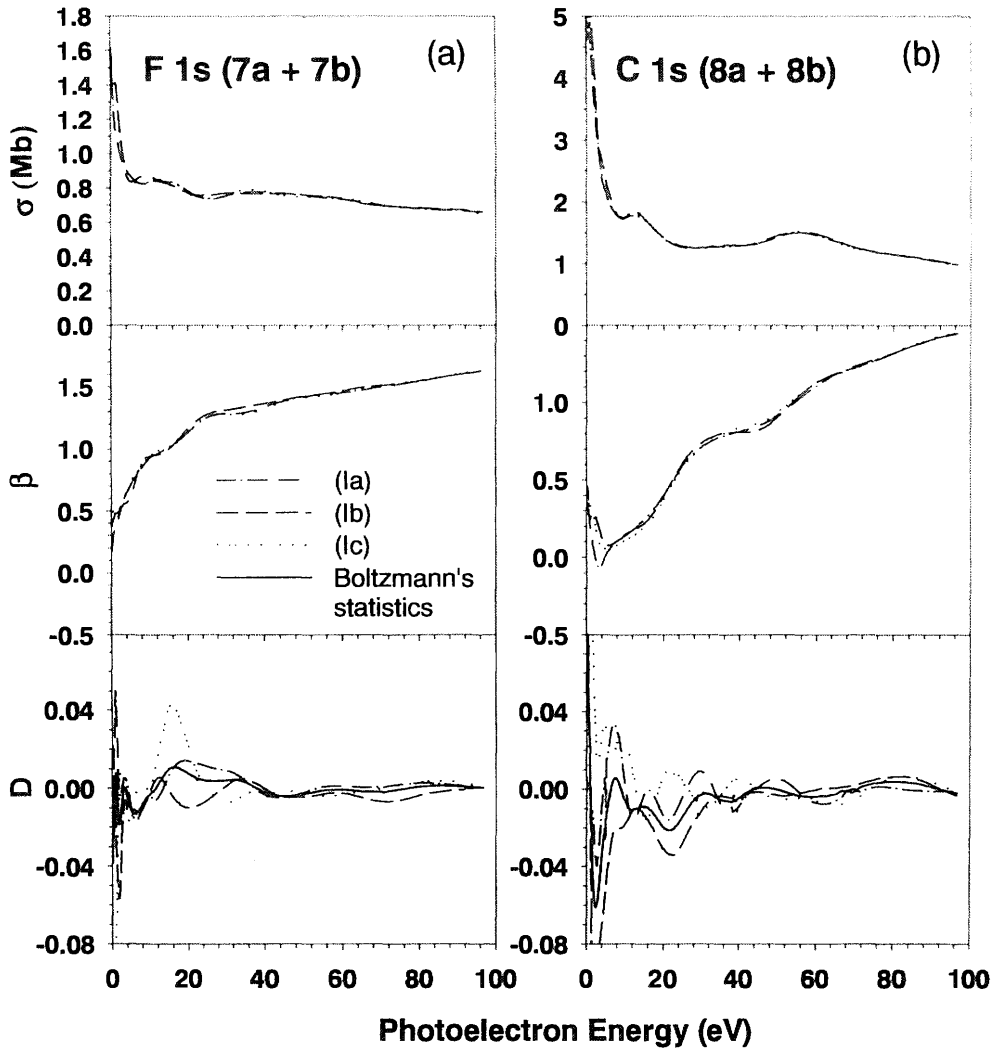

Figure 6.3: Cross section (σ), asymmetry parameter (β) and dichroic parameter (*D*) relative to the total core F 1s (7a + 7b) and C 1s (8a + 8b) orbitals of the conformers of (1R,2R)-1,2-dibromo-1,2-dichloro-1,2-difluoroethane **(I)**. The averaged *D* values obtained on the basis of the Boltzmann's statistics are also displayed.

The core F 1s and C 1s photoionization parameter profiles analysis has shown that the dichroic parameter is significantly affected by the conformation of molecule

(I), both in terms of relative values and shape with respect to the kinetic energy. On the other hand the cross section and the asymmetry parameter are almost insensitive to conformational changes.

Since F 1s and C 1s are highly localized states, it is expected that they are negligibly affected by the C–C rotation. This suggests that the variations in the CDAD effect observed in the F 1s and C 1s states along the conformers **(Ia)**, **(Ib)** and **(Ic)**, should be merely ascribed to the continuum final state, which is completely delocalized over the molecule and therefore feels the changes of the effective molecular potential during the C–C rotation. The core states maintain very well their IP position along the conformers and as a consequence we can speculate about the possibility of using the calculated dichroic parameter profiles relative to core states, as a *fingerprint* of the conformers of a molecule.

Valence Dichroism

In Fig. 6.4 the photoionization parameter profiles relative to the 28b orbital, the lone pair of fluorine atoms, are displayed. We start the analysis with the cross section profiles; close to threshold σ shows notable variations along the conformers **(Ia)**, **(Ib)** and **(Ic)**. The conformer **(Ib)** displays a maximum structure in the cross section profile centered at 5.5 eV, which is significantly lowered for conformer **(Ic)** and almost disappears for **(Ia)**. At the same photoelectron energy a minimum structure is present in the asymmetry parameter profile, which suggest that the 28b photoionization spectra exhibit a shape resonance process [28]. It is interesting therefore to notice how the shape resonance in the 28b cross section profile is rather sensitive to the particular molecular conformation. The shape resonance problem is typically described as a one-electron continuum phenomenon in which the ejected photoelectron is resonantly trapped by a potential barrier [29]. Therefore the shape resonance process will depend sensitively on the details of the molecular potential. It turns out that the observed sensitivity of the shape resonance that appears in the 28b photoionization channel to the rearrangement of the nuclei as a consequence of the C–C rotation is generally expected, albeit this behavior has not been mentioned in the shape resonance studies appeared in literature up to now. This effect could be an important source of information on the conformational structure of molecules, and deserves future investigation. The asymmetry parameter does not change significantly along the conformers and only a minor effect is found in the profile of conformer **(Ic)**.

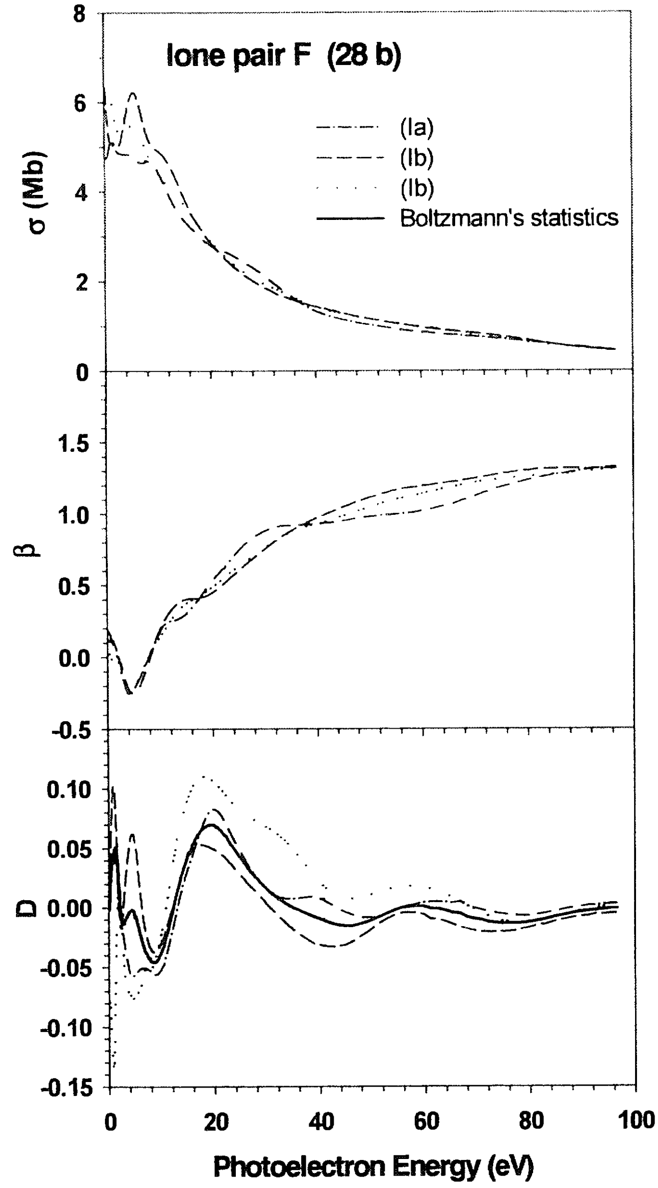

Figure 6.4: Cross section (σ), asymmetry parameter (β) and dichroic parameter (*D*) relative to the 28b orbital (lone pair of fluorine atoms) of the conformers of (1R,2R)-1,2-dibromo-1,2-dichloro-1,2-difluoroethane **(I)**. The averaged *D* values obtained according to the Boltzmann's statistics are also displayed.

Finally we consider the dichroic parameter *D*: a large effect is found for all three conformers (from −0.14 up to +0.12) and a significant sensitivity to the conformational structure is also displayed. The conformer **(Ia)** shows an oscillating behavior near the threshold with values in the range ± 0.05, a maximum up to 0.08 at 20 eV followed by rapid decay within 40 eV above the threshold. Conformers **(Ib)** and **(Ic)** display pronounced oscillation near the threshold, opposite in sign between each other, while at higher energies both have a maximum at 20 eV followed by smooth oscillations up to about 70 eV. It is worth noting that the sudden oscillation displayed by all the conformers at 5.5 eV should be associated with the shape resonance, since the increased electron–ion core coupling at shape resonance allows the electron to become more sensitive to the molecular potential. Anyway a direct correlation between the intensity of the shape resonance centered at 5.5 eV in the cross section profile, and the magnitude of the dichroic parameter at this energy is not straightforward, suggesting that *D* is certainly affected by the shape resonance process but, as already remarked in Ref. [11], it should be more sensitive to tiny asymmetries than to continuum collapse effects. The averaged dichroic parameter profile is depicted by the solid thick line: the CDAD effect relative to the orbital 28b is fairly intense, with *D* from −0.05 up to +0.05 within 40 eV above the threshold. This is a rather wide energetic range that makes the 28b orbital very suitable to be explored experimentally. Furthermore, the *D* parameters relative to the conformers **(Ia)**, **(Ib)** and **(Ic)** show significant differences up to 50 eV in the kinetic energy scale, supporting the idea that the *D* profiles could be used as a tool to distinguish between the conformers of a molecule.

In Fig. 6.5 the photoionization parameters profiles relative to HOMO-1 and HOMO states of the conformers **(Ia)**, **(Ib)** and **(Ic)** are displayed. Concerning the HOMO-1 orbital [see Fig. 6.5(a)] the σ parameter is quite insensitive to the particular conformational structure of the molecule, but significant differences are observed in the immediate threshold region where the cross section is very steep (an atomic effect, due to the large spatial extension of Bromine 4p orbitals) and so probably difficult to observe experimentally. This differences are attributed to variations of the HOMO-1 composition along the conformers **(Ia)**, **(Ib)** and **(Ic)**, and therefore to differences in terms of the initial bound state. This is also evident after inspection of the asymmetry parameter in the middle panel. The conformers have similar β profiles, but some minor differences between **(Ia)** and **(Ib)**, **(Ic)** are found in the structures centered approximately at 18 eV, and in the high energy range. The comparison with the β profile relative to 28b [see Fig. 6.4], whose nature is well maintained along the conformers, shows that the observed, still minor, variations in β should be attributed to more marked differences in terms of the initial bound state. Again the *D* profiles display different shapes according to the conformer: **(Ic)** shows a very large and positive D value near the threshold, followed by a rapid decay at higher energies, while **(Ia)** and **(Ib)** have a wider oscillating behavior, with a significant CDAD effect up to 60 eV. In particular, **(Ib)** shows a pronounced maximum close to the threshold and reduced but still significant oscillations up to 80 eV; **(Ia)** has small *D* values near the threshold but oscillations up to +0.07 at 26 eV and –0.08 at 48 eV. In Fig. 6.5(a) the Boltzmann's averaged *D* profile is not displayed, since HOMO-1 does not retain very well the IP position along the conformers **(Ia)**, **(Ib)** and **(Ic)**. We finally consider the HOMO state [see Fig. 6.5(b)]: the σ parameter profiles are almost superimposed while β parameter displays some changes along the conformers, again attributed to variations of the HOMO composition along the conformers. Once more it is the *D* parameter that carries more information about the conformational structure of the molecule.

Despite showing a rather large CDAD effect, HOMO and HOMO-1 have a localized character since they are essentially constituted by Br 4p functions. In particular, it has been previously observed that in all conformers the main contribution to the HOMO-1 is given by the Br 4p function orthogonal to the C–C bond; this state has therefore, with good approximation, a local reflection plane. This means that the observed dichroism in photoemission and its sensitivity to the particular conformer should be attributed to the molecular effective potential that acts on the photoelectron wave function, which is completely delocalized and therefore feels the global asymmetry of the molecule. This observation is in agreement with previous studies on the CDAD effect [6,11,12]. In particular, the comparison of the *D* profile relative to HOMO and HOMO-1 with the experimental profile relative to bromine lone pair in bromocamphor [6] does not present any similarity. The *D* profile in bromocamphor is close to zero in almost all experimental points, while in both HOMO and HOMO-1 states of (**I**) significant *D* values have been calculated for all considered conformations. This observation again indicates that the CDAD effect is much more affected by the particular molecular structure than the initial state.

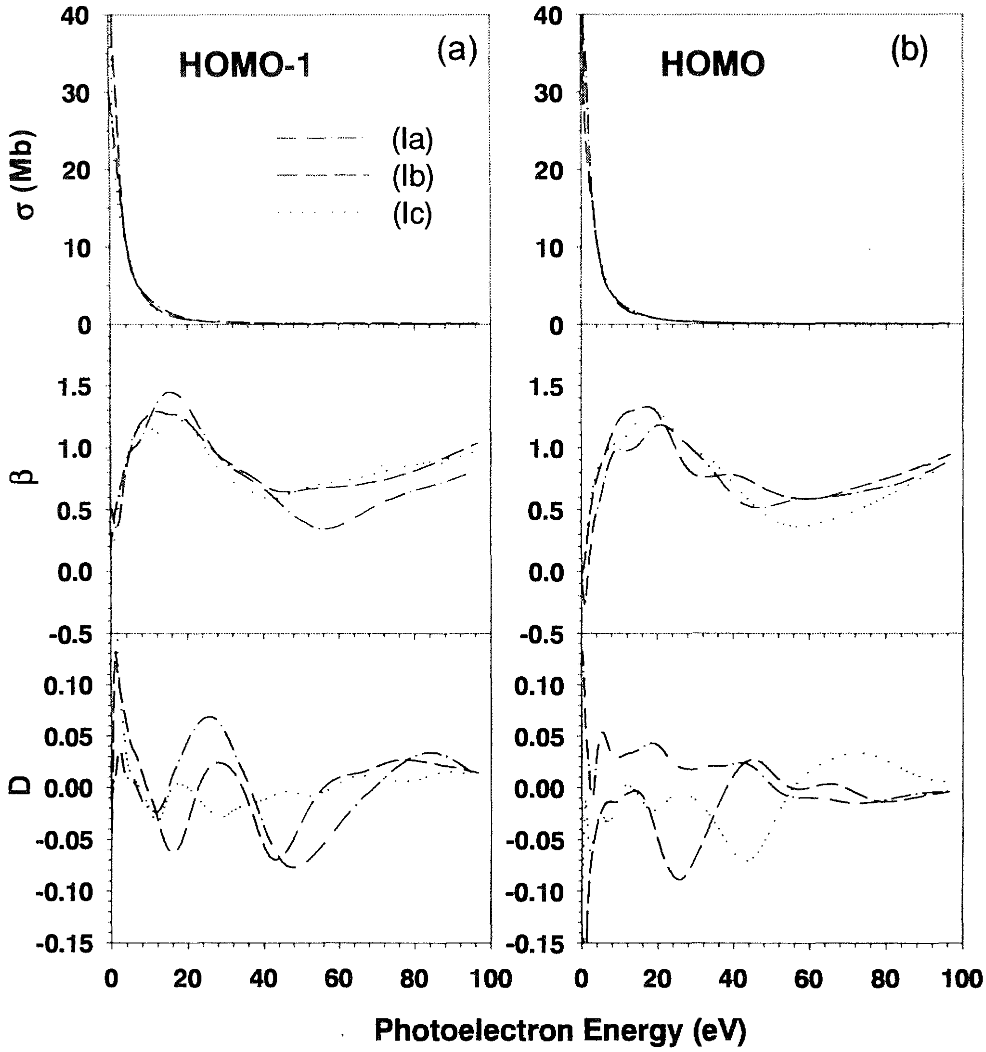

Figure 6.5: Cross section (σ), asymmetry parameter (β) and dichroic parameter (*D*) relative to the HOMO-1 and HOMO orbitals of the conformers of (1R,2R)-1,2-dibromo-1,2-dichloro-1,2-difluoroethane (**I**).

6.4.2 (S)-methyloxirane (II)

Potential Barrier

In the lower panel of Fig. 6.2 the potential energy curve for internal rotation around the C–CH_3 bond of methyloxirane (**II**) is displayed. The energies for internal rotation are calculated from the differences between the energy of each conformation and that of the most stable conformer (0° in Fig. 6.2). The maximum point on the potential energy correspond to the eclipsed structure with respect to the dihedral angle ∠H–C–C–H. The potential barrier is 2.75 Kcal/mol, not very high, allowing a free rotation of the methyl group.

Ionisation Potential

The analysis of the KS-LB94 electronic spectrum of methyloxirane, considered in its most stable conformation **(0°)**, and a comparison with the experimental ionisation potentials has been considered in detail in Ref. [7,11]. Differences in ionisation potentials among the conformers are all within 0.1 eV, so methyl rotation does not significantly change the vertical ionisation energies of methyloxirane **(I)**, justifying therefore a comparison of the photoionization parameters for the conformations in Fig. 6.2.

Photoionization Parameters

In Fig. 6.6 the σ, β and D profiles relative to the orbital 14a of (S)-methyloxirane **(II)** in the conformations **(0°)-(105°)** are displayed. This orbital has been considered as an example to display the different behavior of the photoionization parameters to the conformational changes, but the same conclusions hold for the other valence orbitals. The orbital 14a is quite delocalized on the whole molecule with a significant contribution from H 1s orbitals of the methyl moiety. The most immediate observation concerns the different sensitivity of the parameters to the methyl rotation: σ and β change negligibly while D displays unexpected dramatic variations. The cross section and asymmetry parameter relative to the other orbitals of (S)-methyloxirane **(II)** are also little affected by the conformational variations; in the following the discussion will be therefore limited to the effect of the methyl rotation on the dichroic parameter.

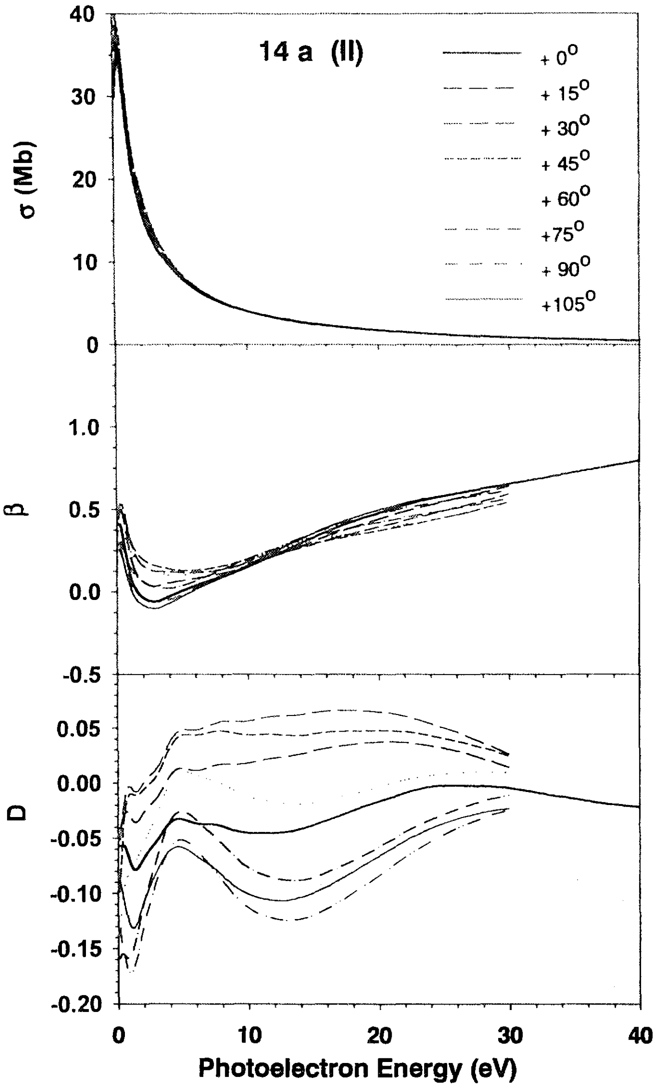

Figure 6.6: Cross section (σ), asymmetry parameter (β) and dichroic parameter (*D*) relative to the 14a orbital of (S)-methyloxirane (**II**) considered in the conformations **(0°)-(105°)**.

Core Dichroism

The dichroic parameter profiles relative to the core states of (S)-methyloxirane (**II**) are considered in Fig. 6.7. The O 1s dichroic parameter profiles show some differences just very near the threshold; on the other hand C(1) 1s and C(2) 1s orbitals display significant differences in the CDAD effect (up to 0.05) between the conformations **(0°)-(105°)**. Considering the conformer **(0°)** as reference, differences in the *D* profile become more and more pronounced as we approach the eclipsed conformation **(60°)**, and the differences with respect to **(0°)** reduce as the conformation approaches to the equivalent conformer (120°). The dichroic parameter profile relative to the C(3) 1s orbital is rather less sensitive than C(1) and C(2) to the conformational changes.

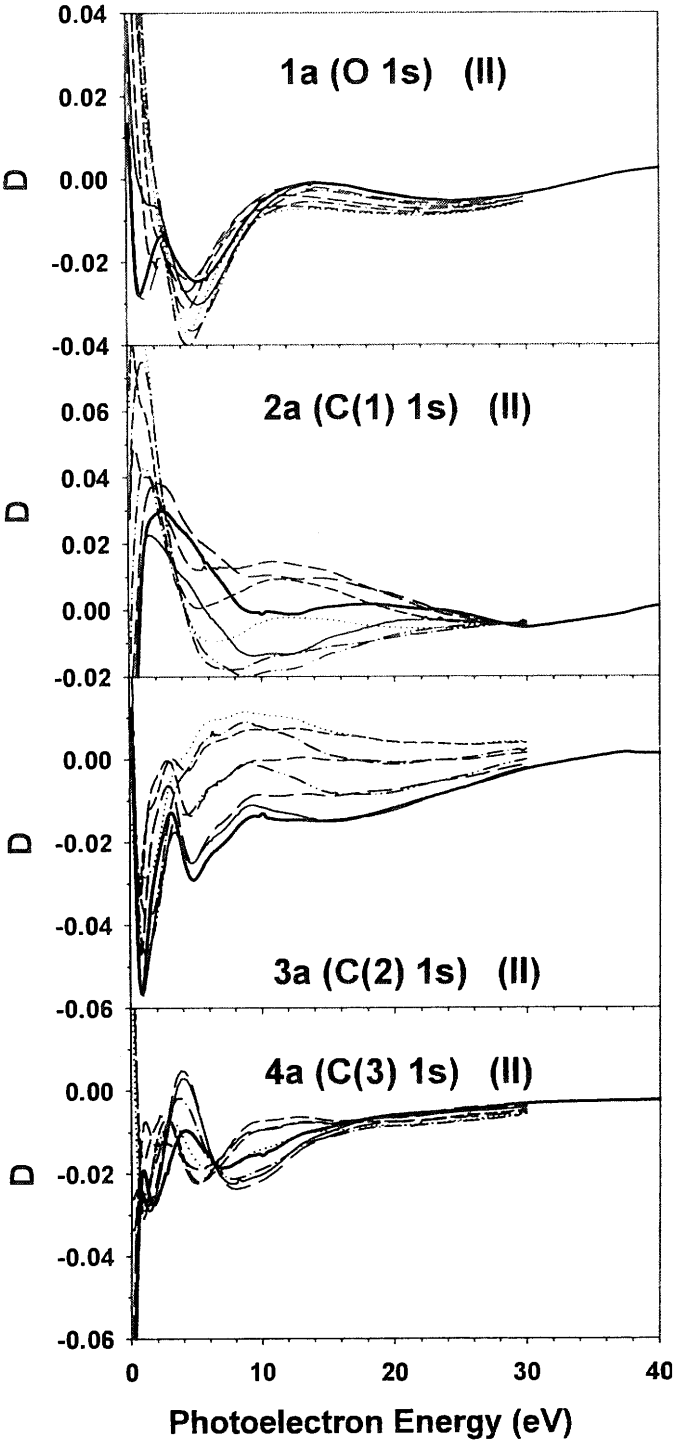

Figure 6.7: Dichroic parameters (*D*) relative to the core orbitals (1a-4a) of (S)-methyloxirane **(II)** considered in the conformations **(0°)-(105°)**. For the meaning of the lines see legend in Fig. 6.6.

It has been already pointed out that for core states, like 1a-4a, the photoemission dichroism must be definitely a final state effect [11] since the initial 1s orbitals retain their atomic nature and their spherical symmetry along the conformations. Therefore, the intensity of the dichroic effect is ascribed to the photoelectron wave function, which is delocalized and can probe the whole effective molecular potential extracting information on its dissimmetry. The question now is how to rationalize the different sensitivity of the core CDAD effect to the $-CH_3$ rotation: *D* relative to O 1s orbital is rather insensitive while for C(1), C(2) 1s orbitals it shows significant changes; again modest variations are displayed by C(3) 1s initial state. It is unlikely that the variation of the CDAD effect between the conformations **(0°)-(105°)** is an initial state effect; in fact the rotation of $-CH_3$ should negligibly perturb the core 1s states. The magnitude of the CDAD variations with $-CH_3$ rotation should mainly be attributed to transition dipole moment effects. The core 1s states do not change their nature during the $-CH_3$ rotation but they have a different localized spatial position; this should indicate that the different sensitivity of the CDAD effect to the $-CH_3$ rotation is probably associated with more pronounced variations of the photoelectron wave function close to the C(1) and C(2) atomic position than close to the O and C(3) atomic positions.

Valence Dichroism

In Fig. 6.8 the influence of methyl rotation on the valence dichroism is displayed. Apart from the orbital 16a, the dichroic parameter profiles show dramatic variations. In particular, the conformer **(0°)** and the conformations **(15°)** and **(105°)**, which fractional population given by the Boltzmann distribution law is **(0°)/(15°)/(105°)** = 0.45/0.22/0.22, display differences of 0.06-0.08 in the CDAD effect relative to the orbitals 11a-15a. The other less populated conformations display differences even more pronounced with respect to **(0°)**. The analysis of the ADF-KS eigenvectors shows that the molecular orbitals 11a-15a are rather delocalized on the whole molecule, while the 16a orbital can be clearly ascribed to the localized oxygen lone pair [11]. Furthermore the analysis displays that the atomic orbital composition is rather well maintained along the conformations. The sensitivity of the photoelectron dichroism to conformational changes should not be associated to the initial state, but merely to changes of the photoelectron wave function on the whole molecular structure but in proximity of the O position. This could explain the minor sensitivity of the *D* parameter relative to HOMO state, in agreement with the behavior displayed by the O 1s orbital.

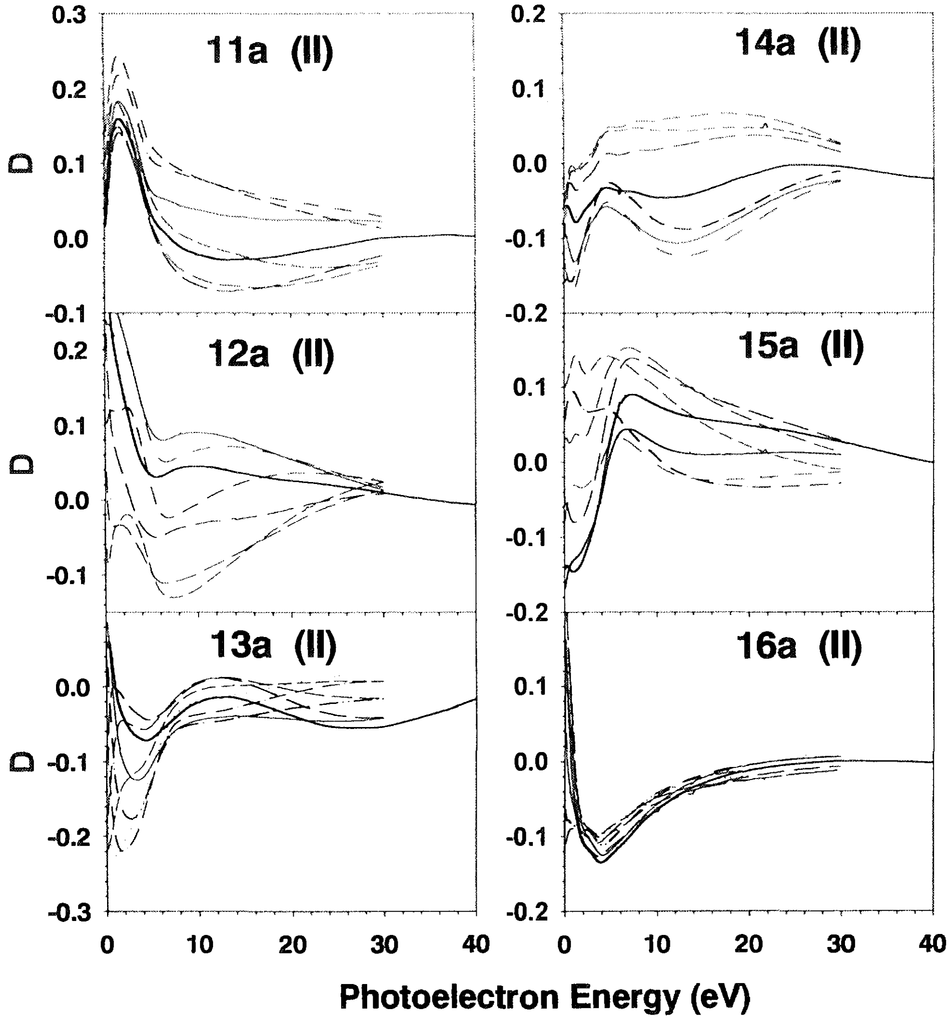

Figure 6.8: Dichroic parameters (*D*) relative to the valence 11a-16a orbitals of (S)-methyloxirane (**II**) considered in the conformations (0°)-(105°). For the meaning of the lines see legend in Fig. 6.6.

Finally, the conformational averaged profiles of the dichroic parameter obtained on the basis of the Boltzmann's statistics are displayed in Fig. 6.9. The results do not move far away from the values calculated at the most stable conformation (**0°**). This is rather surprising because of the dramatic variations displayed by the dichroic parameter with the methyl rotation. A detailed analysis of Fig. 6.8 shows that for the orbitals 11a-15a the conformations **(15°)** and **(105°)**, which fractional population is 0.22, have opposite values with respect to **(0°)**: the Boltzmann's statistics tends therefore to cancel most of the deviations of the conformations **(15°)**, **(105°)** from the values of the dichroic parameter associated with the conformer **(0°)**. However, it is worth noting that the averaged *D* values are in slight better agreement with the experimental results [7].

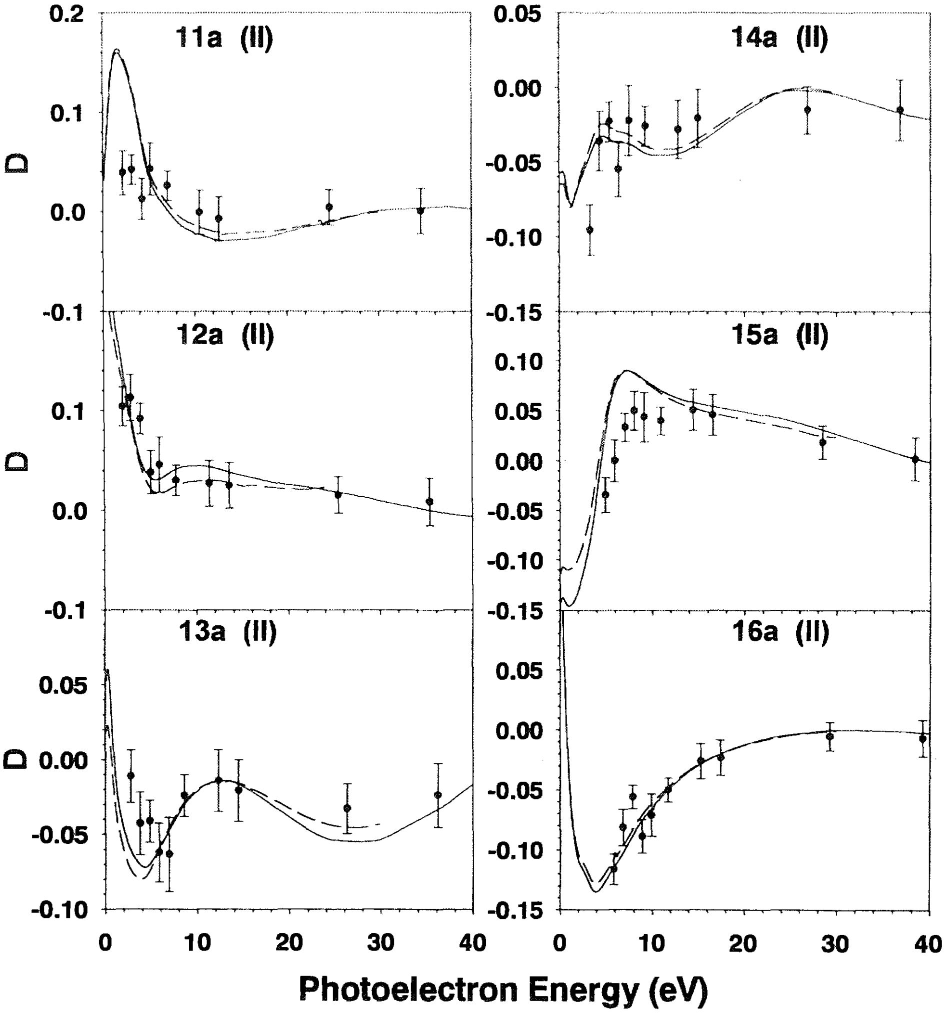

Figure 6.9. Dichroic parameter (*D*) relative to the 11a-16a orbitals of (S)-methyloxirane **(I)** obtained on the basis of the Boltzmann's statistics (– – –). Calculation on the conformer **(0°)**, (——) and the experimental data [7] (•) are also displayed.

The assumption that methyl rotation does not affect the calculation of the CDAD effect is therefore not correct. In fact dramatic and unexpected variations of the dichroic parameter have been calculated in (S)-methyloxirane **(II)**. Despite this fact the deviations from the most stable conformation tend approximately to cancel, so that the assumption previously made is essentially valid and so are results previously reported. Although this behavior appears likely in general, it is by no means guaranteed, and an average over thermally important conformations can significantly influence the calculated profiles.

6.5 Conclusions

In the present work the influence of the conformational factors on the photoionization dynamical parameters, with special attention to the CDAD effect, has been considered. The LCAO B-spline DFT method has been successfully applied to the molecule (1R,2R)-1,2-dibromo-1,2-dichloro-1,2-difluoroethane considered with different conformational structures. The cross section, asymmetry, and dichroic parameters relative to the core and to the valence orbitals retaining their nature along the conformers have been systematically studied. The cross section and asymmetry parameters show minor to minimum variations; on the other hand the dichroic parameter relative to both core and valence states displays a great sensitivity to the conformation of the molecule. The dichroic parameter profiles could be a useful tool for conformational analysis, or they could be employed as ***fingerprints*** of the conformers of a molecule.

The LCAO B-spline DFT method has also been applied to study the photoionization process of the (S)-methyloxirane, considered in the different conformations obtained by internal rotation of the C–CH_3 bond, in order to verify the assumption that methyl rotation does not significantly affect the calculated values of the CDAD effect. Unexpected and dramatic variations of the dichroic parameter profile with the methyl rotation, both in core and valence states, have been found instead. The magnitude of the CDAD variations with –CH_3 rotation should mainly be attributed to final-state and transition dipole moment effects. However, it has been demonstrated for (S)-methyloxirane that Boltzmann average over all the conformations tends to cancel the strong deviations from the calculated values of the dichroic parameter associated with the most stable conformation.

7 Branching Ratios Deviations from Statistical Behaviour in Core Photoionization

Accurate calculations of carbon 1s photoionization cross sections have been performed at the Density Functional level with the B-spline Linear Combination of Atomic Orbitals approach. The molecules considered are $FC\equiv CH$, $FC\equiv CCH_3$, $FC\equiv CCN$, $F_2C=CH_2$, $CF_3COOCH_2CH_3$ and C_3H_5O. The variation of the Branching Ratios relative to inequivalent C 1s ionisations have been evaluated from threshold to about 100 eV photoelectron kinetic energy. Large deviations from the statistical ratios are observed at low energies, which remain often significant several tens of eV above threshold. The importance of taking into account core Branching Ratios for peak deconvolution and quantitative analysis, as well as an additional tool for structural information, is pointed out. Strong shape resonant effects are found to largely cancel in branching ratios. Their nature and variation along the series is analyzed in the framework of excitations into σ^* valence orbitals.

7.1 Introduction

Traditionally it has been assumed more or less implicitly that Branching Ratios (BR) in core ionisations follow the statistical ratio. In large part this comes from the vast amount of experimental spectra in the core region obtained at high photon energies: the ESCA period of the Mg Kα and Al Kα spectra opened up by K. Siegbahn and coworkers [1]. At those energies, intensities from chemically inequivalent atomic sites of the same species appeared to be close to the 1:1 ratio, as seen for instance in the famous test case of $CF_3COOCH_2CH_3$ [2]. The study of core ionisations has received a new impulse by the availability of tunable radiation in the soft X-ray range with high fluxes and very high resolution at synchrotron radiation laboratories. This allows a detailed investigation of more complex samples, involving several sites separated by small chemical shifts, which have shown the potential of new chemical insights into their electronic structure [3,4,5]. However, even at the lower energies required to improve resolution, the statistical ratio is generally assumed, for example in the deconvolution of the spectra. Knowledge of the BRs is of course of paramount importance for the application of XPS as a quantitative analysis technique.

As a matter of fact the study of core ionisation cross sections has been mostly neglected, despite the fact that they could provide important new quantitative information of structural type, both electronic and geometrical, pertaining to the different sites probed by core ionisation, as well as a possible assignment tool in ambiguous situations, where Ionisation Potentials (IP) alone do not provide a clearcut answer. An interesting example is the study of resolved core ionisation from equivalent sites in the cases of N_2 [6] and C_2H_2 [7], where the separation of the σ_g and σ_u initial states has brilliantly confirmed the σ_u* nature of the shape resonant state, which appears now only in the σ_g ionisation channel, showing conspicuously in the σ_g/σ_u ratio.

Strong shape resonances are usually found in core absorption spectra, in the so called NEXAFS region, up to rougly 50 eV from threshold, so that corresponding strong features should be observed in photoionization cross sections. Actually our initial interest in this problem came from a casual observation of a significant deviation from the expected intensity of the CH_3 ionisation in methyloxyrane, which will be discussed in the following.

The wide application of core electron spectra reflects the ease of experimental detection and the more immediate interpretation with respect to valence spectra. Core spectra allow to single out a single chemical species in a complex environment, and chemical shifts are often directly linked to the chemical environment. In fact several recent studies have focussed on a refined interpretation of these data, uncovering non trivial correlations with chemical structure [8]. While absolute cross section measurements are notoriously difficult, relative intensities of neighbouring peaks in photoelectron spectra can be obtained much more easily, at least when the peaks are sufficiently resolved, so that this information is also readily available. Given the large interest of core ionisation spectra as a structural probe and an analytical technique not only for isolated molecules, but also in solid state and surface studies, including absorption on surfaces and heterogeneous catalysis, we found it interesting to investigate these effects with the aid of theoretical calculations.

Also calculations of core ionisation cross sections are rather scarce, especially in complex systems with reduced symmetry and several inequivalent atomic sites. Most accurate computational tools employ some form of one center expansion, which, although adequate for the central atom, is difficult to converge for core states in off center atoms. A recent example is the study of core ionisations in CH_4, CF_4 and CCl_4 [9]. Of the two most available techniques for complex systems, Stieltjes Imaging [10] suffers from limited resolution, and Multiple-Scattering calculations [11] are not considered quantitatively very dependable. We have recently developed a novel approach [12], based on a multicenter B-spline basis and a least squares approach, which is capable to treat accurately the molecular potential, including core states, and to give convergent results within the chosen hamiltonian. For large systems we employ a DFT approach, which has proven quite accurate in the case of 1s ionisations, as several studies on small molecules have demonstrated [13].

Of course such an approach cannot describe violent many-body effects. These are of two main types: correlations in the initial and final bound states, and correlations in the continuum. The former are static, that is independent of photoelectron energy, and persist in the high energy limit. The main effect is the redistribution of the spectral intensity from the primary peak towards satellite states. In the present context this amounts to a significant reduction of the intensity of the main line. Few examples are known in which the many-body effects cause deviations of the BR's from the statistical ratio in the high energy limit, like C_3O_2 [14] and the ratio of multiplet peaks in open shell systems, like O_2 and NO [15], or Transition Metal compounds [16], where correlation effects play a larger role, and may become dramatic in particular situations, as is the case for molecules absorbed on metal surfaces [17]. In the case of organic molecules the reduction is often very similar for all atoms of the same type, so that BRs are little affected. This is confirmed by the BRs observed in the high energy limit, like in $CF_3COOCH_2CH_3$ [2], and can be taken into account by a separete correlayed calculation of the spectral strengths. For instance we have computed spectral strengths of .6831 and .6913 for C1 and C2 in

FCCH respectively, at the CISD level. Main correlation effects in the continuum give rise to interchannel coupling and autoionization resonances, which can give strong deviations from the computed single channel BRs. Interchannel coupling can be well described at the TDDFT level, and our previous investigations of N1s and C1s ionisations in N2 [18] and C2H2 [19] have shown it to be of minor importance. Advances in the implementation of TDDFT algorithms [20] will soon allow a more thorough investigation in complex systems. Two electron excitations are likely to have a profound influence on the cross sections, which is however limited to a narrow energy range. In any case consistent deviations between experimental and calculated BR's with the DFT approach could be another unexploited tool for the quantitative detection of such effects.

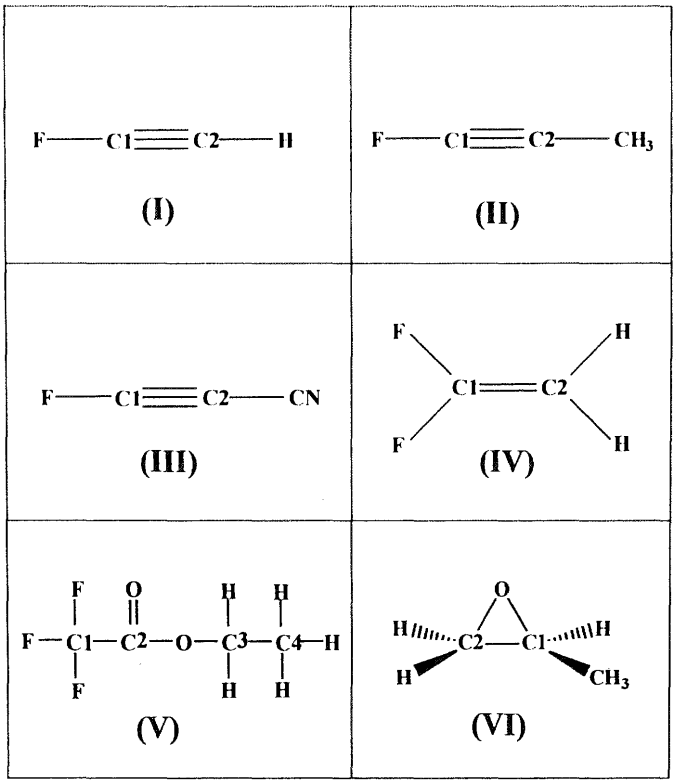

Figure 7.1: Structures of the molecules considered in this study: **(I)** fluoroacetylene; **(II)** fluoromethylacetylene; **(III)** fluorocyanoacetylene; **(IV)** (1,1)difluoroethene; **(V)** ethyl trifluoroacetate; **(VI)** methyloxyrane.

From the above arguments it is expected that the results of the present investigation will be sufficiently realistic to afford a clear picture of the variations of the BR's that can be expected in organic molecules. Beside methyloxyrane we have chosen a series of fluorinated compounds, in order to have well separated C 1s ionisations, which could be amenable to an experimental verification. The molecules chosen are $FC{\equiv}CH$, $FC{\equiv}CCH_3$, $FC{\equiv}CCN$, $F_2C{=}CH_2$, $CF_3COOCH_2CH_3$ (Figure 7.1). Because of the efficiency of the computations, theoretical results may prove generally helpful to screen molecules before an experimental study, to check experimental results in difficult situations, like poorly resolved states, and in general to assist interpretation of the observed features.

7.2 Theoretical Method

In this work the LCAO B-spline DFT method has been employed to calculate the photoionization properties of the molecules reported in Figure 7.1, in the gas phase with random molecular orientation. Such process is described by the differential cross section $d\sigma/d\Omega$ [21], which, for linearly polarized incident light and in the electric dipole approximation, is completely defined by the partial cross section σ_i and the asymmetry parameter β_i of the residual system in the i-th state

$$\frac{d\sigma_i}{d\Omega} = \frac{\sigma_i}{4\pi}\left[1 + \beta_i P_2(\cos\theta)\right], \qquad (7.1)$$

where P_2 is the Legendre polynomial of second degree and θ is the scattering angle as measured from the polarization vector $\hat{k}$ of the incident light.

From the computational point of view the photoionization process is completely described, at the one-electron level, by the dipole transition moment between the ionised orbital and the photoelectron continuum orbital . Therefore the problem is recast to have efficient and accurate algorithms for the molecular continuum. The LCAO B-spline DFT method [12] has proven to be accurate, computationally economic and numerically stable and it has already been employed to study the photoionization of medium-sized molecules with explicit treatment of the continuum photoelectron wave function [22,23].

Continuum calculations are performed at the DFT level, employing a Kohn-Sham hamiltonian

$$h_{KS}\varphi_E = E\varphi_E \tag{7.2}$$

The initial ground state density, which fixes the potential, is obtained by a conventional LCAO calculation employing the ADF program [24,25]. The LB94 exchange correlation potential [26] has been employed, because of the correct Coulomb tail, which is important for the accurate description of the continuum properties [13]. Moreover it has already been shown that LB94 with the same GS potential for all final ionic states, including core ionisation, is always the best choice [13,18,19], allowing to obtain all continuum cross sections with a single calculation. Both bound and continuum orbitals are expanded in a very accurate basis, built from B-spline radial basis functions, which can describe both decaying and oscillatory behavior. This avoids any approximation to the molecular potential, as in the MS-Xα approach, but is still able to treat rather large, non symmetric molecules, difficult to treat with pure one center expansions, typical of more sophisticated approaches.

The LCAO basis set consists in a large one center expansion (OCE) located on a chosen origin O:

$$\chi^{O}_{nlh\lambda\mu} = \frac{1}{r_O} B_n(r_O) X_{lh\lambda\mu}(\vartheta_O, \varphi_O), \tag{7.3}$$

where

$$X_{lh\lambda\mu}(\vartheta, \varphi) = \sum_m Y^R_{lm}(\vartheta, \varphi) b_{lmh\lambda\mu} \tag{7.4}$$

are symmetry adapted linear combinations of real spherical harmonics [27] and B_n is the *n*th spline monodimensional function [28]. These are supplemented by functions of the same type, which are symmetrized combinations of functions centered at the off-center positions j

$$\chi^{i}_{nlh\lambda\mu} = \sum_{j \in Q_i} \frac{1}{r_j} B_n(r_j) \sum_m b_{lmh\lambda\mu j} Y^R_{lm}(\vartheta_j, \varphi_j), \tag{7.5}$$

where i is an index which runs over the nonequivalent nuclei, Q_i is the set of equivalent nuclei, j runs over the equivalent nuclei and gives the origin of the off-center spherical coordinates $r_j, \vartheta_j, \varphi_j$. The coefficients $b_{lmh\lambda\mu}$ and $b_{lmh\lambda\mu j}$ are determined by symmetry, $\lambda\mu$ are the irreducible representation (IR) labels. The B-splines are built over the radial intervals $[0, R^O_{MAX}]$ for the set $\left\{\chi^O_{nlh\lambda\mu}\right\}$ and $[0, R^j_{MAX}]$ for the set $\left\{\chi^j_{nlh\lambda\mu}\right\}$. The B-splines are completely defined by their order and by the grids of knots for all the radial intervals $[0, R^O_{MAX}]$ and $[0, R^j_{MAX}]$. In practice the most important computational choice regarding the basis set, which has a fundamental impact on the accuracy and the computational economy, is the maximum value of the angular expansion L_{MAXO} for the OCE.

The bound state of the system is obtained by means of a generalized diagonalization of the KS Hamiltonian matrix in the LCAO B-spline basis set. The continuum states are extracted, for each photoelectron energy E, as the eigenvectors of the energy dependent matrix $\mathbf{A}^+\mathbf{A}$

$$\mathbf{A}^+\mathbf{A}(E)c = ac, \qquad \mathbf{A}(E) = \mathbf{H} - E\mathbf{S} \tag{7.6}$$

corresponding to the minimum modulus eigenvalues, employing a very efficient inverse iteration procedure [29], where in Eq. (6) **H** and **S** are the Hamiltonian and overlap matrix, a and c refer to the minimum modulus eigenvalues and continuum eigenvectors , respectively.

The continuum states are then normalized to the **K** matrix conditions, matching the asymptotic part of the continuum eigenvectors with respect to the regular and irregular Coulomb wave functions [30]. The Coulomb wave functions employed are of charge +1 due to the correct asymptotic behaviour of the LB94 potential. The **K**-normalized continuum orbitals are further transformed to incoming wave **S**-matrix boundary conditions and from such states the dipole matrix elements are finally obtained

$$D^{\lambda\mu-}_{lh}(\lambda_r) = \sqrt{\frac{4\pi}{3}}\left\langle \varphi^{\lambda\mu-}_{lh} \middle| rY_{1\lambda_r} \middle| \varphi_i \right\rangle \tag{7.7}$$

The cross section and the asymmetry parameter are then computed according to the angular momentum transfer formalism [31].

7.3 Computational Details

For all the systems considered in the present work the calculations have been executed as follows. First the ground-state (GS) electron density is calculated by means of the ADF program [24,25] employing an all-electron double zeta plus polarization (DZP) basis set of Slater type orbitals (STO), taken from the ADF database. Such density is then used to build the KS hamiltonian with the B-spline LCAO program, from which the bound and the continuum states are extracted and used to calculate the cross section and asymmetry parameter. B-splines of order 10 are employed.

Since the experimental geometry is not available for all the molecules under study and to be internally consistent, we have employed the optimized geometries, obtained with the ADF code using the same DZP basis set but with the VWN exchange correlation potential [32], which furnishes accurate molecular structures [33]. Notice that VWN potential has been employed only for geometry optimization; in all the other instances the LB94 potential has been employed, as stated previously.

To improve convergence the origin of the expansion should minimize the distance from all heavy atoms. If such a point is close to a heavy atom it is convenient to set the origin on this nucleus. The OCE has been set on C1 atom in **(I)**, **(II)**, **(IV)**, **(VI)** and on C2 in **(III)** and **(V)**.

Point-group symmetry has been exploited in all system. In particular the geometry of the molecule **(V)** has been optimized in an *anti* conformation that exploits the C_S point-group symmetry; actually we expect that different conformation of the system will not change significantly the cross section and asymmetry parameter profiles . The most important choice for the calculation is the maximum angular momentum (L_{MAXO}) employed in the expansion on the origin. For the largest molecule considered in the present work, ethyl trifluoroacetate **(V)**, the model proposed in Ref. [12], the analysis of the LCAO B-spline eigenvalues and the experience based on previous calculation [22], have suggested that $L_{MAXO} = 15$ should give convergent results with respect to the basis set size. The same value has been employed for all molecules. The maximum angular momentum (L_{MAXi}) employed in the off-center expansions has been kept fixed to $L_{MAXi} = 2$ for C, O, N, F and $L_{MAXi} = 1$ for H. The expansion on the origin is divided with a radial grid with step size of 0.2 a.u. up to $R^{O}_{MAX} = 20$ a.u.; the intervals so obtained are supplemented with additional knots near the position of the nuclei in order to make the basis more flexible in the region of core orbitals. To take maximum advantage of the off-center expansion, the radial intervals $[0, R^{i}_{MAX}]$ have taken different extension depending on the atomic weight of the nuclei and on the distance of the atom from the one-center expansion, under the constraint that in the present implementation of the method the spheres of radius R^{i}_{MAX} cannot intersect each other [12]. The expansion on the off-center nuclei is divided with a five-steps radial linear grid up to: $R^{i}_{MAX} = 1.3$ a.u. for fluorine in all molecules but **(I)**, where $R^{i}_{MAX} = 1.2$ a.u.; $R^{i}_{MAX} = 1.2$ a.u. for oxygen in **(V)** and $R^{i}_{MAX} = 1.0$ a.u. in **(VI)**; $R^{i}_{MAX} = 1.0$ a.u. for carbon in **(I)**, **(II)**, **(IV)**, **(V)** and $R^{i}_{MAX} = 1.2$ a.u. in **(III)**, **(VI)**; $R^{i}_{MAX} = 1.1$ a.u. for nitrogen in **(III)**; $R^{i}_{MAX} = 1.0$ for hydrogen in **(I)**, **(II)**, **(V)**, $R^{i}_{MAX} = 0.8$ a.u. in **(III)** and $R^{i}_{MAX} = 0.7$ in **(VI)**.

7.4 Results and Discussion

7.4.1 Ionisation Potentials

Let us consider briefly the ionisation potentials. The ones employed in the present study, also to define ionisation thresholds, are the DFT–LB94 eigenvalues, which are reported in Table 7.1. It is well established that the exact Kohn–Sham eigenvalue of the highest occupied molecular orbital corresponds, with the sign changed, to its ionisation potential [34]. However, it has been pointed out that also the Kohn–Sham eigenvalues for inner orbitals are actually approximations of IP's [35]. In the present work we are more interested in a realistic evaluation of the chemical shifts of the carbon 1s ionisations than in the absolute value of the Ionisation Potentials. A ΔSCF calculation using the VWN exchange-correlation potential has also been performed on the ethyl trifluoroacetate, to compare with the chemical shifts obtained from the LB94 eigenvalues and the experimental data, also reported in Table 7.1. The agreement of both approaches with the experimental chemical shifts is reasonably good, although some differences are apparent. Also incompleteness of the DZP basis may affect the results up to a few tenths of an eV. For instance the LB94 chemical shift between C3 and C4 is 2.00 eV with LCAO DZP and 1.77 eV from the B-spline LCAO eigenvalues. It is clear however that for the purpose of the present work the use of the LB94 eigenvalues is completely adequate.

Table 7.1: Carbon 1s Ionisation Potentials (IP) of the molecules reported in Figure 7.1 obtained with the ADF program. Also reported are the available experimental IP. Values in eV.

		$-\varepsilon$	
Molecule	*Atom*	*ADF-LB94*	*IP exp*
Fluoroacetylene (**I**)	C1	292.88	
	C2	290.95	
Fluoromethylacetilene (**II**)	C1	292.24	
	C2	290.72	
	$-CH_3$	291.30	
Fluorocyanoacetylene (**III**)	C1	294.36	
	C2	292.47	
	$-CN$	292.21	
(1,1)difluoroethene (**IV**)	C1	295.31	296.10[8]
	C2	291.12	291.33
methyloxyrane (**VI**)	C1	292.08	292.5[35]
	C2	291.85	292.0
	$-CH_3$	290.50	291.2
Ethyl trifluoroacetate (**V**)	C1	298.18	299.5[2]
	C2	294.88	296.0
	C3	292.99	293.0
	C4	290.99	291.2
		IP VWN-ΔSCF	
Ethyl trifluoroacetate (**V**)	C1	297.88	
	C2	294.91	
	C3	292.76	
	C4	290.93	

The analysis of the carbon 1s IPs in the molecules under study, reported in Table 7.1, shows the expected trend for the carbon bound to fluorine C1, whose IP increases continuously going throughout the series fluoroacetylene, (1,1)difluoroethylene and ethyl trifluoroacetate, taking into account the increasing positive charge on C1 due to the increased number of fluorine substituents. Beside this obvious trend, there is an interesting result that involves the C 1s IPs in fluoroacetylene and in fluoromethylacetylene: the substitution of –H with $-CH_3$ affects much more the IPs of C1 1s, which is 0.64 eV lower in $F-C\equiv C-CH_3$ than in $F-C\equiv C-H$, with respect to the IPs of C2 1s, which is 0.23 eV lower in $F-C\equiv C-CH_3$ than in $F-C\equiv C-H$. This result is apparently unexpected since C2 is the atom bound to $-CH_3$ group. A similar result has been found in the propyne and ethyne molecules [3], and the significant negative shift in the ionisation energy of the $HC\equiv$ propyne atom is explained in terms of a more negative charge in the vicinity of the core-ionised atom compared with the $HC\equiv$ ethyne atom, and rationalized in terms of a resonance structure where the $HC\equiv$ atom in the propyne molecule is negative.

In analogy with the propyne molecule, we propose the following resonance structures for fluoromethylacetylene:

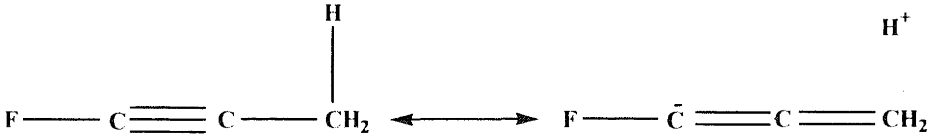

$$F-C\equiv C-CH_2(H) \longleftrightarrow F-\bar{C}=C=CH_2 \quad H^{+}$$

I II

In **II** there has been transfer of electrons from the $-CH_3$ group to the C1 atom, explaining wherefore the shift in the 1s IP of C1 upon substitution is more significant than in C2. The proposed resonance structure **II** could also rationalize the higher value of the 1s IP in $-CH_3$ with respect to C2, due to the positive charge localized on the $-CH_3$ group. The presence of the resonance structure **II** for fluoromethylacetylene is confirmed by the ADF-LB94 calculated dipole moment with direction as indicated in **II**, and with modulus 0.879 D, almost four times larger than in fluoroacetylene, 0.247 D, which reflects the molecular charge distribution induced by the $-CH_3$ group. The substitution of –H with –CN also determines a slightly higher positive shift for C1 1s IP, 1.52 eV, than C2 1s IP, 1.48 eV in fluorocyanoacetylene. These results imply that there is a positive charge in the vicinity of C1 that we explain in terms of two resonance structures:

$$F-C\equiv C-C\equiv N \longleftrightarrow F-C^{+}=C=C=\bar{N}$$

I II

The resonance structure **II** reflects the positive charge on C1. The calculated dipole moment is 3.454 D and the direction is as indicated in **II**.

7.4.2 Cross Sections and Branching Ratios

We shall first analyze BR's and relate them to features of the corresponding cross sections and then discuss in more detail the origin of the shape resonances in the spectra and their correlation to chemical structure. In the present analysis the Branching Ratio is defined as the ratio of one C 1s channel to the total C 1s channels in the molecule, normalized to the number of C atoms, so that the statistical value is always one.

FC≡CH. The results obtained are reported in Figure 7.2. Both carbon 1s ionisations show a strong shape resonance, attributed to a 1s $\rightarrow \sigma^*$ transition, typical of the acethylene moiety. Since the two cross section profiles almost superimpose the effect on the BRs is much less pronounced than it would be expected if resonances were well separated in energy. Actually this is a typical characteristic of shape resonances, which correspond to excitations into a well localized quasibound orbital in the continuum, and appear therefore at a rather well defined electron kinetic energy. Actually the maximum of the cross section occurs at slightly different energies (Table 7.2), since dipole excitation from different sites probe different parts of the final continuum, and the width of the resonance, about 7 eV, spreads it over a broad range. In any case this will be a rather general situation so that large cross section variations due to shape resonances shall largely cancel out. It would be different, of course, when comparing BR's of ionisations from different molecules, and the presence of shape resonances should give therefore a very large effect. In the present case, because of the shift in the maximum of the resonance on the photon energy scale due to the chemical shift (Table 7.1), the resonance appears in the BR profile as a curious rapidly oscillating behaviour around 310 eV, which would not be observed on the kinetic energy scale. Apart from the shape resonance, the profiles of the cross sections show interesting differences both at the low energy side, where the C2 cross section shows a significantly deeper minimum, and at the high energy side, where again the C2 cross section has an oscillatory behaviour around the smoother decay of the C1 profile. These are reflected in significant structures in the BR profile: at low energy the largest deviation from the statistical ratio is observed, giving a 1.10 : 0.90 ratio of C1 : C2 1s intensity at about 300 eV, and an oscillatory behaviour at higher energies, which, although reduced, should be still observable up to about 100 eV above threshold, being 1.04 : 0.96 at about 380 eV. A last observation concerns the large difference in β values relative to the two ionisations in the low energy range, which amounts to 1 β unit up to about 20 eV above threshold. This would give a large additional deviation for the cross section ratios if photoelectrons were not collected at the magic angle. For instance, at 18.8 eV one gets βC1 ~ 0.4 and βC2 ~ 1.4. For an observation at 90 degrees, $\cos\theta = 0$, $P_2(\cos\theta) = -1/2$, and this would give for linearly polarized light an additional ratio of 0.8 : 0.3, a very large effect, while for unpolarized light it reduces to 1.1 : 1.35, still significant although less dramatic.

Table 7.2: The minimal basis set GS-LB94 KS eigenvalues (ε, in eV) of the σ valence virtual orbitals of F–C≡C–H, F–C≡C–CH_3, F–C≡C–CN and $F_2C{=}CH_2$. Also reported are the C1–C2 bonds lengths (in Å) obtained from the optimized geometry, the energy position of the resonances (E_r, in eV), the populations of C1 and C2 $2p_z$ orbitals in the valence orbitals involved in the resonant process and the oscillator strengths (f numbers) of the C 1s → V_σ transition.

				E_r		C $2p_z$ population		$F \times 10^2$	
Molecule	Orbital	Bond length	ε	C1	C2	C1	C2	C1 1s	C2 1s
F–C≡C–H	9σ	1.199	4.8					2.90	3.44
	10σ		22.0	17.7	18.5	37.1	37.2	9.49	9.63
F–C≡C–CH_3	11a1	1.200	5.4	1.22		7.1	9.6	1.51	2.06
	12a1		6.1					1.46	1.23
	13a1		22.4	19.3	19.3	36.9	38.7	9.34	10.00
F–C≡C–CN	13σ	1.203	3.4					2.33	3.19
	14σ		15.3	14.1		19.5		4.88	1.15
	15σ		23.4	20.4	20.4	20.5	35.3	5.22	9.60
$F_2C{=}CH_2$	10a1	1.313	5.0					0.26	2.78
	11a1		11.2	5.85	6.7	37.8	36.6	8.42	7.16

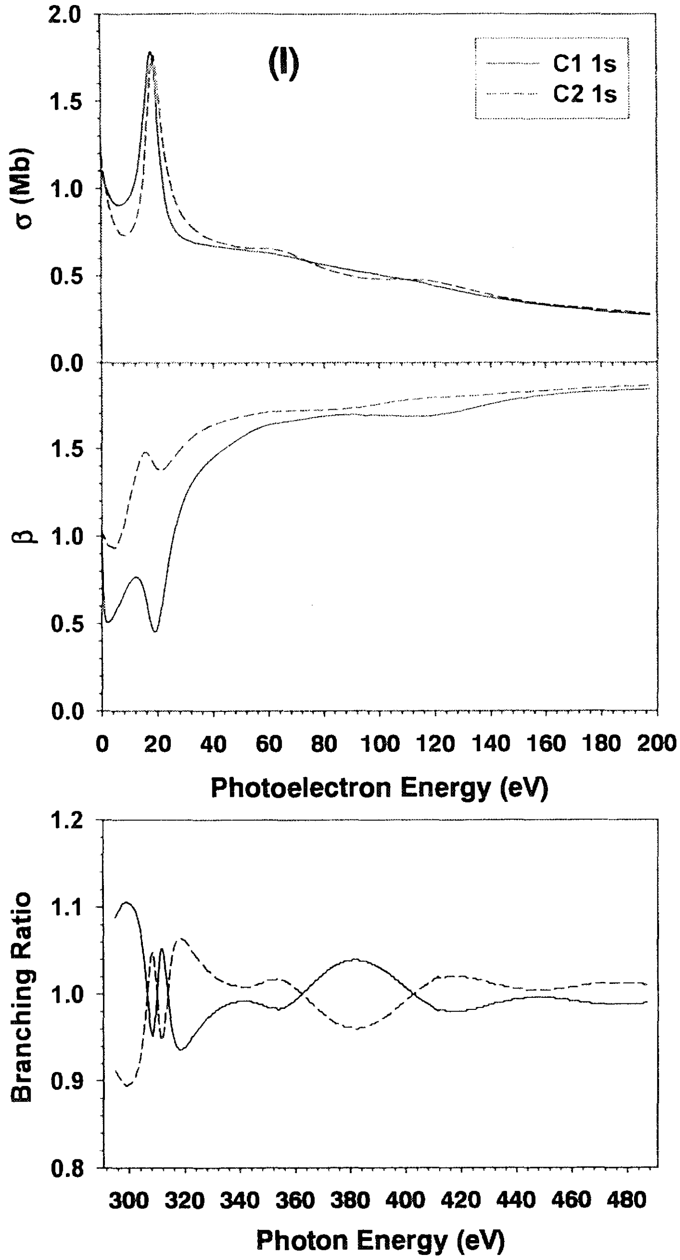

Figure 7.2: The cross section, asymmetry parameter and branching ratio profiles of the C 1s states in fluoroacetylene. The branching ratio profiles are normalized with respect to the number of carbon atoms in the molecule.

FC≡CCH$_3$. The addition of a methyl group has a very modest influence on the cross section profiles of C1 and C2 ionisations (Figure 7.3), although the shape resonance peak shifts significantly, by about 1.6 eV for C1 and 0.8 eV for C2, to higher kinetic energy, as can be seen in Table 7.2. In fact, on the kinetic energy scale, they almost coincide, so that the final shift in photon energy is entirely due to the change in the IP's of C1 and C2. This gives rise to two maxima, separated by 2.4 eV in the BRs of C1 and C2 ionisations, around the shape resonance at 310 eV. In the same region a deep minimum in the BR of the methyl group is apparent, due to the much reduced amplitude of the resonance for this ionisation.

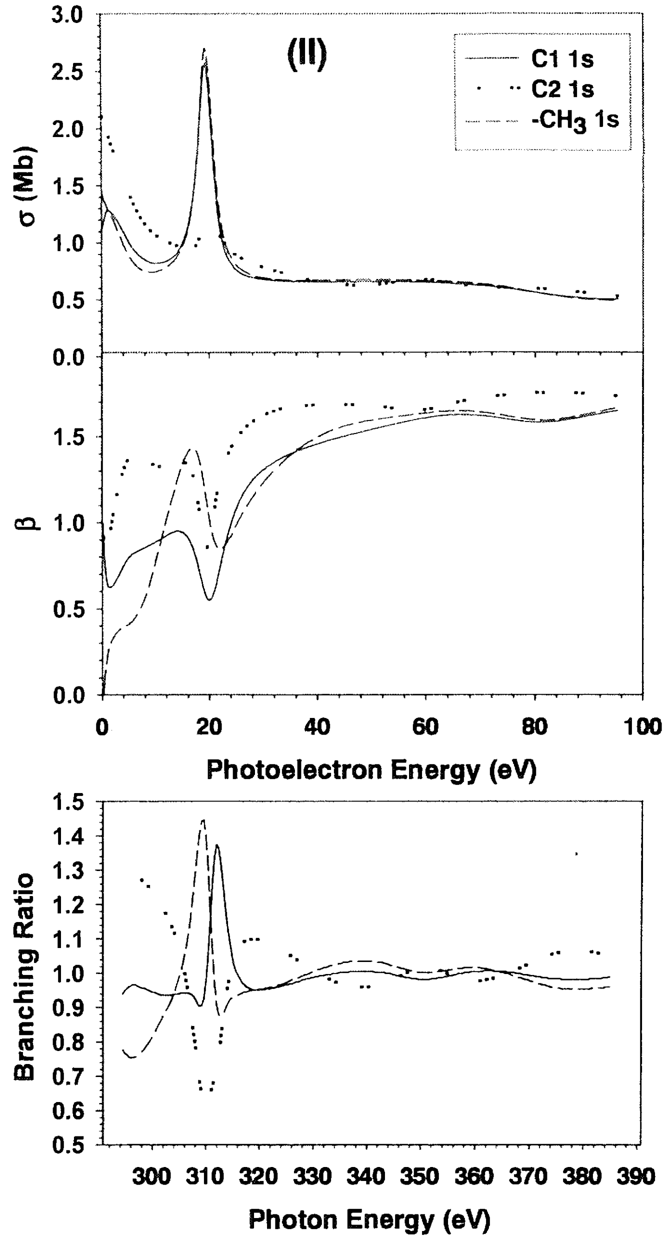

Figure 7.3: The cross section, asymmetry parameter and branching ratio profiles of the C 1s states in fluoromethylacetylene. The branching ratio profiles are normalized with respect to the number of carbon atoms in the molecule.

As expected the cross section profile of the methyl C 1s ionisation is significantly different from those of the acetylenic carbons. Besides the much reduced shape resonance, the cross section is much higher at low energies, below the shape resonance, and after has a marked oscillatory character which shows up in the BR. So its ratio drops from 1.26 at 295 eV to 0.63 at 310 eV, a factor of two, and then keeps oscillating, although with much reduced amplitude. At 380 eV its BR is about 1.09, still 10% above the statistical ratio. The oscillation which appears in the cross section at about 60 eV kinetic energy may be the first term of EXAFS oscillations. Here also β values are significantly different up to about 30 eV above threshold.

FC≡CCN. The substitution of the methyl with a cyano group has a profound influence on the cross sections (Figure 7.4). A second σ^* shape resonance is expected, associated with the –CN group. Curiously the least affected profile is that of C2, directly linked to –CN. Athough the main shape resonance is similar in all three channels, the intensity of C1 is much reduced, while that of –CN carbon is halfway that of the acetylenic carbons. Moreover a second shape resonance, as expected, appears now with much larger intensity at the lower energy side of the main one, both in C1 and –CN ionisations. Although it might be loosely related to the barely visible resonance in the C1 ionisation in $FC{\equiv}CCH_3$, very close to threshold, pushed at much higer energy, an analysis of the continuum orbital involved (see below) shows their different nature. In any case it is apparent that the strong influence of the molecular effective potential on the delocalized photoelectron wave function actually causes important deviations of the cross section profiles, even for very localized initial orbitals as C 1s states and for carbons that, from the classical chemical perspective, should not be dramatically affected from the substitution. Small oscillations are present at larger energies, as before, more marked for the carbon –CN ionisation. The comparison of the 1s cross section profiles associated with the carbon atom of $-CH_3$ and –CN shows another interesting point: the two profiles have completely different behavior at low energies, but at high energies present an oscillation centered, for both of them, at 58.5 eV. An interesting point is if this oscillation could be correlated to the structure FC≡C–, which is common for the two substituents, as this could be a first EXAFS oscillation, as already mentioned.

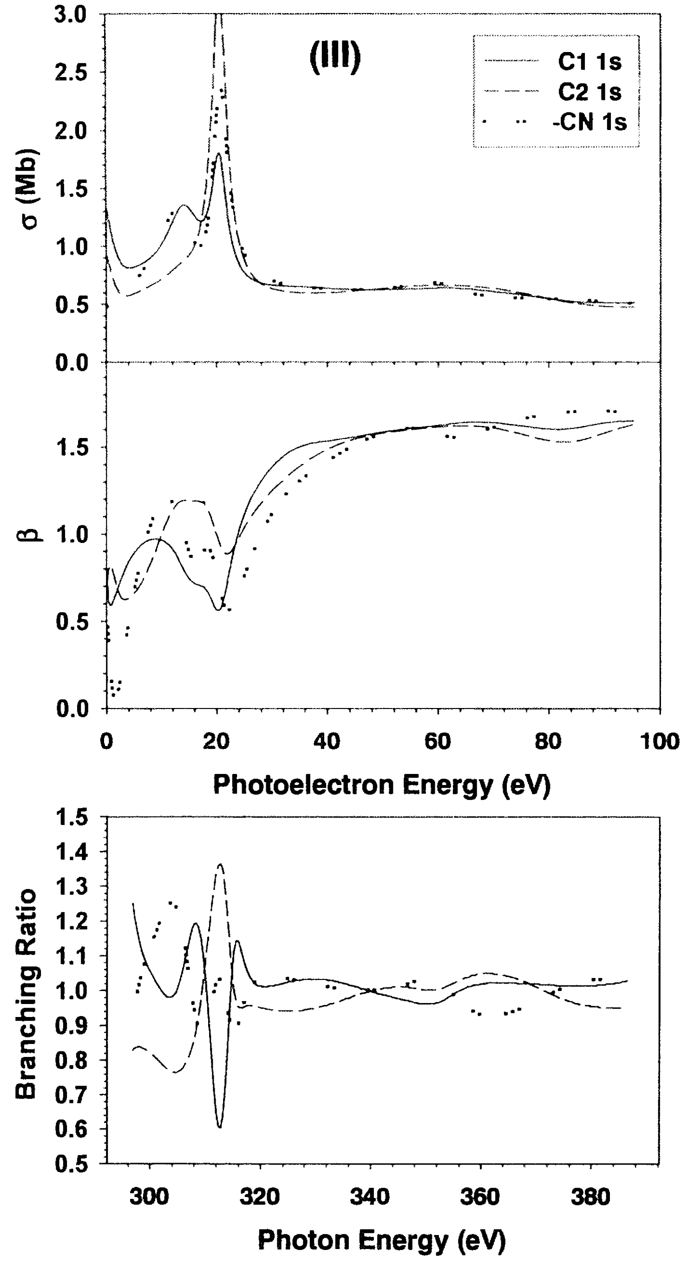

Figure 7.4: The cross section, asymmetry parameter and branching ratio profiles of the C 1s states in fluorocyanoacetylene. The branching ratio profiles are normalized with respect to the number of carbon atoms in the molecule.

The BRs show large deviations from the statistical value up to 315 eV, just past the large shape resonance. At the resonance the C1 BR shows a deep minimum, down to 0.6, surrounded by two maxima. Also the other two BRs are very structured, although the small chemical shift computed may prevent individual deconvolution of the relevant peaks. At higher energy usual oscillations of moderate amplitude are present.

The calculated ionisation potentials (Table 7.1) indicate that the shift between C2 and –CN (C2 and $-CH_3$ in **(II)**) is quite small. It is worth stressing the possible usefulness of taking into account the significant differences between the branching ratios of the C2 and –CN carbon ionisations in the region 295 – 320 eV, for the assignment of the peaks and a correct deconvolution of the spectra. When two peaks are superimposed in the experimental photoelectron spectra often a single, broad and featureless peak is apparent. To resolve the peaks in a standard fitting procedure usually the signals of the two different carbons are constrained to have the same area [3]. Inclusion of the theoretical ratio in the fitting procedure could be employed to obtain a more accurate deconvolution, and the degree of agreement obtained could give a strong support to the assignment of individual ionizatons under the same band.

$F_2C=CH_2$. The results depicted in Figure 7.5 show that also in this molecule C 1s cross sections are dominated by the strong σ^* shape resonance, which appears at much lower energy than in the substituted acetylenes. The detailed profile of the resonance is significantly different between C1 and C2, and moreover the C1 profile shows important oscillations up to about 100 eV above threshold. This is reflected in the BRs, which show a strong oscillatory character not only at the shape resonance, around 302 eV, but also at higher energy, with C1 BR dropping to about 0.88 at 335 eV and rising to about 1.08 at 365 eV.

$CF_3COOCH_2CH_3$. This molecules has been a historic show case for chemical shifts and spectrometer resolution, since the first observation of four well resolved peaks by Siegbahn and coworkers, and a beautiful fully resolved ESCA spectrum [2]. The large chemical shifts of all four carbon ionisations, allowing a complete separation of the peaks, makes it an ideal candidate for an accurate study of the BR behaviour. Moreover the four carbons have a quite different chemical environment, and one could expect this to be reflected in their cross sections and BRs profiles. The latter appear very close to the statistical ratio in the high energy XPS spectrum [2] at 1487 eV.

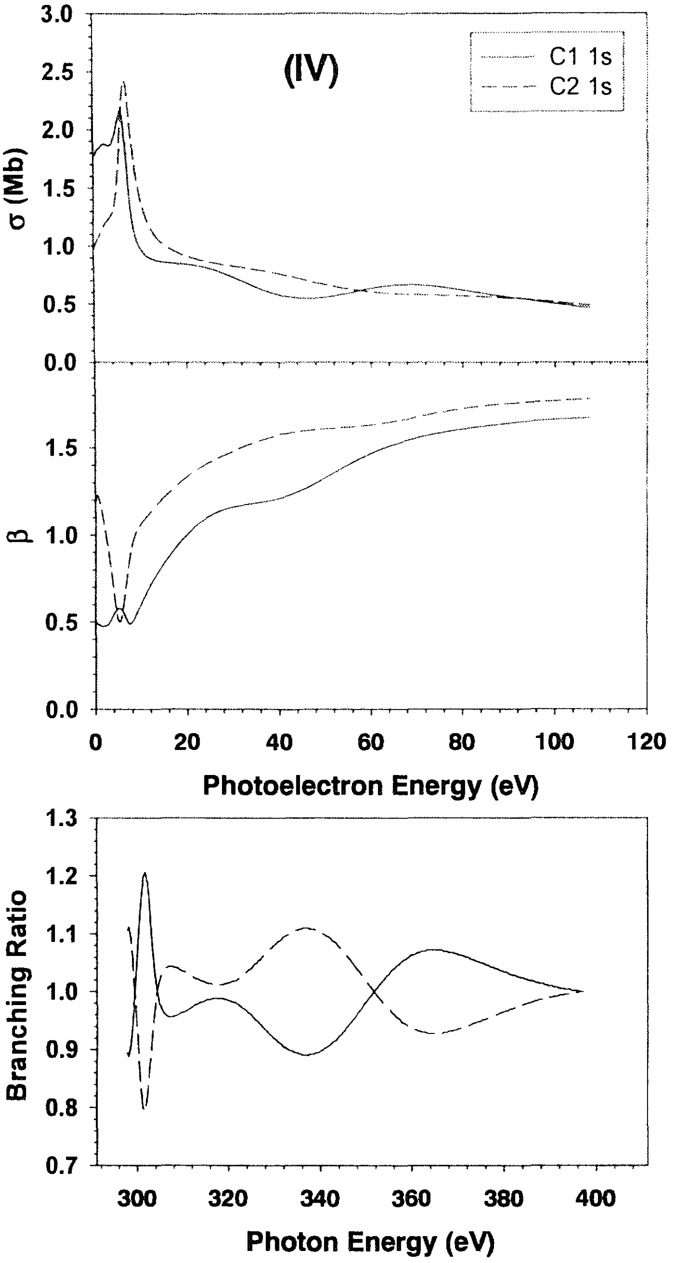

Figure 7.5: The cross section, asymmetry parameter and branching ratio profiles of the C 1s states in (1,1)difluoroethene. The branching ratio profiles are normalized with respect to the number of carbon atoms in the molecule.

The cross sections reported in Figure 7.6 show indeed strongly different profiles in the low energy range. The C2 (carbonyl) ionisation is dominated by two very sharp shape resonances close to threshold, which are also seen, although much reduced, in the C1 (CF_3) profile. The latter has distinctly lower cross section up to rather high energy, around 50 eV above threshold, where it crosses the others and then stays consistently higher up to around 80 eV kinetic energy. The two C3 (–CH_2–) and C4 (–CH_3) profiles are much more similar, and indeed similar to the C 1s profile in CH_4 [9], do not show the shape resonant behavior (although it is still apparent in the β profile for C3), but show out of phase oscillations better seen in the BR profiles.

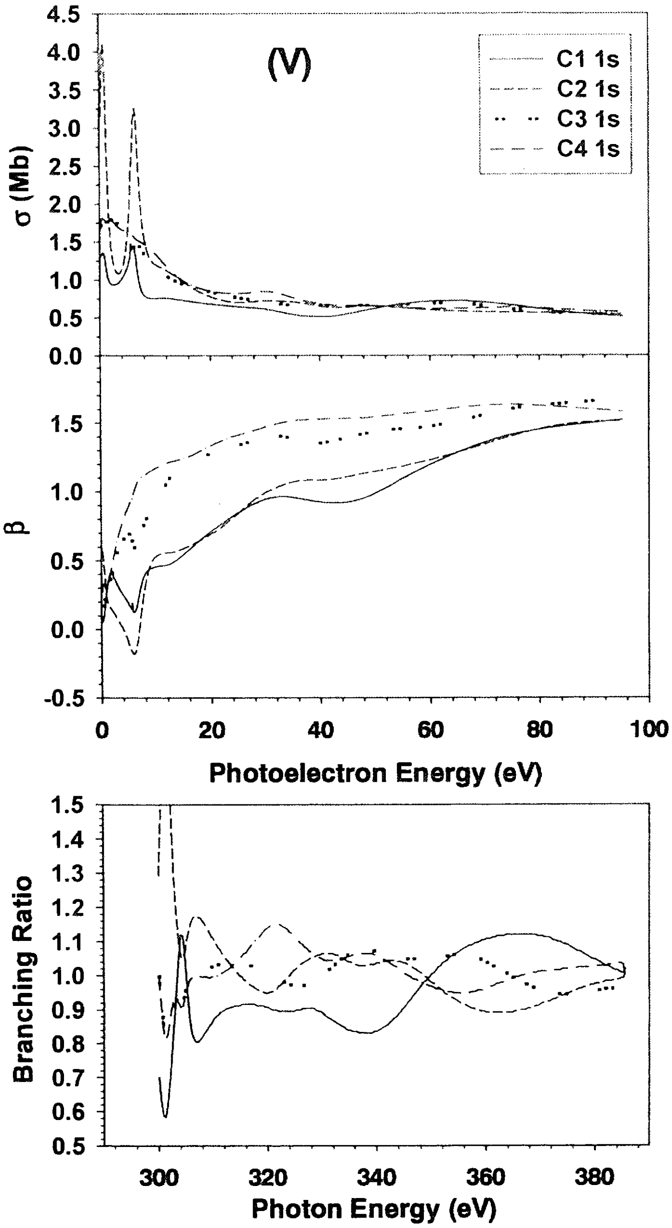

Figure 7.6: The cross section, asymmetry parameter and branching ratio profiles of the C 1s states in ethyl trifluoroacetate. The branching ratio profiles are normalized with respect to the number of carbon atoms in the molecule.

Close to threshold the BR's are dominated by the huge resonant peaks of C2, which may be however difficult to observe, at low kinetic energy. Above about 305 eV all BRs oscillate. For instance C1 stays lower by 10% of the statistical ratio up to about 345 eV, with minima around 0.80 at about 306 and 338 eV, and then goes up to about 1.12 around 365 eV. So the C1/C2 ratio varies by ± 25% along the energy range considered.

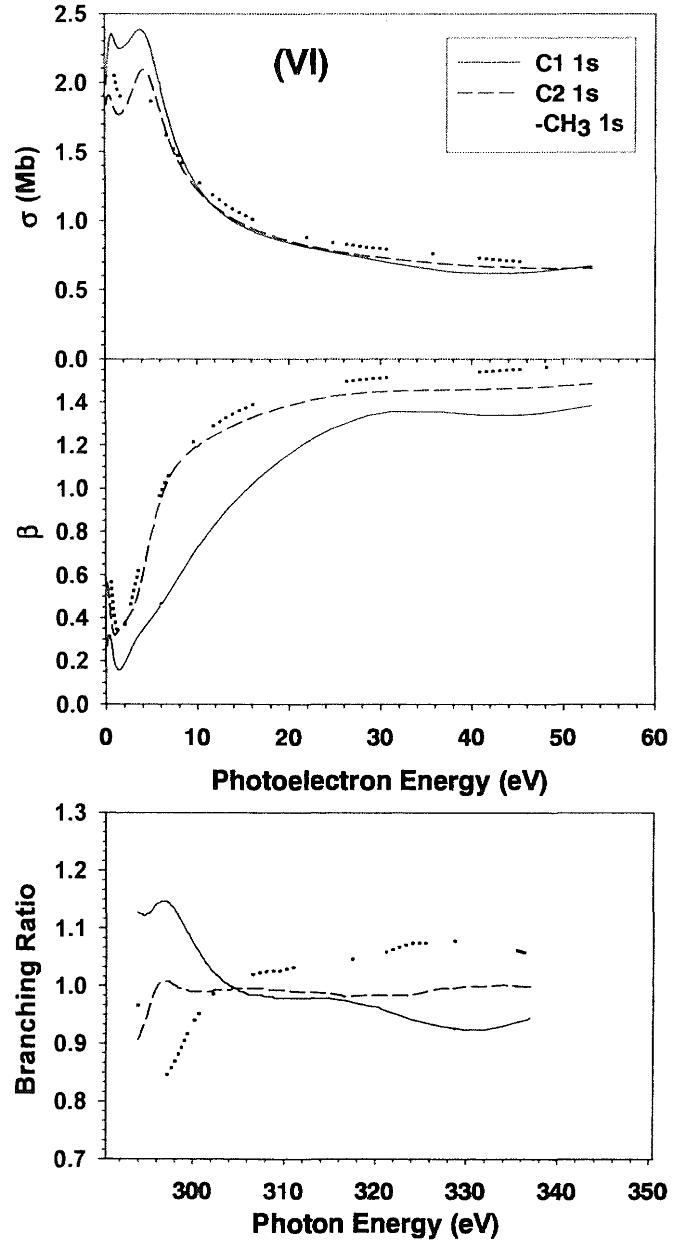

Figure 7.7: The cross section, asymmetry parameter and branching ratio profiles of the C 1s states in methyloxyrane. The branching ratio profiles are normalized with respect to the number of carbon atoms in the molecule.

CH_2OCHCH_3 (VI). It was this molecule that actually drew our attention to this problem, when a preliminary XPS spectrum at 300 eV was obtained by Avaldi et al. [36], showing a marked deviation from the statistical ratio. Methyloxirane has already been investigated in connection with circular dichroism in photoemission from chiral molecules [23]. From Figure 7.7 it is possible to notice that because of shape resonances close to threshold, both the C1 and $-CH_3$ C 1s ionisations show marked deviations from the statistical ratio in the low energy range, where the $-CH_3$ BR is distinctly lower. Although the two ring ionisations C1 and C2 are very close (we compute about 0.2 eV shift, with C1 at higher IP, ab-initio KT results in [37] give 0.06 eV with C2 lying higher) and cannot probably be disentangled, the $-CH_3$ peak at 300 eV has significantly lower intensity than half the sum of two unresolved C1, C2 ionisations, with a BR of 0.75, in good agreement with present results. We predict this ratio to reverse at higher energy, with $-CH_3$ BR being almost 10% higher than the statistical ratio around 330 eV.

7.4.3 Shape Resonance Characterization in F–C≡C–R and F_2C=CH_2.

The aim of the present section is to discuss the origin and the nature of the resonances that appear in the C 1s cross section profiles of the fluoroacetylene series and (1,1)difluoroethene. The cross section profiles of C1 and C2, together with the partial channel contribution for C1 in FC≡CH, are reported in Figure 7.8. From the partial channel contribution it is clear that the resonance originates from the 1s → kσ partial channel, as is well known in acetylene and ethene [19,38,39], and the same behaviour is shown for C1 and C2 in all molecules. This can be interpreted as a $\sigma \rightarrow \sigma^*$ transition, involving a valence antibonding σ^* orbital, correlated with the position and strength of Mulliken N → V_σ charge-transfer excitation [40]. In accordance with Mulliken's molecular-orbital-based analysis of molecular spectra [41] the virtual valence orbitals are obtained from minimal-basis-set calculation. We have therefore performed additional GS-LB94 single-zeta (SZ) minimal basis calculation for the molecules mentioned in this section. In Table 7.2 are reported the energy position of the resonances, the eigenvalues of the valence virtual orbitals with σ symmetry above the threshold, the populations of C1 and C2 $2p_z$ orbitals, and the oscillator strengths of the relevant transitions. In Figure 7.9 are displayed the contour plots of these virtual valence orbitals. In Figures 7.10 and 7.11 are reported the plots of the so called "dipole prepared" continuum orbital [42] for the C2 1s → kσ and C1 1s → kσ channels, respectively, calculated at the photoelectron kinetic energy of the shape resonances.

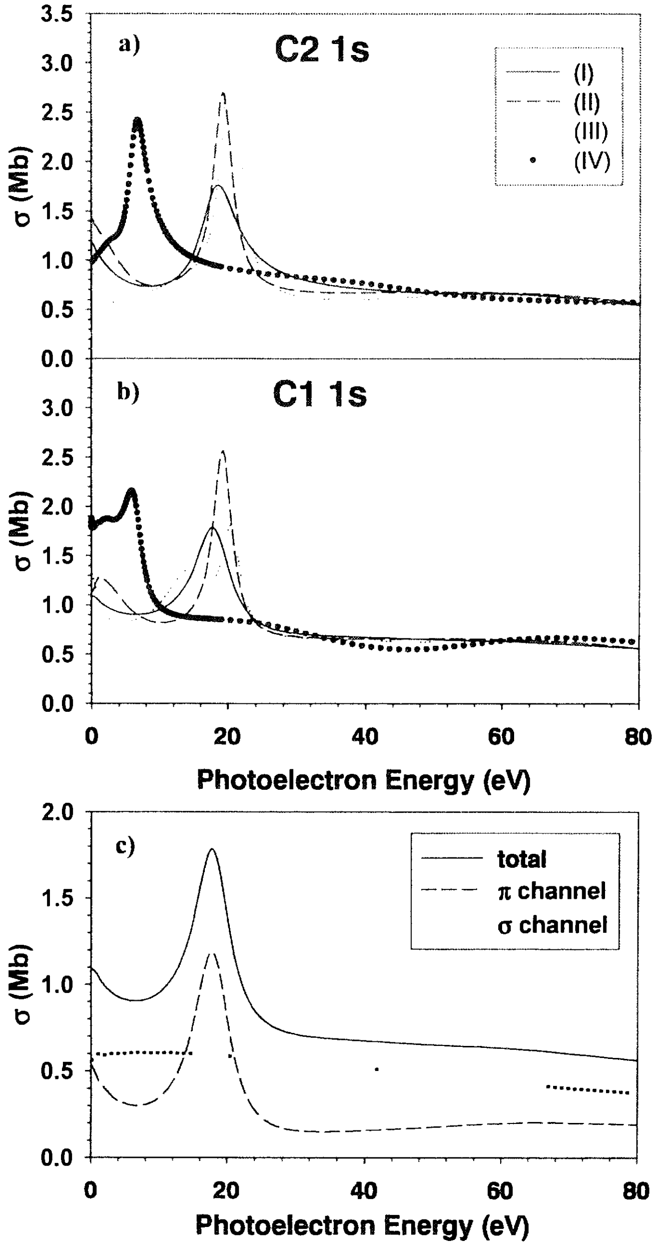

Figure 7.8: **(a)** The cross section and asymmetry parameter profiles of the C2 1s state in F–C≡C–R (R = H **(I)**, CH_3 **(II)**, CN **(III)**) and in $F_2C{=}CH_2$ **(IV)**. **(b)** The cross section and asymmetry parameter profiles of the C1 1s state in F–C≡C–R (R = H **(I)**, CH_3 **(II)**, CN **(III)**) and in $F_2C{=}CH_2$ **(IV)**. **(c)** The C1 1s total and partial-channels cross section profiles in fluoroacetylene.

It is important to underline the limitation of the shape resonance interpretation in terms of virtual valence orbitals obtained by SZ calculation. Specifically, not all virtual orbitals will correspond to shape resonances and not all shape resonances will correspond to virtual orbitals. In the present analysis one does find, however, that many, if not most, virtual orbitals and shape resonances have a one-to-one correspondence.

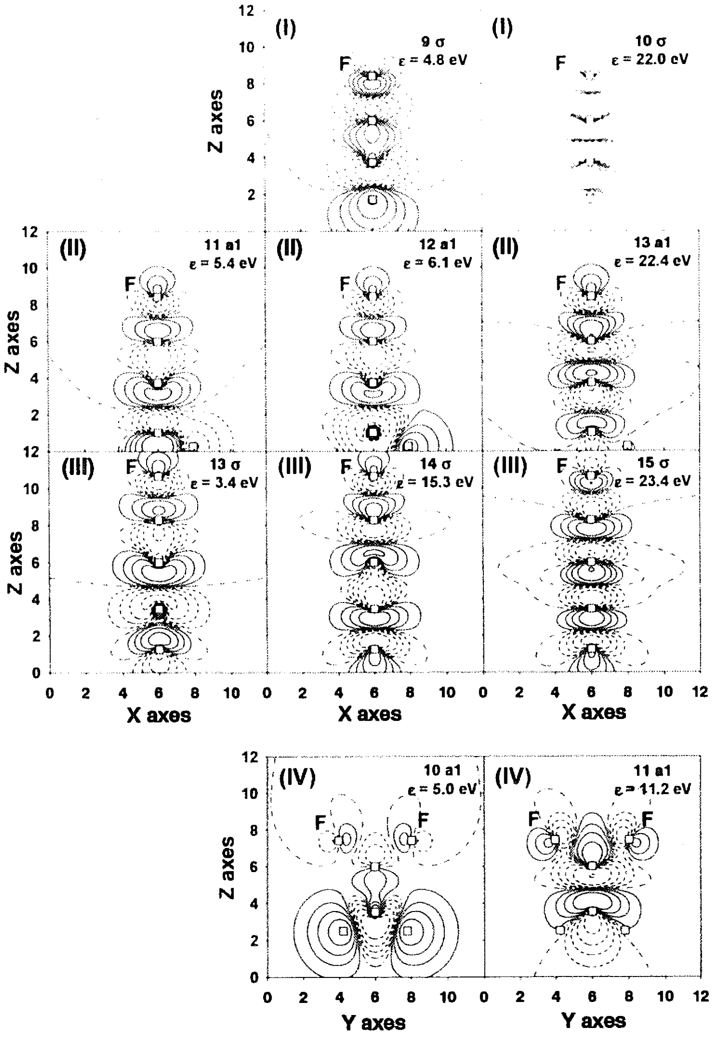

Figure 7.9: Contour plots relative to some SZ-LB94 KS eigenvalues of F–C≡C–R (R = H **(I)**, CH_3 **(II)**, CN **(III)**) and in $F_2C{=}CH_2$ **(IV)**. Side in atomic units, solid line positive contribution, dash line negative contribution, dash-dotted line zero contribution (nodal line). The white square symbol (□) correspond to the position of the atoms. Axes are explicitly given in the figure.

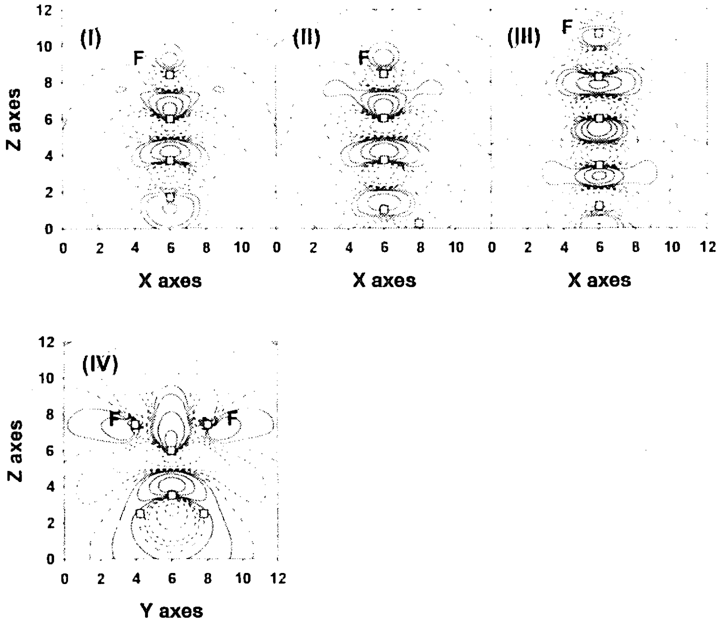

Figure 7.10: Contour plots relative of the final continuum orbitals for the C2 1s → kσ ionisation channel in F–C≡C–H **(I)**, F–C≡C–CN **(III)**, and for the C2 1s → ka1 ionisation channel for F–C≡C–CH$_3$ **(II)**, F$_2$C=CH$_2$ **(IV)**, obtained at the photoelectron kinetic energies reported in the figure and corresponding to the resonance structures in the C2 1s cross section profile (Figure 7.8a).

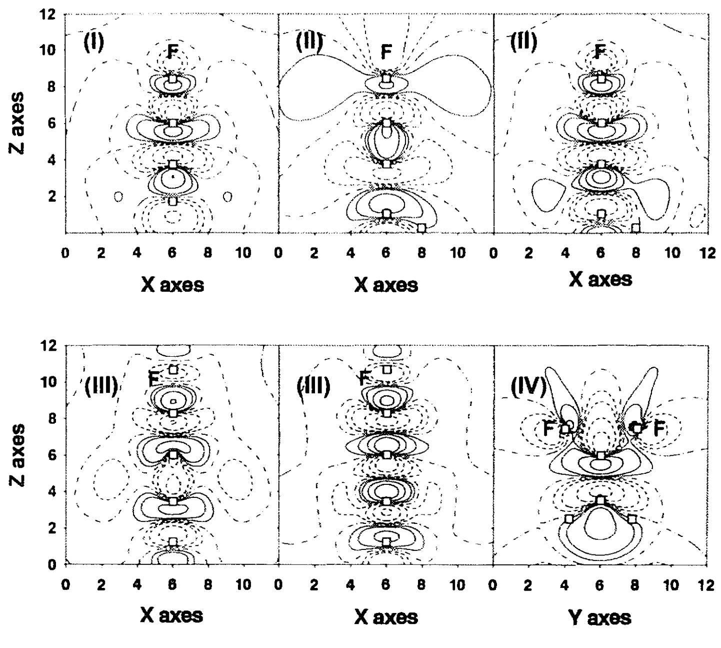

Figure 7.11: Contour plots relative of the final continuum orbitals for the C1 1s → kσ ionisation channel in F–C≡C–H **(I)**, F–C≡C–CN **(III)**, and for the C1 1s → ka1 ionisation channel for F–C≡C–CH$_3$ **(II)**, F$_2$C=CH$_2$ **(IV)**, obtained at the photoelectron kinetic energies reported in the figure and corresponding to the resonance structures in the C1 1s cross section profile (Figure 7.8b).

We start the analysis of the shape resonances with the C2 1s cross section profile, displayed in Figure 7.8a. In the fluoroacetylene molecular series, all three molecules show a distinct resonance structure positioned around 20 eV above the threshold. The analysis of the SZ states reported in Table 7.2 shows, for all three molecules, the presence of a valence orbital positioned 20 eV above the threshold with σ* character along all bonds. To verify if these virtual valence orbitals are effectively involved as quasi-bound states in the resonant process, we compare their countor plot, in Figure 7.9, with the countor plot of the "dipole prepared" continuum orbitals for C2 1s states, in Figure 7.10. In fluoroacetylene the orbital 10σ shows an anti-bonding character along all atomic bonds, with strong $2p_z$ component for all the atoms but hydrogen. The contour plot of the final continuum orbital for the C2 1s → kσ channel, obtained at the kinetic energy of the resonance structure (18.50 eV) has a very similar profile to the 10σ orbital, explaining the presence of the shape resonance in the C2 1s cross section profile in terms of charge-transfer excitation involving the virtual valence orbital 10σ. The same holds true in fluoromethylacetylene for the 13a1 orbital, and in fluorocyanoacetylene for the 15σ orbital. Also in (1,1)difluoroethene the comparison with the dipole prepared orbital clearly identifies the 11a1 valence orbital as associated with the resonance. In this case this might not have been obvious on purely energy grounds, since the resonance energy (6.67 eV) is closer to the eigenvalue of the 10a1 orbital (5.0 eV) than to the 11a1 one (11.2 eV). While in all cases resonance position is shifted to lower energy from the corresponding orbital eigenvalue, the lowering is much larger in (1,1)difluoroethene compared with the fluoroacetylene molecules **(I,II,III)**. This result demonstates the usefulness of the analysis of the "dipole prepared" continuum wavefunction to characterize and assign the shape resonances in terms of virtual valence orbitals.

In all cases the shape resonances in the C2 1s cross section can be properly described in terms of virtual valence orbitals of σ* character along the C1–C2 bond with considerable participation of $2p_z$ atoms component which can be correlated to C2 1s → V_σ charge-transfer excitation, as observed in previous dynamical photoionization studies on acetylene and ethene [19,38,39]. Furthermore the kinetic energy position of the C 1s shape resonance in the hydrocarbons is similar to the C2

1s resonance position in the corresponding substituted molecules. This suggests that the C2 1s shape resonance of the substituted acetylene molecules could be ascribed to the chromophoric –C≡C– bond, while the C2 1s shape resonance of (1,1)difluoroethene could be ascribed to the chromophoric –C=C– bond.

In the C1 1s profiles (Figure 7.8b) the shape resonance positioned near 20 eV for the series $F{-}C{\equiv}C{-}R$, as well as the resonance at 5.85 eV in $F_2C{=}CH_2$ can be described in terms of the excitation into the same σ^* valence virtual orbital, as confirmed by the contour plots in Figure 7.11. At variance with C2 1s, the cross section profile of C1 1s state in fluoromethylacetylene and in fluorocyanoacetylene shows a second less pronounced shape resonance, closer to the threshold. For fluoromethylacetylene the contour plot of the final continuum function at the resonance position (1.22 eV) is closer to the 11a1 orbital, although both 11a1 and 12a1 virtual orbitals show σ^* character along the C1–F, C2–CH_3, C–H bonds and σ character along the C1–C2 bond, as in the dipole prepared orbital. For fluorocyanoacetylene the characterization of the shape resonance at 14.1 eV is clearcut. Both the eigenvalue position and the contour plot of the orbital 14σ (Figure 7.9) show that it is the virtual state involved in the continuum resonance. An analysis of the kσ orbital at 14.10 and 20.40 eV (Figure 7.11), or the corresponding 14σ and 15σ orbitals, shows that they can be well characterized as approximate symmetric and antisymmetric combinations of the two σ^* orbitals from the CC and CN moieties. This offers also an interesting explanation of the different resonant behaviour of the three C1s ionisations. The C2 atom is at the approximate center of the molecule, so that the C2 1s orbital has "g" symmetry, and the same the resonance at 14.10 eV, which is then dipole forbidden. The "u" resonance at 20.40 eV is correspondingly enhanced. On the contrary both C1 and C3 have no definite symmetry, and both resonances are excited. In the same vein, the weak resonance at 1.22 eV in FCCCH3 looks like a bonding combination of σ^* CF and CCH3 orbitals, (C1-C2 bonding). Also in this case the resonance is suppressed in C2, and apparent in C1.

In Figure 7.8 it is possible to notice that the maximum position of the main C 1s shape resonance both for C1 and C2 moves drastically to lower energies for the larger bond length $F_2C=CH_2$ with respect to the molecular series F–C≡C–*R*, analogously to what happens for the carbon 1s shape resonance for acetylene and ethene. The dependence of the continuum resonance on the C–C bond length is in fact related to a shape resonance with σ* C1–C2 character. The smaller variations within the fluoroacetylene series show instead no correlation (it is actually of the opposite sign) with bond lengths, which are essentially constant along the series and are therefore a purely electronic effect. Actually the behaviour is fairly well reproduced by the trend in the σ* virtual eigenvalues, which generally overestimate the resonance energy by 3-4 eV for F–C≡C–*R* and about 5 eV for $F_2C=CH_2$. In fact even eigenvalues cannot explain the fact that the resonance shows at a different energy in C1 and C2 channels in some molecules, a more subtle electronic effect, which may be tied to the different probing of the continuum orbital by the dipole transitions from different core orbitals.

Comparing the C1 1s and C2 1s shape resonances positioned near 20 eV for the molecular series F–C≡C–*R*, it is possible to notice that for R = –H, $-CH_3$ the intensity of the resonance structure does not change significantly, while for R = –CN it changes quite dramatically, being much more intense in the C2 1s cross section profile. The intensity variations correlate very well with both oscillator strengths and C $2p_z$ populations evaluated at the SZ model, which can be used to rationalized the data, and shows also the direct information available from experimentally observed intensity changes in shape resonances, as a mean to monitor orbital composition of unoccupied virtual orbitals. In fact it predicts well the almost constant intensity relative to C2 excitation, the equality of C2 and C1 intensity in all molecules, and the splitting of the C1 resonance into two components, the one at lower energy of lower intensity, observed in fluorocyanoacetylene. Also some finer details like a slight increase in the C2 relative to C1 intensity in F–C≡C–CH_3 with respect to strict equality in F–C≡C–H is correctly reproduced.

7.5 Conclusions

It has been demonstrated that cross section variations induce strong non statistical behavior of the Branching Ratios relative to core ionisations up to several tens of eV above threshold. This phenomenon appears completely general, and adds to the non statistical ratios which may be associated with many-body excitations, which survive in the high energy limit. The importance of core Branching Ratios, an observable which should be easily attainable experimentally, both as a tool for structural determination and for spectral assignment, and for a correct quantitative analysis and spectral deconvolution, is pointed out. The nature of the strong shape resonant effects in the C 1s cross sections of the molecules considered has been analyzed in detail, and the energy and intensity variations interpreted in the framework of the nature of the σ^* antibonding valence orbitals associated with the final state.

8 Development of a Methodology for the Localisation and Characterisation of Shape Resonances

Shape resonances are rather common phenomena appearing in the continuum spectra of a large class of molecule but their rationalisation is still under debate by the photoionization and scattering community. In the present work a methodology to localise and characterise in molecular terms the shape resonances in the framework of the B-spline Density Functional Theory approach is presented. Starting from a benchmark system the development of the methodology is outlined and the extension to the molecular case is considered. Finally the method is applied to localise and the characterise the "textbook" shape resonances in the photoionization of core and valence σ_g orbitals in N_2.

8.1 Introduction

Shape resonances are above-threshold continuum resonant processes commonly observed in molecules, both isolated and adsorbed on surfaces. Shape resonances produce many unusual features in molecular photoionization, including maxima in cross section profile, rapid variations in photoelectron angular distribution, and non-Franck–Condon effects in vibrationally resolved spectra [1]. Molecular shape resonances are usually ascribed to a one-electron continuum state phenomenon in which the ejected electron is resonantly trapped by a potential barrier through which it eventually tunnels and emerges in the continuum [1,2]. Over the last few decades, this basic resonant mechanism has been receiving a prominent interest in molecular photoionization area.

The expanding interest in shape resonant phenomena arises from a few key factors. *First*, shape resonant effects are being identified in the spectra of a growing and diverse collection of molecules. *Second*, being quasi-bound inside a potential barrier on the perimeter of the molecule, such resonances are localized, have enhanced electron density in the molecular core, and are decoupled from the external environment of the molecule. Consequently this resonance effects appear both in free and adsorbed molecules and one of the most challenging applications of shape resonances is the determination of molecular orientation on surface from analysis of the angle-dependent resonance intensities [4]. *Third*, the predominantly one-electron nature of the phenomena lends itself to theoretical treatment by realistic, independent-electron methods.

Although the model for shape resonances based on the potential barrier concept is physically correct, it is not suitable either in finding out correlations between shape resonances and electronic/structural properties of molecules, or in predicting the number and position of shape resonances.

A second model more connected with the chemical aspects of shape resonances has been proposed by Langhoff [5]. Resonance structures that appear in the molecular continuum spectra are interpreted as transition involving valence-like, antibonding virtual orbitals (VOs), placed above ionisation threshold. In accordance with Mulliken's molecular-orbital-based analysis of molecular spectra [6], VOs are obtained from minimal-basis-set calculation. Despite its simplicity, this method has proven to be rather useful for resonance interpretation in a remarkable number of small molecules [7], but also for rationalisation of the so-called bond-lengths-with-a-ruler method, where an empirical relationship has been proposed between the energy position of a shape resonance relative to the ionisation potential and the bond length between the excited atom and its neighbour(s) [8]. However, a detailed analysis of the experimental evidence shows that not all VOs will correspond to shape resonances and not all shape resonances can be associated to transition towards VOs.

At last it is worth mentioning the explicit analysis of the continuum wave function at the photoelectron energies relevant for the structures in the cross section profiles, by means of the B-spline DFT method [9,10]. In principle, the continuum wave function has an infinite degeneracy due to all the possible directions of the momentum k of the photoelectron. Working with a finite basis set the degeneracy is no longer infinite but remains high since it is equal to the number of the open channels which obey the asymptotic continuum boundary conditions. However, it is still possible to remove the degeneracy employing the so-called dipole-prepared continuum orbitals [11], which are obtained by performing a unitary transformation on the degenerate set in order to extract only one orbital which will carry all the cross section. This method has proven to be very useful in a rather large class of molecules [11-14] to characterise in molecular terms the shape resonances and to show the localisation of the resonant continuum wave function within the molecular region, but still represents a qualitative approach to the problem. In fact, the knowledge of the maximum positions in the cross section profile is necessary and only analysis *a posteriori* is possible.

The aim of the present work is to design a methodology to localise and characterise in molecular terms the shape resonance profiles, always in the framework of the B-spline DFT approach. Based on the observation that the inner part of the scattering wave function, at an energy in the resonant region, very much looks like the wave function of the bound state [15], the development of a method to study shape resonances considered, as a starting point, the following basic ideas:

- Determination of the VOs that could be associated to the resonances and calculation of shape resonance positions by means of the stabilization method.
- Analysis of VOs contribution to the resonant final state through analysis of the norm of the projection of continuum wave function on the VOs.

As an initial approach we have considered a single-channel model photoionization problem, which is easier to be handled than a real molecular case. In Sec. 8.2 the model potential and the numerical methods employed are presented. Starting from this benchmark system the development of a simple model for the characterisation of the shape resonances is outlined in the first part of Sec. 8.3. The extension of the method to the molecular B-spline DFT code and its application to the shape resonance that arise in the photoionization of core and valence σ_g orbitals are finally considered.

8.2 Model Potential and Methods of Solution

As a starting point we shall confine ourselves to a model photoionization problem [16] where the potential is defined by

$$V(r) = \begin{array}{ll} -V_0, & 0 \le r \le a_0 \\ V_b, & a_0 \le r \le 1.2a_0\ , \\ 0, & r > 1.2a_0 \end{array} \tag{8.1}$$

where the well potential V_0 and the barrier height V_b are arbitrary. The expression for the photoionization can be written in the form

$$\sigma(E) = \frac{2}{3}\pi^2 \alpha a_0^2 (E - E_0) \left| \langle \Psi_0 | r | \Psi_k^-(E) \rangle \right|^2 \tag{8.2}$$

Here α is the fine-structure constant (1/137), a_0 is the Bohr radius, E_0 and Ψ_0 are the energy and eigenfunction of the ground state, E and $\Psi_k^-(E)$ is the energy and eigenfunction of the photoelectron.

Determination of bound and continuum states of the model system (8.1) is performed numerically. The eigenstate of the radial Schrödinger equation corresponding to the Hamiltonian of the model potential (8.1) are expanded in terms of B-spline functions [17] over the interval $[0, R_{MAX}]$. A linear grid with step size of 0.05 a.u. supplemented with additional knots near the discontinuity of the potential barrier, in order to make the basis more flexible, and B-splines of order 9 are employed through all calculations on the model system (8.1).

The bound states of the system are obtained by means of a generalized diagonalization of the Hamiltonian matrix. Continuum states are extracted at any selected energy E employing a general least squares approach [18] and normalised fixing the asymptotic amplitude of the numerically calculated radial wave function $R_{El}(r)$ as follows [19]:

$$R_{El}(r) \xrightarrow[r\to\infty]{} \left(\frac{2}{\pi k}\right)^{1/2} \frac{\sin(kr - l\pi/2 + \delta_l)}{kr} \tag{8.4}$$

8.3 Results and Discussion

To test the correctness of the implementation outlined in the previous section, applications are reported in the case of the lowest p-wave resonance arising from the photoionization of the s ground state of the model system (8.1). In Fig. 8.1 are shown the cross sections for a well depth of 5 a.u. and various barrier heights (V_h = 5, 10, 20, 40, 80 a.u.). As may be seen, perfect agreement is displayed between represent the analytic solutions (lines) and our numerical results (symbols). It is possible to notice that the line centers move monotonically to higher energy with increasing value of V_h.

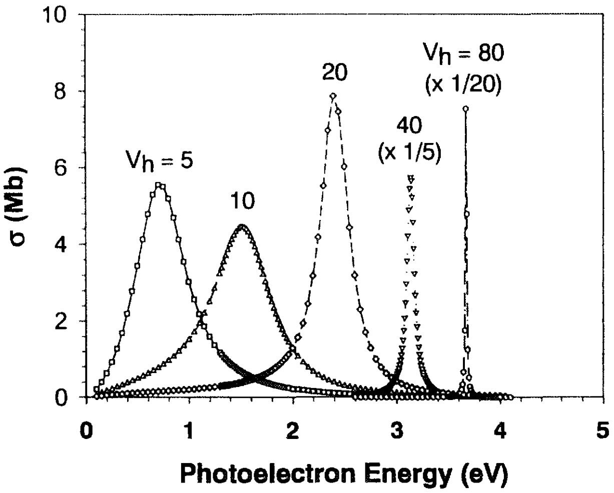

Figure 8.1: Cross section for photoionization of the ground state of the potential of Eqt. (8.1) for V_0 = 5 a.u. and V_h = 5, 10, 20, 40, 80 a.u.. Note that the two very narrow lines profiles (V_h = 40, 80 a.u.) have been reduced by appropriate factors (1/5 and 1/20, respectively) in order to fit conveniently on the figure.

8.3.1 The Stabilization Method

One of the most simple and general procedure that has appeared in literature to detect resonances is the stabilization method [15,20-22]. In stabilization calculations one usually performs a variational treatment within a basis set $\{\chi_i(\tau)_{i=1,\dots,N}\}$ depending upon a parameter τ, which is then varied. This parameter can be a scaling factor in the basis and/or the size of the box the system in enclosed in.

The treatment discretizes the continuum energy spectrum and yields L^2-integrable representations for the corresponding wave function. Unless a resonant, quasi-bound state is present, the "continuum" energies obtained vary with τ. On the other hand, a near constancy, or stability, often appears for the eigensolutions representing resonant states. An heuristic explanation for the slow variation of stable eigenvalues follows from the fact that resonant wave functions are mostly localised in a region of configuration space, so that their energies are less sensitive to variations of τ than ordinary continuum ones. Hence, an eigenvalue E_n that varies little with respect to τ is taken as approximating a resonance energy in the cross section profile, while the n-th eigenvector is considered as an approximation of the resonant continuum wave function. The method consists, therefore, in the solution of a secular equation for the Hamiltonian in the chosen representation, for several values of τ. Relatively to the implementation discussed in the section 8.2, the parameter τ is given by R_{MAX}, which represents the box size where the system is enclose in.

In Fig. 8.2 the stabilization graphs for the p-states associated with a well depth of 5 a.u. and barrier heights V_{HF} = 10, 40 a.u. are displayed. Results show that a stabilization pattern appears only if the barrier is high enough. In fact, a standard variational behaviour is displayed by the p-states associated with V_h = 5, 10 a.u. [see Fig. 8.2(a)]. On the other hand when V_h = 20, 40, 80 a.u. a plateaux is clearly visible in the stabilization graph [see Fig. 8.2(b)] and the energy corresponding to the "stable" behaviour of the eigenvalues well approximates the resonance energy in the cross section profile (see Fig. 8.1), as summarised in Table 8.1.

Table 8.1: Comparison of the exact (see Fig. 8.1) and approximated (see Fig. 8.2) energy resonance position for V_0 = 5 a.u. and V_h = 20, 40, 80 a.u.

V_h (a.u.)	E^r exact (a.u.) (cross section profile, Fig. 8.1)	E^r approximated (a.u.) (stabilization graph, Fig. 8.2)
20.	2.40	~ 2.4
40.	3.14	~ 3.2
80.	3.67	~ 3.7

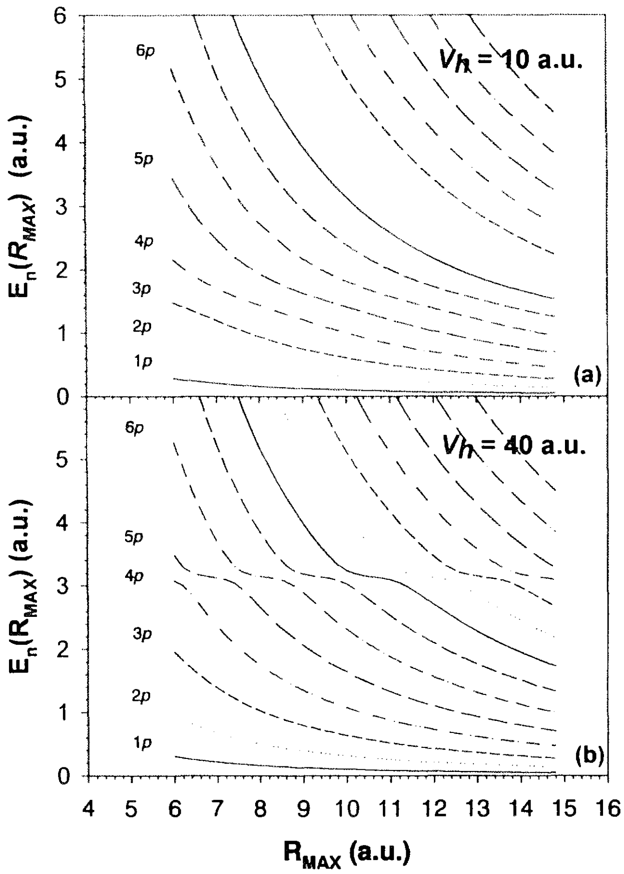

Figure 8.2: Stabilization graphs for the p-states of the model system (8.1) with a well depth of $V_0 = 5$ a.u. and barrier height $V_h = 10$ (a), 40 a.u. (b).

Relatively to the potential barrier $V_h = 40$ a.u., a plot of the continuum resonant wave function ($E^r = 3.14$ a.u.) and of the stabilized one, $6p$, corresponding to $R_{MAX} = 8.0$ a.u. ($E_{6p} = 3.12$ a.u.) is presented in Fig. 8.3. The continuum wave function has been arbitrarily normalised so that its amplitude corresponds to the amplitude of $6p$ at the first maximum. Figure 8.3 clearly shows that, apart from the arbitrary normalisation factor, the square-integrable eigenfunction ($6p$ in this case) associated with a "stable" eigenenergy is a good approximation to the inner part of the exact resonant photoelectron wave function. This result is in agreement with previous works [15] and represents our basic idea for the characterisation of shape resonances: find out the virtual valence orbital "image" of the inner part of the resonant continuum wave function. However, determination of the "resonant" VO by means of the stabilization method is only possible when the potential barrier is sufficiently high (V_h = 20, 40, 80 a.u.), and is therefore not very useful, at least as a single tool, if the aim is to handle the more complex molecular problem.

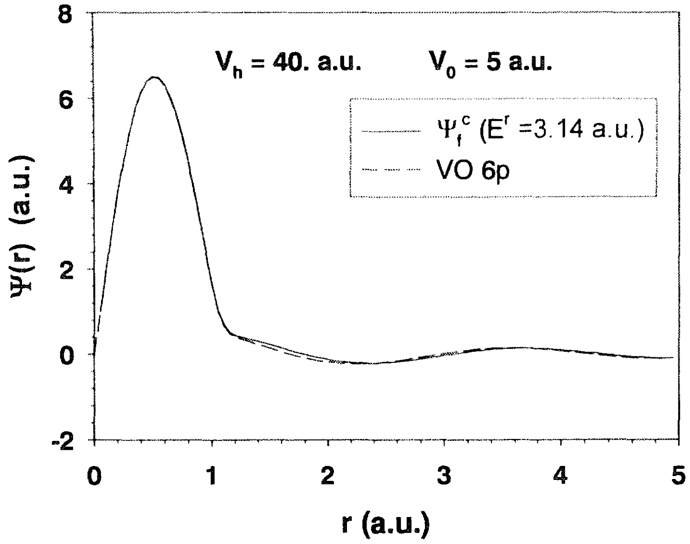

Figure 8.3: Comparison of the exact the continuum resonant wave function (E^r = 3.14 a.u.) and of the stabilized one, 6*p* (E_{6p} = 3.12 a.u.), corresponding to R_{MAX} = 8.0 a.u., for V_0 = 5 a.u. and V_h = 40 a.u.

8.3.2 Projection of the Continuum Wave Functions on the Virtual Orbitals

Following Thiele [23] we consider the decomposition of the continuum wave function into two orthogonal components:

$$\Psi_f^c(E) = \Psi_{res} + \Psi_{nr} \tag{8.5}$$

The component Ψ_{res} is confined in the potential barrier region and is assumed to be of dominant importance at the resonance, whereas Ψ_{nr} is a scattering function whose amplitude varies slowly with energy. The function Ψ_{res} can be defined by an expansion in the basis of the VOs Ψ_i^b of the system (8.1):

$$\Psi_{res} = \sum c_{fi} \Psi_i^b \tag{8.6}$$

with

$$c_{fi} = \left\langle \Psi_i^b \middle| \Psi_f^c(E) \right\rangle \tag{8.7}$$

Now, c_{fi} depends on the photoelectron energy E. From calculation of the energetic profile of the expansion coefficients (8.7) it should be possible to evaluate the contribution of the i-th virtual valence orbital on the resonant continuum wave function, and therefore find out the VO "image" of the inner part of the resonant continuum wave function. The energetic profiles of the coefficients $c_{fi}(E)$ associated with p-type states of the model system (8.1) have been therefore calculated. Figure 8.4 illustrates the energy dependence of the absolute coefficient values $\left|c_{fi}(E)\right|$ associated with the projection of the continuum p-wave function on $4p$ and $5p$ VOs, corresponding to $R_{MAX} = 8.0$ a.u, relative to the well depth of 5 a.u. and barrier height of $V_h = 10$ a.u.

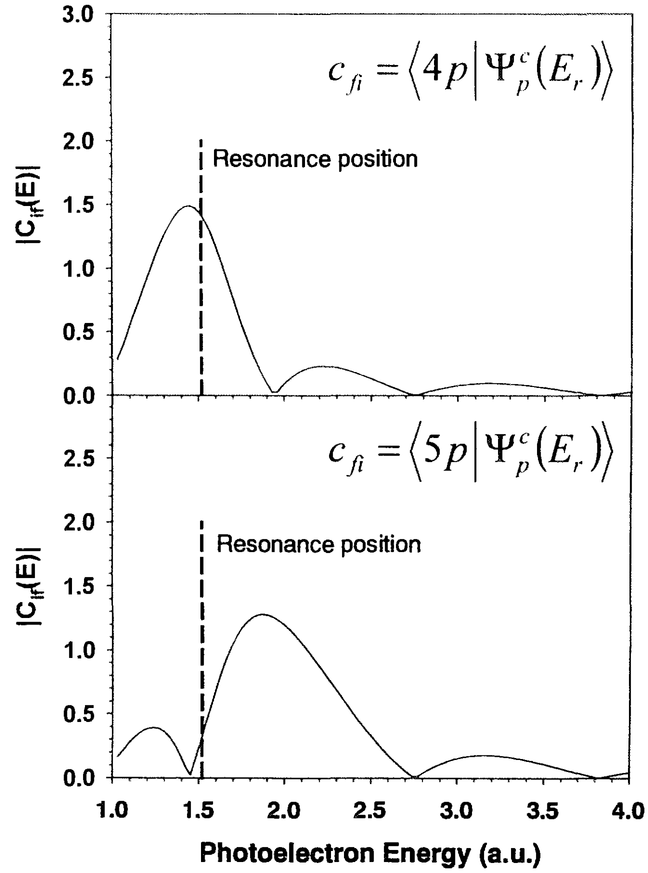

Figure 8.4: Absolute coefficient values $\left|c_{fi}(E)\right|$ associated with the projection of the continuum p-wave function on $4p$ (a) and $5p$ (b) VOs, corresponding to $R_{MAX} = 8.0$ a.u. and relative to the well depth of 5 a.u. and barrier height of $V_h = 10$. The red straight line indicates the energy resonance position ($E^r = 1.52$ a.u.).

It is worth noting that the stabilization graph associated with $V_0 = 5$ a.u. and barrier height of $V_h = 10$ a.u. does not display any "plateaux" [see Fig. 8.2(a)] and it was not possible to determinate the VO "image" of the resonant continuum wave. From analysis of $\left|c_{fi}(E)\right|$ profiles, at the resonance position ($E^r = 1.52$ a.u.) the VO 4*p* displays a pronounced maximum while the other orbitals show negligible contribution to the continuum wave function [e.g. the orbital 5*p* in Fig. 8.4(b)]. Therefore, the VO 4*p* could be considered as the "image" of the resonant continuum wave function. To verify this hypothesis the resonant continuum orbital ($E^r = 1.52$ a.u) and the 4*p* orbital ($E_{4p} = 1.44$ a.u.), corresponding to $R_{MAX} = 8.0$ a.u., are plotted in Fig. 8.5. Apart from the arbitrary normalisation factor, the VO 4*p* is a good approximation to the inner part of the resonant photoelectron wave function.

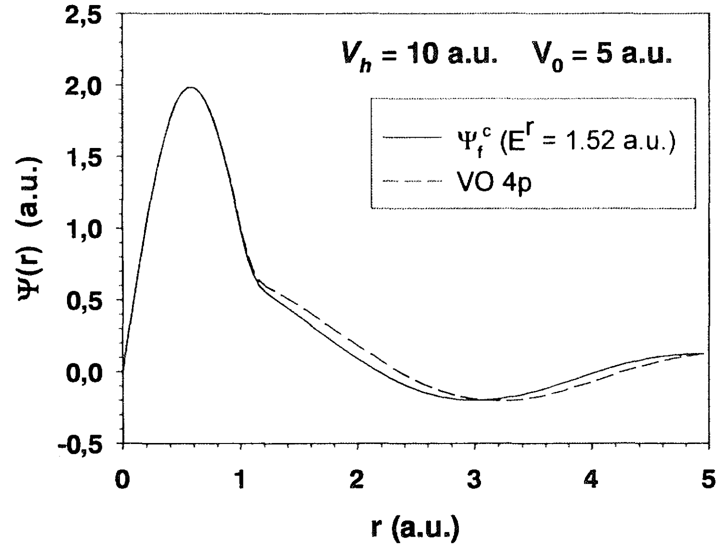

Figure 8.5: Comparison of the continuum resonant wave function ($E^r = 1.52$ a.u.) and of the VO 4*p* ($E_{4p} = 1.44$ a.u.), corresponding to $R_{MAX} = 8.0$ a.u., for $V_0 = 5$ a.u. and $V_h = 10$ a.u.

However, it is fair to say that the determination of the virtual valence orbital 4*p* through figure 8.4 requires the knowledge, *a priori*, of the shape resonance kinetic energy position. Without this piece of information it is not possible to discriminate between 4*p*, which is the "real image" of the resonant continuum wave function, and the other VOs. This apparently unexpected situation, which has been observed for all barrier heights V_h, can be explained with the observation, made in the context of the stabilization method [15], the VOs Ψ_i^b belonging to the "non-stable" eigenvalues E_i^r as given by the diagonalization procedure, closely approximate, apart from a normalisation constant, the inner part of the exact scattering functions $\Psi_f^c(E)$ at $E = E_i^r$, even though these $\Psi_f^c(E)$ represent non-resonant scattering states. The appearance of maxima structures in the absolute coefficient profiles, which represent a significative contribution of the VO to the inner part of the photoelectron wave function, are therefore justified. In fact, the VO 5*p* (E_{5p} = 1.94 a.u) has maximum overlap with the non-resonant photoelectron wave functions at $E \approx E_{5p}$ [see Fig. 8.4(a)].

The aim of the present work is to develop a method able to localise the shape resonances without making reference to the maxima positions in the cross section profile. It follows that the behaviour displayed by $|c_{fi}(E)|$ in Fig. 8.4 is not suited for this purpose. An ideal situation would be a Gaussian-like profile of $|c_{fi}(E)|$ centred at the shape resonance position and with negligible overlap between VOs and continuum states outside the resonant region. In this way the "resonant" VO could be determined without ambiguity.

It should be remarked that in Fig. 8.4 the continuum states have been projected on bound orbitals corresponding to R_{MAX} = 8.0 a.u. Probably a basis set so diffuse is not appropriate because it also represents the background continuum. We have therefore considered the influence of the energy-dependent coefficients $|c_{fi}(E)|$ on the R_{MAX} parameter. Fig. 8.6 illustrates the $|c_{fi}(E)|$ profiles associated with the projection of the continuum *p*-wave function on the *p* VOs, the latter corresponding to R_{MAX} = 1.2 a.u., relatively to the well depth of 5 a.u. and barrier height of V_h = 5, 10 a.u. This particular choice for R_{MAX} in bound state calculation corresponds to the enclosure of the system in a box which size is that of the model system size.

From the analysis of Fig. 8.6 it is obvious that the VOs contribution to the resonant continuum wave function reaches a maximum very close to the resonance energy. Furthermore, the annoying oscillations out of the resonant region disappear: with the basis set employed (R_{MAX} = 1.2 a.u.) we span just the resonant wave functions of the continuum spectrum. Hence, to a good approximation, the component Ψ_{res} of the continuum wave function can be represented by a single VO, namely 1p. Similar behaviour is displayed by the square-well potentials defined by V_h = 20, 40, 80 a.u.

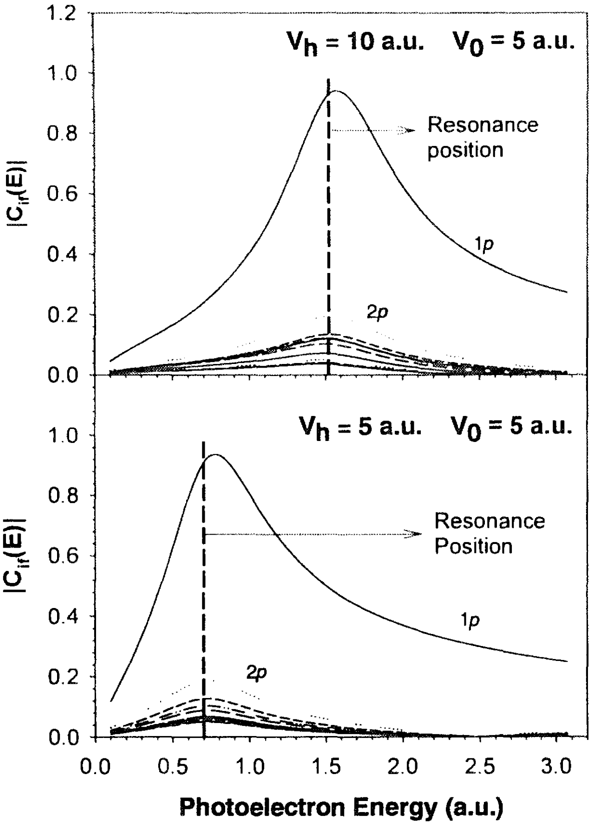

Figure 8.6: Absolute coefficient values $\left|c_{fi}(E)\right|$ associated with the projection of the continuum p-wave function on p VOs, the latter corresponding to R_{MAX} = 1.2 a.u. and relative to the well depth of 5 a.u. and barrier height of V_h = 10 a.u. (a), and V_h = 5 a.u. (b). The dashed line indicates the energy resonance position (E^r = 1.52 a.u. and E^r = 0.70 a.u. for V_h = 10, 5 a.u., respectively).

Summarising the above results, a methodology for shape resonance characterisation in terms of virtual valence orbitals could be based on projection of the continuum wave function on the VOs, the latter expanded in terms of B-spline functions built over the interval $\left[0, R_{MAXO}\right]$ where R_{MAXO} is very similar to the radial extension of the system.

Before considering the implementation of the method above mentioned in the B-spline DFT approach and some results on a molecular case, we discuss the evolution of the "resonant" VO with R_{MAX}, whose value defines box size where the system in enclosed in. In the spirit of the stabilization method, this analysis has been performed by means of the overlap between the VOs corresponding to R_{MAXO} = 1.2 a.u. and the VOs at increasing values of R_{MAX}, i.e.

$$S_{i_0 j}(n) = \left\langle \Psi_i^{n_0} \middle| \Psi_j^{n} \right\rangle, \tag{8.7a}$$

$$\hat{H}\Psi_i^{n_0} = E_i^{n_0}\Psi_i^{n_0} \qquad \hat{H}\Psi_j^{n} = E_j^{n}\Psi_j^{n} \tag{8.7b}$$

where the n_0, n stand for R_{MAXO} and R_{MAX}, respectively, while the lower indexes i, j refer to the bound eigenvectors. Figure 8.7 displays the R_{MAX} dependence of the overlap $S_{i_0 j}(n)$ for the VOs 1p, 2p, corresponding to R_{MAXO} = 1.2 a.u. and relatively to the model potential defined by V_0 = 5 a.u. and V_h = 10 a.u.

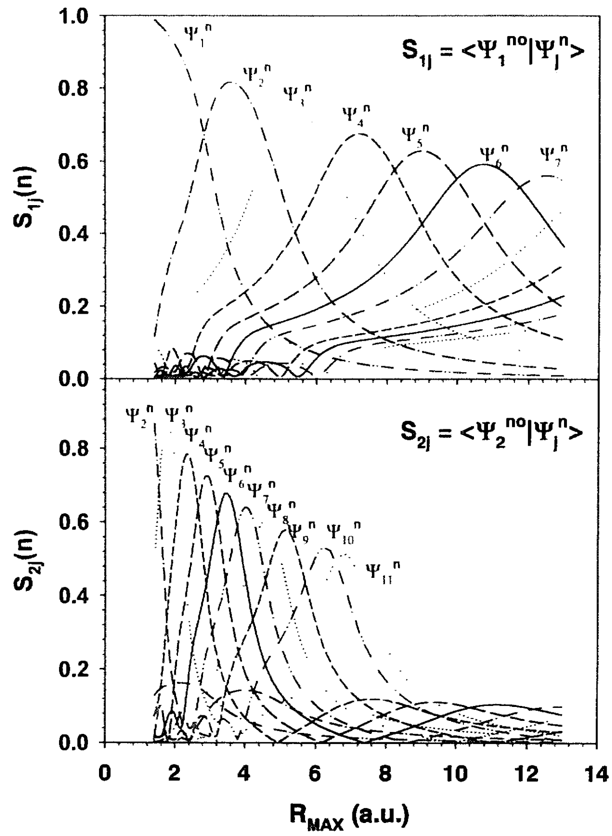

Figure 8.7: R_{MAX} dependence of the overlap $S_{i_0 j}(n) = \left\langle \Psi_i^{n_0} \middle| \Psi_j^{n} \right\rangle$ for the "resonant" 1p and "non-resonant" 2p VOs corresponding to R_{MAXO} = 1.2 a.u. and relatively to V_0 = 5 a.u. and V_h = 10 a.u.

Concerning the evolution of the "resonant" $1p$ orbital [see Fig. 8.7(a)] the following main observations can be made: in accordance with stabilization method, increasing the size of the box (R_{MAX}) the VO "image" of the continuum resonant wave function changes. Furthermore, the contribution of more than a single VO to the inner part of the resonant continuum wave function increases as the size of the basis set gets larger, and the resonance cannot be assigned to a single VO. This justifies the use of short R_{MAX} values, similar to the radial extension of the system, for the determination of the "resonant" virtual orbital. However, if significant contributions by more than a single VO to the resonant continuum wave function appear already in the simple model potential (8.1), complications are expected in the more complex molecular case.

8.3.3 Implementation in the B-spline DFT approach and Applications

The implementation of the method discussed in the previous subsection within the B-spline DFT approach [9,10] is based on the projection of the dipole-prepared continuum wave function [11] on the bound orbitals, the latter expanded in a B-spline basis set built over the interval $[0, R_{MAXO}]$, where R_{MAXO} refers to the large One Centre Expansion (OCE) and is placed at the radial position of the atom more distant from the origin. If the multicentre approach is employed [10] the radii of the spheres placed on the out-of-centre atoms have to be taken into account.

As a first test case we have considered the shape resonance in the ionisation of core and valence σ_g orbitals of N_2, which has been studied both experimentally [24-26] and theoretically [27-29], since many years ago. Bound and continuum states have been obtained by means of LCAO B-spline DFT calculations [10]. The experimental equilibrium geometry (2.068 a.u.) has been employed; the OCE expansion has been placed on the centre of the molecule while for the out-of-centre B-spline basis $R^{i}_{MAX} = 1.0$ a.u. is employed. Concerning the shape resonance characterisation through projection analysis of the dipole-prepared continuum orbital on the VOs, bound states are expanded in a B-spline basis set where R_{MAXO} equals the distance of the nitrogen atom from the origin (1.034 a.u.) plus half of the out-of-centre sphere's radii (1.0 a.u.).

Relatively to $1\sigma_g$ ionisation, figure 8.8 illustrates the projection of the symmetry-allowed continuum orbitals $k\sigma_u$ and $k\pi_u$ on the VOs $n\sigma_u$ and $n\pi_u$, respectively. The contribution of the $3\sigma_u$ orbital to the resonant continuum function reaches a rather pronounced maximum at 0.36 a.u. We predict therefore the existence of a shape resonance centred approximately at 0.36 a.u. (9.8 eV) that we characterise in terms of the valence antibonding $3\sigma_u$ orbital. No resonances are expected in the $1\sigma_g \rightarrow k\pi_u$ ionisation channel. These results are in agreement with the previous experimental [24] theoretical [27-29] studies on core $1\sigma_g$ photoionization in N_2. Analogous results are displayed by $2\sigma_g$ and $3\sigma_g$ orbitals.

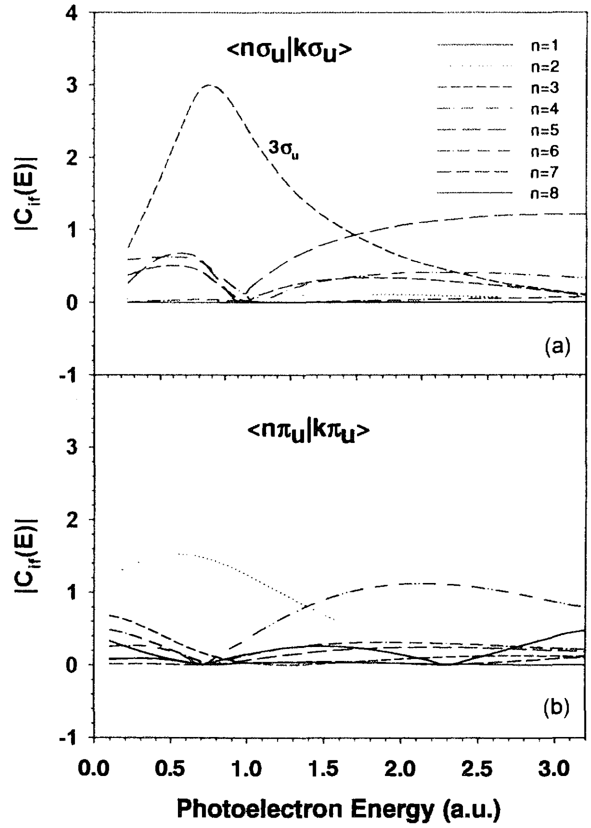

Figure 8.8: Absolute coefficient values $\left|c_{fi}(E)\right|$ for core $1\sigma_g$ ionisation in N_2 associated with the projection of the symmetry allowed final states $k\sigma_u$ on the VO $n\sigma_u$ (a), and $k\pi_u$ on the $n\pi_u$ (b), as a function of the photoelerctron energy.

Finally, total and partial-channel cross section profiles for photoionization of the $1\sigma_g$ core level in N_2 are displayed in Fig. 8.9. The shape resonance is centred at

0.40 a.u. (10.9 eV), in good agreement with 9.8 eV, the position of the maxima in the $\langle 3\sigma_u | k\sigma_u \rangle$ profile [see Fig. 8.8(a)]. From the partial-channels profiles shape resonance is clearly ascribed to the $1\sigma_g \rightarrow k\sigma_u$ channel, and the previous characterisation in terms of transition toward the virtual valence $3\sigma_u$ orbital is therefore justified.

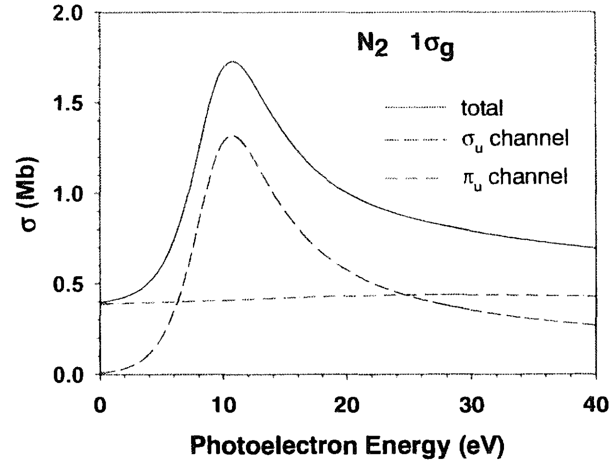

Figure 8.9: The $1\sigma_g$ total and partial-channels cross section profiles in N_2.

8.4 Conclusions

In the present work a methodology to localise and characterise in molecular terms the shape resonances in the framework of the B-spline Density Functional Theory method is presented. Starting from a model system, a procedure based on the concepts of stabilization method and projection of the final continuum state on the virtual valence orbitals has been developed. The conditions for the application of the method are determined. The one-electron continuum resonances are described in terms of contribution from virtual valence orbitals lying above threshold. The method has been ultimately implemented in the B-spline DFT approach and applied to study the shape resonances in the photoionization of core and valence σ_g orbitals in N_2. The shape resonances are rationalised in terms of the valence antibonding $3\sigma_u$

orbital. This result is in agreement with previous theoretical and experimental studies on N_2 photoionization.

Bibliography

Chapter 1

[1] A. F. Starace, "Theory of atomic photoionization", in *Handbuch der Physik*, Vol. 31., edited by S. Flugge (Springer-Verlag, Berlin, 1982).

[2] C. N. Yang, Phys. Rev. **74**, 764 (1948).

[3] B. Ritchie, Phys. Rev. A **13**,1411 (1976).

[4] N. A. Cherepkov, Chem. Phys. Lett. **87**, 344 (1982).

[5] P. G. Burke, Adv. Atom. Molec. Phys. **4**, 173 (1968).

[6] U. Fano, Phys. Rev. 124, 1866 (1961).

[7] R. D. Cowan, *The Theory of Atomic Structure and Spectra*, Chemical Abstracts Service (Columbus, Ohio, 1981).

[8] S. T. Manson, J. W. Cooper, Phys. Rev. **165**, 126 (1968).

[9] J. L. Dehmer, J. Chem. Phys. **56**, (1972) 4496.

[10] J. L. Dehmer, in *Resonances in Electron-Molecule Scattering van der Walls Complexes and Reactive Chemical Dynamics*, vol. 263, edited by D.G. Truhlar (Ed.American Chemical Society, Washington DC, 1984).

[11] P.W. Langhoff, in *Resonances in Electron-Molecule Scattering van der Walls Complexes and Reactive Chemical Dynamics*, vol. 263, edited by D.G. Truhlar (Ed.American Chemical Society, Washington DC, 1984).

[12] D. W. Turner, C. Baker, a. D. Baker, A. D. Baker and C. R. Brundle, *Molecular photoelectron spectroscopy* (Wiley-Interscience, London, 1970).

[13] H. Siegbahn and L. Karlsson, "Photoelectron Spectroscopy", in *Handbuch der Physik*, Vol. 31., edited by S. Flugge (Springer-Verlag, Berlin, 1982).

[14] R. K. Nesbet, *Variational Methods in in Electron-Atom Scattering Theory* (Plenum, New York, 1980).

[15] R. Arneberg, J. Müller, and R. Manne, Chem. Phys. **64**, 249 (1982).

[16] J. R. Taylor, *Scattering Theory* (John Wiley and Sons, New York, 1972).

[17] A. Messiah, *Quantum Mechanics* (North Holland, Amsterdam, 1985).

[18] N. Chandra, Chem. Phys. **108**, 301 (1986).

[19] G. Breit and H. A. Bethe, Phys. Rev. **93**, 888 (1954).

[20] C. J. Joachain, *Quantum Collision Theory* §14.2 (North-Holland publishing, Amsterdam, 1975).

[21] P. G. Burke, N. Chandra, and F. A. Gianturco, J. Phys. B **5**, 2212 (1972).

[22] D. Dill and J. L. Dehmer, J. Chem. Phys. **61**, 692 (1974).

[23] R. J. W. Henry and L. Lipsky, Phys. Rev. **153**, 51 (1967).

[24] N. Chandra, J. Phys. B **20**, 3405 (1987).

[25] A. R. Edmonds, *Angular Momentum in Quantum Mechanics* (Princeton University Press, Princeton, NJ, 1974).

[26] H. A. Bethe and E. Salpeter, *Quantum Mechanics of One- and Two- Electron Atoms* (Springer, Berlin, 1957).

[27] F. A. Gianturco and A. Jain, Phys. Rep. **143**, 347 (1986).

[28] F. A. Gianturco, V. di Martino and A. Jain, Nuovo Cimento **14D**, 411 (1992).

[29] K. H. Johnson, Adv. Quantum Chem. 7, 143 (1973).

[30] B. I. Schneider and L. A. Collins, Phys. Rev. A **24**, 1264 (1981).

[31] I. Cacelli, V. Carravetta, A. Rizzo and R. Moccia, Phys. Rep. **205**, 283 (1991).

[32] P. W. Langhoff, in: *Electron-Molecule and Photon-Molecule Collisions*, edited by T. Rescigno, V. McKoy, B. Schneider (Plenum Press, New York, p. 183., 1979).

[33] R. R. Lucchese, K. Tbatsuba and V. McKoy, Phys. Rep. **131**, 147 (1986).

[34] R. Moccia and P. Spizzo, J. Phys. B **18**, 3537 (1985).

Chapter 2

[1] C. de Boor, *A Pratical Guide to Splines* (Springer, New York, 1978).

[2] P. Decleva, A. Lisini, and M. Venuti, Int. J. Quantum. Chem. **56**, 27 (1995).

[3] M-K. Chen, J. Phys. B **27**, 865 (1994).

[4] H. Bachau, E. Cormier, P. Decleva, J. E. Hansen and F. Martin, Rep. Prog. Phys. **64**, 1815 (2001).

[5] J.R. Rice, *Numerical methods, Software and Analysis* (Singapore, McGraw-Hill, 1983).

[6] J. Stoer and R. Bulirsch, *Introduction to Numerical Analysis* (New York, Springer, 1983)

[7] M. Brosolo, P. Decleva, and A. Lisini, Computer Phys. Commun. **71**, 207 (1992).

[8] G. Golub and C. F. Van Loan, *Matrix Computations* (Johns Hopkins University Press, Baltimore, MD, 1983).

[9] H. R. Schwarz, *Finite Element Methods* (Academic Press, New York, 1988).

[10] M. Brosolo, PhD Thesis, University of Trieste, 1993.

[11] R. G. Parr and W. Yang, *Density Functional Theory of Atoms and Molecules* (Oxford University Press, Oxford, 1989).

[12] W. Koch, M. C. Holthausen, *A Chemist's Guide to Density Functional Theory* (New York, WILEY-VCH, 2002).

[13] M. Stener, A. Lisini, and P. Decleva, Int. J. Quant. Chem. **53**, 229 (1995).

[14] S. H. Vosko, L. Wilk, and M. Nusair, Can. J. Phys. B **28**, 1200 (1980).

[15] W. Kohn and W. J. Sham, Phys. Rev. **140**, A1133 (1965).

[16] P.A. M. Dirac, Proc. Cambridge Phil. Soc. **26**, 376 (1930).

[17] D. M. Ceperley and B. J. Alder, Phys. Rev. Lett. **45**, 566 (1980).

[18] C. O. Almbladh and A. C. Pedroza, Phys. Rev. A **29**, 2322 (1984).

[19] M. Levy, J. P. Perdew and V. Sahni, Phys. Rev. A **30**, 2745, (1984).

[20] R. van Leeuwen and E. J. Baerends, Phys. Rev. A **49**, 2421 (1994).

[21] T. Grabo and E. K. U. Gross **240**, 141 (1995).

[22] X. M. Tong and S-H. Chu, Phys. Rev. A **55**, 3406 (1997).

[23] A. Görling, Phys. Rev. Lett **83**, 5459 (1999).

[24] M. Stener, S. Furlan , and P. Decleva, J. Phys. B **33**, 1081 (2000).

[25] M. Venuti, M. Stener, and P. Decleva, Chem. Phys. **234**, 95 (1998).

[26] D. Bishop, *Advances in Quantum Chemistry*, Vol. 3, edited by P-O Lodwin (Academic Press, New York, 1967).

[27] P. G. Burke, N. Chandra, and F. A. Gianturco, J. Phys. B **5**, 2212 (1972).

[28] D. Toffoli, M. Stener, G. Fronzoni, and P. Decleva, Chem. Phys. **276**, 25 (2002).

[29] R. McWeeny, *Methods of Molecular Quantum Mechanics* (Academic, New York, 1978).

[30] A. Szabo and N. Ostlund, *Modern Quantum Chemistry*, (New York, Dover, 1977).

[31] M. Brosolo, P. Decleva, and A. Lisini, Chem. Phys. Lett. **203**, 586 (1992).

[32] M. Brosolo, P. Decleva, and A. Lisini, Int. J. Quantum Chem. **52**, 507 (1994).

[33] A. R. Barnett, Comput. Phys. Commun **27**, 147 (1982).

[34] E. J. Baerends , D. E. Ellis, and P. Ros, Chem. Phys. **2**, 41 (1973).

[35] C. Fonseca Guerra, J.G. Snijders, te Velòde, and J. Baerends, Theor. Chem. Acc. **99**, 391 (1998).

Chapter 3

[1] L. Alagna, T. Prosperi, S. Turchini, J. Goulon, A. Rogalev, C. Goulon-Ginet, C.R. Natoli, R.D. Peacock, B. Stewart, Phys. Rev. Lett. **80**, 4799 (1998).

[2] G. Schütz, W. Wagner, W. Wilhelm, P. Kienle, R. Zeller, R. Frahm, and G. Materlik, Phys. Rev. Lett. **58**, 737 (1987).

[3] B. Ritchie, Phys. Rev. A **13**, 1411 (1976).

[4] N. A. Cherepkov, Chem. Phys. Lett. **87**, (1982) 344.

[5] N. Böwering, T. Lischke, B. Schmidtke, N. Müller, T. Khalil, U. Heinzmann, Phys. Rev. Lett. **86**, 1187 (2001).

[6] G. A. Garcia, L. Nahon, M. Lebech, J. C. Houver, D. Dowek and I. Powis, J. Chem. Phys. **119**, 8781 (2003).

[7] S. Turchini, N. Zema, G. Contini, G. Alberti, M. Alagia, S. Stranges, G. Fronzoni, M. Stener, P. Decleva, and T. Prosperi, Phys. Rev. A., **70**, 14502 (2004).

[8] I. Powis, J. Chem. Phys. 112, 301 (2000).

[9] I. Powis, J. Phys. Chem. A 104, 878 (2000).

[10] K. Kimura, S. Katsumata, Y. Achiba, T. Yamazaki, and S. Iwata, *Handbook of HeI Photoelectron Spectra of Fundamental Organic Compounds* (Japan Scientific Society Press, Tokyo, 1981)

[11] E. J. McAlduff and K. N. Houk, Can. J. Chem. **55**, 318 (1977).

[12] H. Hollenstein, D. Luckhaus, J. Pochert, M. Quack and G. Seyfang, Angew. Chem. Int. Ed. Engl. **36**, 140 (1997).

[13] N. Chandra, J. Phys. B **20**, 3405 (1987).

[14] D. Toffoli, M. Stener, G. Fronzoni and P. Decleva, Chem. Phys. **276**, 25 (2002).

[15] M. Venuti, M. Stener, and P. Decleva, Chem. Phys. **234**, 95 (1998).

[16] P. G. Burke, N. Chandra and F. A. Gianturco, J. Phys. B **5**, 2212 (1972).

[17] C. de Boor, *A Practical Guide to Splines* (Springer, New York, 1978).

[18] R. G. Parr and W. Yang, *Density Functional Theory of Atoms and Molecules*, (Oxford University Press, New York 1989).

[19] E. J. Baerends, D. E. Ellis and P. Ros, Chem. Phys. **2**, 41 (1973).

[20] C Fonseca Guerra, J G Snijders, G te Velde, and E J Baerends, Theor. Chem. Acc. **99**, 391 (1998).

[21] R. Van Leeuwen and E. J. Baerends, Phys. Rev. A **49**, 2412 (1994).

[22] M. Stener, S. Furlan and P. Decleva, J. Phys. B **33**, 1081 (2000).

[23] M. Brosolo and P. Decleva, Chem. Phys. **159**, 185 (1992).

[24] A. R. Barnett, Comput. Phys. Commun. **27**, 147 (1982).

[25] A. R. Edmonds, *Angular Momentum in Quantum Mechanics* (Princeton University Press, Princeton, NJ, 1974).

[26] S. H. Vosko, L. Wilk and M. Nusair, Can. J. Phys. **58**, 1200 (1980).

[27] M. Stener and M. Calligaris, J. of Molecular Structure (Theochem) **497**, 91 (2000).

[28] J. P. Perdew, R. G. Parr, M. Levy and J. L. Balduz Jr., Phys. Rev. Lett. **49**, 1691 (1982).

[29] D. P. Chong, O. V. Gritsenko and E. J. Baerends, J. Chem. Phys. **116**, 1760 (2002).

[30] M. Stener, G. De Alti and P. Decleva, Theor. Chem. Acc. **101**, 247 (1999).

[31] M. Stener, A. Lisini and P. Decleva, Int. J. Quantum Chem. **53**, 229 (1995).

[32] M. Stener, G. Fronzoni, D. Toffoli and P. Decleva, Chem. Phys. **282**, 337 (2002).

[33] C. M. Truesdale, D. W. Lindle, P. H. Kobrin, U. E. Becker, H. G. Kerkhoff, P. A. Heimann, T. A. Ferrett and D. A. Shirley, J. Chem. Phys. **80**, 2319 (1984).

Chapter 4

[1] B. Ritchie, Phys. Rev. A **13**, 1411 (1976).

[2] N. Böwering, T. Lischke, B. Schmidtke, N. Müller, T. Khalil, U. Heinzmann, Phys. Rev. Lett. **86**, 1187 (2001).

[3] G. Garcia, L. Nahon, M. Lebech, J. C. Houver, D. Dowek and I. Powis, J. Chem. Phys. **119**, 8781 (2003).

[4] U. Hergenhahn, E. E. Rennie, O. Kugeler, S. Marburger, T. Lischke, I. Powis and G. Garcia, J. Chem. Phys. **120**, 4553 (2004).

[5] T. Lischke, N. Böwering, B. Schmidtke, N. Müller, T. Khalil and U. Heinzmann, Phys. Rev. A **70**, 022507 (2004).

[6] S. Turchini, N. Zema, G. Contini, G. Alberti, M. Alagia, S. Stranges, G. Fronzoni, M. Stener, P. Decleva and T. Prosperi, Phys. Rev. A **70**, 14502 (2004).

[7] I. Powis, J. Chem. Phys. **112**, 301 (2000).

[8] I. Powis, J. Phys. Chem. A **104**, 878 (2000).

[9] M. Stener, G. Fronzoni, D. Di Tommaso and P. Decleva, J. Chem. Phys. 120, 3284 (2004).

[10] E. E. Rennie, I. Powis, U. Hergenhahn, O. Kugeler, G. Garcia, T. Lischke and S. Marburger, J. Electron. Spectrosc. and Relat. Phenom. **125**, 197 (2002).

[11] G. A. Garcia, L. Nahon, C. J. Harding, E. A. Mikajlo, and I. Powis, in preparation (2005).

[12] A. F. Starace, “Theory of atomic photoionization”, in *Handbuch der Physik*, Vol. 31., edited by S. Flugge (Springer-Verlag, Berlin, 1982).

[13] D. Toffoli, M. Stener, G. Fronzoni and P. Decleva, Chem. Phys. **276**, 25 (2002).

[14] A. Giardini, D. Catone, S. Stranges, M. Satta, S. Piccirillo, S.Turchini, N. Zema, G. Contini, T. Prosperi, P.Decleva, D. Di Tommaso, G. Fronzoni, M. Stener, A. Filippi, and M. Speranza, ChemPhysChem **6**, 1164 (2005).

[15] E. J. Baerends , D. E. Ellis and P. Ros, Chem. Phys. **2**, 41 (1973).

[16] C. Fonseca Guerra, J.G. Snijders, te Velde and J. Baerends, Theor. Chem. Acc. **99**, 391 (1998).

[17] R. Van Leeuwen and J. Baerends, Phys. Rev. A **49**, 85 (1994).

[18] M. Stener, S. Furlan and P. Decleva, J. Phys. B **33**, 1081 (2000).

[19] P. G. Burke, N. Chandra and F. A. Gianturturco, J. Phys. B **5**, 2212 (1972).

[20] H. Bachau , E. Cormier, P. Decleva, J. E. Hansen and F. Martín, Rep. Prog. Phys. **64**, 1601 (2001).

[21] M. Brosolo and P. Decleva, Chem. Phys. **159**, 185 (1992).

[22] N. Chandra, J. Phys. B **20**, 3405 (1987).

[23] D. Dill and J. L. Dehmer, J. Chem. Phys. **61**, 692 (1974); J. W. Davenport, Dissertation, University of Pennsylvania, 1976.

[24] P. Downie and I. Powis, J. Chem. Phys. **111**, 4535 (1999).

[25] J. C. Slater, *Quantum theory of molecules and solids* (Mc-Graw Hill, New York, 1974).

[26] J. Kong, C. A. White, A. I. Krylov, D. Sherrill, R. D. Adamson, T. R. Furlani, M. S. Lee, A. M. Lee, S. R. Gwaltney, T. R. Adams, C. Ochsenfeld, A. T. B. Gilbert, G. S. Kedziora, V. A. Rassolov, D. R. Maurice, N. Nair, Y. H. Shao, N. A. Besley, P. E. Maslen, J. P. Dombroski, H. Daschel, W. M. Zhang, P. P. Korambath, J. Baker, E. F. C. Byrd, T. Van Voorhis, M. Oumi, S. Hirata, C. P. Hsu, N. Ishikawa, J. Florian, A. Warshel, B. G. Johnson, P. M. W. Gill, M. Head-Gordon, and J. A. Pople, J. Comput. Chem. **21**, 1532 (2000).

[27] Y. Takai and K. H. Johnson, Chem. Phys. Lett. **189**, 518 (1992).

[28] J. G. Norman, Jr., Mol. Phys. **31**, 1191 (1976).

[29] C. J. Harding and I. Powis, J. Chem. Phys., *submitted* (2005).

[30] P. Colavita, G. De Alti, G. Fronzoni, M. Stener and P. Decleva, Phys. Chem. Chem. Phys. **3**, 4481 (2001).

[31] M. B. Robin, Chem. Phys. Lett. **119**, 33 (1985)

[32] M. Stener, P. Decleva and A. Lisini, J. of Molecular Structure (Theochem) **357**, 125 (1995).

[33] M. Stener and P. Decleva, J. Chem. Phys. **112**, 10871 (2000).

[34] M. Stener, G. Fronzoni, D. Toffoli and P. Decleva, Chem. Phys. **282**, 337 (2002).

[35] G. Fronzoni, M. Stener and P. Decleva, J. Chem. Phys. **118**, 10051 (2003).

[36] M. Stener, P. Decleva and A. Lisini, J. Phys. B: At. Mol. Opt. Phys. **28**, 4973 (1995).

[37] M. Stener, G. Fronzoni and P. Decleva, J. Chem. Phys. **122**, 234301 (2005).

[38] G. Fronzoni, M. Stener, S. Furlan, and P.Decleva, Chem. Phys. **273**, 117 (2001).

Chapter 5

[1] L. Pasteur, Ann. Chim. Phys. **24**, 442 (1848).

[2] B. Ritchie, Phys. Rev. A **13**, 1411 (1976).

[3] N. A. Cherepkov, Chem. Phys. Lett. **87**, 344 (1982).

[4] N. A. Cherepkov, J. Phys. Chem. B **16**, 1543 (1983).

[5] N. A. Cherepkov, Adv. At. Mol. Phys. **19**, 395 (1983).

[6] I. Powis, J. Chem. Phys. **112**, 301 (2000).

[7] I. Powis, J. Phys. Chem. A **104**, 878 (2000).

[8] M. Stener, G. Fronzoni, D. Di Tommaso, and P. Decleva, J. Chem. Phys. **120**, 3284 (2004).

[9] N. Böwering, T. Lischke, B. Schmidtke, N. Müller, T. Khalil, and U. Heinzmann, Phys. Rev. Lett. **86**, 1187 (2001).

[10] G. Garcia, L. Nahon, M. Lebech, J. C. Houver, D. Dowek, and I. Powis, J. Chem. Phys. **119** 8781 (2003).

[11] T. Lischke, N. Böwering, B. Schmidtke, N. Müller, T. Khalil, and U. Heinzmann, Phys. Rev. A **70**, 022507 (2004).

[12] S. Turchini, N. Zema, G.Contini, G.Alberti, M. Alagia, S. Stranges, M. Stener, G. Fronzoni, P.Decleva, and T.Prosperi, Phys. Rev. A **70**, 14502 (2004).

[13] R. Walker, B. Diviacco, Rev. Sc. Instrum. **63**, 332 (1992).

[14] A. Derossi, F. Lama, M. Piacentini, T. Prosperi, and N. Gemma, Rev. Mod. Astron. Rev. Sci. Instrum. **66(2)**, 1718 (1995).

[15] R. R. Blyth, R. Delaunay, M. Zitnik, J. Krempasky, R. Krempaska, J. Slezak, K. C. Prince, R. Richter, M. Vondracek, R. Camilloni, L. Avaldi, M. Coreno, G. de Stefani, C. Furlani, M. de Simone, S. Stranges, and M.-Y. Adam, J. Electron. Spectrosc. Relat. Phenom. **101-103**, 959 (1999).

[16] D. Desiderio, S. Di Fonzo, B, Diviacco W. Jark, J. Krempasky, R. Krempaska, F. Lama, M. Luce, H. C. Mertins, M. Piacentini, T. Prosperi, S. Rinaldi, G. Sullie', F. Schaefers, F. Schmolla, L. Stichauer, S. Turchini, R. P. Walzer, and N. Zema, Synchr. Radiat. News **12**, 34 (1999).

[17] D. Toffoli, M. Stener, G. Fronzoni, and P. Decleva, Chem. Phys. **276**, 25 (2002).

[18] N. Chandra, J. Phys. B **20**, 3405 (1987).

[19] C. Fonseca Guerra, J.G. Snijders, te Velòde, and J. Baerends, Theor. Chem. Acc. **99**, 391 (1998).

[20] Gaussian 03, Revision B.05, M, Frisch, G. W. Trucks, H. B. Schlegel, G. E. Scuseria, M. A. Robb, J. R. Cheeseman, J. A. Montgomery Jr., T. Vreven, K. N. Kudin, J. C. Burant, J. M. Millam, S. S. Iyengar, J. Tomasi, V. Barone, B. Mennucci, M. Cossi, G. Scalmani, N. Rega, G. A. Petersson, H. Nakatsuji, M. Hada, M. Ehara, K. Toyota, R. Fukuda, J. Hasegawa, M. Ispida, T. Nakajima, Y. Honda, O. Kitao, H. Hakai, M. Klene, X. Li, J. E. Knox, H. P. Hratchian, J. B. Cross, C. Adamo, J. Jaramillo, R. Gomperts, R. E. Stratmann, O. Yazyev, A. J. Austin, R. Cammi, C. Pomellij, J. W. Ochterski, P. Y.Ayala, K. Morokuma, G.A. Voth, P. Salvador, J. J. Dannenberg, V. G. Zakrzewski, S. Dapprich, A. D. Daniels, M. C. Strain, O. Farkas, D. K. Malick, A. D. Rabuck, K. Raghavachari, J. B. Foresman, J. V. Ortiz, Q. Cui, A. G.Baboul, S. Clifford, J. Cioslowski, B. B. Stefanov, G. Liu, A. Liashenko, P.Piskorz, I. Komaromi, R. L. Martin, D. J. Fox, T. Keith, M. A. Al-Laham, C. Y.Peng, A.Nanayakkara, M. Challacombe, P. M. W. Gill, B. Johnson, W. Chen, M. W. Wong, C. Gonzalez, and J. A. Pople, Gaussian Inc., Pittsburgh PA, **2003**.

[23] G. Berthier, B. Cadioli, E. Gallinella, A. Aamouche, and M. Ghomi, J. Mol. Struct. **390**, 11 (1997).

Chapter 6

[1] B. Ritchie, Phys. Rev. A **13**,1411 (1976).

[2] N. A. Cherepkov, Chem. Phys. Lett. **87**, 344 (1982).

[3] N. Böwering, T. Lischke, B. Schmidtke, N. Müller, T. Khalil, and U. Heinzmann, Phys. Rev. Lett. **86**, 1187 (2001).

[4] G. Garcia, L. Nahon, M. Lebech, J. C. Houver, D. Dowek, and I. Powis, J. Chem. Phys. **119** 8781 (2003).

[5] U. Hergenhahn, E. E. Rennie, O. Kugeler, S. Marburger, T. Lischke, I. Powis and G. Garcia, J. Chem. Phys. **120**, 4553 (2004).

[6] T. Lischke, N. Böwering, B. Schmidtke, N. Müller, T. Khalil, and U. Heinzmann, Phys. Rev. A **70**, 022507 (2004).

[7] S. Stranges, S. Turchini, G. Alberti, G. Contini, P. Decleva, G. Fronzoni, M. Stener, N. Zema, and T. Prosperi, J. Chem. Phys. **122**, 244303 (2005).

[8] A. Giardini, D. Catone, S. Stranges, M. Satta, S. Piccirillo, S. Turchini, N. Zema, G. Contini, T. Prosperi, P.Decleva, D. Di Tommaso, G. Fronzoni, M. Stener, A. Filippi, and M. Speranza, ChemPhysChem **6**, (2005) 1164.

[9] I. Powis, J. Chem. Phys. **112**, 301 (2000).

[10] I. Powis, J. Phys. Chem. A **104**, 878 (2000).

[11] M. Stener, G. Fronzoni, D. Di Tommaso, and P. Decleva, J. Chem. Phys. **120,** 3284 (2004).

[12] M. Stener, D. Di Tommaso, G. Fronzoni, P. Decleva, and I. Powis, J. Chem. Phys., accepted.

[13] K. Okuhara, J. Org. Chem **43**, 2745 (1978).

[14] D. Di Tommaso and P. Decleva, J. Chem. Phys. **123**, 06431 (2005).

[15] A. F. Starace, "Theory of atomic photoionization", in *Handbuch der Physik*, Vol. 31., edited by S. Flugge (Springer-Verlag, Berlin, 1982).

[16] D. Toffoli, M. Stener, G. Fronzoni, and P. Decleva, Chem. Phys. **276**, 25 (2002).

[17] E. J. Baerends , D. E. Ellis, and P. Ros, Chem. Phys. **2**, 41 (1973).

[18] C. Fonseca Guerra, J.G. Snijders, te Velòde, and J. Baerends, Theor. Chem. Acc. **99**, 391 (1998).

[19] R. Van Leuwen and J. Baerends, Phys. Rev. A **49**, 85 (1994).

[21] P. G. Burke, N. Chandra, and F. A. Gianturturco, J. Phys. B **5**, 2212 (1972).

[22] H. Bachau , E. Cormier, P. Decleva, J. E. Hansen, and F. Martín, Rep. Prog. Phys. **64**, 1601 (2001).

[23] M. Brosolo and P. Decleva, Chem. Phys. **159**, 185 (1992).

[24] N. Chandra, J. Phys. B **20**, 3405 (1987).

[25] S. H. Vosko, L. Wilk, and M. Nusair, Can. J. Phys. **58**, (1980) 1200.

[26] A. D. Becke, Phys Rev A **38**, 3089 (1988).

[27] J.P. Perdew, Phys Rev B **33**, 8822 (1986).

[28] J. L. Dehmer and D. Dill, Phys. Rev. Lett. **35**, 213 (1975).

[29] J. L. Dehmer, in *Resonances in Electron-Molecule Scattering van der Walls Complexes and Reactive Chemical Dynamics*, vol. 263, edited by D.G. Truhlar (Ed.American Chemical Society, Washington DC, 1984).

Chapter 7

[1] K. Siegbahn, C. Nordling, G. Johansson, J. Hedman, P. F. Hedén, K. Hamrin, U. Gelius, T. Bergmark, L.-O. Werme, R. Manne and Y. Baer, *ESCA Applied to Free Molecules* (North-Holland Publishing Company, Amsterdam, 1969).

[2] K. Siegbahn, J. Electron. Spectrosc. and Relat. Phenom. **5**, 3 (1974).

[3] L. J. Sæthre, N. Berrah, J. D. Bozek, K. J. Børve, T. X. Carrol, E. Kukk, G. L. Gard, R. Winter and T. D. Thomas, J. Am. Chem. Soc. **123**, 10729 (2001).

[4] T. D. Thomas, L. J. Sæthre, K. J. Børve, J. D. Bozek, M. Huttula and E. Kukk, J. Phys. Chem. A **108**, 4983 (2004).

[5] V. M. Oltedal, K. J. Børve, L. J. Sæthre, T. D. Thomas, J. D. Bozek and E. Kukk, Phys. Chem. Chem. Phys. **6**, 4254 (2004).

[6] U. Hergenhahn, O. Kugeler, A. Rüdel, E. E. Rennie and A. M. Bradshaw, J. Phys. Chem. A **105**, 5704 (2001).

[7] T. D. Thomas, N. Berrah, D. Bozek, T. X. Carrol, J. Hahne, T. Karlsen, E. Kukk and L. J. Sæthre, Phys. Rev. Lett. **82**, 1120 (1999).

[8] R. L. A. Haiduke, A. E. de Oliveira, N. H. Moreira and R. E. Bruns, J. Phys. Chem. A **108**, 866 (2004).

[9] A. P. P. Natalense, L. M. Brescansin and R. R. Lucchese, Phys. Rev. A **68**, 32701 (2003).

[10] P. W. Langhoff, in *Electron-Molecule and Photon-Molecule Collisions*, edited by T. Rescigno, V. McKoy and B. Schneider (Plenum, New York, 1979).

[11] J. L. Dehmer and D. Dill, in *Electron-Molecule and Photon-Molecule Collisions*, edited by T. Rescigno, V. McKoy and B. Schneider (Plenum, New York, 1979).

[12] D. Toffoli, M. Stener, G. Fronzoni and P. Decleva, Chem. Phys. **276**, 25 (2002).

[13] M. Stener, S. Furlan and P. Decleva, J. Phys. B **33**, 1081 (2000).

[14] V. Gelius, C. J. Allan, D. A. Allison, H. Siegbahn and K. Siegbahn, Chem. Phys. Lett. **11** 224 (1971).

[15] P. S. Bagus, M. Schrehk, D. W. Davis, D. A. Shirley, Phys. Rev. A **9**, 1090 (1974).

[16] P. S. Bagus, A. J. Freeman and F. Sasaki, Phys. Rev. Lett. **30**, 850 (1973).

[17] N. Mårtensson and A. Nilsson, J. Electron. Spectrosc. and Relat. Phenom. **52**, 1 (1990); A. Nilsson, H. Tiborg and N. Mårtensson, Phys. Rev. Lett. **67**, 1015 (1990); A. Nilsson and N. Mårtensson, Phys. Rev. B **40**, 10249 (1989).

[18] M. Stener, G. Fronzoni and P. Decleva, Chem. Phys. Lett. **351** 469 (2002).

[19] G. Fronzoni, M. Stener and P. Decleva, Chem. Phys. **298** 141 (2004).

[20] M. Stener, G. Fronzoni and P. Decleva, J. Chem. Phys. **122**, 234301 (2005).

[21] A. F. Starace, "Theory of atomic photoionization", in *Handbuch der Physik*, Vol. 31., edited by S. Flugge (Springer-Verlag, Berlin, 1982).

[22] M. Stener, G. Fronzoni, D. Di Tommaso and P. Decleva, J. Chem. Phys. **120**, (2004) 3284.

[23] S. Turchini, N. Zema, G. Contini, G. Alberti, M. Alagia, S. Stranges, G. Fronzoni, M. Stener, P. Decleva and T. Prosperi, Phys. Rev. A **70**, (2004) 14502.

[24] E. J. Baerends , D. E. Ellis and P. Ros, Chem. Phys. **2**, (1973) 41.

[25] C. Fonseca Guerra, J.G. Snijders, G. te Velde and E.J. Baerends, Theor. Chem. Acc. **99**, (1998) 391.

[26] R. Van Leuwen and E.J. Baerends, Phys. Rev. A **49**, (1994) 2421.

[27] P. G. Burke, N. Chandra and F. A. Gianturco, J. Phys. B **5**, (1972) 2212.

[28] H. Bachau , E. Cormier, P. Decleva, J. E. Hansen and F. Martín, "Applications of B-splines in Atomic and Molecular Physics", Rep. Prog. Phys. **64**, (2001) 1601.

[29] M. Brosolo and P. Decleva, Chem. Phys. **159**, (1992) 185.

[30] A. R. Barnett, Comput. Phys. Commun. **27**, (1982) 147.

[31] N. Chandra, J. Phys. B **20**, (1987) 3405.

[32] S. H. Vosko, L. Wilk and M. Nusair, Can. J. Phys. **58**, (1980) 1200.

[33] M. Stener and M. Calligaris, J. Mol. Struct.: TEOCHEM **497**, (2000) 91.

[34] J. P. Perdew, R. G. Parr, M. Levy and J. L. Balduz Jr., Phys. Rev. Lett. **49**, (1982) 1691.

[35] D.P. Chong, O. V. Gritsenko and E.J. Baerends, J. Chem. Phys. **116**, (2002) 1760.

[36] L. Avaldi et al., Private Comm.

[37] V. Carravetta, O. Plachkevytch, O. Vahtras, H. Ågren, Chem. Phys. Lett. **275**, (1997) 70.

[38] R. R. Farren, J. A. Sheehy and P. W. Langhoff, Chem. Phys. Lett. **177**, (1991) 307.

[39] N. Haac, G.Ceballos, H. Wende, K. Baberschke, D. Arvanitis, A. L. Ankudinov and J. J. Rehr, Phys. Rev. Lett. 84, (2000) 614.

[40] P.W. Langhoff, in Resonances in *Electron-Molecule Scattering van der Walls Complexes and Reactive Chemical Dynamics*, vol. 263, edited by D.G. Truhlar (Ed.American Chemical Society, Washington DC, 1984).

[41] R. S. Mulliken, J. Chem. Phys. **7**, 20 (1939).

[42] G. Fronzoni, M. Stener, S. Furlan and P.Decleva, Chem. Phys. **273**, 117 (2001).

Chapter 8

[1] J. L. Dehmer and D. Dill, in *Electronic and atomic collisions*, edited by N. Oda and K. Takayanagi (North-Holland, Amsterdam, 1980) p. 195.

[2] J. L. Dehmer, J. Chem. Phys. **56**, (1972) 4496.

[3] J. L. Dehmer, in *Resonances in Electron-Molecule Scattering van der Walls Complexes and Reactive Chemical Dynamics*, vol. 263, edited by D.G. Truhlar (Ed.American Chemical Society, Washington DC, 1984).

[4] G. Apai, P. S. Wehner, R. S. Williams, J. Stöhr, and D. A. Shirley, Phys. Rev. Lett. **29**, 1497 (1976); R. F. Davis, S. D. Kevan, D. H. Rosenblatt, M. G. Mason, J. G. Tobin and D. A. Shirley, Phys. Rev. Lett. **45**, 1877 (1980); J. Stöhr, K. Baberschke, R. Jaeger, R. Treichler, and S. Brennan, Phys. Rev. Lett. **47**, 281 (1981); J. Stöhr and D. A. Outka, Phys. Rev B **36**, 7891 (1987).

[5] P.W. Langhoff, in Resonances in *Electron-Molecule Scattering van der Walls Complexes and Reactive Chemical Dynamics*, vol. 263, edited by D.G. Truhlar (Ed.American Chemical Society, Washington DC, 1984).

[6] R. S. Mulliken, J. Chem. Phys. **7**, 20 (1939).

[7] J. Kreile, A. Schweig, and W. Thiel, Chem. Phys. Lett. **108**, 259 (1984).

[8] J. A. Sheehy, T. J. Gil, C. L. Winstead, R. E. Farren, and P. W. Langhoff, J. Chem. Phys. **91**, 1796 (1989).

[9] M. Venuti, M. Stener, and P. Decleva, Chem. Phys. **234**, 95 (1998).

[10] D. Toffoli, M. Stener, G. Fronzoni and P. Decleva, Chem. Phys. **276**, 25 (2002).

[11] G. Fronzoni, M. Stener, S. Furlan and P.Decleva, Chem. Phys. **273**, 117 (2001).

[12] M. Stener, G. Fronzoni, D. Toffoli, P. Colavita, S. Furlan, and P. Decleva, J. Phys. B **35**, 1421 (2002).

[13] Di Tommaso and P. Decleva, J. Chem. Phys. **123**, 064311 (2005).

[14] M. Stener, D. Di Tommaso, G. Fronzoni, P. Decleva, and I. Powis, J. Chem. Phys., in press.

[15] A. U. Hazi, H. S. Taylor, Phys. Rev. A **1**, 1109 (1970).

[16] C. L. Winstead and P. W. Langhoff, Chem. Phys. Lett. **151**, 417 (1988).

[17] C. de Boor, *A Pratical Guide to Splines* (Springer, New York, 1978).

[18] M. Brosolo, P. Decleva, and A. Lisini, Computer Phys. Commun. **71**, 207 (1992).

[19] A. F. Starace, "Theory of atomic photoionization", in *Handbuch der Physik*, Vol. 31., edited by S. Flugge (Springer-Verlag, Berlin, 1982).

[20] H. S. Taylor, Advan. Chem. Phys. **18**, 91 (1970).

[21] E. Holøien and J. Midtal, J. Chem. Phys. **45**, 2209 (1966).

[22] A. Riera, J. Phys. Chem **97**, 1558 (1993).

[23] W. Thiele, J. Electr. Spectrosc. and Relat. Phenom. **31**, 151 (1983).

[24] H. Hergenhahn, O. Kugeler, A. Rüdel, E. E. Rennie, and A. Bradshaw, J. Phys. Chem. A **105**, 5704 (2001).

[25] D. W. Lindle, C. M. Truesdale, P. H. Kobrin, T. A. Ferret, P. A. Heimann, U. Becker, H. G. Kerkoff, and D. A. Shirley, J. Chem. Phys. **81**, 5375 (1984).

[26] B. Kempgens, A. Kivimäki, M. Neeb, H. M. Köppe, A. M. Bradshaw, J. Feldhaus, J. Phys. B **29**, 5389 (1996).

[27] D. Dill and J. L. Dehmer, Phys. Rev. Lett. **35**, 213 (1975).

[28] D. Loomba, S. Wallace, D. Dill, and J. L. Dehmer, J. Chem. Phys. **75**, 4546 (1981).

[29] M. Stener, G. Fronzoni, and P. Decleva, Chem. Phys. Lett. **112**, 469 (2002).

List of Publications

M. Stener, G. Fronzoni, D. Di Tommaso, and P. Decleva "*Density Functional study on the Circular Dichroism of photoelectron Angular Distribution from chiral derivatives of oxirane*", J. Chem. Phys **120**, 3284 (2004); Chapter 3.

M. Stener, D. Di Tommaso, G. Fronzoni, P. Decleva, and I. Powis, *Theoretical study on the circular dichroism in core and valence photoelectron angular distributions of camphor enantiomers*, J. Chem. Phys., in press; Chapter 4.

A. Giardini, D. Catone, S. Stranges, M. Satta, S. Piccirillo, S. Turchini, N. Zema, G. Contini, T. Prosperi, P.Decleva, D. Di Tommaso, G. Fronzoni, M. Stener, A. Filippi, and M. Speranza, *Angle Resolved Photoelectron Spectroscopy of Randomly Oriented 3-Hydroxytetrahydrofuran Enantiomers*, ChemPhysChem **6**, 1164-1168 (2005); Chapter 5.

D. Di Tommaso, M. Stener, G. Fronzoni, and P. Decleva, *Conformational Effects on the Circular Dichroism in the photoelectron Angular Distribution*, ChemPhysChem, in press; Chapter 6.

Di Tommaso and P. Decleva, *Branching Ratio Deviations from Statistical Behaviour in Core Photoionization*, J. Chem. Phys. **123**, 064311 (2005); Chapter 7.

Riassunto della Tesi

Lo scopo della presente tesi è l'applicazione e lo sviluppo del metodo LCAO B-spline DFT, basato sulla Combinazione Lineare degli Orbitali Atomici (LCAO), sulla Teoria del Funzionale Densità (DFT) e sull'impiego delle funzioni di base B-spline, per lo studio della fotoionizzazione molecolare.

Nel Capitolo 1 viene considerata una breve introduzione al processo di fotoionizzazione e alla teoria della fotoionizzazione molecolare. Nel Capitolo 2 vengono presentati i metodi computazionali utilizzati durante il presente lavoro di tesi. I risultati ottenuti sono presentati nei successivi Capitoli della tesi.

Il lavoro è suddiviso in tre parti.

Nella prima parte (Capitoli 3-6) il metodo LCAO B-spline DFT è applicato allo studio del Dicroismo Circolare nella Distribuzione Angolare (CDAD) dei fotoelettroni emessi da molecole chirali, ionizzate da luce circolarmente polarizzata di definita elicità.

Un primo studio computazionale sull'effetto CDAD è focalizzato su una serie di derivati chirali dell'ossirano, con lo scopo di identificare tendenze lungo la serie molecolare. I risultati evidenziano una inaspettata sensibilità da parte del dicroismo circolare verso cambiamenti nella struttura elettronica molecolare. Inoltre i valori calcolati sottolineano come l'intensità dell'effetto CDAD è da attribuire non tanto alla chiralità dello stato iniziale, ma bensì alla capacità della funzione d'onda del fotoelettrone (completamente delocalizzata su tutta la molecola) di sondare l'asimmetria nel potenziale molecolare effettivo.

Il metodo LCAO B-spline DFT è quindi applicato allo studio del dicroismo circolare nella distribuzione angolare dei fotoelettroni emessi dai livelli di core e di valenza degli enantiomeri della canfora. I risultati sono confrontati con i valori calcolati attraverso l'approccio Continuum Multiple Scattering: i due metodi teorici mostrano un sostanziale accordo nei risultati. Inoltre, un confronto dei risultati calcolati con i dati sperimentali disponibili mostra un accordo sostanziale se non addirittura quantitativo.

E' inoltre presentato uno studio teorico e sperimentale sul dicroismo circolare nella distribuzione angolare dei fotoelettroni emessi dai livelli di valenza del 3-idrossitetraidrofurano, il quale è una molecola relativamente flessibile. Questo lavoro mette luce su nuove caratteristiche del dicroismo in fotoemissione, il quale appare molto sensibile a fattori di tipo conformazionale.

L'influenza degli effetti conformazionali sui parametri dinamici di fotoionizzazione, con particolare attenzione all'effetto CDAD, è quindi investigata in dettaglio. Il metodo LCAO B-spline DFT è applicato ai conformeri della molecola (1R,2R)-1,2-dibromo-1,2-dicloro-1,2-difluoroetano. Il parametro dicroico mostra una significativa sensibilità verso il conformero della molecola. Ciò suggerisce che il profilo energetico del parametro dicroico potrebbe essere utilizzato come un *fingerprint* dei conformeri di una molecola chirale. Il metodo computazionale è anche applicato alla rotazione del metile nella molecola (S)-ossirano, in modo da verificare l'assunzione che la rotazione del metile non influisca in maniera significativa sui valori calcolati dell'effetto CDAD. Si verifica invece come la rotazione del gruppo metile provochi variazioni inaspettate e drammatiche sul profilo del parametro dicroico.

La seconda parte del lavoro (Capitolo 7) riguarda l'investigazione teorica sulla correttezza dell'assunzione che il Branching Ratio nella ionizzazione dei livelli di core di siti atomici chimicamente diversi dello stesso elemento, segua il rapporto statistico. Il metodo LCAO B-spline DFT è stato impiegato per calcolare in maniera accurata le sezioni d'urto associate alla ionizzazione degli orbitali 1s dei carboni per un set di molecole organiche scelte. I risultati mostrano che deviazioni nella sezione d'urto inducono forti andamenti non statistici da parte dei Branching Ratios relativi alla ionizzazione dei livelli core, fino a diversi eV sopra la soglia di ionizzazione.

La parte finale della tesi (Capitolo 8) riguarda il problema delle shape resonances. La razionalizzazione delle strutture risonanti, spesso presenti nello spettro molecolare del continuo, è un problema ampiamente discusso. Nel presente lavoro una nuova metodologia per localizzare e caratterizzare in termini molecolari le shape resonances viene proposta. Partendo da un sistema modello, è stato sviluppato un metodo per caratterizzare le risonanze in termini di contributo da parte degli orbitali virtuali di valenza. Il metodo sviluppato è quindi esteso al caso molecolare ed applicato alla localizzazione e caratterizzazione delle shape resonances che appaiono nella fotoionizzazione dei livelli σ_g di core e di valenza di N_2.